Mechanical and configurational degeneracy in transition metal cyanide materials

Andrew B. Cairns

Wadham College

A thesis submitted to the University of Oxford for the degree of Doctor of Philosophy

Inorganic Chemistry Laboratory

Trinity Term 2015

The work presented in this thesis was carried out between October 2011 and June 2015 in the Inorganic Chemistry Laboratory, University of Oxford under the supervision of Prof. Andrew L. Goodwin. All of the work is my own unless otherwise stated, and has not been submitted previously for any degree at this or any other university.

Andrew Brian Cairns

June 2015

Mechanical and configurational degeneracy in transition metal cyanide materials

Andrew B. Cairns, Wadham College
D.Phil., Trinity Term 2015

Molecular framework materials—materials constructed like atomic scaffolding where anionic *polyatomic* linkers join cationic metal nodes—have great currency in contemporary functional material design. In this thesis the structures and properties of transition metal cyanides are investigated, focusing on the impact of mechanical and configurational degeneracy. These related phenomena give rise to materials with unusual and extreme *negative* mechanical responses on the one hand, and exotic structural states on the other.

The mechanical response of primary interest here is negative linear compressibility (NLC), a rare but desirable property where a material actually expands in one direction against increasing hydrostatic pressure. The performance of NLC materials—for use in areas such as sensitive pressure sensing, actuators, and development of artificial muscle—critically depends on the intrinsic NLC response. Until recently very few NLC materials were known and, of those, the expansion was small in comparison to the normal contraction of common engineering materials.

Here I show that several dicyanometallate frameworks, those based on the almost-linear $[M(CN)_2]^-$ (M = Ag, Au) linker, exhibit a prolonged NLC response up to ten times larger than established NLC candidates. Using two structure design modifications—soft-mode frustration to prevent structure collapse and supramolecular motifs that enhance compressibility—both the range over which NLC is observed and the magnitude of response have been increased. In the former, the extended perovskite-like system $KM[M'(CN)_2]_3$ is used as a model system, whilst 'spring'-like supramolecular interactions in zinc(II) dicyanoaurate(I), $Zn[Au(CN)_2]_2$, gives rise to an exceptional response—the first report of 'giant' NLC.

Variable-pressure studies on the canonical isotropic negative thermal expansion (NTE) material zinc (II) cyanide reveals both its intrinsic phase transition behaviour, giving insight into the mechanism of NTE, and NLC as a result of the improper ferroelastic phase transition at 1.52 GPa. This investigation resolves several discrepancies and contradictions in the field and suggests the mechanical responses of isostructural frameworks may be understood in terms of underlying dynamic instabilities, in much the same way as for many conventional ceramic materials.

In the second part of this thesis, configurational degeneracy is explored focusing on structural disorder. Beginning with a summary of well-characterised examples of disorder in molecular frameworks, I go on explore the collective states arising from degeneracy in the 'simple' chain cyanides AgCN, AuCN and $(Ag_{1/2}Au_{1/2})CN$. By considering chains as geometric objects with simple pairwise interactions, we find the emergence of complex structural states that are directly related to the XY magnetic structures on a triangular lattice. Structurally degenerate states appear inherent in a range of framework materials; many possibilities exist in this field for targeting, enhancing and coupling counterintuitive mechanics and complex states with other functionalities.

Acknowledgements

I would like to begin by thanking my supervisor, Prof. Andrew L. Goodwin, for his immeasurable help with the work contained in this thesis: it simply would not have been possible to achieve any of this without his patience, good humour, imagination and brilliance (encapsulated in the many "I was just thinking about X..." moments). When I first came to speak to Andrew about doing a Master's project I had no idea what would result, and I definitely did not imagine staying for five years and doing so much amazing science. I am consistently amazed by your work and I look forward to working with you in the future.

This work was supported financially by the EPSRC and ERC, including funding my doctoral studentship for which I am very thankful.

No thesis is possible without the guidance and assistance of many talented colleagues, especially in experimental science. Much of the supplementary crystallographic and spectroscopic work contained in this work were carried out by Dr Julien Haines and his team in France for which I am immensely grateful—Jadna Catafesta, Claire Levelut, Jérôme Rouquette, Arie van der Lee, Lars Peters, Patrick Hermet, David Maurin and Jean-Louis Bantignies. Thank you to François-Xavier Coudert for your beautiful computational work that helped so much in Chapter 7. To those in Chem Cryst Oxford (Dr Amber Thompson, Prof. Richard Cooper) plus Dr Phil Wiseman, who helped with all things crystallographic (including keeping the machines running), thank you. Most of the experiments described here were performed at central facilities, and I am very thankful to the various beamline and instrument scientists who helped make these happen. To Dr Matthew Tucker (ISIS/Diamond), your assistance has had the biggest impact on my work from the moment you gave some 'commissioning time' to squeeze one of my cyanide frameworks. I cannot count the number of experiments that you have been critical in ensuring the success of (often whilst running four other instruments at the same time!). Others who I have worked directly with include: Vladimir Dmitriev and Phillip Pattison (ESRF); Julia E. Parker, Chiu C. Tang and Dominik Daisenberger (Diamond Light Source); David Keen, Aziz Daoud-Aladine and Kevin Knight (ISIS). I am also thankful to ISIS Spallation Neutron Source, Diamond Light Source, and the ESRF for the award of beamtime.

Parts of this thesis are modelled or taken directly from published papers that have arisen from its content. As such, the co-authors of these papers—having offered sugges-

tions and contribution in terms of content, structure and phasing—will have also contributed in a similar way to this thesis. These publications are indicated in the list of publications that immediately precedes the main text. I would also like to thank Prof. Paul Madden and Prof. Tony Cheetham for examining this thesis, and for their insightful comments and suggestions offered as part of that process.

A research group is about more than just the work carried out. I have been very lucky to share this experience with some good friends, and some brilliant colleagues. Thank you to Ines, Callum, Jasper and Joe who were there from the start: for teaching me so much (especially Ines) and making the group a fun place to be. Joe has been around as long as I have and I thank him for showing us all there's always the Joe way, for introducing me to the world of frustrated magnetism, and for your sense of calm and humour. Josh H. arrived as a very keen Part II student and has been my partner-in-cyanide-research ever since. You definitely *do* know more about cyanides than I do! I also thank Nick for reminding us all to be a more rigorous, Matt for reminding us that a Rietveld refinement is never really perfect, Peter for being a voice of (Danish) reason, Sam for proofreading this thesis, all the wonderful Part IIs over the years, and the newcomers who keep the group evolving. I remember vividly my first day in CG11 when the Goodwin Group formed and I hope it continues to grow and prosper.

To my friends new and old, I thank you all for wonderful times away from work. Karim has always been there to distract me (in work or not): thanks for convincing me that going to Hawaii was a good idea, and for your friendship. Matt S you are a wonderful person, and you have always been there for me. Thank you to my Trinity friends, Jack, Caroline, Emer, Becky, Dave, Steve, Greg, Wanzhen, and to the multiple generations of Nightline volunteers I have worked with, especially Rachel S., Rob, Sarah E-.D., Sarah D., Jonny, Vicki, Rich, Hari, Helen, Zara, Claire R. Having a fun and caring home in Oxford has been very important through this process, and I am thankful to my adopted home at extended 65b (Alice, Andrew, Chris, Eva, Howard, Ioanna, Laura, Libby, Liz and Steph) and my current housemates (Alice, Dan, Josh and Steph) for cooking extravaganzas, late night chats, 'normal tea with milk', and for caring.

I am incredibly fortunate to have been supported through this process by Josh, a most wonderful person who I am thankful to have in my life. Thank you for listening, for caring about my work, for putting up with my random thoughts, and for helping me so much in the last stretch of writing this thesis. You are one of the most dedicated scientists I know, and I truly believe your hard work will change the world one day. I can't wait to see what you will achieve as we both move into the next stages of our lives.

Finally, I would like to thank my parents and brother for their love and support throughout my extended education. You have always been interested in my work, even if the relevance to the real world was never that clear ("Chemistry, but not the bubbly test tube kind" is a close enough description!). You helped me in so many ways so I could get to where I am today.

Contents

Abbreviations

2θ	scattering angle (diffraction)
Å	Ångström (= 10^{-10} metres)
α_ℓ	linear coefficient of thermal expansion
α-Po	α-polonium (cubic) net
a, b, c	crystallographic axis
a, b, c	unit cell axis vectors
a-MOF	amorphous metal-organic framework
B_0	bulk modulus (GPa)
cm^{-1}	wavenumber (inverse centimetre)
CRN	continuous random network
d	d-spacing
DAC	diamond anvil cell
EoS	equation of state
IR	infrared
K_ℓ	linear compressibility
L	linker anion (general)
M	metal cation (general)
MC	(direct) Monte Carlo
MOF	metal–organic framework
NLC	negative linear compressibility
NMR	nuclear magnetic resonance
NPD	neutron powder diffraction
NTE	negative thermal expansion
PDF	pair distribution function

P-E	Paris-Edinburgh press
PLC	positive linear compressibility
PTE	positive thermal expansion
PTM	pressure transmitting medium
PXRD	powder X-ray diffraction
RMC	reverse Monte Carlo
RUM	rigid-unit mode
SC XRD	single crystal X-ray diffraction
STEM	scanning tunnelling electron microscopy
VT	variable temperature
VP	variable pressure
XRD	X-ray diffraction
ZIF	zeolitic imidazolate framework
ZTE	zero thermal expansion

Publications

Full list of publications arising during the course of this work; those that are incorporated into the main text of this thesis are indicated by an asterisk.

- *Cairns, A. B., Cliffe, M. J., Paddison, J. A. M., Daisenberger, D., Tucker, M. G., Coudert, F.-X., and Goodwin, A. L. Encoding complexity within supramolecular analogues of frustrated magnets *Nature Chem.*, 2016 (in press, DOI: 10.1038/nchem.2462).

- Paddison, J. A. M., Cairns, A. B., Khalyavin, D. D., Manuel, P., Daoud-Aladine, A., Ehlers, G., Petrenko, O. A., Gardner, J. S., Zhou, H. D., Goodwin, A. L. and Stewart, J. R. Nature of partial magnetic order in the frustrated antiferromagnet $Gd_2Ti_2O_7$ *Phys. Rev. Lett.*, 2015 (submitted, arXiv: 1506.05045).

- *Cairns, A. B. and Goodwin, A. L. Negative linear compressibility *Phys. Chem. Chem. Phys.*, 2015, **17**, 20449–20465.

- Hill, J. A., Cairns, A. B., Lim, J. J. K., Cassidy, S. J., Clarke, S. J. and Goodwin, A. L. Zero-strain reductive intercalation in a molecular framework *CrystEngComm*, 2015, **17**, 2925–2928.

- Tominaka, S., Hamoudi, H., Suga, T., Bennett, T. D., Cairns, A. B. and Cheetham, A. K. Solid-state conversion of a dense metal–organic framework from a crystalline insulator to an amorphous semiconductor *Chem. Sci.*, 2015, **6**, 1465–1473.

- Hunt, S. J., Cliffe, M. J., Hill, J. A., Cairns, A. B., Funnell, N. P. and Goodwin, A. L. Flexibility transition and guest-driven reconstruction in a ferroelastic metal–organic framework *CrystEngComm*, 2015, **17**, 361–369.

- Hodgson, S. A., Adamson, J., Hunt, S. J., Cliffe, M. J., Cairns, A. B., Thompson, A. L., Tucker, M. G., Funnell, N. P. and Goodwin. A. L. Negative area compressibility in silver(I) tricyanomethanide *Chem. Commun.*, 2014, **50**, 5264–5266.

- Hermet, P., Catafesta, J., Bantignies, J.-L., Levelut, C., Maurin, D., Cairns, A. B., Goodwin, A. L. and Haines, J. Vibrational and thermal properties of $Ag_3[Co(CN)_6]$ from first principles calculations and infrared spectroscopy *J. Phys. Chem. C*, 2013, **117**, 12848–12857.

- *Collings, I. E., Cairns, A. B., Thompson, A. L., Parker, J. E., Tang, C. C., Tucker, M. G., Catafesta, J., Levelut, C., Haines, J., Pattison, P., Dmitriev, V. and Goodwin, A. L. Homologous critical behaviour in the diamondoid frameworks $Zn(CN)_2$ and Cd(imidazolate)$_2$ *J. Am. Chem. Soc.* 2013, **135**, 7610–7620.
Adapted with permission, copyright 2013 American Chemical Society.

- *Cairns, A. B. and Goodwin, A. L. Structural disorder in molecular framework materials *Chem. Soc. Rev.*, 2013, **42**, 4881–4893.
Reproduced by permission of The Royal Society of Chemistry

- *Cairns, A. B., Catafesta, J., Levelut, C., Rouquette, J., van der Lee, A., Peters, L., Thompson, A. L., Dmitriev, V., Haines, J. and Goodwin, A. L. Giant negative linear compressibility in zinc dicyanoaurate *Nature Mater.*, 2013, **12**, 212–216.

- Cairns, A. B., Thompson, A. L., Tucker, M. G., Haines, J. and Goodwin, A. L. Rational design of materials with extreme negative compressibility: Selective soft-mode frustration in $KMn[Ag(CN)_2]_3$ *J. Am. Chem. Soc.*, 2012, **134** , 4455–4456.

Chapter 1

Introduction

Some the most exciting developments in materials science in the last decade have come from a new class of material called molecular framework materials. These materials could provide next-generation gas storage and catalysis solutions, multifunctional response components in electronic circuits, advanced sensing capabilities, and many other applications besides. This thesis explores the utility of structure design in molecular frameworks, in particular the structures and properties of transition metal cyanide materials. Cyanides may be thought of as inorganic chemistry in its most traditional form: materials with canonical structures and well-understood properties. However, the simple premise of these frameworks—the connecting in one, two or three dimensions of metal cations with molecular linkers—produces a surprising structural diversity and materials with extremely unusual properties. In this introduction I explore flexibility and disorder in materials by focusing on the concept of degeneracy; I then summarise how we might measure mechanical responses of materials, and the principles of diffraction that will be the main characterisation technique applied in this work; following this I will summarise why the chemistry of molecular frameworks in particular might be useful in the study of unusual physical properties of materials.

1.1 Degeneracy

In the physical sciences, degeneracy is a phenomenon encountered most commonly in quantum mechanics [1]. Degeneracy arises when a particle (*e.g.* an electron) exists in different measurable states with essentially the same energy. For a chemist, degeneracy most obviously arises when describing the electronic structure of atoms: the atomic or molecular orbitals that underpin our understanding of matter. For atoms where the angular quantum number $l > 1$ there exist $(2l + 1)$ degenerate states (*e.g.* for the atomic p orbitals, $l = 1$ and there are three degenerate orbitals p_x, p_y, p_z). This degeneracy may

be lifted by perturbing the system, for example the effects of ligands around transition metal cations means that the critical d orbitals are no longer degenerate, giving rise to preferential bonding geometries and the vibrant colours of many metal complexes [2].

The simple concept of degeneracy in fact arises in many other areas of science. For example, in biological systems components that are structurally different may appear to be functionally equivalent under some conditions, but distinct under others [5]. These degenerate components—like the degeneracy of certain parts of the genetic code that encode identical proteins (polypeptides)—are furthermore seen as a key to the evolution of life [5, 6]. The critical importance of this functionality means that degeneracy is distinct from redundancy.

Here we consider degeneracy in the context of materials science and the structures of solid matter: how materials may have many structures with essentially equivalent energies that may exist under different conditions. There are two manifestations of degenerate states of matter that we will consider. First, *dis*order arises in materials where many structurally distinct configurations are found in the solid state, with there being an infinite number of equivalent ground state structures at absolute zero [7]. Here I term

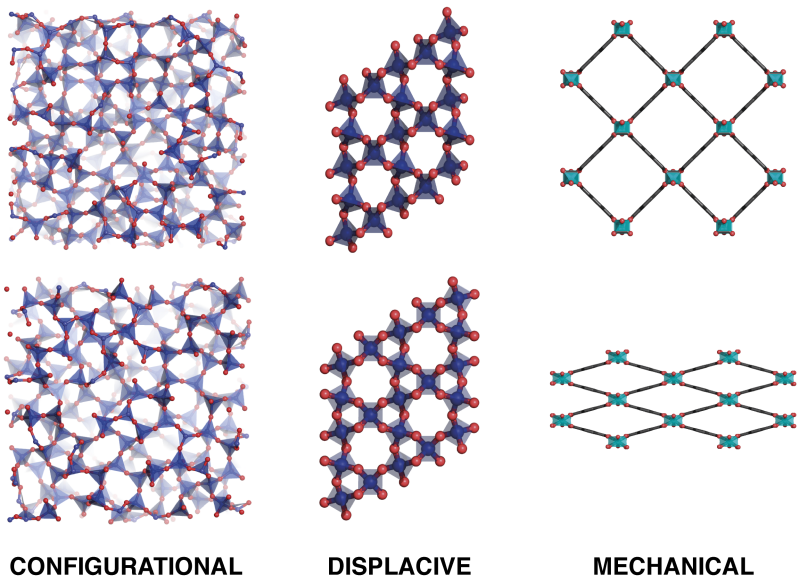

Figure 1.1: Configurational, displacive and mechanical degeneracy in network solids *(l-r)* Configurational degeneracy shown in two equivalent continuous random network models for silica glass, displacive degeneracy shown in the $\alpha \rightarrow \beta$ transition in quartz (structures from Ref. 3), and mechanical degeneracy in going from the large pore to narrow pore structures of MIL-54(Al) (structures from Ref. 4).

this *configurational degeneracy*. Second, flexibility arises where a material's structure is the minimum in a shallow potential energy valley. External stimuli such as application of pressure or temperature result in large structural changes, but where the change in structure energy can be small [8, 9]. Implicit here are both *displacive degeneracy*, where bonds change length or direction within a structure with little change in energy [10], and *mechanical degeneracy*, where different mechanical states are observed with similar energies [Fig. 1.1]. In all cases degeneracy arises where local bonding interactions dominate. In the following sections these phenomena are explored in more detail using key examples from the literature.

1.1.1 Configurational degeneracy

The structure of functional materials is often (rightly) based on a description of regularly repeating, well ordered—crystalline—atoms or molecules. In many of the highest-profile areas of research within contemporary solid state science, however—from spin frustration in cooperative paramagnets [11] to thermoelectrics [12], through to polar nano-domain formation in relaxor ferroelectrics [13]—*dis*order plays a central role in driving function. Configurational degeneracy occurs when the local symmetry of the system does not translate to long-range order, *i.e.* there is irregularity to the arrangement of atoms or molecules. Complete lack of crystalline order exists in amorphous or 'glassy' systems; between total order and total structural disorder there exists a continuum of materials with partial order including those with point defects, dislocations, dynamic and correlated disorder.

Silica glass (SiO_2) is perhaps the canonical amorphous material and is one of many natural 'glasses formers', a class that also includes very large molecule materials, such as glycerol, and polymer systems such as polystyrene, rubbers and epoxy resins. Other materials can be forced to adopt an amorphous structure by rapid quenching, cold surface condensation or application of mechanical pressure [15]. The lack of long-range order means that there are multiple stable configurations with essentially the same energy: local bonding interactions are not sufficiently unique to give long-range order (they are underconstrained). Structures of underconstrained systems may be related to liquid-like

solid states, random packing of individual spheres, polyhedra or other larger assemblies in 1, 2 or 3 dimensions [16].

Such apparently 'random' underconstrained structures is one manifestation of *frustration* [Fig. 1.2]. Frustration arises where symmetry-incompatibility exists between local and extended degrees of freedom [18]. For a hard sphere solid—a solid where the average atom–atom bond distances are well determined from the Lennard-Jones potential—if there is no directional bonding, frustration between local and global close packing an amorphous state results [15].* Locally the most stable configuration for four isolated interacting atoms is a regular tetrahedron, however the regular tetrahedral dihedral angle is not a multiple of 2π so tetrahedra cannot perfectly fill Euclidian space [17, 19] [Fig. 1.3]. The dense random packing of spheres proceeds such that each additional sphere touches three others and no voids are left that could accommodate another sphere [17]. Experimental realisations of this frustrated packing is observed in the metallic alloy glasses such as $Au_{75}Si_{25}$, formed by rapid cooling from the liquid state [20].

The mechanical properties of glasses have long been known, with many being brittle and optically transparent, and when heated going through a glass transition T_g to a plastic

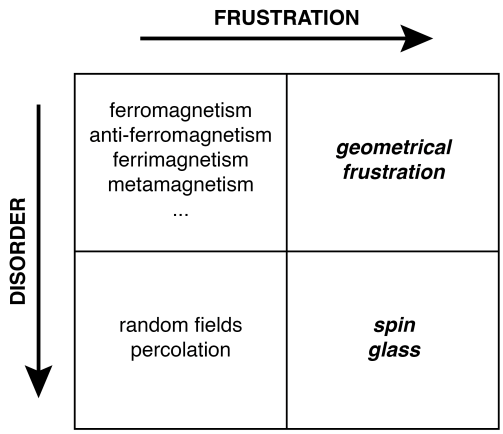

Figure 1.2: Relationship between structural frustration and disorder in magnetic systems. The existence of disorder and frustration can give rise to a range of interesting phenomena in magnetic systems. Well-known ordering occurs when neither are present (ferromagnetism *etc.*) whereas exotic states such as 'spin glasses' and 'geometrical frustration' emerge where frustration is present. Figure adapted from Ref. 14.

---

* The formation of an amorphous vs. a quasi-crystalline state strictly depends on the packing density [17]

phase characterised by a large change in thermal expansion coefficient. The structures of glasses are, however, more difficult to characterise and pose a much greater challenge within structural science [22]. The 1932 Zachariasen model of a 2D glass [21] —based on the continuous random connection of 2D triangular SiO_3 units to form rings of various sizes—was hugely influential and widely used to describe the 3D structure of silica glass. This model was recently verified experimentally [Fig. 1.4] by atomic resolution scanning tunnelling electron microscopy (STEM) [23]. For silica glass, the local geometry is made up of $[SiO_4]$ tetrahedra that form a corner sharing network. Strongly directional local bonding can be accommodated by an essentially random connection of tetrahedra to form a 'continuous random network' (CRN) [24]. This model is constructed such that there is a small random variation in the angle between a tetrahedron and its neighbour. How these random variations propagate through the structure leads to a very large number of configurations that are equivalent CRNs [Fig. 1.1]. The various bond length, bond-angle and torsion-angle distributions in this phase are remarkably similar to those in the crystalline polymorph α-cristobalite, despite the absence of any long-range structural periodicity (the network has no unit cell).

Structural underconstraint leading to *partial* disorder is found in the structure of cubic water ice (ice I_c), as first suggested by Pauling [25, 26]. Here one component of

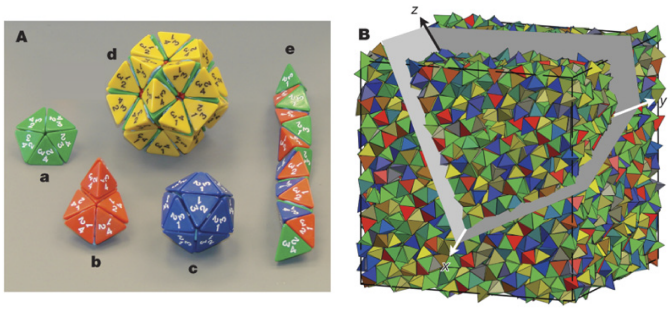

Figure 1.3: Relationship between structural frustration and disorder. A Ideal local packing motifs built from tetrahedral dice stuck together with modelling putty. The pentagonal dipyramid (a), the nonamer (b) and the icosahedron (c) maximise local packing density. The icosahedron can be extended by adding a second shell (d), but then the large gaps between the outer tetrahedra lower the density. The tetrahelix (e) maximises packing density in one dimension. **B** A quasicrystal with packing fraction 0.8324 is obtained by first equilibrating an initially disordered fluid of 13,824 hard tetrahedra using Monte Carlo simulation and subsequent numerical compression. Reprinted by permission from Macmillan Publishers Ltd: *N*ature, Ref. 17, copyright 2009.

the system is well ordered (the oxygen atoms), whilst the other component (the hydrogen atoms that connect the oxygen atoms) is disordered. This disorder is not random but rather is *correlated*. Oxygen atom positions in real water ice form a pyrochlore lattice (corner sharing tetrahedra); illustration of the correlated nature of disorder is more easily shown however on a 2D equivalent system known as 'square ice' [Fig. 1.5]. The molecular nature of water means that two hydrogens are covalently bonded to each oxygen, with each oxygen forming two additional 'hydrogen bonds'. These 2-in-2-out 'ice rules' lead to a very large number of possible ice configurations. The correlated disorder state shown in Figure 1.5(b) is visually different to both (a) the fully ordered system and (c) a random disordered state, also seen through the forms of their diffraction patterns [Fig. 1.5(d–f), see §1.3.1]. In the 3D case, this disorder is characterised by each H_2O molecule pointing towards a tetrahedron edge on the pyrochlore lattice with the local rules ensuring that none of these edges meet [Fig. 1.6].

Consequences of this structural disorder include a significant diffuse scattering component to the single-crystal diffraction patterns as simulated in Figure 1.5(e). The origin of this unusual diffraction pattern is discussed in further detail in the following section, but here we can see that it is clearly distinct from those of both the completely ordered and disordered systems. Degenerate ground states are critical in the understanding of the unusual properties of ice, including its finite excess entropy as the sample is cooled to absolute zero [26] and its lack of average electric dipole. Inspection of the diffraction patterns

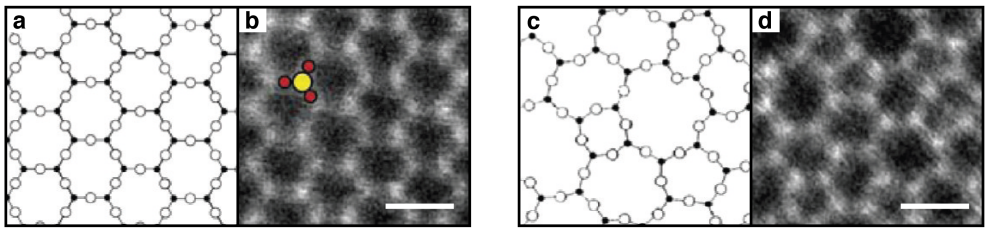

Figure 1.4: The Zachariasen model of 2D-crystalline and glass SiO_2 compared to atomic-resolution images of 2-layer SiO_2 on graphene. SiO_2 supported on graphene forms structures analogous to the crystalline (left) and amorphous (right) 2D Zachariasen models [21]. The models (a,c) have a strong qualitative match to the ADF-STEM images (b,d) showing the formation of a 2D glass that obeys the continuous random model. Adapted with permission from *Nano Lett.* 2012, **12**, 1081–1086. Copyright 2012 American Chemical Society.

of structurally similar systems reveals striking motifs: in pyrochlore-structured superionic conductor α-$Cu_{1.8}Se$, negative thermal expansion material $Cd(CN)_2$, and $Yb_2Ti_2O_7$ [Fig. 1.6]. Here, almost identical rules to the pattern of disorder—local structural rules—give rise to the same scattering motifs. The existence and properties of frustrated magnetic 'spin ice' and 'spin glass' systems like $Yb_2Ti_2O_7$ are well established. The properties of these systems are strongly related to ice itself, characterised by an energy landscape with many nearly-degenerate ground state configurations separated by barriers of random height. Electronic 'charge ice' states as seen in $Cd(CN)_2$ are furthermore thought to be critical to the understanding of its unusual negative thermal expansion behaviour [29]. In all of these cases, orientational disorder is frozen well above the hypothetical ordering temperature due to the high activation energy required for relaxational processes compared to the ordering energy [30].

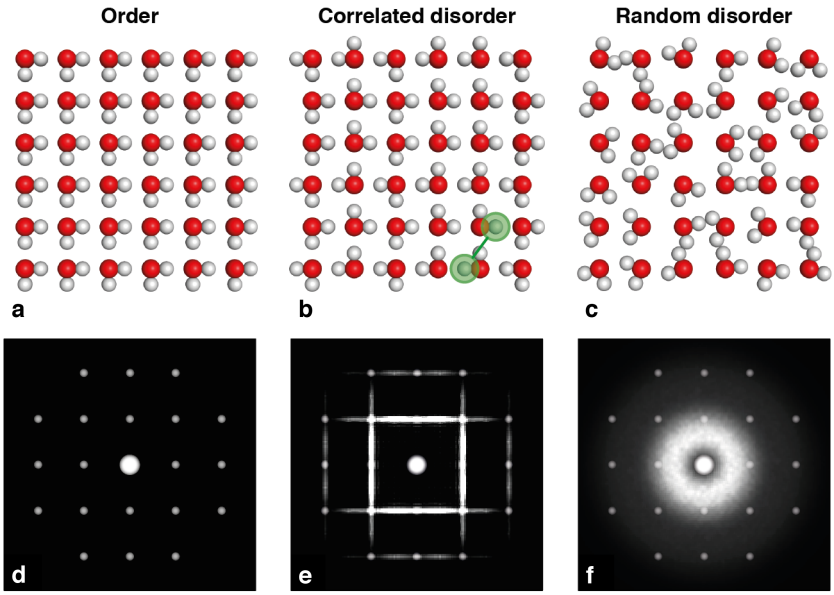

Figure 1.5: Structural underconstraint and correlated disorder in 'square ice'. Using a simplified version of 3D ice, here we see that each oxygen atom (red spheres) is covalently bonded to two hydrogen atoms (white spheres) at 90°. How this bonding propagates across the structure is not well-constrained. In the first case, all water molecules point in one direction so giving a fully ordered model which gives rise to only Bragg reflections (a,d), whilst in the random case there is a broad diffuse scattering component as well as Bragg reflections due to the positions of oxygen atoms (c,f). Applying the constraint that each oxygen must be covalently bonded to only two hydrogens and hydrogen bonded to two others, correlated disorder arises (b). A correlation not found in (a) or (c) is highlighted in green. This gives rise to characteristic lines of diffuse scattering (e), as calculated using DISCUS [27]. Adapted by permission from Macmillan Publishers Ltd: *Nature*, Ref. 28, copyright 2015.

Other orientational glasses include mixed molecular systems where anisotropic molecules are substituted by isotropic atoms: *e.g.* KCl:KOH, KCN:KBr [30]. Disordered anisotropic dipolar, quadrupolar or octopolar electrostatic forces lead to glassy ground states where the orientations of the non-spherical component are not long-range ordered, whilst above a certain temperature a plastic-like phase emerges [30]. Cyanide glasses, in particular, have acted as a model system for rationalising the properties of amorphous materials where disorder arises as an orientational perturbation on the translational order of the lattice. Furthermore, these systems show strong coupling between orientational degrees of freedom and translational phonon modes [30], directly analogous to the disordering of magnetic interactions in a spin glass system like CuMn, where dilute Mn atoms sit in random sites [14, 30].

Geometric frustration arises when the underlying structural motif is inconsistent with the interactions on that motif, without the need to introduce structural disorder [30]. The classic examples of this are Ising spins on a 2D triangular lattice [Fig. 1.7]. For an idealised system where all interaction strengths are equal and structural distortion is negligible, there is a large number of ground states where within each triangle two spins are aligned; in the extended system this results in a pattern where each spin is surrounded by four antiferromagnetic interactions and two ferromagnetic. This large number of equiva-

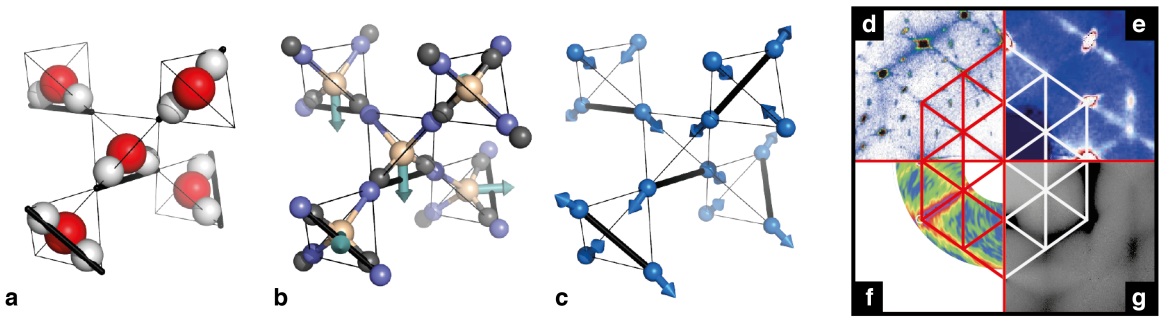

Figure 1.6: Ice-like states on the pyrochlore lattice. (a) Extension of the 'square ice' state to 3D means that each H_2O molecule in ice I_c can be seen as orientated towards one edge of a pyrochlore lattice with many different degenerate states that satisfy the local 'ice rules'. Similar displacements are also found experimentally in so-called 'charge ices' e.g. in $Cd(CN)_2$ where metal cation off-centering is thought to drive negative thermal expansion (NTE), and spin orientations in 'spin ice' system. Diffraction patterns of (d) the superionic conductor α-$Cu_{1.8}Se$ (e) $Cd(CN)_2$ (f) the spin ice $Yb_2Ti_2O_7$ and (g) water ice all show qualitatively similar diffraction patterns arising from similar disordering mechanisms. Adapted by permission from Macmillan Publishers Ltd: *N*ature, Ref. 28, copyright 2015.

lent ground states arises because of frustration and results in a finite residual entropy of approximately $S \simeq 0.32\,\mathrm{k_B}$. The 2D triangular system as described has been the focus of a huge amount of interest however it is difficult to find a system where such frustration exists that is maintained to low temperature. Structural distortions are likely to reduce the frustration before this point, as well as anisotropy in the plane or interactions between planes which disrupts frustration. Realisable geometrically frustrated magnetic systems are in general related to the triangular motif but in three dimensions, such as the face centred cubic FCC (edge sharing triangles) and pyrochlore (corner sharing triangles) lattices. Due to the fact that triangular packing is the most efficient in two dimensions, there are diverse other examples of frustration on this lattice beyond magnetic systems alone [Fig. 1.7].

1.1.2 Displacive degeneracy

Displacive degeneracy arises in a structure when bond lengths or directions change—either dynamically or due to a phase transition—with little change in overall energy [31]. The vibrational modes that arise from correlated displacive motions of atoms within materials are known as *phonon modes*, a low energy subset of which are known as 'soft

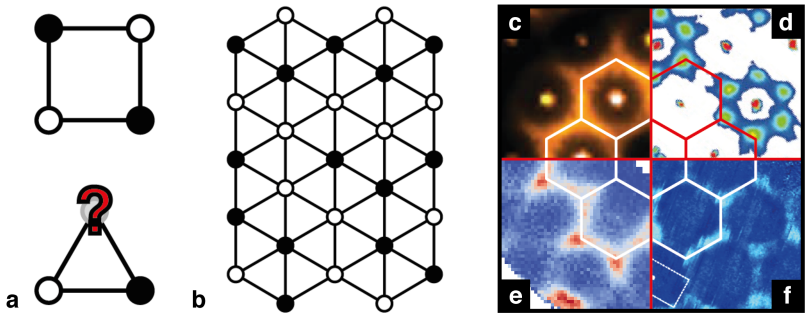

Figure 1.7: Geometric frustration arising from lattice geometry. An Ising spin can adopt one of two states *i.e.* 'up' or 'down', here shown as black and white circles. (a) On a square lattice the antiferromagnetic interactions of such spins is allowed as each spin is antiparallel to each of its own neighbours, however on a triangular lattice the third spin cannot simultaneously satisfy the requirement to be antiparallel to both of its neighbours. (b) In an extended 2D system the local solution means each spin is antiparallel to four of its nearest neighbours. Geometric frustration of this kind can be seen in the single crystal diffraction patterns of (c) the packing of the Gag protein, (d) orbital orientations in $Ba_3CuSb_2O_9$, (e) the emergent spin structure of β-Mn and (f) the electronic structure of graphene. Adapted by permission from Macmillan Publishers Ltd: *N*ature, Ref. 28, copyright 2015.

modes' [32–34]. In this thesis I will refer to low-energy phonon and soft modes collectively as 'flexibility modes'. These modes underpin the dynamic responses of many functional materials, from ferroelectricity [35] to negative thermal expansion [36, 37]. Under external stimuli, such as temperature or pressure, these modes drive *displacive phase transitions*. The critical response of materials at a phase transition is directly linked to the dynamical properties of the parent material, therefore identification and understanding of phase transitions is of great importance in structural studies [34].

The phenomenology of displacive modes and displacive phase transitions—those that involve small symmetry-breaking displacements of atoms over the length scale of several unit cells [8]—encompasses several related phenomena:

- rotational transitions characterised by small correlated tilts of polyhedra.
- ferroelectric transitions from the breaking of a centre of symmetry that gives rise to a spontaneous dielectric polarisation.
- ferroelastic transitions from a displacive transition accompanied by a spontaneous strain.

Landau theory emerges from considering the free energy of a system of interest and is extraordinarily efficient in rationalising displacive phenomena [9, 34]. For example, the idea of *structural order parameters* is widely used to explore the response of these materials [38]. Here we explore displacive degeneracy in bridged oxide materials—the broad family of perovskites, the polymorphs of silica, and polymorphs of TiO_2—by considering these related concepts [34].

First, we define some of the ideas highlighted above in more detail. In a crystalline system, a phonon mode is a lattice vibration describing the elastic excitation of atoms where atoms or molecules oscillate at a single frequency [7]. Phonons may be measured using inelastic neutron or X-ray scattering (see §1.3), Brillouin scattering, or calculated by lattice or molecular dynamics simulations, or density functional theory (DFT) calculations. There are a very large number of phonons possible and phonon dispersion curves

are used to plot the frequencies of phonon modes at high-symmetry points and along high-symmetry lines in the Brillouin zone [7]. The wave-like displacement of atoms leads to the classification of each mode as either acoustic (coherent displacements of atoms) or optical (out of phase displacements); within each class both longitudinal (LA and LO) and transverse (TA and TO) waves are possible.

A material phase is defined as a homogenous part of a system distinguishable by a set of intrinsic properties in thermodynamic equilibrium under specified external conditions [38]. Phase transitions are associated with significant changes in the properties of a physical system. Landau theory suggests that phase transitions arise due to "hidden variables" in thermodynamics: variables that affect the properties of the system even when the thermodynamic functions are set by external conditions. This concept is important as phase transitions can appear discontinuous in terms of thermodynamic variables (such as volume), but continuous when considering other variables such as symmetry properties [9]. Changes in variables such as those related to the symmetry of a phase are defined by an order parameter: a factor that describes the continuous change between phases and the driving force of such transitions. Landau theory provides a thermodynamic framework that links a wide range of observations and describes the behaviour of materials over large changes in conditions [33].

Quantifying displacive flexibility is possible by considering the number of degrees of freedom (F) and the number of independent constraints (C) in a system. As simple examples, in the square model shown in Figure 1.8 it can be seen that each rod has three degrees of freedom (rotation and two translations), whilst each joint imparts two

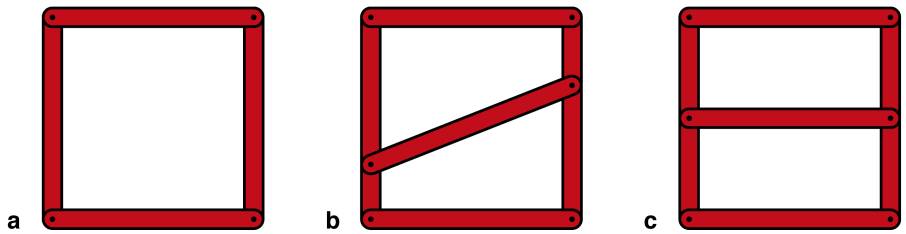

Figure 1.8: Rigidity and flexibility in frameworks (a) Four rods hinged at the corners to give a flexible structure that is easily sheared. (b) By diagonally cross-bracing the structure a rigid structure is formed, while (c) a brace parallel to two of the other rods does not result in a stiffened structure [39].

constraints; in total $F = 12$ and $C = 8$ meaning there are $(F - C) = 4$ degrees of mechanical freedom [8, 40]. These correspond to two translations of the whole structure, one rotation and the shear of the square. For the cross-braced structure [Fig. 1.8(b)] we are only left with the three rotational and translational modes, meaning the structure is mechanically rigid [39]. This rationalisation is complicated by the third option which appears at first glance to have the same number of degrees of freedom and constraints as the second. Here, however, the number of *independent* constraints is actually lower than that calculated previously as the cross-bracing bar must always be parallel to the others. This only adds three constraints to the system, so the shear distortion is still allowed [39].

In three dimensions flexibility modes can be thought of as polyhedral tilts or atomic displacements. Displacements like this occur in a periodic manner in crystalline systems—they are the phonon modes or soft modes discussed above—and are often so-called Rigid Unit Modes (RUMs). A RUM is identified where the number of flexibility modes in 3D $(F - C - 6) > 0$. As before it is important to only consider the number of independent constraints on a system, and in many cases for crystalline materials constraints may be themselves degenerate. (Formally displacive motions like these in the parent structure lead to phase transitions at T_c driven by the condensation of a critical phonon mode at certain k-points in reciprocal space.) Flexibility modes can be calculated for any suitable system using the programme CRUSH [41]. This uses a split-atom energy calculation to identify low-energy displacive modes, with many successes in calculating RUMs for framework silicates and perovskites alike.

The change in symmetry as a material goes through a phase transition from lower- to higher-symmetry at elevated temperature can appear counterintuitive. Close packed structures are often thought of as high density, high symmetry states that would be favoured at low temperature. Furthermore, considering the whole phase diagram the eventual melting of a solid results in a liquid state that appears highly unsymmetrical [42]. A key observation is that each point in space in the liquid state is actually more symmetrical on average than in the solid case: when averaged over time each position

is visited by as many atoms as any other. Consequently there are no unique axes or directions, and the system possesses complete translational and rotational symmetry [42]. Considering the solid case, high-symmetry high-temperature phases retain some of this complete symmetry which is gradually lost on cooling where a series of phase transitions exist. In many cases high temperature states are stabilised by entropic contributions from disorder. Displacive transitions can therefore be related to order–disorder phenomena: these high-symmetry phases occur due to atoms hopping between the positions corresponding to the different domains of the low-symmetry phase, so that there is dynamic disorder in the high-symmetry phase [43].

Key systems where displacive instabilities are critical to the understanding of properties—namely the broad family of perovskites, the polymorphs of silica and of TiO_2—are highlighted in the following sections. These examples aim to illustrate the concepts introduced above more fully.

Perovskites

The canonical ABX_3 perovskite structure is made up of corner-sharing $[BX_6]$ octahedral units, making up an extended cubic net, with interstitial A-site cations located in the centre of each cube [44]. The chemistry of perovskite materials has proved to be extremely significant. Many compositions are possible—substituting A, B and X—whilst subtle structural variations based on both octahedral tilts and cation off-centring lead to functionalities that have revolutionised many technologies. For example, the industry based on the piezoelectric, dielectric and ferroelectric responses of barium titanate, $BaTiO_3$, alone is worth around \$2.5 billion annually [45]. The broad class of perovskites also encompases perovskite silicates, such as $MgSiO_3$.

The perovskite aristotype structure is cubic with each octahedron aligned and the A-site cation in the centre of the unit cell. This is illustrated in Figure 1.10 in each of the high-temperature structures. One type of structural distortion in this system is cation off-centring; this is responsible for the electronic properties of $BaTiO_3$ and many other ferroelectric perovskites. In $BaTiO_3$ the Ti^{4+} are displaced away from the centre of the

octahedron, and on heating to the cubic phase at $\sim 763\,\mathrm{K}$ these become disordered over 8 equivalent sites, but on average lie in the centre of the octahedron [Fig. 1.9] [47]. This order–disorder displacive transition is often coupled with the tilt transitions of interest here and is similar to the cases discussed in the previous section [48].

Another type of distortion is possible in this structure type, namely octahedral tilting. Much of what is understood about the properties of perovskites can be thought of as originating in tilt transitions [52, 53]. These occur because a network of corner sharing octahedra is underconstrained, as the number of independent constraints is smaller than the number of degrees of freedom [48] which allows cooperative rotations of octahedra in opposite directions [Fig. 1.10] [54]. Such a distortion is a soft mode as the energy required is much smaller than, for example, cation off-centring or other polyhedral distortions. These are the RUMs characteristic of corner-sharing octahedral networks.

This transition can be most clearly seen in FeF_3 at 678 K from a rhombohedral distorted to cubic ordered state [Fig. 1.10]. FeF_3 has the simple cubic network structure of ReO_3 and is equivalent to an A-site-free perovskite. The lack of A-site cation means the tilting transition is much more pronounced than in typical perovskites, with tilting in both layers shown being visually obvious. The magnitudes of movements are $< 0.8\,\text{Å}$ for such tilt transitions [55]. The high-symmetry phase is in the ReO_3 cubic structure; this is the high-temperature high-volume ('large pore') state [55] and continuous rotations of

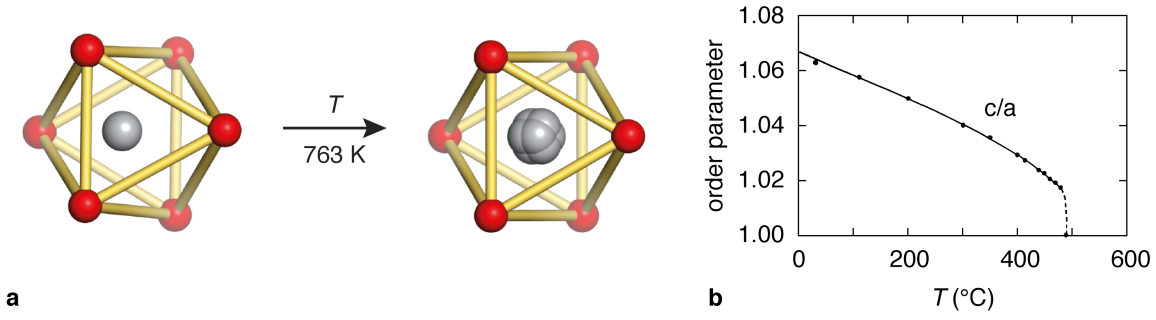

Figure 1.9: Order-disorder in the off-centering transition of Ti^{4+} in ferroelectric $BaTiO_4$. (a) Under ambient conditions the Ti^{4+} cation is displaced away from the centre of the octahedron (here, to the left) resulting in oxygen displacements and an overall polarity. This state emerges from symmetry lowering from the high-temperature structure where the average structure is given by the dynamic partial occupation of 8 equivalent sites. (b) The order parameter (defined as the c/a ratio as given in Ref. 46) shows close to first order behaviour.

octahedra results in a continuous reduction in volume. For these systems the tilt angle(s) act as an order parameter for the transition around the critical temperature.

In $SrTiO_3$ a tilt transition of this kind occurs at a much lower temperature (105 K) but with a much smaller magnitude of tilt angle [Fig. 1.10] [48, 51]. This transition is second-order in nature, meaning it is continuous in volume, and the tilt angles of the $[TiO_6]$ octahedra describe well the critical behaviour around 105 K. The rotations that occur around the tetragonal 4-fold axes of the low-temperature structure are of the order of 2°, confirmed by inelastic neutron spectroscopy measurements [39]. These measurements identify a soft zone boundary mode that leads to the observed doubling of the lattice parameters in the **a**-**b** plane (M point in reciprocal space) [51, 57], as it

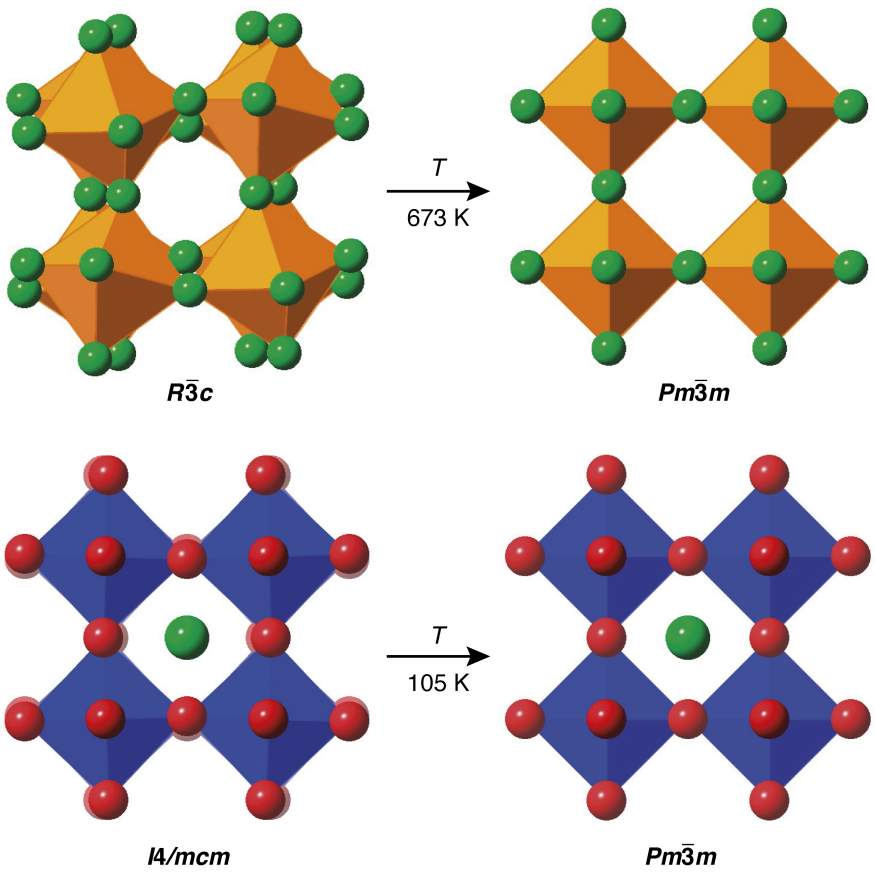

Figure 1.10: Degenerate displacive 'tilts' in corner-sharing octahedral networks. The ambient temperature structure of FeF_3 adopts a distorted ReO_3 structure with correlated tilts in each layer due to the common RUM-like distortion of corner-sharing octahedra [49]. In the perovskite structure of $SrTiO_3$ similar tilts are present but of much smaller magnitude (enhanced depth fading show off-set oxygen anions in the next layer) [50, 51], but on heating both structures transform to the aristotype cubic structure.

uniformly softens on cooling towards the transition temperature. This displacive phase transition is perhaps the most widely studied due to its accessible transition temperature and the fact it may be instructive to many other more complicated transitions, so a huge number of experimental techniques have been used to study it. Here we note one: total scattering and interpretation by reverse Monte Carlo (RMC) modelling that show the local rotations about the centre of each Ti octahedron going through the transition are consistent with displacements calculated from RUM models [Fig. 1.11] [51].

With such a chemically diverse family as perovskites, many theories are used to quantify the structures formed and (sometimes multiple) tilt transitions that characterise their behaviour. Of the most successful theories, the Goldschmidt tolerance factor (t) and the Glazer system of tilt transitions stand out. The former defines the 'ideal' cubic perovskite in terms of the ionic radii of each ion (r_{A}, r_{B}, r_{X}) [58]

$$t = \frac{(r_{\mathrm{A}} + r_{\mathrm{O}})}{\sqrt{2}(r_{\mathrm{B}} + r_{\mathrm{O}})}. \tag{1.1}$$

Here the closer the ratio is to unity the more likely the structure is to form (i) a perovskite structure and (ii) one closer to the cubic aristotype. The Glazer system of tilts defines allowed tilt transitions based on the symmetry constraints of the soft modes of each

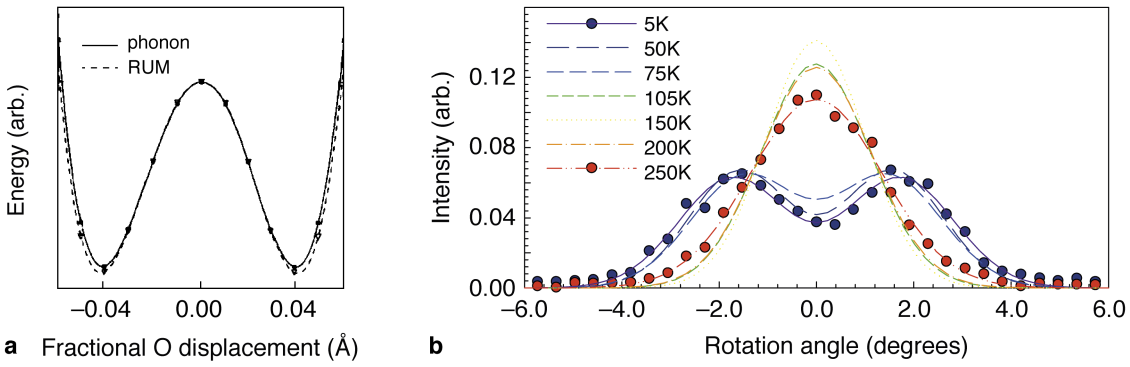

Figure 1.11: Perovskite tilts predicted from RUM and phonon calculation, and from experiment. (a) the calculated energy associated with oxygen displacements away from the cubic octahedral site (equivalent to octahedral tilts) show displacement is favourable as given by both RUM and phonon models. Reproduced with permission from Ref. 56, copyright © 1997 Taylor & Francis. (b) This is observed experimentally where the distribution of octahedral angles as described using geometric analysis (z rotor distributions) clearly splits at low temperature, suggesting the freezing in of alternate RUM tilts in the low symmetry structure. Reproduced with permission from Ref. 51 © 2005 IOP Publishing. All rights reserved.

transition [52, 59].

Silica polymorphs

Although the perovskite family is structurally simple and the displacive transitions are readily understood in terms of RUMs in favourable cases, there are subtleties complicating the dynamical behaviour of these materials. The validity of assuming the octahedra are rigid (our example of $PbTiO_3$ shows this is not necessarily true) and the flexibility criterion only being satisfied by degeneracy of constraints [54] are two challenges. Framework silicates have more complex structures and yet their displacive transitions have been extensively studied. Their particular importance in earth sciences drives much work on their temperature- and pressure-dependent properties [60].

Framework silicates are based on corner-sharing SiO_4 tetrahedra. These rigid tetrahedra form structures based on random joining (silica glass), and crystalline forms including quartz and cristobalite. For corner-sharing tetrahedra the flexibility constraints are equal to the number of degrees of freedom (both 6), so a continuous corner-sharing network will be borderline between flexible and rigid [39]. In the case of silica glass, there will be one or more RUMs for each wave vector, so the number of RUMs will be non-zero (a few percent of total number of RUMs) [39]. In other words, the lack of long-range order necessarily causes simple degree-of-freedom counting to fail [40, 48, 61].

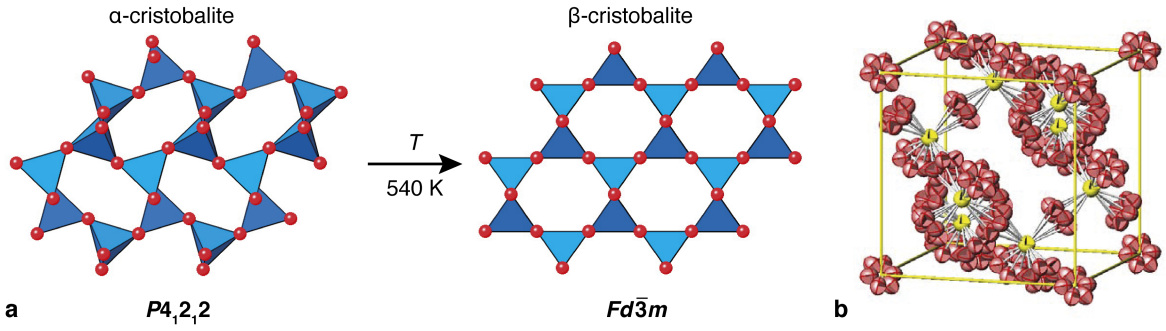

Figure 1.12: Order-disorder displacive transition in β-cristobalite. (a) β-cristobalite undergoes an order-disorder transition at 540 K on cooling, driven by displacive soft modes giving rise to a cubic $Fd\bar{3}m$ structure. (b) This high-symmetry structure is characterised by dynamic disorder where tetrahedra are rapidly rotating about their average positions by $\sim 17°$, here shown as multiple oxygen positions with partial occupancies from local structure modelling. Reproduced with permission from Ref. 62

The $\alpha \rightarrow \beta$ transition of quartz and cristobalite have parallels to the perovskite systems discussed, with both going from a low-symmetry to high-symmetry phase but by subtly different mechanisms [Fig. 1.12]. For cristobalite this transition is considered an order-disorder phenomenon, whilst the transition of quartz is purely displacive [33].

In the cubic symmetry that high-temperature β-cristobalite adopts ($Fd\bar{3}m$), the Si–O–Si bond angle lies along the $\langle 111 \rangle$ directions giving a bond angle of 180° with unphysically short bond lengths [64]. Calculation of the possible RUMs in the high-symmetry phase show that this is resolved by rotations of about 17°. Furthermore the transition to the low temperature form ($P4_12_12$) is the condensation of one of several RUMs that lie on a common plane in reciprocal space [33, 48]. So the high-temperature state is a displacively disordered phase with multiple degenerate RUMs giving rise to the observed average structure [33, 62]. Total scattering methods that can observe local dynamic distortions as static distortions in a large box model confirm that the observed average structure is a result of many phonon fluctuations associated with the other RUMs in the $\langle 1, \bar{1}, 0 \rangle$ zones in reciprocal space [Fig. 1.12b] [62], which is also supported by single crystal electron diffraction.

At 847 K quartz undergoes a second-order displacive phase transition from trigonal to hexagonal symmetry [39]. There appear to be a large number of soft modes in the high-temperature phase, many of which could act as the driving force to the low-temperature, α phase [33]. It can be rationalised that the correct RUM for this transition (the Γ_5 mode)

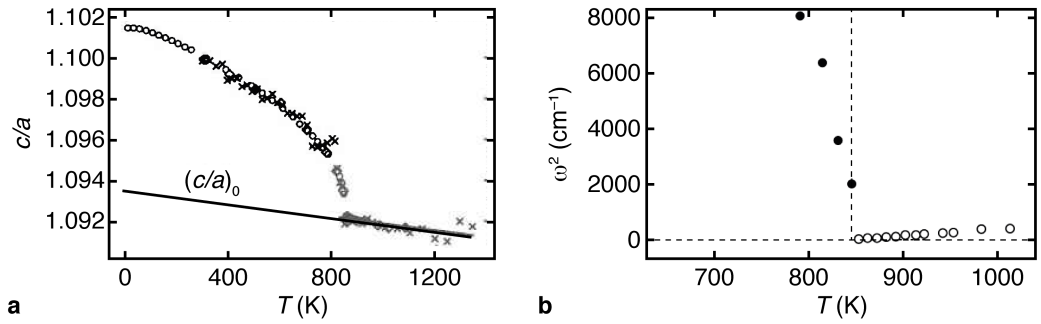

Figure 1.13: Order parameter and phonon mode frequency variation going through $\alpha \rightarrow \beta$ transition in quartz. (a) Variable-temperature evolution of the defined order parameter (c/a ratio) going through the $\alpha \rightarrow \beta$ transition in quartz showing the second order nature of this phase transition and (b) the variation of the squared frequency of soft mode going through the transition, indicating softening behaviour at T_c. Reproduced with permission from Ref. 63.

is the one that preserves the correct Si–O–Si bond angle, reduces volume and maximises dispersive interactions between O atoms [33], which are found experimentally to be the driving forces for the $\alpha \rightarrow \beta$ transition [Fig. 1.13].

Seemingly all other dense silica polymorphs have been analysed in similar ways, employing a combination of lattice dynamical, RUM and experimental techniques to rationalise high-temperature and high-pressure behaviour. The final example here is that of the class of materials known as zeolites. Zeolites are open porous structures that are made up of corner sharing tetrahedra forming well-ordered voids. Zeolites are known to have displacive flexibility, including the potential to allow local distortions (over the length scale of a few unit cells) in response to chemical stimuli such as incorporation of ions, impurities or guest molecules [48].

TiO_2 polymorphs

Polymorphs of titanium dioxide (TiO_2)—rutile, brookite and anatase—have not been extensively explored in the context of low-energy displacive transitions, largely due to edge sharing in these structures. However, as will be explored more fully in Chapters 2 and 5, displacive structural flexibility is important to understand the functional properties of these materials. Many authors would not identify this class of structures as flexible bridged 'framework' structures like the perovskites or silica polymorphs above [44].

Anatase, rutile and brookite-structured TiO_2 are differentiated by the manner of the close packing of oxygen anions, with the cations occupying half the octahedral holes in each case [Fig. 1.14]. For anatase the close packing is cubic (–ABCA– stacking sequence) and the structure is a defect-NaCl structure, whilst rutile is based on hexagonally close packed oxygen layers (–ABAB– sequence). In contrast brookite is not strictly cubic or hexagonally close packed, with a somewhat-unique stacking sequence of –ABABCAB– [2, 44]. For anatase and brookite the octahedral coordination of Ti^{4+} is heavily distorted [66, sect. 18-A-2].

The well-known tetragonal crystal structure of rutile (crystal symmetry $P4_2/mnm$) consists of columns of edge-sharing octahedra which are in turn connected at their corners

[Fig. 1.14(d)]. This structure has a well-known ferroelastic instability associated with correlated rotations of neighbouring columns of octahedra [67, 68]. Activation of this tilt system under increasing pressure or temperature lowers the crystal symmetry from tetragonal to orthorhombic, resulting in the (equally well-known) $CaCl_2$ structure. In order to conserve volume, the lattice is forced to expand along one of the two directions perpendicular to the column axis [69, 70]. This transition can be viewed as a progression towards the defect-NiAs-type structure of FeS_2 marcasite [Fig. 1.14(d)] and is thought to be driven largely by anion packing efficiency [65].

1.1.3 Mechanical degeneracy

Our discussion on flexibility in canonical solid state structures leads us to consider, in a much more general sense, mechanical degeneracy. It is straightforward to think of a structure that is mechanically floppy, such as the set of four rods joined into a square in Figure 1.8 [39]. Here we consider materials that have topologies related to these flexible

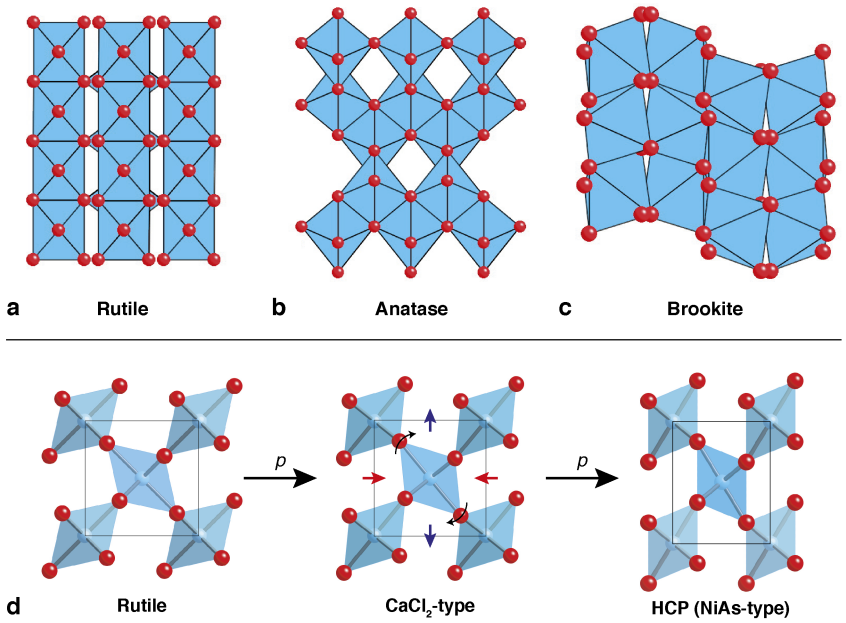

Figure 1.14: Crystal structures of TiO_2 polymorphs and the ferroelastic instability associated with the rutile structure-type. The structures of (a) rutile (b) anatase and (c) brookite polymorphs of TiO_2 viewed perpendicular to the edge-sharing chain direction. (d) The ferroelastic instability of the rutile structure type corresponds to a progressive distortion towards a defect NiAs structure and involves expansion in the vertical direction [65], as viewed down the chain direction. In all cases oxygen anions are shown as red spheres and titanium as blue octahedra.

models, where atomic connectivity is based on multi-atom linkers so that the number of mechanical constraints is small.

This mechanical degeneracy results in very flexible structures that respond to stimuli in extreme ways [71]: formally there exist low enthalpy valleys linking different continuous mechanical states. Dynamic crystalline frameworks adopt different mechanical states in response to changes in temperature, pressure or adsorption of chemical species with only small changes in energy. The materials considered here are crystalline materials based on metal nodes connected by molecular linkers—so-called molecular frameworks or coordination polymers [72]—that are the main focus of §1.4 and so are introduced more formally there.

Considering the structures illustrated in Figure 1.15, we see a direct correspondence with the simple models of flexibility introduced previously and these atomic structures with the 'Nuremberg scissors' topology. Materials with this structural motif are widely referred to in the literature as 'wine-rack' materials, as their responses to stimuli can be seen as similar to the response of a folding wine-rack [71]. Long multi-atom struts link metal nodes at either end, and critically there is no cross-bracing in these systems. The systems illustrated are of the MIL (Materiaux d'Institute Lavoisier) and DMOF-1 (DABCO metal–organic framework) families of frameworks. The former is made up of chains of M(OH) linked together by 1,4-benzenedicarboxylate (BDC) linkers, and the latter Zn^{2+} nodes constructed into square one-dimensional channels built on 1,4-diazabicyclo[2.2.2]octane (DABCO) pillars. The low energy shear of these structures means that the components of the mechanical strain ε_{kl}, which describe the state of deformation of a solid body, are large and direction-dependent [71].

These anisotropic properties mean that all of these materials are mechanically compliant. The MIL-53(Al) host structure (as shown) can change volume by up to 40% on gas loading [55, 73] or mechanical pressure [74]. These deformations are known as 'breathing' transitions—although others have called similar phenomena 'dynamic frameworks', 'springlike', 'spongelike' or 'accordion' effects—and are found in many frameworks with

a 'wine-rack'-type structure. Atomic displacements in this system can reach several Å, whereas the displacive transitions discussed for perovskites were generally < 0.8 Å. In many respects the two are related with the major difference being the magnitudes of response [55]; those discussed here are often observable using optical microscopy.

Such large reversible responses are mainly due to contrasting strength, directionality and nature of bonding that are unique to coordination polymers. Breathing transitions in MIL-type materials have been attributed to the existence of 'weak points' or non-rigid components in the structure, identified as flexible rotations about the M–O–L bonds of the carboxylate linker [55]. In MIL-53(Cr) for example, the dihedral angle about this point varies from 180° to 139° on the high temperature (*ht*) → low temperature (*lt*) transition [75]. For the aluminium analogue the 3D variation of the stiffness of the material (known as the Young's Modulus or elastic modulus) shows clearly the directionality of response and the extremely low stiffnesses in directions where the framework can easily hinge [Fig. 1.15(b–d)] [76]. The importance of topology is highlighted by contrasting these networks to MIL-68, where triangular rather than square channels impart significant

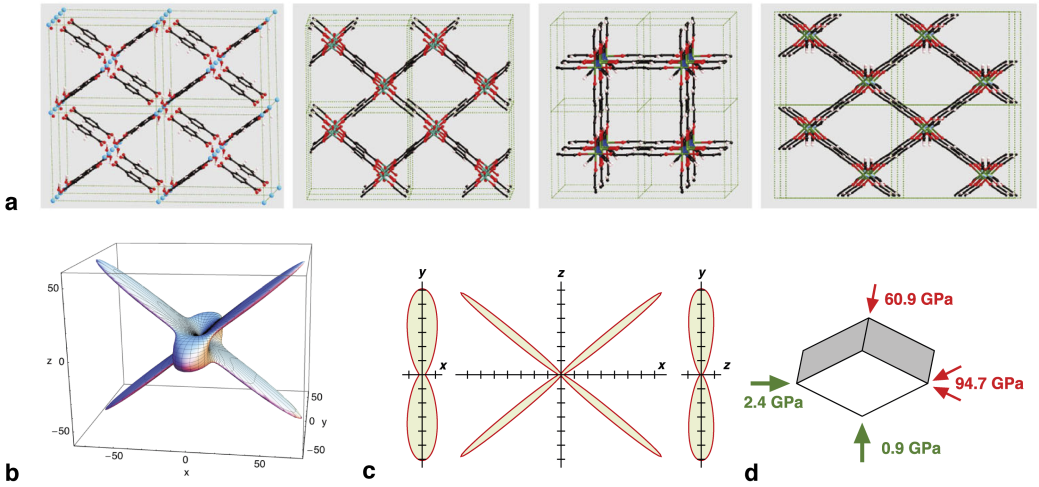

Figure 1.15: Flexible 'wine-rack' coordination polymers (a, *left–right*) MIL-53(Al)-*lp*, MIL-47, DMOF1-sq and DMOF1-loz showing structural similarity to the mechanically underconstrained, flexible 'wine-rack' structure. Calculation of the Young's moduli for MIL-53 shows large positive stiffnesses along the strut directions, and very large compliance in other directions depicted as a 3D surface (b) and projection in the *xy*, *xz*, and *zy* planes (c, one tick is 10 GPa). (d) A scheme showing the stiffest and weakest directions of the lozenge- shaped pore. Reprinted figure with permission from A. U. Ortiz, A. Boutin, A. H. Fuchs, and F.-X. Coudert, *Phys. Rev. Lett.* **109**, 195502 (2012). Copyright 2012 by the American Physical Society.

stiffness to the structure [55].

Similar results are found for all of the frameworks in Fig. 1.15, however the exact behaviour is also determined by the included guests in the large pores shown. As an example, the empty pore *ht* MIL-53(Al) is unstable to water reabsorption, making measuring mechanical properties experimentally difficult [73]. Another strategy to find large responses in such materials is to look at interpenetrated (catenated) frameworks [77] where accessible pore volumes are very small but the topologies shown previously are retained, with only weak van der Waals, hydrogen-bonding or other weak interactions between frameworks.

A second example of mechanical degeneracy of this kind here is the cyanide framework material silver hexacyanocobaltate, $Ag_3[Co(CN)_6]$ [78, 79]. $Ag_3[Co(CN)_6]$ is constructed from octahedral Co^{3+} centres joined by the almost-linear $[Ag(CN)_2]^-$ linkers to form a distorted simple cubic (α-Po) net [80]. Three such networks interpenetrate as shown in Figure 1.16; linking these networks are weak 'argentophilic' interactions between neighbouring networks' Ag^+ centres. Upon cooling or application of pressure the framework responds in a dramatic way with the framework 'folding' to reduce its volume as rapidly as possible. This flexibility is imparted by (i) the framework topology, as shown for the MIL-type frameworks (ii) the very weak cross-linking interactions driving rapid change and (iii) relatively rigid linear linkages that prevent framework bucking [78, 79, 81].

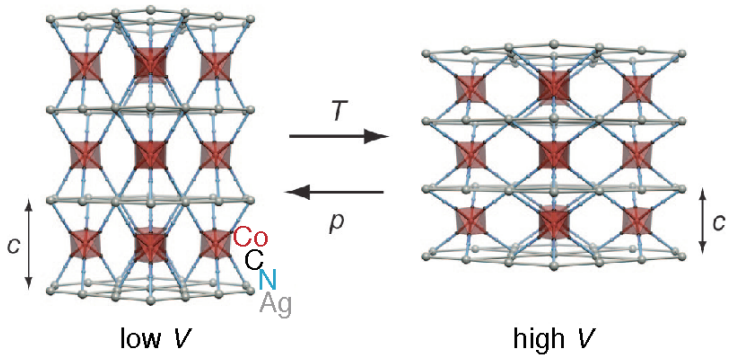

Figure 1.16: Flexibility under changes in temperature and pressure of cyanide framework material silver hexacyanocobaltate. External stimuli cause the cross-linked structure of $Ag_3[Co(CN)_6]$ to hinge about the metal nodes such that volume contraction is associated with expansion in one direction and collapse in perpendicular directions. This exceptional flexibility comes about because of the very weak 'argentophilic' interactions cross-linking the structure. Figure reproduced from Ref. 78, copyright © 2008 National Academy of Sciences U.S.A.

The magnitude of pressure- and temperature-dependant responses in $Ag_3[Co(CN)_6]$ are an order of magnitude larger than those of conventional materials, with contraction in c shown in Figure 1.16 of $\sim$ 1.25% over 100 K [79]. Note that the large changes in structure includes very large and unusual *expansion* on cooling—known as negative thermal expansion (NTE)—which is also found in the MIL systems above [82]. Under changes in pressure this material was also found to admit very large strains ($\sim$10 %) and had a very large negative linear compressibility (NLC) [79]. This phenomenon is discussed in more detail in Sections 1.2 and 1.4.

1.1.4 Relevance to this thesis

Throughout these diverse examples, it is clear that degeneracy in materials design—and solid state physics more generally—gives rise to interesting phenomena and properties. At first we might say that there is not much to link the structure of ice or magnetic frustration to the structure and properties of cyanides. In this thesis we will come to see that understanding the impact of degenerate states in general allows us to draw new and unexpected links between disparate fields in solid state physics and materials science. The emergence of unusual phenomena is also encountered, such as negative linear compressibility (NLC), and frustrated structural states that have never before been measured a real material. Furthermore, there is a general sensitivity to perturbation in these systems and so using the tools of variable-temperature and -pressure diffraction we might be able to see interesting physics emerge. I will now outline more formally the background to these studies, the tools used in this thesis to characterise them, and the specific types of materials we will be interested in, namely cyanide framework materials.

1.2 Mechanical properties of materials

Considering the response of materials to mechanical stress as a consequence of spring-like bonding forces between atoms, whilst simplistic, leads us to consider elasticity theory in more detail [83]. In the case of small stresses the relationship is linear and thus obeys Hooke's Law where displacement ($\propto$ strain) is related to mechanical force ($\propto$ stress).

Formally the stress σ_{ij} describes the forces acting on a crystal in a continuum, whilst the strain ε_{kl} describes the state of deformation of a solid body [84]. This relationship is given by the elastic compliance tensor $\mathbf{S}$; as four directions are involved this is a fourth rank tensor [83, 85]:

$$\varepsilon_{ij} = -\sum_{k,l=1}^{3} S_{ijkl}\sigma_{kl}. \tag{1.2}$$

Both the stress and strain tensors are symmetric second rank tensors where diagonal components ($\varepsilon_{11}, \varepsilon_{22}, \varepsilon_{33}$) represent tensile components, whilst off-diagonals ($\varepsilon_{12}, \varepsilon_{13}, \varepsilon_{23}$) are shear components [83]. In the following two sections we consider the strain properties of thermal expansion and compressibility, *i.e.* fractional changes in shape of a material upon change in temperature or on application of pressure.

Of the other elastic constants, the Young's Modulus, E, is a measure of the longitudinal elongation on application of a tensile stress, *i.e.* the ratio of the stress along an axis to the strain along that axis in the range that Hooke's Law holds ($E = 1/S_{11}$). The Poisson's Ratio, ν, is the ratio of transverse contraction to longitudinal elongation ($\nu = -S_{12}/S_{11}$) and the Rigidity Modulus, G, is a measure of shear strain under shear stress ($G = 1/S_{44} - 1/2(S_{11} - S_{12})$) [86, 87]. Only one of these fundamental elastic properties—the Poisson's Ratio—may take a negative value. Materials with a negative Poisson's Ratio are known as auxetics and find application in shock absorbing applications such as bullet-proof vests [87–91].

1.2.1 Thermal expansion: theory and measurement

When a material is heated uniformly it changes shape as described by the relationship

$$\varepsilon_{ij} = \alpha_{ij}\Delta T, \tag{1.3}$$

where α_{ij} are the thermal expansion coefficients. It is conventional to write Eq. (1.3) in terms of the change in linear dimensions, ℓ, with temperature at constant pressure,

$$\alpha_\ell = \frac{1}{\ell}\left(\frac{\partial \ell}{\partial T}\right)_p . \tag{1.4}$$

Coefficients of thermal expansion range from $1 \times 10^{-6}\,\mathrm{K}^{-1}$ ($\equiv 1\,\mathrm{MK}^{-1}$, $1\,\mathrm{ppm\,K}^{-1}$) for oxides like silica glass to $1000\,\mathrm{MK}^{-1}$ for polymers [83], with a few materials known to show negative responses. As temperature is a scalar quantity thermal expansion is given by a symmetric second rank tensor and the coefficients can be positive or negative as described further below. Unlike stress or strain (formally field tensors) thermal expansion is a property tensor and therefore obeys Newman's principle [92, 93]. This states that the symmetry of any physical property must include the symmetry elements of the point group of the crystal (not precluding the symmetry of any property being higher than that of the crystal) [83].

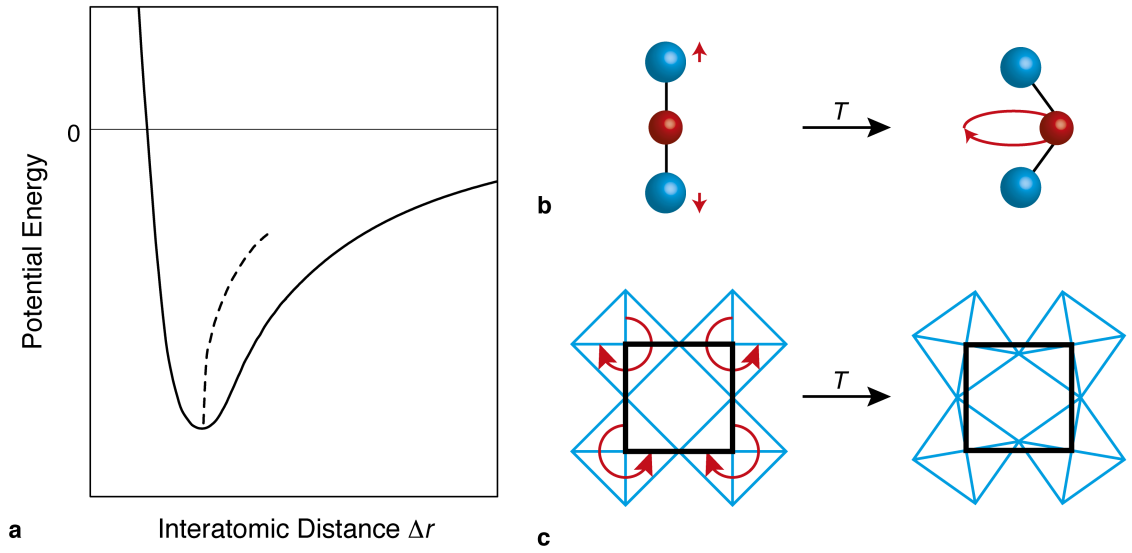

Figure 1.17: Interatomic potential and thermal expansion caused by longitudinal and transverse vibrations. (a) The interatomic potential shows that in general atoms become further apart on increased temperature (along dashed line), as shown on the right hand side of (b) as a longitudinal vibrational mode (blue atoms shown bridged by a single red sphere). These vibrations result in positive thermal expansion. Where transverse vibrations dominate (b, right) increased thermal population can result in contraction of distances between atoms, which when propagated through a crystalline structure gives rise to RUM modes that cause the structure to 'fold up' at high temperature.

There is therefore a strong dependence of thermal expansion coefficients on a material's crystal structure. The number of measurements to completely describe the thermal expansion of a crystal ranges from one in the cubic case to six for the general case (a triclinic crystal). The eigenvectors of the thermal expansion matrix describe an orthogonal coordinate system that brings it into diagonal form; these are the 'principal' coefficients of thermal expansion. In general, increasing temperature causes increased thermal motion and consequently an increase in interatomic distance [Fig 1.17]. From the shape of the potential energy well it can be seen that the forces for atoms moving closer together are much stronger than moving apart, and consequently on heating atoms will move further apart [7]. The magnitude of distortion depends on the strength of the bonding force, with weaker bonds having a shallower and broader potential energy curve and so more extreme thermal expansion.

Negative thermal expansion (NTE) occurs when one or more of the principal coefficients of thermal expansion take negative values [94, 95]. Isotropic NTE (*i.e.* volume negative thermal expansion) may occur in real systems as the thermodynamic requirement $\mathrm{d}U = T\mathrm{d}S - p\mathrm{d}V$ is satisfied for decreasing volume on increasing temperature by increasing system entropy [96]. Many of the canonical NTE materials are bridged frameworks—made up of [M—L—M] motifs, L = linker atom or molecule—where transverse vibrational modes are implicated in the mechanism, *e.g.* zirconium tungstate ZrW_2O_8 and zinc (II) cyanide $Zn(CN)_2$ [97]. Transverse vibrational modes allow for an increase in interatomic distance on heating, but their transverse nature results in decreasing M$\cdots$M distance. In three dimensions these vibrations can be generalised so that cooperative transverse vibrations result in low energy rotations of undistorted polyhedra, *i.e.* RUMs [7, 33] [Fig 1.17]. Further examples of these materials are discussed elsewhere in this introduction.

Negative thermal expansion materials may find use in development of zero thermal expansion composites for ultra-sensitive optical or mechanical components [97], electronic applications (*e.g.* zero thermal expansion heat sinks and substrates), composites in printed circuit boards, dental applications, *etc.* [94, 98]. There has been a significant research

effort to understand the origins of NTE and control this response to increase the range over which NTE is observed as well as its magnitude (either targeting zero thermal response or very large negative response) [94, 95, 98–100].

Determining coefficients of thermal expansion

Measurement of coefficients of thermal expansion is of interest to physicists, ceramists, geologists and chemists alike. A coefficient of thermal expansion α_ℓ is defined as the rate of change of a linear dimension with temperature as given by Equation 1.4. Classical techniques include the use of push-rod dilatometers or optical interferometers to measure these changes.

Such changes can however be measured directly using crystallographic techniques where the dimensions of the unit cell (given by lengths a, b, c and angles α, β, γ) give the six measurements necessary for full determination of the thermal expansion tensor [83, 85]. Thermal expansion is in general non-linear across very large changes in temperature, especially close to 0 K, and therefore a polynomial function is used to fit changes in length of the principal directions with changing temperature [83]. It is found however that for typical experiments (across several hundred K) behaviours can be approximated as linear, *i.e.* [101],

$$\ell_i(T) = \ell_0(1 + \alpha_i T). \tag{1.5}$$

The volume expansivity, α_V, is given by the sum of the principal coefficients of thermal expansion [83],

$$\alpha_V = \alpha_{11} + \alpha_{22} + \alpha_{33}. \tag{1.6}$$

Calculation of linear coefficients of thermal expansion is readily calculated from variable-temperature lattice parameters using programmes such as PASCal [101]. Thermal expansion around 0 K is usually well characterised by considering the Debye model where all interactions are assumed to be harmonic and where electronic contributions are considered

[97]. The temperature-dependent crystal volumes are therefore given by

$$V(T) = V_0 + \frac{9Nk_{\mathrm{B}}\gamma}{K} T \left(\frac{T}{\theta}\right)^3 \int_0^{\theta/T} \mathrm{d}x \frac{x^3}{e^x - 1}, \tag{1.7}$$

where θ is the Debye temperature, K is the bulk modulus, γ is the Grüneisen parameter and V_0 is the system volume at reference temperature T_0. Analysis of variable-temperature unit cell volumes can be carried out using a quasi-harmonic Debye model with a programme such as GIBBS [102].

1.2.2 Compressibility: theory and measurement

The compressibility of a material (analogous to the thermal expansion) describes the relative rate of collapse of its linear dimensions with respect to pressure, measured or calculated at constant temperature [83, 85]:

$$K_\ell = -\frac{1}{\ell}\left(\frac{\partial \ell}{\partial p}\right)_T. \tag{1.8}$$

The minus sign means that positive compressibilities correspond to length reduction under increasing pressure. Conventional engineering materials such as steel and concrete contract by $\sim 0.5\%$ in every direction for each gigapascal of applied pressure (10 kbar), corresponding to a linear compressibility $K = 5\,\mathrm{TPa}^{-1}$ [103]. Compressibility magnitudes usually reflect bond strengths, and so softer materials such as polymers and foams exhibit much larger values; for example, the linear compressibility of polystyrene is $K \simeq 100\,\mathrm{TPa}^{-1}$ [Fig. 1.18] [104].

Crystalline materials generally have different compressibilities in different directions. For example, a layered material will usually be more compressible along the stacking axis than it is along a perpendicular direction [105]. This directional dependence can be relatively complex, especially when the crystal symmetry is low. The theory of compressibility is introduced here in its most general form before explaining how the situation can be simplified as symmetry increases. The starting point is the formal definition of

compressibility as a second-rank tensor [85]:

$$\mathbf{K} = -\frac{\partial}{\partial p}\begin{bmatrix} \varepsilon_{11} & \varepsilon_{12} & \varepsilon_{13} \\ \varepsilon_{21} & \varepsilon_{22} & \varepsilon_{23} \\ \varepsilon_{31} & \varepsilon_{32} & \varepsilon_{33} \end{bmatrix}. \tag{1.9}$$

Here the ε_{ij} are functions of hydrostatic pressure p and represent the pressure-induced strain experienced by axis j along axis i. The eigenvectors of Eq. 1.9 describe an orthogonal coordinate system that brings $\mathbf{K}$ into diagonal form. These vectors are the principal axes of compressibility (sometimes labelled $\mathbf{x}_1; \mathbf{x}_2; \mathbf{x}_3$) which can be interpreted as the crystal directions along which hydrostatic compression does not lead to any shear component. The eigenvalues of $\mathbf{K}$, which we term $K_1; K_2; K_3$, correspond to the compressibilities along these principal axes and are the unique descriptors of linear compressibility for any crystalline material. These principal axes are analogous but not necessarily coincident with the principal axes of thermal expansion as described in the previous section.

Defined in this way, the linear principal compressibilities are directly related to the volume compressibility, and in turn to the bulk modulus:

$$K_V = -\frac{1}{V}\left(\frac{\partial V}{\partial p}\right)_T = \mathrm{Tr}(\mathbf{K}) = K_1 + K_2 + K_3, \tag{1.10}$$

$$B = K_V^{-1} = \frac{1}{K_1 + K_2 + K_3}. \tag{1.11}$$

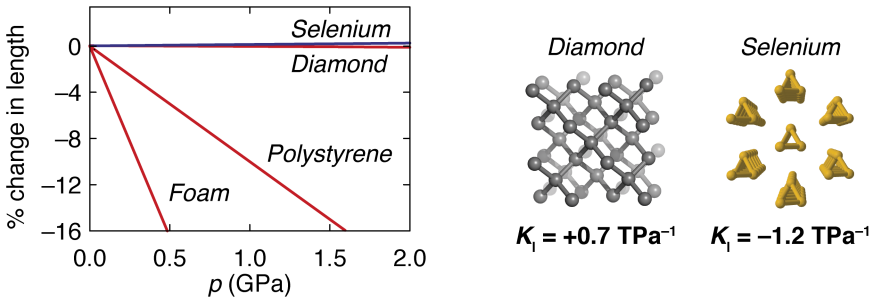

Figure 1.18: Comparison of compressibilities of various materials. The compressibility of materials varies dramatically with micro and meso structure, and bond stiffness with orders of magnitude difference between the compressibilities of *e.g.* diamond and expanded foam. The small negative compressibility of trigonal elemental selenium is shown.

A suitable equation of state (EoS) is used to fit changes in material volume [106, 107]. In general an EoS describes the volume change, and therefore the density change, with pressure (or temperature) of a material, parameterised in terms of the zero-pressure bulk modulus, B_0, and its pressure derivatives, $B_0' = \partial B/\partial p$ and $B_0'' = \partial^2 B/\partial p^2$. Unlike the EoS for gases, there is no absolute thermodynamic basis for the correct form of an EoS for solids, and therefore they are based on a number of assumptions, the validity of each is judged on its ability to reproduce experimental data for volume or elasticity. Common EoS for solids include the Murnaghan, Birch-Murnaghan, natural strain and Vinet formulations [86]. If the bulk modulus takes very large values then the material is mechanically stiff; small values indicate much softer materials. Due to the fact that the volume must decrease with increasing pressure, bulk moduli are always positive, with the pressure derivatives taking positive or negative values. The bulk modulus can also be calculated directly from elastic properties as it is one of the fundamental elastic constants.

Negative linear compressibility (NLC) is the bizarre material property whereby a system expands along one direction when compressed uniformly [108, 109]. Bizarre, because our intuition is that materials should shrink when squeezed—an intuition that is (rightly) grounded in the thermodynamic requirement that volume be reduced at increased pressure. Yet NLC does not violate thermodynamics: it simply arises whenever volume reduction can be coupled to linear expansion [83, 85]. This phenonomon is the focus if the Chapter 2, but here we note that the formal requirement for NLC is that at least one of the K_i is negative. Because the volume compressibility must be positive, any system for which one of the linear compressibilities exceeds the bulk compressibility (*i.e.* $K_i > K_V = B^{-1}$) must exhibit NLC. This is the type of approach to identifying NLC materials employed in Ref. 109.

It is worth noting at this point that conventions vary in terms of the symbols used to denote these various elastic parameters. Compressibilities are denoted by some using the symbol β [85], which is used by others to mean the volumetric coefficient of thermal expansion [110], and by perhaps very many more to mean one of the unit cell angles.

Likewise the bulk modulus is denoted by K within much of the mineralogical literature, despite this symbol assuming the inverse meaning of compressibility when used in a physics text [111]. To prevent confusion I adopt the conventions of the condensed matter physics community, *i.e.* K for compressibility and B for bulk modulus, which are felt to be the least likely to cause confusion.

Compressibilities from variable-pressure crystallographic measurements

As mentioned above, the tensor algebra associated with compressibility determination is simplified enormously by consideration of crystal symmetry. For systems of orthorhombic crystal symmetry or higher, the principal axes coincide with the crystal axes. This means that the lattice parameter compressibilities

$$K_a = -\frac{1}{a}\left(\frac{\partial a}{\partial p}\right)_T, \tag{1.12}$$

$$K_b = -\frac{1}{b}\left(\frac{\partial b}{\partial p}\right)_T, \tag{1.13}$$

$$K_c = -\frac{1}{c}\left(\frac{\partial c}{\partial p}\right)_T, \tag{1.14}$$

which can be determined using variable-pressure crystallographic measurements, give directly the principal axis compressibilities. In other words, the K_i reflect the relative rate of change of the lattice parameters with respect to pressure, and NLC materials can be identified as those for which at least one lattice parameter increases under hydrostatic pressure. Unfortunately this equivalence between lattice and principal axis compressibilities does not hold for systems with monoclinic or triclinic crystal symmetries; lattice parameter compressibilities can have very little direct physical meaning in these cases [101]. In particular, a negative value of one or more lattice parameter compressibilities would no longer imply NLC because the principal axis compressibilities may nonetheless remain positive. For such situations, there are software packages that facilitate the conversion from lattice parameter to principal axis compressibilities: PASCal and EoSfit are two examples [101, 112].

One further complication in converting variable-pressure lattice parameters to linear compressibilities is the tendency for lattice parameters to depend non-linearly on pressure; *i.e.* the K_i are themselves pressure-dependent [Fig. 1.19]. (Indeed if any K_i were truly constant then there would exist a finite pressure at which the corresponding material length would vanish: $p_{\mathrm{crit}} = 1/K_i$). In contrast to crystal volume, there is no thermodynamic requirement for the K_i to depend on pressure in any particular way. Instead the lattice parameters are usually fitted to some empirical parameterisation of choice. In the simplest case this would be the linear relationship

$$\ell(p) = \ell_0[1 - K_\ell p], \tag{1.15}$$

where ℓ_0 represents the length at zero pressure. The nonlinearity left unaccounted for by this simple parameterisation can be included via higher-order polynomial expansions:

$$\ell(p) = \ell_0 \left[1 + \sum_{i=1}^{n} \alpha_i p^i\right]. \tag{1.16}$$

Some authors then identify the value $-\alpha_1$ with the linear compressibility K_ℓ; however, this tends to overestimate the compressibility in cases where there is a strong pressure dependence [79, 113, 114]. In this work, as proposed elsewhere [79, 101, 115], we have found that the alternative parameterisation

$$\ell(p) = \ell_0 + \lambda(p - p_c)^\nu \tag{1.17}$$

actually captures better the pressure-dependence of lattice parameters for most systems. The corresponding compressibilities are determined straightforwardly from the pressure derivative of Eq. 1.17:

$$K(p) = -\frac{1}{\ell(p)}\lambda\nu(p - p_c)^{\nu-1}. \tag{1.18}$$

The value of $K(p)$ determined in this way diverges at $p = p_c$, since $\nu < 1$; often this divergence has physical significance in terms of the elastic instability at a pressure-induced

phase transition. Figure 1.19 compares the linear compressibilities determined in these different ways for some representative variable-pressure lattice parameter data.

Whichever parameterisation is used, accurate determination of the K_i generally relies on access to a relatively large number of lattice parameter measurements over the pressure interval of interest. Experimental claims of NLC are sometimes made on the basis of just two measurements [116]; however a general rule of thumb is that 10 measurements are needed for accurate compressibility determination with little improvement for more than 20 measurements [86].

Compressibilities from elastic compliances

Because lattice compressibilities are one aspect of the more general elastic behaviour of materials, determination of the elastic stiffness tensor $\mathbf{C}$ provides an alternative means of characterising NLC [83]. The relationship between the K_i and $\mathbf{C}$ is most straightforwardly established by considering the elements of the elastic compliance tensor $\mathbf{S}$ (the inverse of $\mathbf{C}$), which relate strains ε_{ij} to applied stresses σ_{ij} given by Equation 1.2. Here all terms are defined in the limit of infinitesimal strain. Eq. (1.2) is essentially a form of Hookes law that

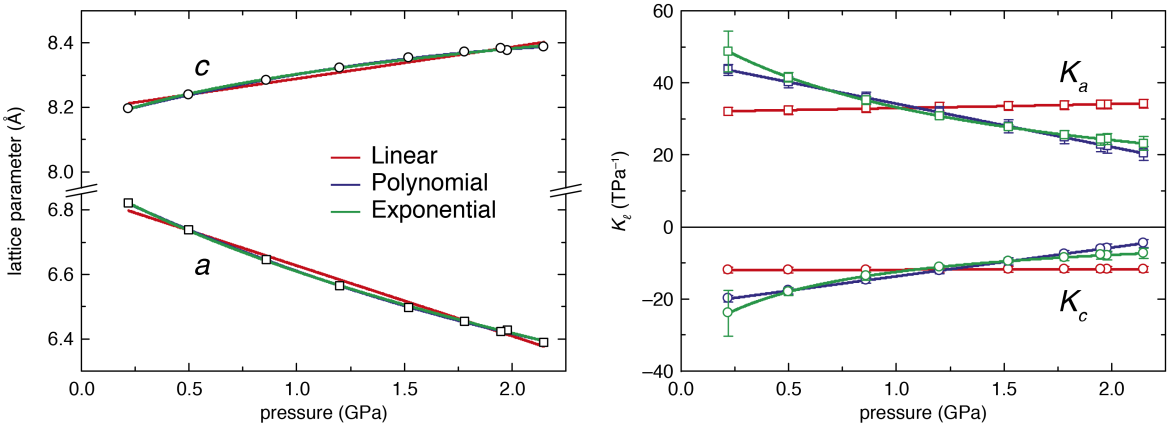

Figure 1.19: Extraction of linear compressibilities from variable-pressure lattice parameter measurements. The top panel shows representative lattice parameter data for a smoothly-compressible material—in this case measured for $KMn[Ag(CN)_2]_3$ [115]. The three common approaches to fitting lattice parameter data represented by Eqs. 1.15–1.17 give the fits to data shown in red, blue, and green, respectively. The corresponding compressibilities are shown in the lower panel. All three methods obtain comparable average compressibility values over the entire pressure range for which data are fitted. The reduction in magnitude of K at higher pressures is unaccounted for by the linear fitting method, and is treated slightly differently by the two non-linear fits. The extrapolated values of K at $p = 0$ are very different in all three cases.

relates displacement ($\propto$ strain) to mechanical force ($\propto$ stress). Hydrostatic compression is the specific situation where axial stresses are all equal to the applied pressure and shear stresses are absent; that is,

$$\sigma_{ii} = p \qquad \forall i, \tag{1.19}$$

$$\sigma_{ij} = 0 \qquad \forall i \neq j. \tag{1.20}$$

By design, the principal axes are those for which axial compression does not induce any shear strain, and so Eq. (1.2) reduces to

$$\varepsilon_{ii} = -p \sum_{k=1}^{3} S_{ik} \tag{1.21}$$

when expressed in the principal axis coordinate system (noting that we have now switched to Voigt notation so that $S_{ik} \equiv S_{iikk}$). Substitution into Eq. (1.9) gives the simple relationship,

$$K_i = \sum_{j=1}^{3} S_{ij} \tag{1.22}$$

that often appears in texts on the subject [83]. Consequently, determination of the elastic stiffness tensor $\mathbf{C}$ (either experimentally or computationally) can also yield the linear compressibilities K_i via the compliance tensor $\mathbf{S} = \mathbf{C}^{-1}$.

Experimental techniques capable of probing the tensor $\mathbf{C}$ include resonant ultrasound spectroscopy (RUS) [117], Brillouin scattering [118, 119], inelastic neutron scattering [120], nanoindentation [121] and shear-wave velocity [67] measurements. In most cases these measurements are indirectly sensitive to a subset of the elements, or combinations of elements, of $\mathbf{C}$. Consequently interpretation of the experimental data is often carried out via a parameterised lattice-dynamical model (containing fewer free parameters than $\mathbf{C}$ itself), from which $\mathbf{C}$ is subsequently calculable using software packages such as GULP [122]. The single most important distinction between experimental compressibilities determined via elastic compliances and those obtained from variable-pressure crystallographic measure-

ments is that the former correspond to values obtained *in the limit of zero applied pressure* and hence are usually much larger in magnitude.

Ab initio methods also allow determination of uniaxial compressibilities in an analogous way. Starting from the optimised geometry for a given crystal, sampling of every possible pairwise combination of strains $\varepsilon_{ij}, \varepsilon_{kl}$ allows the C_{ijkl} to be evaluated directly from the corresponding second derivatives of the lattice energy [123]:

$$C_{ijkl} = \frac{1}{V}\left(\frac{\partial^2 E}{\partial\varepsilon_{ij}\partial\varepsilon_{kl}}\right). \tag{1.23}$$

The tensor $\mathbf{S}$ is obtained by inversion and the K_i calculated according to Eq. (1.22). Such an approach is implemented in, for example, the CRYSTAL09 code [124, 125], and has been applied to the exploration of negative compressibility of simple inorganics [84, 126], zeolites [123], and metal–organic frameworks alike [71, 76]. Once again, the compressibilities obtained in this way represent the zero-pressure limit and as such can be vastly more, extreme than those determined across finite pressure ranges [76].

This link between linear compressibilities and the more general elastic properties of materials means that the observation of NLC is often diagnostic of other anomalous mechanical responses. Examples include extreme mechanical anisotropy [76], unusual values of the Poissons ratio [127], negative thermal expansion (NTE) [105, 128], and a propensity towards dynamic instabilities [79]. Importantly, this correspondence works both ways. Severe structural anisotropy (such as that arising from the preferred orientations of molecules in a particular packing arrangement or the symmetry of a given framework topology), or the observation of uniaxial or biaxial NTE are increasingly found to be strong predictors of NLC behaviour [129, 130].

Compressibility capacity

Because of the pressure dependence of the K_i it is important that compressibility values are quoted with reference to the pressure range over which they have been determined. This pressure range may correspond to the entire stability field of the phase in question, may be imposed by experimental constraints, or may be of relevance to a specific industrial

process (by way of example, most machining processes subject materials to pressures of *ca* 1–2 GPa [131]). One obvious limitation in comparing the NLC behaviour of different materials in terms of the magnitudes of K_i alone is that these values may be determined over very different pressure ranges for different materials.

A metric that is useful for comparing the degree of NLC behaviour for different materials is what I term the compressibility capacity:

$$\chi_K = -\int_{p_{\min}}^{p_{\max}} K(p)dp, \tag{1.24}$$

where $p_{\max}, p_{\min}$ denotes the pressure range over which NLC is observed. The value of χ_K is a dimensionless quantity that takes into account both the magnitude of NLC and the pressure range over which NLC occurs. It simply represents the maximum total fraction by which a crystal can expand under application of hydrostatic pressure. χ_K values for both new and well-established NLC materials will be reported throughout this work as and when each is introduced; anticipating these results, we find that $\chi_K \sim 1\%$ or the majority of known NLC systems, with values closer to 10% only observed in the most exceptional cases.

1.2.3 Coexistence of NTE, NLC and auxeticity

The existence of NLC in a material suggests intrinsic anisotropy in the system as NLC is a directional response. Models used to explain the origin of NLC are conceptually very similar to those explaining the origin of anisotropic NTE. Whilst there is no thermodynamic requirement for NTE and NLC to coexist, what is emerging is an empirical interdependence of the two phenomena [78, 132]. So, for example, the framework material $Ag_3[Co(CN)_6]$ shows 'colossal' NTE along the *c*-axis of its trigonal crystal lattice; NLC is found in the same direction with $K_c = -75\,\mathrm{TPa}^{-1}$ until a phase transition at 0.19 GPa [78, 79].

This generality has been previously proposed [78] and seems reasonable on an intuitive level: T usually results in a volume increase, which in a uniaxial NTE material is linked to

contraction along the NTE direction. If the same mechanism operates under hydrostatic pressure, then volume reduction on increasing pressure will be linked to uniaxial expansion along the NTE/NLC direction. This is shown schematically in the simple 'wine-rack' model (Fig. 1.20). The relationship for cross-linked structures can be quantified by suitable assumptions based on the formulation of the Grüneisen parameter [105, 133]. The Grüneisen parameter (γ) relates the volumetric thermal expansion of a material (α_V) to its volume (V), specific heat at constant volume (C_V), and volumetric compressibility (K_V),

$$\alpha_V = \frac{\gamma C_V K_V}{V}. \tag{1.25}$$

For linear responses, we must consider the elastic compliances (S_{ij}) in each direction for the system in question. In the following discussion we consider two extreme examples as illustrated in Figure 1.20: (i) a layered system where Grüneisen components are highly anisotropic, and (ii) a cross-linked framework where Grüneisen components are isotropic and there is strong elastic cross-linking (*i.e.* S_{13} is non-zero) [78]. Equation 1.25 can be formulated as,

$$\alpha_i = \frac{C_T}{V} \sum_j S_{ij}\gamma_j, \tag{1.26}$$

for the linear case. Here C_T is the isothermal specific heat, V is the unit cell volume, S_{ij} are the elastic compliances and γ_j are the components of the anisotropic Grüneisen parameters (weighted sums over the individual mode Grüneisen parameters). For a uniaxial system

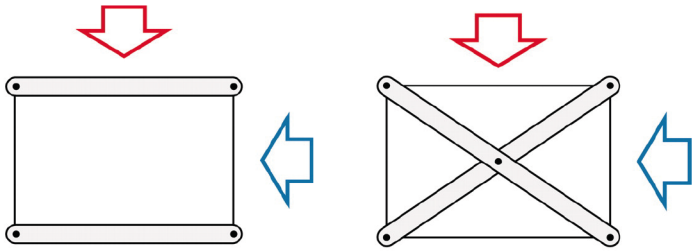

Figure 1.20: Comparison between the mechanical response of layered and cross-linked frameworks. Uniaxial compression in layered materials is strongly direction dependent (left) whereas that in connected frameworks produces similar internal strains for very different applied directions (right). Figure adapted from Ref. 78, copyright © 2008 National Academy of Sciences U.S.A.

as illustrated in Figure 1.20 we include the elastic compliances in the **a** and **c** directions,

$$\alpha_a = \frac{C_T}{V}[(S_{11} + S_{12})\gamma_a + S_{13}\gamma_c], \tag{1.27}$$

$$\alpha_c = \frac{C_T}{V}[2S_{13}\gamma_a + S_{33}\gamma_c], \tag{1.28}$$

where γ_a and γ_c are the components of the anisotropic Grüneisen parameter along a and c. Substituting the compressibilities along each direction as shown in Eq. 1.22 we obtain

$$\alpha_a = \frac{C_T}{V}[K_a\gamma_a + S_{13}(\gamma_c - \gamma_a)], \tag{1.29}$$

$$\alpha_c = \frac{C_T}{V}[K_c\gamma_c - 2S_{13}(\gamma_c - \gamma_a)]. \tag{1.30}$$

For strongly coupled frameworks, where the Grüneisen parameter is isotropic, the second term becomes a second-order correction and there is a direct correspondence between K_ℓ and α_ℓ. On the other hand, for layered systems the cross linking term is large because of the Grüneisen anisotropy, *e.g.* for graphite, $\gamma_a/\gamma_c \simeq -163\%$, Ref. 105. Therefore for strongly coupled, 'wine-rack'-like systems there is good reason to believe that there is a strong correspondence between axes of NLC and NTE.

Mechanistically the link between NTE and NLC is perhaps intuitive, whilst the formal link is much more complex due to the temperature-dependence of the elastic constants. These can be extreme as predicted in $TlGaSe_2$ where negative compressibility occurs only between 180–220 K due to a rapid changes in the elastic constants [134]. Highly anisotropic elastic constants (a requirement for NLC) are found empirically to give rise to other unusual mechanical properties, such as a negative Poisson's Ratio (auxeticity) [135]. Of 121 zeolites of the same composition [123], 16 were found to potentially show NLC based on the elastic tensors alone (see §2.2.2) of which 10 are auxetic in at least one direction. This compares to only 13% of non-NLC zeolites showing auxeticity [135]. Rationalising such links for pressure responses only would be possible but as yet no systematic study

has been carried out.

1.3 Diffraction techniques

The main technique employed in this thesis are based on diffraction. As this technique underpins many of the results presented in the main experimental chapters, here I summarise the experimental principles and what we might aim to learn from each type of experiment. For example, from many diffraction experiments we are able to readily determine the unit cell of the material (*i.e.* the dimensions of the crystal structure), which when measured as a function of temperature or pressure allows the calculation of thermal expansion or compressibility [86]. As well as the bulk material response these experiments can give information on the atomic-scale mechanisms that give rise to responses. Over the course of this work I have made use of in-house X-ray, synchrotron X-ray and neutron diffraction techniques on single-crystal and polycrystalline powder samples. In many cases experiments have been carried out under variable-pressure and -temperature conditions. Total-scattering experiments have also been carried out. Where appropriate technical details of experiments are given in each chapter and additional detail is given in Appendix A.

1.3.1 Basic scattering theory

Max von Laue first reported the diffraction of X-rays by a crystalline solid in 1912 [136]. Diffraction is characterised as the splitting of an incident X-ray beam by interference with the atomic structure into many diffracted beams. The diffracted beams of these early experiments could then be recorded on photographic film, with the form of the resulting *diffraction pattern* being a direct result of the atomic structure of the crystal used [136]. Figure 1.21(a) gives the geometry of a diffraction experiment showing the incoming beam of radiation, the sample and a suitable detector. Subsequently it was discovered by W. H. Bragg and W. L. Bragg that diffraction patterns could be interpreted by considering a crystal as a series of equally spaced planes of atoms, and therefore the constructive

interference of the scattered radiation could be defined by Bragg's Law [137]

$$2d \sin\theta = \lambda. \tag{1.31}$$

Here d is the separation of lattice planes, θ is the angle that the radiation is incident upon the crystal, and λ is the wavelength of the radiation used. Equation 1.31 can be thought of in a simplistic way by considering the diffraction of X-rays as equivalent to optical light reflecting from a series of equally spaced semi-transparent mirrors [Fig 1.21(b)].

Equation 1.31 allows the direct interpretation of a diffraction pattern (assuming it is measured with monochromatic radiation) to measure the spacing between planes of atoms (d, or d-spacing). By measuring the crystal in many orientations θ (or measuring a polycrystalline sample) we are able to determine the spacing between many sets of planes, and therefore construct a full 3D structure of a material. This is crystallography, a science that has been fundamental to many scientific advances in the last 100 years (twenty nine Nobel prizes have been awarded in the broad field of crystallography [138]).

Formally, the interaction of radiation with atoms within a crystal can be considered on

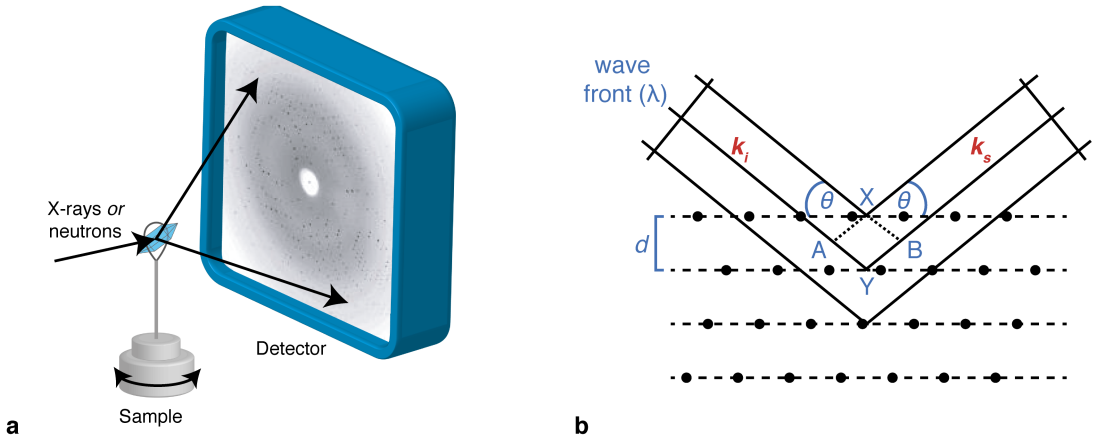

Figure 1.21: Diffraction from a crystalline system to give Bragg reflections. (a) A single crystal gives rise to discreet points in the diffraction experiment that can be measured using a 2D detector. During the experiment the sample is rotated to collect all unique reflections to allow structure solution. (b) Bragg reflections can be thought of as arising from the reflection of incident radiation ($\mathbf{k}_i$) of wavelength λ at angle θ by a series of well-aligned semi-transparent mirrors. The interference of this radiation gives peaks in the scattered radiation ($\mathbf{k}_s$) that is characteristic of the inter-planar separation, d.

the basis of elastic scattering theory. Incident radiation of wave vector $\mathbf{k_i}$ interacts with the sample, producing a wave $\mathbf{k_s}$ [139]. If we consider only elastic scattering, then there is no energy transfer and therefore the energy of both waves is identical. The scattering vector is given by $\mathbf{Q} = (\mathbf{k_i} - \mathbf{k_s})$; interference occurs when two waves are scattered by separate atoms causing constructive or destructive interference. The Fourier transform of the density function, $\rho(r)$, gives $F(Q)$, the total scattering factor [139]. For perfectly long-range periodic systems, $F(Q)$ is non-zero only for a periodic set of $\mathbf{Q}$, defined above as Bragg reflections. In a single-crystal or powder experiment these reflections can be indexed according to the allowed symmetry of 3D periodic systems [Table A.1.1]. It is worth noting here that for systems that are not long-range periodic $F(Q)$ is not zero and diffuse scattering is observed instead of, or in addition to, the Bragg scattering.

Reflection positions give the unit cell dimensions (the smallest repeating unit of the crystal), whilst the presence or absence of certain reflections (allowed or forbidden reflection conditions) give the centring and direction of translational symmetry elements of the space group [140]. The simplest description of the contents of a unit cell is called the asymmetric unit, and when certain symmetry operations are applied this reproduces the crystal structure; a full description of the symmetry elements within a unit cell is described within the space group. Restrictions on the continuous tiling of 3D space within a crystal, and the symmetry restrictions within certain types or centring of cell, mean there are only 230 space groups. These arise from: 7 lattice families that describe the dimensions of the unit cell $(a, b, c, \alpha, \beta, \gamma)$; 14 Bravais lattices that give the unique centring in each of the basic lattice families, and describe the basic translational symmetry; 32 crystallographic point groups giving the rotations, reflections and inversion allowed; additional glide and screw axes that combine reflections or rotations with translations. Every commensurate non-magnetic crystal structure is fully described by one of the 230 space groups; additional space groups arise where there is incommensurate or magnetic order.

The diffraction pattern is not just a measure of the dimensions of the unit cell, but

also the contents of the unit cell. Modern diffraction methods allow us to study materials with unit cells containing anything from a few atoms or molecules, to an entire virus [141]. This information is not given by the positions of Bragg reflections but by the amplitude and phase of diffracted peaks. These are calculated from the structure factor equation for each (hkl) plane [142]

$$F_{hkl} = \sum_j f_j \exp[2\pi \mathrm{i}(hx_j + ky_j + lx_j)], \tag{1.32}$$

$$= \sum_j f_j \cos[2\pi(hx_j + ky_j + lx_j)] + \mathrm{i} \sum_j f_j \sin[2\pi(hx_j + ky_j + lx_j)]. \tag{1.33}$$

This sum is over all atoms in the asymmetric unit, with f_j being the scattering factor of the j^{th} atom and (x_j, y_j, z_j) its positional coordinates within the unit cell. The intensities of diffraction peaks are proportional to the square of the amplitude of the diffracted wave and no information can be measured in a diffraction experiment to give the phase (the complex part of Eq. 1.33). Diffraction intensity is also a function of thermal motion of atoms, lattice strain and absorption effects.

The majority of diffraction experiments are carried out in-house using vacuum-sealed X-ray sources. Within a vacuum-sealed tube a metal target, typically molybdenum, copper, iron or silver, is bombarded by a high-energy electron beam. A continuous spectrum is observed (white radiation) as well as sharp lines that are characteristic of the target [141, 143]. These sharp emissions are caused by electrons stripped from inner atomic orbitals being replaced by electrons from higher energy orbitals. The X-rays produced are a function of the energy levels involved (termed K, L, M etc.) and are of discreet energies: for example the most widely used wavelength used in powder diffraction ($\lambda = 1.541\,\text{Å}$) is due to copper K$\alpha_1$ emission caused by an electronic transition from $2p^{3/2} \rightarrow 1s$ [144]. In general the emission from the K lines is used (Kα_1, Kα_2 and Kβ) as these have the highest energy and intensities [141]. The emission from lab sources is usually monochromated to ensure that a single wavelength hits the sample [145]. There are many cases where a different wavelength might be needed, or tuned wavelengths, and for this synchrotron

radiation is required. Furthermore diffraction by a different form of radiation, *e.g.* neutrons or electrons, may be preferable. In the next two sections I describe briefly modern synchrotron and neutron techniques used in this thesis.

1.3.2 Synchrotron X-ray diffraction

When a charged particle is accelerated it emits electromagnetic radiation; when this acceleration is radial the radiation emitted is known as synchrotron radiation [141]. For particle sciences this energy loss is unwanted but it was quickly realised that the broad energy range (from far infrared to γ-rays) [Fig. 1.22(a)], high polarisation and intensity of emitted radiation could be used for diffraction and other scattering techniques. The first and second generation of dedicated synchrotrons were not however built until the 1960s and 1980s [141]. Due to the very large size (up to 1.5 km in circumference) and expense of these facilities they are usually nationally or internationally funded with work being carried out by researchers in collaboration with facility staff.

Synchrotron light sources (usually known just as synchrotrons) are in fact not a continuously curved electron accelerator, rather they are made up of sections of straight sec-

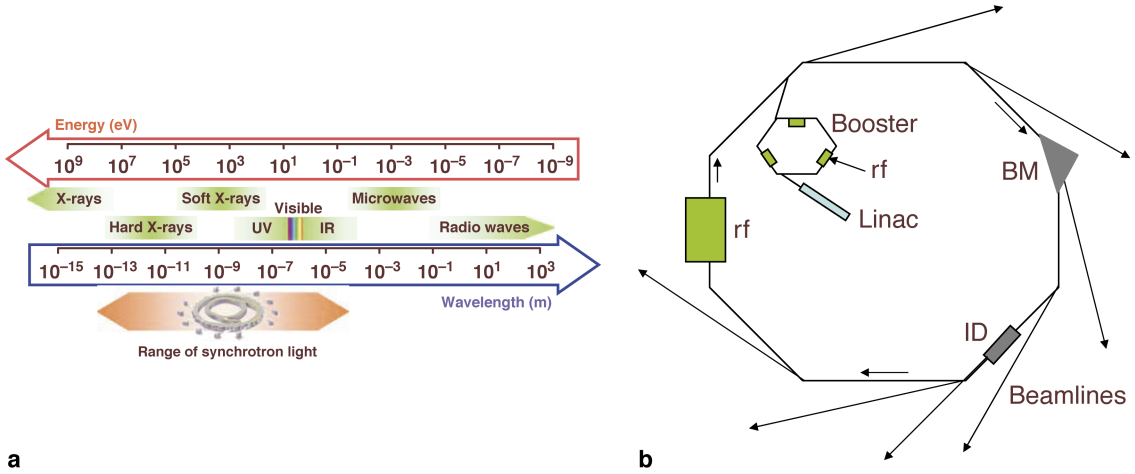

Figure 1.22: Characteristics of synchrotron radiation and schematic instrument layout. (a) Range of wavelengths and energies of electromagnetic radiation highlighting those that can be produced at modern synchrotron sources. (b) The general layout of a synchrotron showing the linear accelerator where electrons are produced and initially accelerated, the booster ring, and the large main storage ring. A bending magnet (BM) and insertion device (ID) are highlighted and radiation is guided along radial paths to beamlines for experiments (arrows). Reproduced from Ref. 141, Chapter 1; with kind permission from Springer Science and Business Media.

tions and curved bending magnets (BM) where radiation is produced. 'Third generation' sources make use of insertion devices (IDs) such as wigglers, undulators and wavelength shifters that are placed in the electron path that produce very brilliant synchrotron light [Fig. 1.22(b)]. These insertion devices use magnetic fields of opposing polarities to change the trajectory of the electron beam, therefore producing radiation of specified characteristics for experiments [141]. Radiation produced by the synchrotron (either BM or ID) is guided away from the main ring, focused, columnated and monochromated along a beamline into an experimental hutch where the sample and detectors are placed. Due to the continuous operation of the synchrotron and the multiple BM and IDs many experimental stations can be operational simultaneously.

The properties of the radiation produced in modern synchrotrons are optimised for the experiments carried out. We might choose to carry out a synchrotron experiment over an in-house X-ray diffraction experiment because [141, 146]:

- continuous spectrum can be used, or monochromation can select a wavelength for each experiment and can be changed in each experimental station (within the characteristics of the BM or ID) and,

- high intensity, good columation (narrow vertical emission), polarisation and pulse structure. The brightness (a function of intensity (photons/s) per area of emitter (cm^2) normalised by the solid angle of the beam) of an undulator beam can be 10^9 times larger than that of a conventional X-ray tube [144].

The U.K. national synchrotron is Diamond Light Source, a 3^{rd} generation 3 GeV source based at the Rutherford Appleton Laboratory. Larger synchrotrons are the European Synchrotron Radiation Facility (ESRF, Grenoble, France), SPring-8 (Hyōgo, Japan), Advanced Photon Source (APS, Chicago, USA) and PETRA III (Hamburg, Germany).

1.3.3 Neutron scattering

To this point, we have only considered diffraction as a process occurring when X-rays interact with a sample. In reality, any radiation of a suitable wavelength can diffract in

exactly the same way as described above: wave-particle duality means that subatomic particles, such as neutrons and electrons with a suitable momentum will diffract from atoms in materials. The wavelength of neutrons is given by the de Broglie relationship

$$\lambda = \frac{h}{p}, \tag{1.34}$$

where h is Planck's constant and $p = m_{\mathrm{n}}v$, the neutron momentum. Neutrons suitable for diffraction ($\lambda = 1.8\,\text{Å}$) will therefore have a velocity of 2.2 km/s, corresponding to an energy of 25.3 meV.

Accepting that beams of electrons and neutrons can diffract like X-rays, we must then consider the characteristics of these particles. Electrons interact with the electrons in the sample (as with X-rays), and as both are charged they penetrate only some 100 nm into the sample resulting in a diffraction pattern that is characteristic of the surface of the sample. Conversely neutrons have much greater mass but are uncharged. As a result neutrons interact primarily with the atomic nuclei *via* the strong nuclear force. The nuclear radius is approximately 10^4 smaller than the atomic radius (the electron cloud) meaning that neutrons very deeply penetrate samples before scattering (some mm at least, X-rays penetrate $\sim 10\,\mu m$ before scattering) [144]. Additionally neutrons have spin and a magnetic moment and therefore are sensitive to the magnetic structure of materials.

These properties of neutrons means that they can be used in a huge array of experiments investigating the structures and dynamics of materials. A neutron beam has an energy comparable to that of thermal excitations in materials and so in inelastic neutron spectroscopy (INS) the energy and wave vectors of vibrational or magnetic excitations can be measured. This is possible because energy E, in wave mechanics, is complementary to time t and so inelastic methods are used to measure energies of quantised excitations ($E = \hbar\omega$). Small-angle neutron scattering (SANS) can measure variations in scattering density over length scales up to a micron, and neutron reflectometry is a diffraction technique used for measuring the structure of thin film samples [144].

For diffraction studies the greatest advantages of neutrons over X-rays are (i) the

variation in scattering lengths b and (ii) the fact that neutrons have spin. The intensities of Bragg reflections given by Equation 1.33 includes the scattering lengths f_j of each atoms involved [139]. The coherent scattering lengths of elements to X-rays increase with the atomic number (*i.e.* the number of electrons), but for neutrons the interaction is with the nucleus and so coherent scattering lengths of neutrons do not vary in the same periodic way [Fig. 1.23(a)]. Thus neutron diffraction can eliminate challenges for X-ray diffraction such as detecting very light elements (due to the small number of electrons, *e.g.* hydrogen), elements very close in the periodic table (due to difficulties in contrast *e.g.* C and N) and with light elements in the presence of very heavy atoms (*e.g.* transition metal hydrides) [140]. Contrast studies make use of the different neutron scattering lengths of isotopes and are widely used in the study of liquids and proteins. For samples with magnetic ions, neutrons are the obvious choice to determine magnetic structure as neutron spin interacts directly with unpaired electrons in the sample giving rise to magnetic Bragg reflections.

The ideal choice of radiation is clearly sample-dependent. Weak scattering, or absorption of neutrons, by certain nuclei can cause problems *e.g.* naturally abundant Gd is a very good neutron absorber and therefore cannot be used. Incoherent scattering—scattering that does not preserve the phase relationship between incident and scattered waves—can be significant for neutrons so nuclei with large incoherent scattering lengths (*e.g.* ^{1}H) should be avoided for diffraction experiments. Consequently isotopic substitution is often

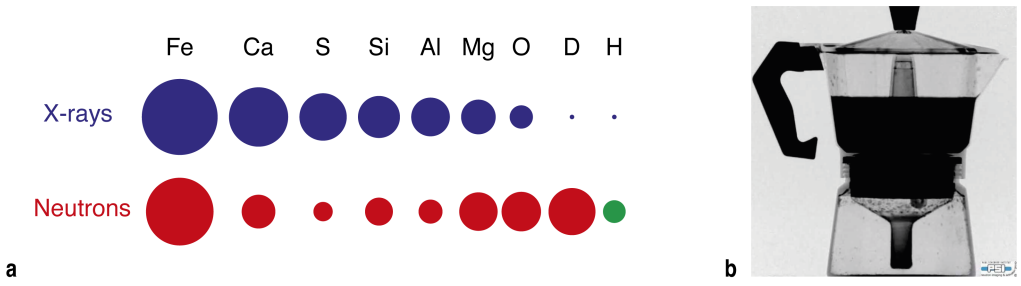

Figure 1.23: Contrasting scattering behaviour of X-rays and neutrons. (a) Comparison of the scattering cross-section of a variety of elements in X-ray and neutron diffraction experiments. The green area indicated for hydrogen indicates the large incoherent signal [147]. (b) An image of an aluminium coffee maker when placed in a neutron beam. Here we see that the water shows up strongly (back areas) whereas the metal is almost invisible. If the same experiment were carried out using X-rays, we would only see the outline of the pot. Image reproduced with permission from the Paul Scherrer Institut.

carried out to ensure maximum coherent scattering in diffraction experiments. A side point here is that materials with very weak scattering can be used to make sample environments as they appear essentially invisible to neutrons (*e.g.* vanadium) [Fig. 1.23(b)].

Considerable practical challenges are encountered when carrying out neutron experiments meaning they are not as widely accessible nor as routine as X-ray experiments. Neutrons are either produced by nuclear fission—necessitating the construction of unpopular nuclear reactors—or by spallation. Spallation is the process of neutrons being emitted from heavy nuclei as a result of being bombarded with high energy particles, typically protons [139]. In the U.K., the national neutron facility is the ISIS spallation source where a variety of instruments arranged around the heavy metal target can carry out a wide variety of neutron scattering experiments [Fig. 1.24]. For diffraction, spallation sources make use of the time-of-flight method for powder and single-crystal diffraction; further experimental details are given in Appendix A. Reactor sources carry out diffraction in essentially the same way as for X-ray studies, with a monochromated constant wavelength beam of neutrons incident on the sample.

1.3.4 Single-crystal diffraction measurement and analysis

We now shift our focus to the details of single crystal and powder diffraction methods. Throughout this thesis the term 'powder' will mean a polycrystalline sample measured and analysed as outlined in the next section, whilst 'single-crystal' will mean an experiment carried out on a single crystallite. Both methods are employed but it is noted that many more results rely on powder methods and so more detail will be given in that section.

Using single-crystal diffraction methods the intensities of individual reflections are measured. In-house single-crystal diffractometers are increasingly powerful with full data sets measurable in a few hours in favourable cases [Fig. 1.25(a)]. Modern diffractometers measure reflections on large 2D area detectors, usually a charge-coupled device (CCD) detector. Focusing of these reflections relies on the correct positioning of the X-ray beam, sample and detector according to the Ewald sphere construction [Fig. 1.25(b)].

The Ewald sphere is defined as a sphere centred on the sample position (the origin

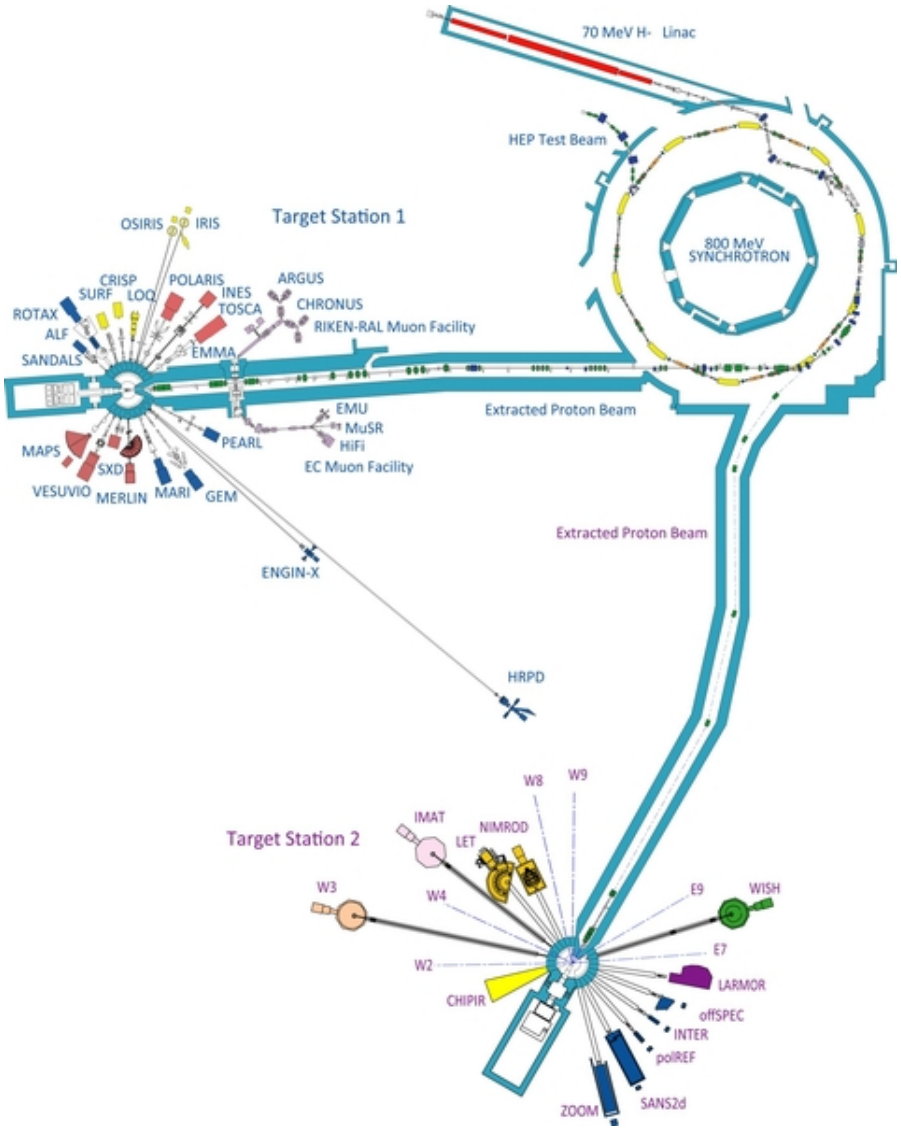

Figure 1.24: Plan of ISIS spallaton neutron source. Pulsed neutron beams are produced by the acceleration of bunches of protons—formed from hydride ions entering the synchrotron through a stripping foil—in the 800 MeV synchrotron, that are then kicked down one of two beam guides to collide with a heavy metal target (TS1 and TS2 shown). Around each target sit liquid moderators that produce a neutron beam profile optimised for experiments in the instruments beyond. Reproduced with thanks, © STFC.

of diffraction) of radius $1/\lambda$ passing through the centre of the reciprocal lattice [150]. A reflection is detected if the reciprocal lattice point intersects with the Ewald sphere. By rotation of the Ewald sphere about its origin (in practice, by rotation of the crystal by three angles ω, ϕ and κ) we can access all reflections within the limiting sphere of the experiment. For small values of λ the Ewald sphere is sufficiently large that multiple lattice points can be measured simultaneously on a 2D detector and the curvature of the sphere can be approximated to be flat [Fig. 1.25(c)].

Once images of reflections covering all of reciprocal space (or some smaller fraction of this, if the symmetry allows) have been collected they are normalised and corrected; following this the individual reflections are indexed and their intensities extracted by fitting a peak profile to the intensity distribution. This data reduction process gives a dataset of (hkl) indices and reflection intensities that allows the refinement of a structural model. The 3D measurement of reflection positions and intensities allows *ab initio* structural solution. As the phase of reflections cannot be measured the "phase problem" must be overcome: in the majority of cases this is achieved by using direct methods. Direct methods estimate phases using statistical methods that will not be covered in detail here. Structure solution and refinement can be carried out using software such as CRYSTALS [151] or SHELEX [152].

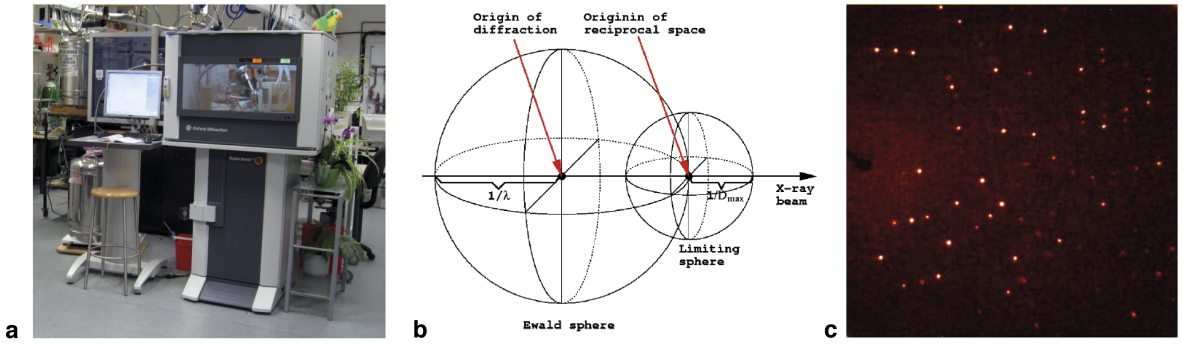

Figure 1.25: Collection of single-crystal diffraction data for crystalline materials (a) A modern Oxford Diffraction (Agilent) SuperNova single-crystal X-ray diffractometer used in this work. (b) Construction of the Ewald sphere and the limiting sphere that gives the condition for a Bragg reflection to be detected in a diffraction experiment, reproduced with thanks from Ref. 148. (c) Diffraction pattern collected on a modern in-house single-crystal diffractometer showing discrete Bragg reflections, reproduced with thanks from Ref. 149.

Materials with structural disorder retain a well-defined diffraction pattern, although this diffraction intensity cannot be interpreted in the same way as outlined above and the pattern is quite unusual. Diffraction intensity detected away from expected Bragg peak positions is known as diffuse scattering [27], as seen in Figure 1.5. As another example, the diffraction pattern of layered materials appears to consist of typical Bragg reflections when viewed along a direction perpendicular to the layers, but rotation of the crystal away from this direction would reveal these 'spots' to be the cross section of diffuse rods that run parallel to that layer stacking axis. Interpretation of diffuse scattering to characterise low dimensionality, correlated and dynamic disorder is considered in more detail in Chapter 6.

1.3.5 Powder diffraction measurement and analysis

In many cases single crystal diffraction is not possible, usually because the size or quality of crystals available is not good enough to collect such data. For these samples the crystallographic technique of choice is powder diffraction, where multiple crystallites are analysed simultaneously. These crystallites are randomly orientated in the sample, meaning the resulting diffraction pattern is a (powder) average of the single reflections observed in single crystal experiment. For this reason powder diffraction is thought of as a 1D method.

This 3D averaging means that within the diffraction experiment, shown schematically

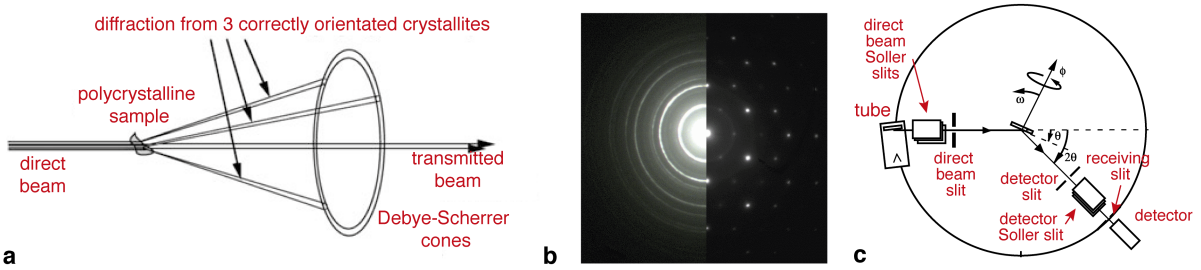

Figure 1.26: Powder-averaging and collection of powder X-ray diffraction data. (a) Multiple randomly-orientated crystallites in a polycrystalline sample create Debye-Scherrer rings of diffraction intensity that can be detected using a point, strip or 2D detector. (b) The rings are shown alongside a single-crystal diffraction pattern of the same material showing the averaging of diffraction intensity. (c) 'Debye-Scherrer' geometry of an in-house X-ray diffraction instrument showing position of X-ray source, sample and detector, with associated slits and Sollers within the focusing ring. Figure adapted from Ref. 144, Chapter 1; with kind permission from Springer Science and Business Media.

in Figure 1.26, the individually illuminated reflections observed previously are replaced with cones of diffraction intensity known as Debye Scherrer cones (with the detected rings in the diffraction experiment known as Debye Scherrer rings). Many randomly-orientated crystallites contribute to diffraction intensity within each ring, and all equivalent reflections at a certain value of 2θ *e.g.* for a cubic system the (111), ($\bar{1}$11), ($\bar{1}\bar{1}$1), ($\bar{1}\bar{1}\bar{1}$) reflections would all contribute to the same Debye Scherrer ring. The rings shown in Figure 1.26b are representative of data collected using a fixed 2D detector with the equivalent single crystal data shown for the same sample on the right of the image. Here we can clearly see the single crystal reflections occur at the same values of 2θ but are averaged in the powder rings. Such an experiment—a sample and detector placed in the direct beam—is the simplest setup to measure powder data, with the subsequent integration of rings and correction carried out by a programme such as Fit2D [153]. Studies using flat plate area detectors are common when carrying out total scattering studies and pressure studies at synchrotron sources. Powder diffraction experiments in this thesis were carried out like this at beamlines I15 and I12 at Diamond Light Source, U.K. and BM01 (Swiss-Norwegian Beamline) at the ESRF, Grenoble, France.

Flat plate experiments are much more common in-house, where strip or point detectors are generally used. The 'Debye-Scherrer' method uses monochromatic radiation and a polycrystalline sample; a point or strip detector then sweeps an arc in 2θ around the sample. This requires precise control and measurement of the positions of the three main components (the X-ray tube, the sample position and the detector) of the experiment. A $\theta - 2\theta$ experiment in Debye-Scherrer geometry keeps the tube stationary and rotates the sample and detector, whilst a Bragg-Brentano geometry moves all three components [Fig. 1.26] [144]. Instruments used in this work include PANalytical X'Pert and Empyrean diffractometers that use Bragg-Brentano geometry.

For a diffraction pattern with good intensity and minimum instrumental broadening a series of slits and Soller slits are used. The direct beam and detector slits each reduce equatorial divergence of the beam, whilst Sollers are made up of a stack of plates that

slice beam into beams each with low axial divergence. Although multiple slits and sollers can reduce instrumental broadening, often this is at the expense of diffraction intensity and therefore the exact setup is largely sample dependent (sample characteristics and mounting type, *i.e.* flat plate or capillary) to give acceptable collection times.

Where the characteristics of in-house diffraction are limiting synchrotron powder diffraction can be used. In dedicated powder diffraction beamlines the layout is very similar to that shown in Figure 1.26(c), where the source is a monochromated X-ray beam from the synchrotron source. High brilliance, downstream focusing and the low intrinsic divergence of the beam mean that very high quality powder patterns can be obtained very quickly. In this work data were collected using the I11 instrument at Diamond Light Source. Samples were packed and sealed in borosilicate capillaries, mounted on the diffractometer spinner, and data were collected using either of the strip detectors available: a position sensitive detector (PSD) that acquires data very rapidly or the banks of multi-analysing crystal (MAC) detectors. Heating and cooling of samples is possible in this geometry by use of a hot air blower or cryostream, as appropriate.

For neutron powder diffraction experiments, samples are generally loaded into a thin-walled vanadium can (as vanadium has a low neutron scattering factor) and placed in the sample tank. These are accessed from above the instruments and the sample can is placed on a centre stick which holds it in the correct position for the beam. The large sample tanks can accommodate furnaces or cryostats for variable temperature studies, as well as pressure cells as detailed below. For a standard neutron diffraction experiment data for all detectors in each bank are averaged and may be normalised to a vanadium rod standard.

Analysis of a powder diffraction pattern usually makes use of full pattern (full profile) fitting, meaning that the data are taken and analysed in their raw form. Refinement methods attempt to represent the whole experimental diffraction pattern with a multi-parameter mathematical model [144]. Using non-linear least squares algorithm the model is refined until the difference between the calculated and experimental diffraction patterns

is minimised. Fitting in this way either uses arbitrary (refined) peak intensities (Pawley or Le Bail refinement), or calculates intensities based on (refined) atomic positions according to Equation 1.33 (Rietveld refinement). Further details on these refinement methods are given in Appendix A.

In this work TOPAS Academic v4.1 and v5 were used for the analysis of powder diffraction data [154]. This programme uses a flexible input language which allows user control of all aspects of the refinement, including defining specific peak shapes, background functions as required. It also allows for parametric refinement, where multiple data files are refined simultaneously (*e.g.* a variable-temperature set of data), and batch refinement where a large number of files are refined sequentially with the previous refinement used as the input to the next. Some refinements are carried out using GSAS (General Structure Analysis Software) which is less flexible but much more well-established Rietveld refinement programme [155].

As for single-crystal experiments the powder-averaged diffraction pattern of a disordered material is well defined. Here the X-ray, neutron or electron diffraction pattern contains a smoothly-varying background instead of, or in addition to, Bragg reflections, known as the total scattering function. The Fourier transform of this entire scattering pattern gives a pair distribution function (PDF) that reflects at once local and long-range order. Powder averaging in this case makes analysis easier than in the case of single crystals: correctly normalised and carefully corrected diffraction pattern can routinely give a PDF that can highlight local structural details not revealed by average structure studies alone [156].

1.3.6 Variable-pressure diffraction

Throughout this thesis we are interested in the mechanical response of materials, and in particular responses under hydrostatic pressure. Hydrostatic pressure is particularly relevant as this is a thermodynamic parameter and therefore the associated response is an intrinsic one based on the fundamental elastic properties of the material [157]. Variable-pressure diffraction experiments are more challenging to carry out than those

under ambient conditions or variable-temperature [86]. In the latter case cryostreams, cryostats, hot air blowers and furnaces are all able to change the temperature at the sample position in a controllable way to access a wide range of temperatures [158].

When applying pressure we must consider several challenges: (i) the best type of radiation for the sample, which also influences (ii) the type of pressure cell used, and (iii) the correct choice of pressure transmitting medium (PTM). In most cases, pressure is applied to a sample by applying a force to a small sample volume filled with the PTM fluid. This external mechanical force can be applied by using either a diamond-anvil cell (DAC) or a Paris-Edinburgh (P-E) press [Fig. 1.27] [159, 161]. In both cases two anvils are driven together on a sample chamber supported by a pre-indented gasket [86]. A DAC is a few centimetres in total diameter and the P-E press is much larger. Force is applied in the case of the former using Allen screws that are manually tightened to increase pressure, or a gas membrane that can be used to change pressure remotely. To increase pressure using a P-E cell an oil piston is used.

The size of each apparatus limits the amount of sample that can be used. For a DAC the sample chamber can accommodate a small single crystal, or a very small amount of

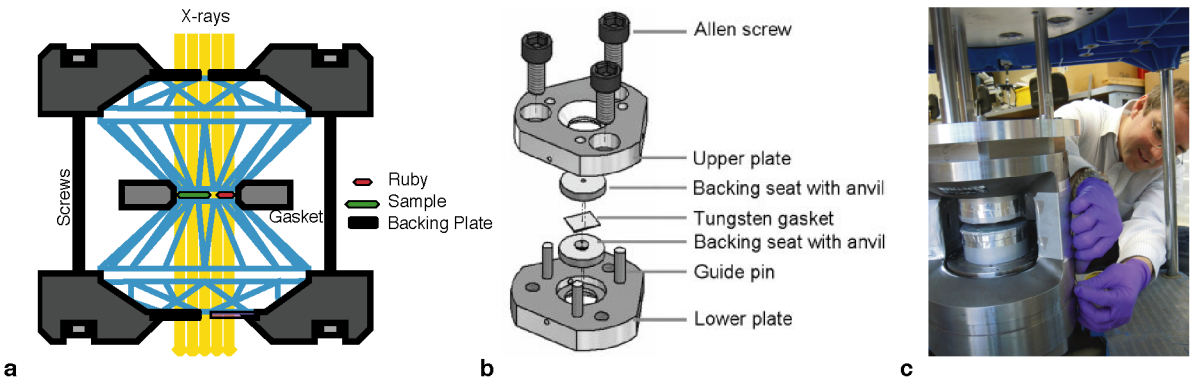

Figure 1.27: Apparatus used for in situ application of pressure to samples during diffraction experiments. (a) The Diamond-Anvil Cell (DAC) shown in profile and (b) expanded view. The diamond anvils are forced together on the gasket which defines the sample chamber; the backing plate holds the diamonds in place and the ruby is used for pressure calibration by the fluorescence method [159]. Figures reproduced from "Schematics of the core of a diamond anvil cell" by Tobias1984 licensed under CC-BY, and Ref. 160, with permission of the International Union of Crystallography. (c) The much larger Paris-Edinburgh press [161] can accommodate the large sample volumes required for neutron diffraction experiments, whilst the unique properties of neutrons means that the large sample environment does not contribute significantly to the background of the data.

polycrystalline sample. Consequently much more intense radiation is required, meaning most DAC powder experiments are carried out at synchrotron sources. Single-crystal experiments can be carried out with modern micro-focused tubes or synchrotrons, with longer collection times needed in most cases. For all X-ray DAC experiments post-experiment data correction is required to mask diamond Bragg reflections [153, 162] and correct absorption [163]. The P-E press is used almost exclusively for neutron powder diffraction as it can accommodate much larger volumes of sample and the press can be designed in such a way as to minimise background. In all cases VP data can pose challenges: we might expect high backgrounds (diffuse or Bragg scattering), the configuration of the cell can obscure many Bragg reflections due to the limiting opening aperture, and the large applied pressures can cause anisotropic strain and therefore large peak broadening under pressure that must be accounted for [78, 159].

The PTM is added to ensure no shear forces are supported in the sample volume [157]. Each PTM has a 'hydrostatic limit' above which the medium freezes and the experiment can no longer be considered hydrostatic [86], giving rise to in homogenous and differential stress and shear stresses on the sample [157, 164]. In general larger-molecule PTMs— such as silicone oil or fluorinert— have a lower limit than smaller molecules, such as methanol/ethanol [157, 165]. Sample reactivity and interactions with the medium of choice must also be considered, especially when studying potentially porous materials. It has been shown that molecules of PTM can enter porous structures [166], and that seemingly unreactive samples can undergo rearrangement under pressures to unexpected high-pressure inclusion structures [167]. Experimentally the choice is often a compromise between these factors for the materials of interest in this thesis.

1.4 Molecular framework materials

Archetypal inorganic material structures are often based on the close-packing of cations or anions, with counterions filling interstitial sites to form lattices where the dominant energetic driving forces are long-range, electrostatic forces [168]. Such materials are widely studied, with implications in understanding the earth's crust, fundamental material me-

chanics and magnetic properties. Some of these materials—depending on the electronic stabilisation gained and strength of bonds formed for certain coordination geometries—have bridged structures, *i.e.* based on corner-sharing polyhedra [44]. Some of these structures have already been explored in this chapter, the canonical bridged oxide material being the huge family of perovskites.

More elaborate perovskite-based structures have recently gained significant prominence. Lead halide perovskites have been shown to have exceptional solar conversion efficiency (up to 20%) for applications in solar panel technology [169]. These materials have 'hybrid' structures: lead and halide cations make up the perovskite framework, whilst the interstitial A site cation is a molecular ammonium-based species. This family show the complexity that can be introduced into the broad perovskite system, the extension of a canonical structure type into the chemistry of hybrid materials and the development of exotic physical properties. The material chemist's challenge—even by just within this one structure type—is to find new materials with specific properties for devices by controlling atomic structures, electronic structure and interactions within the system.

Molecular framework materials are based on the connection in one-, two-, or three dimensions of nodes (usually metal cations or cationic metal clusters) with multi-atom linkers (bi- or multi-dentate molecular species; Figure 1.28). This gives rise to an almost limitless structural diversity: if we consider all possible combinations of metals and link-

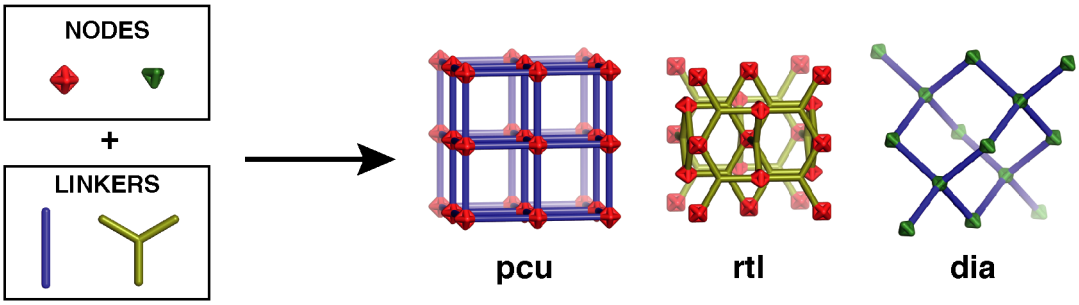

Figure 1.28: The basic design strategy for molecular frameworks involves the linking of nodes (here, red octahedra or green tetrahedra) by molecular bridging units (here, blue rods or yellow triangles) to form a three-dimensional open network. By using nodes and/or linkers of different connectivities it is possible to access a very large number of different network topologies [170], here the primitive cubic (**pcu**), rutile (**rtl**) and diamondoid (**dia**) nets, as designated with TOPOS [171].

ers, well over 6620 unique framework topologies are possible [44, 172, 173]. This class of material includes the prominent metal–organic frameworks (MOFs) that have been the focus of widespread research [172, 174], but also frameworks built on simpler molecular building blocks such as cyanide [175–177] as well as non-porous frameworks.* This design principle gives rise to materials that are inherently predisposed to have structures dictated by strong short-range interactions—covalent bonds within molecules and the polar-covalent interactions between metals and linkers—on the one hand, and long-range van der Waals or other weak structure-directing forces on the other [179, 180]. Structural and mechanical degeneracy dominate properties in such materials that often have open, light and flexible structures.

1.4.1 Metal–organic frameworks

Targeted material design is perhaps one of the greatest challenges in solid state science. Despite many years of dedicated work, predicting precisely what structure a certain stoichiometry of atoms might adopt is still not possible [181]. MOFs and related materials, in one sense, are much more complex than many canonical materials, and yet are the most advanced in terms of targeted design, on the other hand. By judiciously choosing metal nodes and molecular linkers we can synthesise materials with a certain topology, connectivity or chemistry, thereby effectively targeting functional properties [181, 182]. The strong coordination preference for certain metals coupled with the predictable shapes of rigid molecular linkers—with the lack of long-range or other perturbing interactions—goes some way to rationalising this targetability [183, 184]. Material design in this way is known as reticular synthesis [182].

Early MOF chemistry was built on the coordination of dicarboxylate and related ligands with transition metals. For example the canonical MOF-5 is constructed from clus-

---

* Recent IUPAC recommendations [72] strictly define the terms "coordination polymer", "coordination network" and "Metal–Organic Framework" (the first being the general class of materials, and the latter two being subsets of this); these recommendations have not yet been widely implemented and in our work we generally use the term "molecular framework" as an inclusive term somewhat similar to the definition proposed for coordination polymer [178].

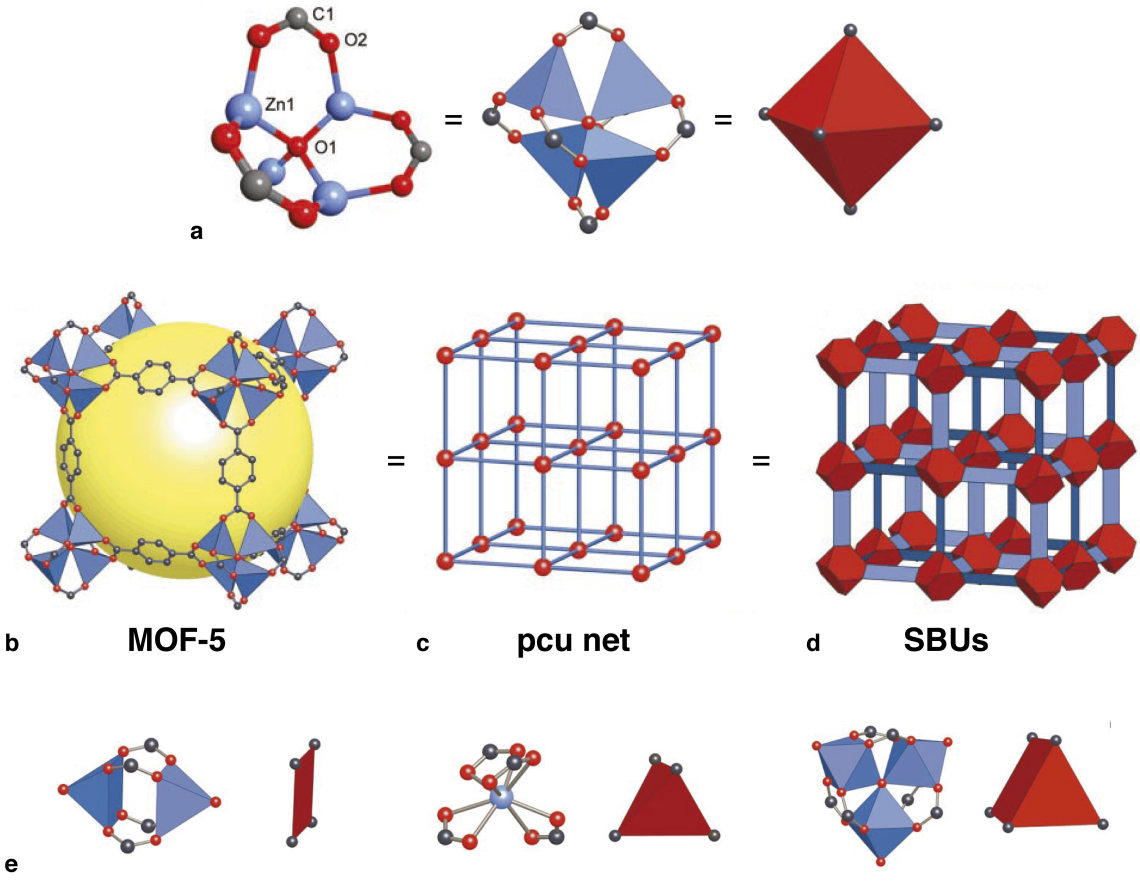

Figure 1.29: Structural representations of MOF-5 and the structures of metal cluster SBUs (a) Atomic and polyhedral representations of the metal cluster in MOF-5 that gives the main octahedral SBU forming the corners of the framework. From Ref. 184, reprinted with permission from AAAS. (b) The MOF-5 structure shown as ZnO_4 tetrahedra (blue polyhedra) joined by benzene dicarboxylate linkers (O, red and C, black) to give an extended 3D cubic framework with interconnected pores of 8 Å aperture width and 12 Å pore (yellow sphere) diameter. (c) The topology of the structure (primitive cubic net) is shown as a ball- and-stick model and (d) as SBUs given by the envelopes of the $(OZn_4)O_{12}$ cluster (red truncated tetrahedron) and benzene dicarboxylate (BDC) ion (blue slat). Note that opposing slats are all at 90°. (d) Examples of SBUs from carboxylate MOFs. O, red; N, green; C, black. In inorganic units metal–oxygen polyhedra are blue, and the polygon or polyhedron defined by carboxylate carbon atoms (SBUs) are red. Reprinted by permission from Macmillan Publishers Ltd: *Nature* Ref. 182, copyright 2003.

ters of tetrahedral Zn^{2+} anions that form an overall octahedral geometry [Fig. 1.29(a)], and the linear benzene dicarboxylate (BDC) ligand [182]. We can view this structure in several ways, as depicted in Figure 1.29: the full atomic structure, with the large resulting pore volume indicated as a large yellow sphere, connections of nodes to form a primitive cubic structure, or the representation of secondary building units (SBUs). By substituting different metals and metal clusters we can form a range of coordination geometries and therefore alternative SBUs [Fig. 1.29(e)], that when added to dicarboxylates can form different nets as shown in Figure 1.28 [182]. Furthermore we can adjust the length of linker used and under almost identical synthesis conditions synthesise isoreticular MOFs (IRMOFs) with diverse pore sizes and functionalities. In the study of Ref. 183 the linkers R2-BDC, R3-BDC, R4-BDC, R5-BDC, R6-BDC, R7-BDC, 2,6-NDC, BPDC, HPDC, PDC, and TPDC were all used instead of BDC, yielding materials with very large adsorption surface areas (pore volume up to 91.1% of the crystal volume).

With such attractive properties, it is no surprise that many other classes of similar materials have emerged. A problem with early MOF systems was poor water stability, as H_2O is more basic than many organic linkers, in addition to low metal coordination numbers, meaning that exposure to water can cause the framework to break down [77]. The UiO (University of Oslo) class of frameworks, *e.g.* UiO-66, are unique due to very high metal coordination using BDC with metals such as Zr, Hf, U to form six-centre octahedral metal clusters that are highly stable to even very harshly acidic or basic conditions [185, 186]. The MIL frameworks introduced previously—built from the terephthalate and benzenedipyrazolate linkers— are unique due to their framework-breathing transitions with very flexible structures based on the 'wine-rack' motif [187, 188]. Our final example of third generation MOFs are zeolitic imidazolate frameworks (ZIFs) [189]. In these materials imidazolate or functioned imidazolate linkers are used to bridge tetrahedral metal (Zn(II), Co(II), or In(III)) centres. This coordination imparts a 145° angle throughout the frameworks *via* coordinating N atoms in the 1,3-positions of the ring [189]. This results in: (i) materials that are water stable, due to the strong binding of the nitrogen–metal

bond, and (ii) materials with topologies identical to zeolites. There are > 150 types of zeolite frameworks, and therefore there is huge potential in this family, with members mimicking the structures of zeolites (*e.g.* ZIF-8), dense quartz or cristobalite structures (*e.g.* $Cd(im)_2$) and even amorphous silica (*am*-ZIF) [190].

Using this chemistry we can exploit structural tools not easily accessible in traditional ceramic materials; for example, chiral organic linkers can be used to produce inherently acentric (and therefore piezoelectric) frameworks [191], and there is a potential for host–guest interactions so we can couple functionality with sensing capabilities [192]. Beyond simply investigating materials for ever-larger pore volumes, these materials have been shown to have a wide range of other interesting functionalities [174]. Recent examples include multiferroicity, order-disorder transitions, and glassy behaviour in transition-metal formates [193, 194], soft-mode displacive instabilities in functionalised lanthanide terephthalates [195], and pressure- and temperature-induced amorphisation in zeolitic imidazolate frameworks (ZIFs) and the canonical MOF-5 [131, 190, 196, 197].

As we have seen, the basic premise of molecular frameworks means that many will be inherently-flexible materials that respond to stimuli in ways not possible in conventional ceramics. Very large deviations in the structure—due to (i) guest uptake, (ii) application

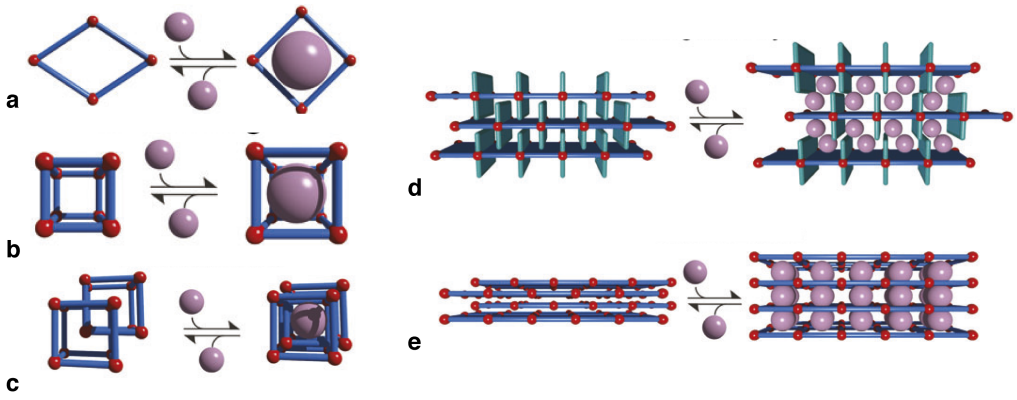

Figure 1.30: The various modes of flexibility within metal–organic frameworks (MOFs) that can five rise to gas-uptake and guest inclusion. Here purple spheres indicate a guest molecule of some kind, and the frameworks are shown as red spheres with blue linkers. The 'breathing' and 'swelling' modes of absorption shown in panels (a) and (b) are exemplified in the MIL family of molecular frameworks [82], while subnetwork displacement can take place in (c) catenated, (d) interdigitated layer or (e) stacked layer MOFs. All modes are also common in cyanide frameworks. Figure adapted from Ref. 198, published by The Royal Society of Chemistry licensed under CC-BY.

of pressure, (iii) change in temperature or (iv) photo-response—can occur with small energetic penalty [179] [Fig. 1.30]. Such massive flexibility has resulted in many MOFs being classed as "soft porous crystals" in the literature [76]. The controllability of topology and geometry make these materials attractive for investigations on mechanical properties, and we also find the other forms of degeneracy (configurational and displacive) play an important role in their structures and properties [198].

Many 'flexibility modes' of MOFs have been proposed, including 'breathing' in MIL systems, 'swelling' in systems such as MIL-88 [199], as well as active rotation of linkers, displacements of catenated networks, expansion of interdigitated or stacked layers. Considering other stimuli, under changes in temperature it has been shown that many MOFs show negative thermal expansion, both isotropic and anisotropic. The canonical MOF-5 shows large isotropic NTE ($\alpha_a = -16\,\mathrm{MK}^{-1}$; Ref. 200) driven by soft shear modes [201]. Recently it has been shown that the relatively rigid UiO-66 framework shows 'colossal' isotropic NTE due to defects in the framework [202], whilst many 'wine rack' structures show anisotropic NTE. These responses are found to be geometry dependent, so by adjusting the SBUs used and therefore the geometry, we can engineer a switch from linear-NTE to area-NTE in related quartz-like frameworks [132].

The role of geometry and mechanical degeneracy also suggests unusual behaviour under pressure in these systems, and during the course of this work negative linear compressibility has been found or predicted in a number of MOFs. These will be discussed in Chapter 2 in more detail; here I summarise other unusual behaviours under pressure focusing on ZIF-8 [189]. Upon hydrostatic compression, ZIF-8 initially shrinks, as expected, but then begins to increase in volume. Rather than violating thermodynamics, it is found that the pressure transmitting medium (typically small-molecule alcohols) enters the porous structure to reduce the overall volume (material + PTM) while also increasing the framework volume [166]. At relatively low pressures (0.34 GPa) the framework collapses to an amorphous state which actually retains porosity [203]. This 'amorphous porosity' can be used to trap waste products, such as radioactive iodine by the application

of moderate pressure [204].

Such an array of structures, functionalities and potential applications means extracting rules governing the behaviour of frameworks is extremely difficult—if not impossible—without a focus on intelligent development of the field. For such an endeavour non-ambient studies are critical, focusing on fundamental properties [205] such as thermal expansion and compressibilities. The hope that such rules might exist is based in what is known about the behaviour of traditional frameworks, where a few key dynamical instabilities can give rise to the huge array of functionalities in perovskite physics [32]. So in frameworks, will certain structural motifs give rise to well-determined properties? Can these then be coupled to other properties using more exotic framework tools, such as host–guest chemistry?

1.4.2 Metal–cyanide frameworks

Cyanide is one of the simplest molecular building blocks in framework chemistry and is therefore a useful prototype linker to better understand the properties of much more complex MOF-like frameworks. By removing much of the crystallographic complexity associated with larger organic linkers—such as static disorder [206], dynamic molecular rearrangements [205] and crystal defects [185]—we can more easily measure fundamental properties.

Structures of the homometallic transition metal cyanides are well known and follow the strong coordination preferences of the metals. For example, the cyanides of iron and cobalt form mixed-oxidation state networks based on octahedral metal centres $M_3^{2+}[M^{3+}(CN)_6]_2$ [207, 208]; group 10 cyanides form structures based on square planar metal centres (*e.g.* $Ni(CN)_2$); group 11 form linear coordination (*e.g.* AgCN) and group 12 tetrahedral coordination (*e.g.* $Zn(CN)_2$). For such simple systems, homometallic cyanide frameworks have been shown to exhibit a rich variety of functional properties. In the octahedral **pcu** net system—commonly known as Prussian blues after the iron-based pigment—negative thermal expansion [180, 209, 210], pressure-induced amorphisation [211], hydrogen storage potential [212] and even high-capacity ion storage for use in batteries [213, 214], have

all been observed.

Strongly bound metal–cyanide clusters can act as SBUs in hybrid coordination polymers where organic bridging units can increase structural variety. The impressive structural work of Hoskins and Robson (and co-workers) pioneered the area of cyanide and pseudo-cyanide framework materials, synthesising many for the first time [176, 215–219]. Organic bridging units between metal–cyanide sheets is a common motif, as are clathrate-type structures and inclusion of small molecules in Prussian blue and other nanoporous frameworks. Such materials also have impressive properties; as an example $Cd(CN)_2$ exhibits one of the largest isotropic NTE effects ($\alpha_a = -20.4\,MK^{-1}$) [37], but the guest-free non-interpenetrated variant has an even larger response ($\alpha_a = -33.5(5)\,MK^{-1}$) [220]. Bi-metallic systems have also found use for unusual vapochromic, luminescent and birefringent behaviours [221–223].

The family of dicyanometallate coordination polymers are based on the almost-linear $[M(CN)_2]^-$ (M = Cu, Ag, Au) linker [177]. This extended cyanide anion results in typical M$\cdots$M distance of $\sim$10 Å and introduces increased complexity due to the presence of the d^{10} metal introducing metallophilic interactions [224, 225]. Metallophilic interactions, and other weak structure-directing interactions, are explored in more detail in the next section. The chemistry of dicyanoaurate has been known since 1977 at least, when $KCo[Au(CN)_2]_3$ was reported as a side product in cobalt-hardened gold electroplating baths [226–228]. In fact the price of $K[Au(CN)_2]$ remains low as it is a key part of the gold purification industry. Other compounds with similar compositions were proposed [226], but not structurally characterised until much later [219, 228, 229]. Dicyanoaurate is much more stable in aqueous solution than dicyanoargentate and both lie lower in the spectrochemical series than cyanide itself [177]. Previous studies have focused on the extreme thermal response of dicyanometallate coordination polymers, *e.g.* $Ag_3[Co(CN)_6]$ as discussed previously [79, 230–232]. Strong temperature and chemical-dependent luminescent responses have also been found [221]. Many of these properties are discussed in more detail in the following chapters.

1.4.3 Supramolecular interactions

Supramolecular chemistry—the chemistry of assemblies of molecules rather than discreet units—is utilised in a huge range of applications, from molecular recognition and self-assembly, to directed synthesis [233, 234]. In designing such architectures a set of units (the molecules) are combined such that the geometry of interactions encodes the desired product. In principle such encoding of similar structural motifs is possible for framework materials [128, 224]. There are several broad classes of non-covalent intermolecular interactions that we might be able to employ to direct the synthesis and geometries of frameworks: hydrogen bonding, $\pi - \pi$ stacking or halogen bonding [128, 235, 236]. Here we specifically explore attractive metallophilic interactions, the dispersive interaction between d^{10} metals such as Au^{I}, Ag^{I} and Cu^{I} [225].

Despite being in the same group, gold and silver show subtle differences in chemistry [237], almost entirely due to the increase of relativistic effects in 3rd row transition metals. Relativity affects the stabilisation of orbitals due to the very high speed of electrons as they move near to heavy nuclei; the relativistic effect on valence shell properties increases down the Group 11 metals as Z^2, where Z is the full nuclear charge [238]. As shown in Figure 1.31, in the non-relativistic model the 5d/6s splitting in Au and 4d/5s splitting in Ag are almost identical due to the lanthanide contraction. Relativity affects those orbitals with fewest angular nodes, *i.e.* the s and p orbitals in Au, causing stabilisation. This means they become more 'core-like' and have a greater screening effect (more penetrating), leading to destabilisation and expansion of the d and f orbitals. Expansion of the 5d/6f orbitals causes stronger Au−L (L = ligand) bonding, with consequently smaller bond lengths of the same order as Ag−L bonds.

More peculiar bonding effects arise due to multipolar dispersive interactions between the diffuse d and f orbitals in Au^{I} ions, where common $Au^{+}\cdots Au^{+}$ distances are often in the order of 3 Å [225, 238, 239]. The interaction energy is in the range 29–46 kJ mol^{-1}, which is similar in strength to many hydrogen bonds [238]. Its origin in dispersion electron correlation effects is inferred from the observed variation of energy as r^{-6}. Two further

comments are made at this stage: (i) Pyykkö advises great caution in the use of DFT in these systems [238] and (ii) softer ligands would be expected to give stronger aurophilic interactions due to increased electron density on Au^+ [224].

Argentophilic interactions arise from similar dispersion effect considerations, but have been suggested to be much weaker due to decreased relativistic effects [Fig. 1.31] [225]. Despite being a weak interaction, argentophilicity has been identified as the origin of unusual mechanical properties and structures in frameworks. The representation in Figure 1.31(b) shows most clearly how the interpenetrated nets in $Ag_3[Co(CN)_6]$ relate to the argentophilic kagome lattice. It was noted [230] that the lattice parameter a is often found to be twice the ideal Ag$\cdots$Ag interaction of $\sim$3.5 Å, and the structures of almost all dicyanoaurates and dicyanometallates are determined in some way by these interactions [224]. Colossal thermal expansion of the Ag$\cdots$Ag interactions therefore leads directly to similar behaviour for the lattice parameter a. Replacement of Ag^+ with D^+ in $D_3[Co(CN)_6]$ reduces the thermal expansion behaviour by an order of magnitude; *i.e.* to that expected of normal materials ($\alpha_a = +14(6)$ MK^{-1}; $\alpha_c = -4(6)$ MK^{-1}). The stronger the interaction between the independent nets the greater the energy that is required to distort them, and so the less extreme their properties [230, 240].

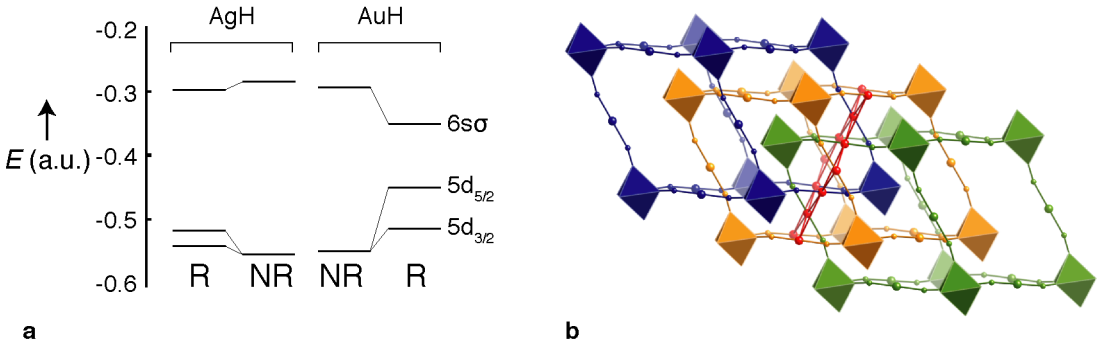

Figure 1.31: Metallophilic interactions arising from relativistic effects and shown cross-linking interpenetrated frameworks in silver hexacynocobaltate (a) Relativistic (R) and non-relativistic (NR) orbital energies of AgH and AuH molecules. The chemical difference between Au and Ag are clearly largely due to relativistic effects (Adapted with permission from Ref. 238) (b) Argentophilic interactions in $Ag_3[Co(CN)_6]$ cross-linking triply-interpenetrated cubic nets. Adapted with permission from *J. Am. Chem. Soc.* 2008, **130**, 9660–9661. Copyright 2008 American Chemical Society.

1.4.4 Disorder in frameworks

In §1.1 we saw how disorder can play a critical role in driving functional responses in traditional solid state chemistry. Yet in the field of molecular framework chemistry, much of the research emphasis remains on developing and characterising highly-crystalline and well-ordered systems [241]. In Chapter 6, I explore some of the few—but important—emerging families of well-characterised disordered molecular frameworks in detail. This focuses on the four main types of disorder; namely topological, static, dynamic, and low-dimensional disorder [Fig. 1.32]. My emphasis is on highlighting how structural disorder can also give rise to interesting and unusual physical properties and how this can be characterised. Here I summarise why such materials might be predisposed, more than has previously expected, to give rise to disorder.

As many molecular frameworks are porous, large-amplitude displacements of the framework linkers can dominate the dynamical behaviour if these pores are empty; likewise dynamic reorientation of guest molecules can dominate if the pores are filled. A second point reiterated throughout this introduction is that the energetics of molecular frameworks are dominated not by long-range electrostatic forces (which play an important role in stabilising *e.g.* oxide-based framework structures) but by covalent bonds within the molecular linkers, on the one hand, and localised polar/covalent interactions between the

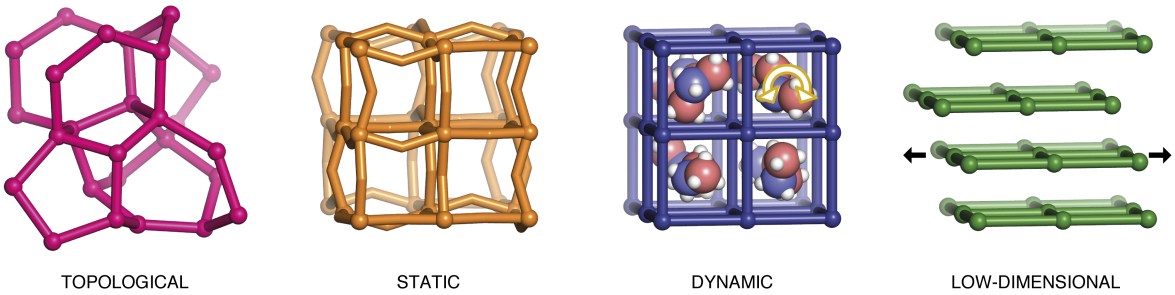

Figure 1.32: Disorder in molecular frameworks. The possible mechanisms by which structural disorder can be introduced into molecular frameworks include: (left–right) topological disorder, where the network itself is inherently aperiodic; static disorder, where regions of the framework under large distortive displacements that are not strongly correlated from one region of the structure to another; dynamic disorder, where some component of the framework (often a guest or counterion occupying the pore system) thermally samples multiple different configurations; and low-dimensional disorder, where the absence of strong bonding interactions in one more directions results in a lack of registration between neighbouring layers or columns of the framework.

metal centres and ligand donor atoms on the other. Consequently, minimisation of the lattice enthalpy often requires only that local bonding geometries be optimised, and so there may be very little enthalpic difference between crystalline and amorphous forms—so long as the local bonding arrangements are similar in both. In the study of conventional glass-forming materials, it is well established that network topology and connectivity also play a crucial role in stabilising disordered states [242], and these are precisely the parameters over which the materials chemist has extraordinary control in the synthesis and design of molecular frameworks. Consequently, like so many other properties in frameworks, disorder might readily be tuned through exploitation of the versatile structural chemistry of this broad family.

1.5 Structure of this thesis

The focus of this thesis is the exploration of structural degeneracy in molecular framework materials. Constructing materials where strong local coordination bonds (around metal nodes and molecular linkers) dominate the energetics of the system as a whole means we are able to study materials with configurational, displacive and mechanical degeneracy. It transpires that both intrinsic mechanical flexibility and disorder are common in framework materials, phenomena that have not previously received much attention in the field. Consequently two topical reviews are presented in the body of this thesis that rationalise work carried out in historically disparate fields; both develop understanding based on the structural origins of material properties and responses.

The first (Chapter 2) summarises the phenomenon of NLC, whilst the second (Chapter 6) explores disorder in framework materials. Both contribute clear summaries of past work and reanalysis of published data, but also a vision for the future of these rapidly-developing areas. We find extreme negative responses primarily arise through the lack of long-range interactions in such materials and the ability to design frameworks with topologies known to favour negative thermal expansion (NTE) and negative linear compressibility (NLC). Analysis of NLC identifies four classes of NLC materials based on mechanism: ferroelastic, titling polyhedra, spiral and wine-rack. These inform a clear strategy for material design

and discovery both within and beyond this thesis.

In Chapter 3 the structural response of an extended perovskite-like family of wine-rack dicyanometallates is explored. Dicyanometallates are known to have extreme thermal and pressure-induced responses, including in this family that I have previously shown* to have strong NTE and NLC properties. In this thesis I clarify the relationship between NTE, NLC and phase transition behaviour in these materials to elucidate further the mechanism of response. Following this I report even larger, so-called 'giant', NLC in materials with framework topologies related to, but distinct from, the wine-rack motif. By structural modification and employing supramolecular chemistry the magnitude and range of response are extended in $Zn[Au(CN)_2]_2$. This exceptional NLC response is found to result from a unique combination of topology and influence of supramolecular "spring" motifs within the structure that maximise response.

Chapter 5 is focused on one material, zinc(II) cyanide, a material that is known to (and will be shown to have) unique properties. This high-symmetry flexible framework has well-documented unusual mechanical properties, such as negative thermal expansion and pressure induced softening. Here I show that under hydrostatic pressure an improper-ferroelastic transition at 1.54 GPa gives rise to exceptional NLC response. This structural transition also informs our understanding of the parent compound (identifying the origin of its NTE response) as well as helping us understand the responses of other related ferroelastic molecular frameworks. My study of $Zn(CN)_2$ reveals the importance of dynamic displacive distortions in the parent compound as the driving force for the large NTE response, critical behaviour that is also found in structural analogues.

Following this in Chapter 6, I turn to explore configurational degeneracy in molecular frameworks, and document interesting cases of structural disorder in this family of materials. In Chapter 7, I explore the low-dimensional chain structured cyanides (AgCN, AuCN and $(Ag_{1/2}Au_{1/2})CN$). I show that subtle structural variations in this system arise by considering simple pairwise interactions between chains using Monte Carlo modelling.

---

* Honour School of Chemistry, Part II Thesis, Oxford, 2011 [243].

What transpires is a strong link between the driving forces in determining the structures of these 'simple' cyanides and magnetic structures in exotic low-dimensional frustrated materials. Indeed, the theoretical magnetic analogues have never been realised so this work is the first experimental exploration of this type of frustrated system. Furthermore hydrostatic pressure is used in an attempt to vary these pairwise interactions in AgCN.

In the conclusion I discuss the implications of the discoveries reported and give a personal perspective on the direction of this field. It is clear that molecular frameworks are extremely versatile in the quest to design mechanical properties, but that for strong and sustained NLC we must also consider the mechanical stability of the material to ensure phase transitions are prevented. Disorder within these systems is found to be instructive in the understanding of flexibility and vice versa, underlining the strong link between these concepts.

Chapter 2

Negative linear compressibility

For the vast majority of materials, application of hydrostatic (uniform) pressure results in a decrease in linear dimension in every direction. The thermodynamic requirement that under such conditions volume must decrease—*i.e.* free energy, ΔG is reduced on increasing pressure, $\Delta G = T\Delta S - p\Delta V$ [86]—is most readily accommodated by contraction in every direction. However, thermodynamics does not preclude volume reduction being coupled to linear expansion. A macroscopic example of this behaviour is the packing away of a collapsible wine rack: when folded it takes up less volume but is longer than the original high-volume state (Fig. 2.1). It is this expansion in one direction under hydrostatic pressure that we call negative linear compressibility (NLC), and by extension expansion in two directions is called negative area compressibility (NAC). This behaviour is counterintuitive and thus, unsurprisingly, is extremely rare—in the only previous review of this phenomenon Baughman *et al.* identified as few as 13 negative compressibility materials [109].

There are good reasons why we might want to focus on this phenomenon in particular in the context of this work. First, where NLC has been identified previously the magnitudes of response have been very much smaller than the normal (positive) compressibility of conventional materials. It has been established that molecular frameworks are in some cases orders of magnitude more flexible than these traditional materials, and so a natural question is whether molecular frameworks might support extreme NLC. Second, the

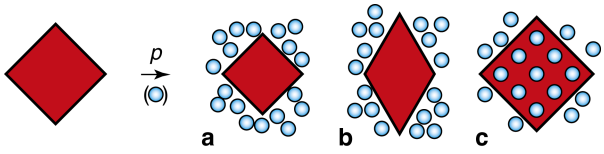

Figure 2.1: Contrasting material response to hydrostatic pressure. (a) positive compressibility—contraction in all directions; (b) negative linear compressibilitylinear expansion in one direction; (c) inflation associated with incorporation of the pressure-transmitting media (blue circles) within the material interior. The system volume (represented here by the solid red area) is reduced in all cases.

chemistry of frameworks makes it easy to target certain structural types, and therefore it is possible to target particular topologies that are known to give rise to NLC. Third, while NLC had been predicted to improve performance in areas like pressure sensing technologies, this has never been shown due largely to the small number of NLC materials and the weak magnitudes of response.

What follows is an overview of the various materials known to exhibit NLC. These are grouped into four classes according to the microscopic mechanism likely to be responsible for NLC in each case: (i) those compounds for which NLC arises as a consequence of proper, improper, or quasi-ferroelastic phase transitions; (ii) network solids for which NLC is driven by correlated polyhedral tilts; (iii) helical systems; and (iv) framework materials with wine-rack, honeycomb, or related topologies, where NLC arises from framework hinging. In this way, we hope to summarise not only the properties of known NLC materials but also the mechanisms that can give rise to the phenomenon itself.

2.1 Contemporary research developments

Interest in the unusual mechanical responses of framework materials is a very fast moving area, and the work presented in this chapter (and the rest of this thesis) has been part of a broader development of the field. Largely due to the apparent rarity of the phenomenon and the weak responses of materials, NLC remained a curiosity for many years. There was no immediate prospect for application, despite many technologies that would be revolutionised by such materials. A brief timeline of developments is given here.

Appreciation of the unusual mechanical properties of the helical elements (Se, Te) is long standing. Historically, however, the most widely investigated mechanism of NLC was the ferroelastic mechanism, in particular in rutile-structured materials. NLC arises as a result of a symmetry-breaking phase transition, and is often associated with similar transitions at low temperatures [244]. Surprisingly these materials were not included in the original review of Ref. 109, perhaps due to the reliance in this work on analysing elastic constants rather than crystallographic measurements. In these cases, NLC only occurs at elevated pressure so such materials may find limited application. No other

work has summarised these responses and rationalised the trends in properties seen. In parallel to these discoveries there were also reports of NLC based on crystallographic and elastic property measurements for materials where mechanical responses are dominated by polyhedral tilting.

The examples presented in this chapter aim to rationalise these historical reports, focusing on the structural mechanisms underpinning NLC. Prompting this analysis has been the rapidly-expanding number of NLC materials in the last five years in framework systems. Here the controllability of atomic-scale structure, the large responses observed and the increased access to variable-pressure measurements have contributed to a renewed interest. Indeed, immediately after the publication of the review presented here [245] another by Marmier *et al* was published [246]. Experimental results that will follow in this thesis are briefly mentioned here as contributing to the design strategies of targeting extreme negative response; we also highlight notable examples from other groups (see, for example, Refs. 123, 247–250) that have been published during the course of this work.

2.2 Mechanisms of NLC

2.2.1 Ferroelastics

Ferroelasticity describes the emergence of spontaneous strain in a symmetry-breaking phase transition [251]. The phenomenon can be considered the mechanical equivalent of ferroelectricity or ferromagnetism, where it is the spontaneous strain—rather than polarisation or magnetisation—that behaves as the ferroic order parameter. A simple example is the square → rhombic transition illustrated in Fig. 2.2, for which the ferroelastic order

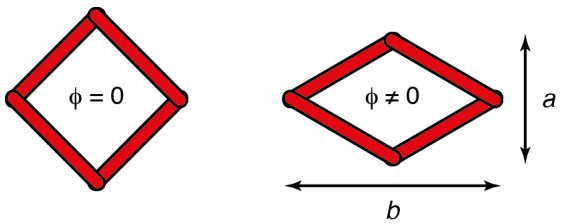

Figure 2.2: Schematic diagram showing the ferroelastic response of a square lattice. The paraelastic (left) and ferroelastic (right) states of the square lattice. The ferroelastic order parameter $\phi = (b - a)/(a + b)$ is a measure of the extent of symmetry-breaking distortion.

parameter is a measure of the distortion away from square symmetry [244, 252, 253]:

$$\phi = \frac{b - a}{a + b}. \tag{2.1}$$

The value of ϕ is zero in the 'paraelastic' high-symmetry phase and non-zero in the ferroelastic low-symmetry phase (square and rhombic geometries in Fig. 2.2, respectively). One result of Landau theory is that any transition for which strain is the primary order parameter must be second-order in nature [244]. So, there being no volume discontinuity across these so-called 'proper ferroelastic transitions', the emergence of spontaneous strain (*i.e.* $\phi = 0$ or, equivalently, $a \neq b$ in Eq. (2.1)) requires at least one axis to increase in length on symmetry lowering. This means that we can expect NLC in any system that supports a pressure-induced proper ferroelastic transition: the lower-symmetry phase stabilised at pressures above the transition must expand along at least one crystallographic axis for at least some finite pressure interval.

Rutiles

A number of simple binary inorganic solids with the TiO_2 rutile structure exhibit NLC *via* precisely this mechanism [65]. Such a pressure-induced ferroelastic transition—and

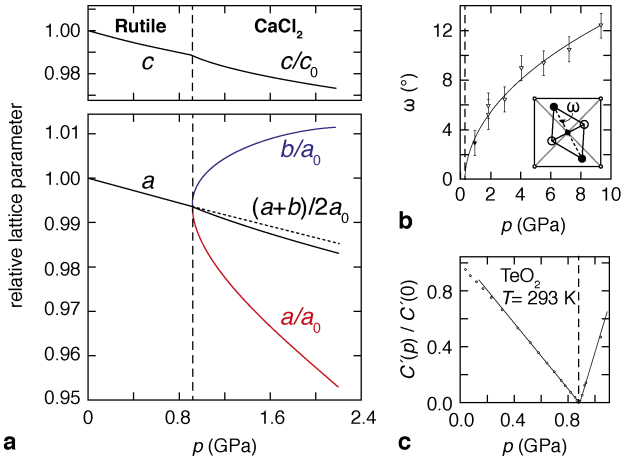

Figure 2.3: Ferroelastic NLC mechanism in rutiles. (a) Pressure-dependence of the lattice parameters of TeO_2, showing the ferroelastic transition at $\sim$ 0.81 GPa [69]. The high-pressure $CaCl_2$-structured phase exhibits NLC along **b**. (b) Evolution of the octahedral tilt parameter ω for the related transition of MnO_2 [68] (c) Softening of the effective elastic constant C' at the ferroelastic transition [67].

hence NLC—arising from this type of instability is displayed by the mineral paratellurite (TeO_2) [69, 254–256]. In nature, TeO_2 is found to occur in polymorphs related to both the rutile and brookite structures; however, synthetic paratellurite adopts a slightly distorted rutile structure with $P4_12_12$ crystal symmetry [254]. Variable-pressure lattice parameter measurements for this material reveal a ferroelastic transition at a critical pressure $p_c \simeq 0.9\,\mathrm{GPa}$, followed by NLC along the b crystal axis of the resulting high-pressure phase [Fig. 2.3(b)]. The proposed mechanism of correlated octahedral tilts can be validated by determining the pressure-dependence of the octahedral tilt angle ω, which also behaves as the displacive order parameter for the transition [Fig. 2.3(c)] [68]. That the transition is truly strain-driven can be deduced from the elastic behaviour near p_c: the effective elastic constant $C' = \frac{1}{2}(C_{11} - C_{12})$ governs the relevant shear mode velocity, and can be seen to vanish at the transition point [Fig. 2.3(d)] [67, 257].

TeO_2 is not an isolated example of this behaviour: a number of rutile-structured dioxides and difluorides exhibit NLC *via* essentially the same mechanism [65]. The magnitude of NLC for these different materials can be determined from the various crystallographic measurements reported in the literature. In the case of TeO_2, the data of Ref. 256 give $K_{\mathrm{NLC}} = -5.1(6)\,\mathrm{TPa}^{-1}$ over the pressure range 0.9–3.25 GPa, corresponding to a compressibility capacity of $\chi_K = 1.20(14)\%$. Table 2.1 compares these values for the various rutiles for which a high-pressure ferroelastic phase transition has been observed. What emerges is that there is a general correspondence between cation radius and extent of NLC, such that TeO_2—which contains the largest of the cations [258]—also shows the most extreme NLC response [Fig. 2.4]. We will show by comparison with other families

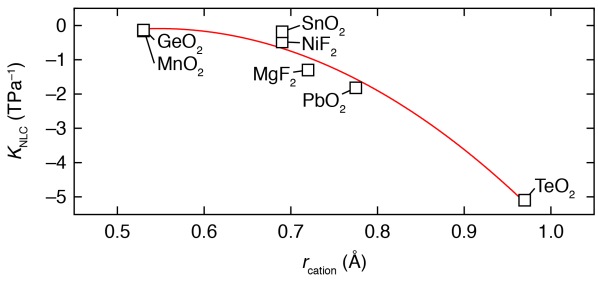

Figure 2.4: Relationship between magnitude of NLC and cation radius for rutile-structured dioxides and difluorides. Radii taken from Ref. 258; the line is a guide to the eye.

Table 2.1: Compressibilities of materials where NLC arises as a consequence of ferroelastic phase transition

	Meth.	K_1 (TPa^{-1})	K_2 (TPa^{-1})	K_3 (TPa^{-1})	B_0 (GPa)[a]	B'	Range (GPa)	χ_K (%)	Ref.
TeO_2	[a]	−5.1(6)	2.1(7)	18.4(6)	52(4)	$\equiv 4$	0.9–3.25	1.20(14)	67, 69, 254–256
NiF_2	[a]	−0.48	0.61	4.42	226	−8.0	1.8–3.2	0.067	259, 260
β-MnO_2	[a]	−0.16(7)	0.269(17)	1.82(10)	280(80)	19(11)	0.3–29.3	0.46(20)	68
MgF_2	[a]	−1.3(3)	2.51(2)	8.05(10)	68(13)	$\equiv 4$	9.1–10.4	0.17(4)	261, 262
PbO_2-I′	[a,d]	−1.83(15)	1.76(7)	4.00(3)	167(18)	$\equiv 4$	3.8–6.1	0.42(3)	263
GeO_2	[a]	−0.137(12)	0.827(14)	2.02(13)	—	—	28–36	0.110(10)	264
SnO_2-II	[a,d]	−0.185	0.394	2.345	204(6)	8(1)	11.8–21	0.170	253, 265
$Zn(CN)_2$-II	[b]	−2.08	11.2	16.8		$\gg 4$	1.52–5	0.724	*This work.*
$Pb_3(PO_4)_2$	[a]	−4.3(4)	5.0(2)	20.98(18)	38.7(5)	$\equiv 4$	0–1.59	0.68(6)	266–268
InS	[a]	−2.41(13)	2.9(4)	15(2)	33.2(18)	$\equiv 4$	0–4.3	1.04(6)	269–271
Sillimanite	[a,c,d]	−3.30	1.45	10.81	112.50	4.73	29.9–37.5	2.51	272
PtS	[b,c]	−0.47 to −0.92	3.3	3.3	167.5	$\equiv 4$	0–10	0.47–0.92	84, 273

[a] Calculated using PASCal [101] from reported lattice parameters. Lattice parameters are given in full in Appendix B. [b] As reported. [c] From DFT calculation. [d] Birch-Murnaghan coefficients as reported.

that a compressibility capacity $\chi_K \simeq 1\%$ is not itself particularly extreme. So while it is the case that a ferroelastic instability mechanism for NLC may give rise to relatively general behaviour, it would seem that—at least in the case of rutiles—the mechanism is unlikely to give rise to especially large NLC responses. One additional complication is that the NLC effect is of course only observed in the non-ambient phase, so future research within this family might likely concentrate on lowering p_c (perhaps even to negative pressures; *i.e.*, studying $CaCl_2$-structured materials) and/or varying cation/anion radii so as to allow the largest possible spontaneous strains to emerge within the ferroelastic phase.

Reverse ferroelastics: lead phosphate and indium sulfide

Lead phosphate, $Pb_3(PO_4)_2$, is the unusual example of a material that exhibits a 'reverse' ferroelastic phase transition on compression: the low-symmetry monoclinic structure converts to a higher-symmetry, more dense rhombohedral phase at a hydrostatic pressure of approximately 1.6 GPa [267, 274]. Because ferroelastic transitions couple expansion and contraction along orthogonal axes, NLC is actually expected irrespective of the direction in which the transition between high symmetry and low symmetry states is traversed. Indeed $Pb_3(PO_4)_2$ shows NLC throughout the entire stability field of the ferroelastic phase with $K_{\mathrm{NLC}} = -4.3(4)\,\mathrm{TPa}^{-1}$ and $\chi_K = 0.68(6)\%$ [267, 275]. The mechanism responsible for NLC—which resembles that observed on heating $Pb_3(PO_4)_2$ at ambient pressure—again involves correlated polyhedral tilts (in this case of the PO_4 tetrahedra) which couple to

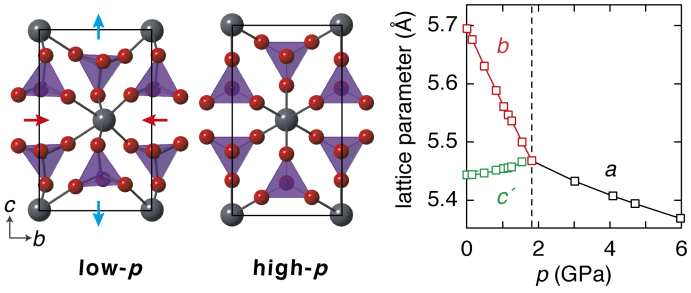

Figure 2.5: NLC from a reverse ferroelastic transition. The ferroelastic state of $Pb_3(PO_4)_2$ is denser than the paraelastic parent, and so application of pressure induces a reverse ferroelastic transition. The c lattice parameter of the ambient phase (the length of which is normalised here as $c' = c/\sqrt{3}$ for comparison) expands as the transition is approached [267]. Pb atoms are shown as large black spheres and PO_4 units as filled tetrahedra.

off-centering of the Pb^{2+} cations [Fig. 2.5(b)]. Doping with Ba^{2+} predictably favours the rhombohedral (cation-centred) state, lowering both the transition pressure and temperature while preserving NLC [251, 266–268, 275].

A less-well characterised example of a possible reverse ferroelastic transition is that of indium(II) sulfide, InS [$\equiv (In_2)^{4+}(S^{2-})_2$] [270, 271]. Certainly its ambient phase (orthorhombic *Pmnn* symmetry) shows NLC over the pressure range 0–4.3 GPa ($K_{\mathrm{NLC}} = -2.41(13)\,\mathrm{TPa}^{-1}$), and this behaviour is qualitatively understandable in terms of the straightening of S–In–In–S "dumbells". The confusion lies in the relationship of this response to the high-pressure InS-II phase that forms at 7.5 GPa. This high-pressure phase was originally reported to have the tetragonal Hg_2Cl_2 structure (*i.e.* with linear S–In–In–S units), which is of exactly the right symmetry to be considered the paraelectric parent of the ambient phase [269]. However, a more recent *in situ* single crystal structure determination reports InS-II to adopt a distorted monoclinic structure in which the same S–In–In–S units remain buckled [270]. So while there is no ambiguity regarding the NLC effect itself, and there is an implied relationship to the existence and nature of a high-pressure phase transition, a detailed mechanistic understanding of this relationship would demand further experimental characterisation of the pressure-dependent behaviour of this system.

NLC from ferroelastic-like phase transitions

Other types of phase transition—which are not strictly ferroelastic, but which share mechanistic similarities—may also give rise to NLC. This point is illustrated with two final examples. The first involves a geologically-relevant isosymmetric transition in the sillimanite polymorph of Al_2SiO_5 [272]. The ambient phase of this framework structure contains four-coordinate Si atoms [276]. Lattice dynamical calculations using well-established interaction potentials optimised for aluminosilicates [277] indicate that the framework undergoes a correlated reorganisation between 30 and 40 GPa that increases the Si coordination number from four to five [272]. All original bonding connectivity is preserved in this process (only new bonds are formed), and there is no change in crystal symmetry;

such a transition is necessarily first-order in nature [278, 279]. As a result of the increased Si coordination number, the high-pressure phase is denser than the low-pressure phase, but the new connectivity results in an increase in length along the c axis of its orthorhombic $Pnma$ cell. As the transition is approached with increasing hydrostatic pressure, the gradual conversion of one phase to the other results in an NLC effect [Fig. 2.6(a)].

The second example is the transformation of PtS from its ambient-pressure structure (tetragonal $P4_2/nmm$) to a high-pressure phase with the PdS structure (tetragonal $P4_2/m$) at pressures of between 2.5 and 3.0 GPa [273]. From an experimental viewpoint, very little is understood regarding this transition. What is known is that the high-pressure phase is metastable under ambient conditions and is expanded by ∼8% along the tetragonal axis and compressed ∼9% along the two perpendicular axes relative to the thermodynamic phase [273]. First principles calculations suggest that the deformation mechanism of the ambient phase under compression resembles a progression towards this

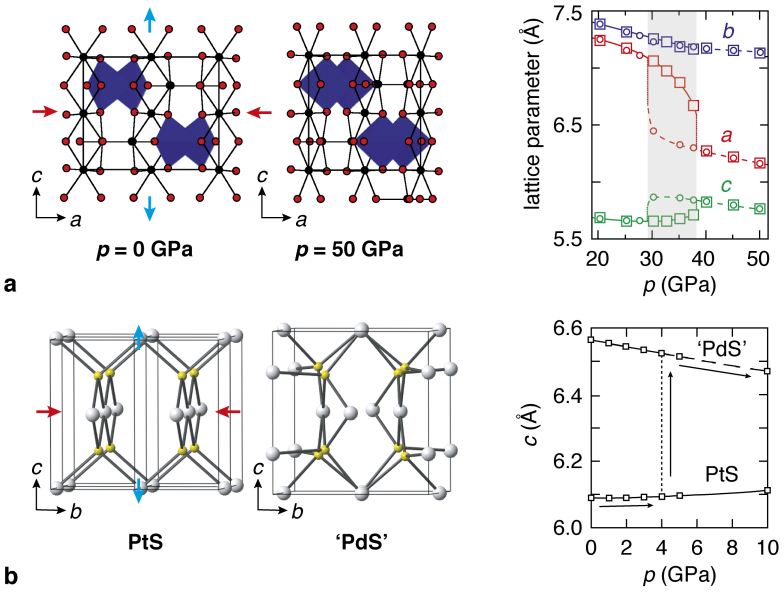

Figure 2.6: NLC arising from ferroelastic-like phase transitions. (a) The first-order isosymmetric transition in sillimanite involves a discontinuous increase in Si coordination number from four to five (SiO_n polyhedra shown in blue). The corresponding lattice rearrangement involves an expansion along the **c** axis [272]. (b) At hydrostatic pressures of $\sim 3-4$ GPa, PtS undergoes a reconstructive transition to the denser PdS structure type [84, 273]. Both phases have tetragonal symmetry but the latter expanded along **c** relative to the former. Quantum mechanical calculations show that, as the transition is approached on increasing pressure, the ambient phase is expected to expand along the same axis [84].

high-pressure structure, which means that coupled PLC/NLC is expected, with NLC occurring along the tetragonal axis [Fig. 2.6(b)] [84]. The magnitude of NLC obtained in these calculations turns out to depend on the particular functionals used: the authors of Ref. 84 find $K_{\mathrm{NLC}} = -0.47\,\mathrm{TPa}^{-1}$ for LDA and $-0.92\,\mathrm{TPa}^{-1}$ for GGA (calculated over the pressure range 0–10 GPa in both instances). The large expansion between the two phases observed experimentally (which places an upper limit on the true value of χ_K) suggests that the real value of K_{NLC} may be higher than these calculated values, and clearly additional experimental characterisation would play a valuable role in understanding better the intriguing NLC behaviour of this system.

So the structural changes that occur near phase transitions can give rise to NLC for a variety of different structural families and different transition mechanisms. NLC is all but guaranteed in the case of proper ferroelastic transitions, given that the development of spontaneous strain without a volume discontinuity requires expansion of the crystal lattice along at least one direction. Ambient-pressure variable-temperature studies may provide a useful method of identifying likely NLC candidates for further study, by virtue of the empirical observation that ferroelastic instabilities observed on cooling are also often observed under hydrostatic pressure. In this respect the recent discovery that some ferroelastic metal–organic frameworks (MOFs) can develop extremely large spontaneous strains on cooling suggests that equally extreme NLC may also be discovered in the very same systems [280].

2.2.2 Tilting networks

The concept that correlated polyhedral tilts might give rise to NLC even in the absence of a phase transition is by no means new—and is actually more likely to yield practically useful systems since NLC is then an intrinsic property of the ambient phase. In the nonlinear optic (NLO) material BiB_3O_6, for example, the dominant deformation mechanism under hydrostatic pressure involves correlated tilts of BO_3 units which act to hinge the connected borate framework [281–283]. This mechanism drives a strong contraction in one direction (parallel to the highly-compressible Bi^{3+} lone pairs) that couples to a moderate expansion

in a perpendicular direction [Fig. 2.7(a)] [281]. There is no change in crystal symmetry throughout this process; in particular the mechanism cannot be thought of as arising in the vicinity of a ferroelastic phase transition.

A further point of interest regarding BiB_3O_6 is that it is one of the few NLC systems for which compressibilities have been determined using two complementary techniques. On the one hand, a variable-pressure crystallographic study reported $K_{\mathrm{NLC}} = -6.7(3)\,\mathrm{TPa}^{-1}$ over the pressure range 0–5 GPa (*i.e.*, $\chi_K = 3.35(15)\%$) [281]. On the other hand, experimental determination of the elastic tensor based on RUS measurements gave $K_{\mathrm{NLC}} = -12.5\,\mathrm{TPa}^{-1}$, which is relevant in the limit $p \to 0$ [Fig. 2.7(b)] [282]. The factor-of-two difference between the two measurements of K_{NLC} does not imply an experimental inconsistency, but rather reflects the real variation in K with pressure as illustrated in Fig. 1.19. That NLC is relatively strong and persistent in BiB_3O_6 likely reflects the openness of its framework structure and the polarisability of the extra-framework Bi^{3+} cation.

Equally strong NLC effects are expected to occur amongst other open framework structures based on connected polyhedra. In a recent computational study of 121 siliceous zeolites, a total of 16 were identified as NLC candidates on the basis of their calculated elastic compliance tensors [123]. Amongst these frameworks, the strongest NLC behaviour is anticipated for the experimentally-realisable GIS zeolite topology [284], with

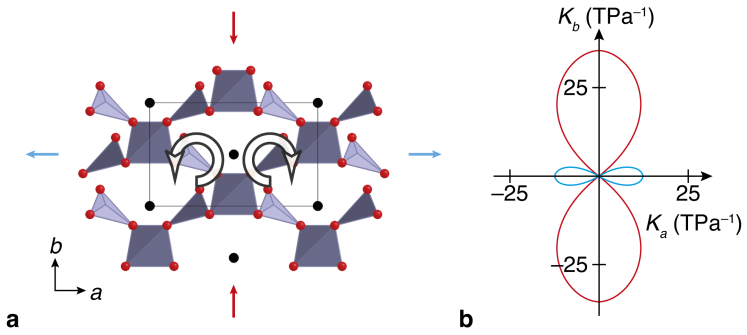

Figure 2.7: Compressibility mechanism in borate framework driven by polyhedral tilts. (a) Correlated tilts of BO_3 units polyhedra lead to hinging of the borate framework in BiB_3O_6 and volume reduction; the network expands along **a** in the process [281]. Bi atoms are shown as isolated black circles and the BO_2 network in polyhedral representation. (b) The compressibility indicatrix [101] determined from RUS measurements shown in the same orientation as (a): red and blue regions indicate, respectively, positive and negative values of the linear compressibility [282].

$K_{\mathrm{NLC}} = -13.7\,\mathrm{TPa}^{-1}$ in the $p \to 0$ limit. What is remarkable here is the unexpected frequency of NLC: if the phenomenon occurs in 13% of a broad family of materials then it is certainly less rare than originally envisaged [123]. The pressure range over which these zeolites exhibit NLC remains to be determined; likewise the effects of Al substitution, extra-framework counterion inclusion, and solvation on NLC offer additional avenues of experimental investigation.

Correlated tilts of PO_4 tetrahedra have also been implicated in the strongly anisotropic elastic response of the widely-studied ferroelectric material CsH_2PO_4 [Fig. 2.8(a)] [285, 287]. To the best of our knowledge, the only variable-pressure crystallographic measurements of the ambient phase of this material are limited to (i) single-crystal neutron diffraction studies of the evolution of diffuse scattering [288], and (ii) low resolution X-ray powder diffraction patterns at 0.29 and 2.89 GPa reported without any subsequent structural analysis [287]. To some extent this paucity of crystallographic data is surprising given the intense interest in the high-pressure ferroelectric behaviour of this material [289]. In the context of NLC it is perhaps even more remarkable because ultrasonic velocity measurements suggest a $p \to 0$ compressibility of $-260\,\mathrm{TPa}^{-1}$ along a direction approximately aligned with the **c** axis of the monoclinic cell [285]. The powder diffraction

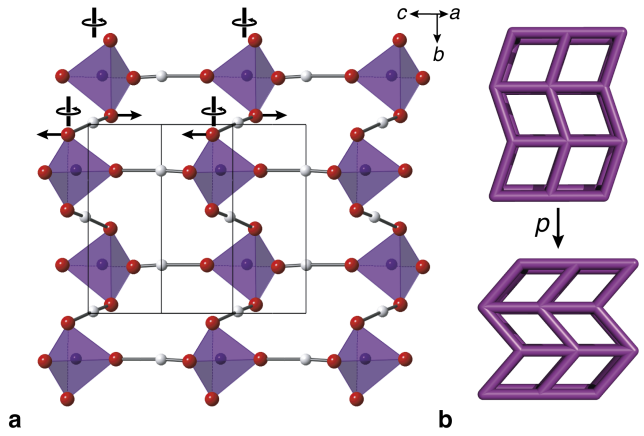

Figure 2.8: PO_4 tetrahedra are thought to drive the NLC response of ferroelectric material CsH_2PO_4. (a) Correlated rotations of PO_4 tetrahedra about the **b** axis would cause the CsH_2PO_4 structure to densify while expanding along a direction parallel to **c** [285]. H atoms are shown as white spheres, PO_4 units in polyhedral representation, and Cs atoms omitted for clarity [286]. (b) The densification mechanism of a generic herringbone lattice, which acts as a geometric model for NLC in CsH_2PO_4.

patterns of Ref. 287 do not show any obvious evidence of extreme NLC, although re-measurement across a larger number of more finely-spaced pressure intervals would help settle the issue definitively. The most likely mechanism responsible for NLC in the system (as suggested in Ref. 285) would involve PO_4 rotation-driven collapse of the herringbone hydrogen-bonding network as illustrated in Figure 2.8(b).

Because extended structures tend to be less dense than their tilted counterparts, more often than not it will be the case that pressure-driven activation of tilt systems will favour PLC rather than NLC. Cristobalite-like BEO_4 (E = P, As) frameworks are an interesting case of *indirect* NLC materials where NLC arises because a tilt-driven PLC mechanism results in a more rapid compression of the crystal lattice than can supported by the bulk material stiffness [290]. Here this mechanism is explained in more detail. Both BPO_4 and $BAsO_4$ adopt the same tetragonal $I\bar{4}$ variant of the cristobalite structure [Fig. 2.9] [292, 293]. The dominant deformation mechanism involves correlated tilting of the BO_4/EO_4 tetrahedra around the tetragonal axis. The tilt angle ϕ is directly related to the a lattice parameter via the projection of the mean B–O/E–O bond length onto the (a, b) plane $r_\perp$ [290]:

$$a^2 = \frac{16r_\perp^2}{\tan^2\phi + 1}. \tag{2.2}$$

Because bending of the B–O–E bonds carries a lower energy penalty than compression of the B–O or E–O bonds, the behaviour of the a lattice parameter on compression is dominated almost exclusively by changes in ϕ. What this means is that K_a is effectively a measure only of the bending stiffness of the B–O–E linkages. In contrast, the bulk

Table 2.2: Compressibilities of materials for which NLC arises as a consequence of correlated polyhedral tilts.

	Meth.	K_{NLC} (TPa^{-1})	K_{PLC} (TPa^{-1})	$\bar{B}$ (GPa)[d]	Range (GPa)	χ_K	Ref(s).
BiB_3O_6	[b]	−6.7(3)			0–5.0	3.35(15)	282, 283
CsH_2PO_4	[c]	−260	430		0	–	285
BPO_4	[a]	−0.92(10)	2.83(12)	256(22)	0–56	5.2(6)	290
$BAsO_4$	[a]	−1.48(15)	3.64(11)	166(13)	0–51	7.5(8)	290

[a] Calculated using PASCAL [101] from reported lattice parameters. Lattice parameters are given in full in Appendix B. [b] As reported. [c] Calculated using ELAM [291] from elastic stiffness components determined by ultrasonic velocity measurements. Elastic data are given in full in Appendix B. [d] Inverse of the volume compressibility calculated in the same way as K_ℓ.

modulus B measures the resistance to compression of the whole oxide lattice, which will depend largely on anion repulsion in three dimensions. For both BPO_4 and $BAsO_4$ this bulk modulus is sufficiently large that the inequality

$$K_c = \frac{1}{\bar{B}} - 2K_a < 0 \tag{2.3}$$

holds and NLC is observed along the tetragonal axis [Table 2.2] [290]. More remarkable than the magnitude of NLC in these systems is the pressure range over which it is observed: compressibilities calculated from lattice parameters in Ref. 290 gives $K_{\mathrm{NLC}} = -0.92(10)$ and $-1.48(15)$ TPa^{-1} for E = P and As, respectively, over a pressure range of 0–53(3) GPa.

2.2.3 Helices

In many ways the mechanisms covered above—ferroelastic instabilities and polyhedral tilting—are similar to those often invoked in descriptions of other mechanical anomalies

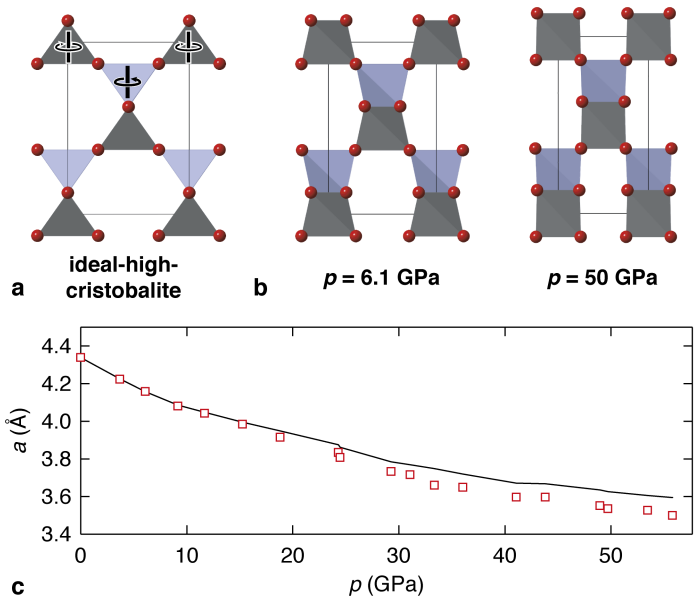

Figure 2.9: Tilt mechanism of NLC in the collapsed-cristobalite system BEO_4. (a) The structure of BEO_4 (E = P, As) compounds is related to that of cubic β-cristobalite *via* decoration of the lattice with alternating BO_4 and EO_4 tetrahedra and subsequent rotation of all tetrahedral units about the tetrad axis by an arbitrary angle $0 < \phi < \pi/4$ [292, 293]. (b) The structures of BPO_4 at high pressures are described by increasingly large values of ϕ [290]. (c) That variations in ϕ dominate the compression mechanism is evident from a comparison of the actual variation in the lattice parameter *a* (open squares) with that obtained from the variation in ϕ *via* Eq. 2.2 (line).

such as NTE [99]. Over the next two sections my focus shifts away from these dynamical mechanisms to a consideration of *topological* motifs that show a similar predisposition towards NLC.

Nature herself favours one particular geometric motif—namely, the helix—as a mechanism of generating and exploiting NLC in muscular response [294]. Just as NLC materials expand under hydrostatic pressure, so do they contract under negative (*i.e.*, internal) pressure. When filled with fluid, helices exhibit precisely this response: their length decreases as the helix cross-section increases. Helical arrays of tendons enable muscle-like contraction that is driven by fluid injection rather than electrical impulse, and such a mechanism is implicated in the movement of certain types of worms, squid, and ancient limbless tetrapods [294]. The NLC community has long been aware of the related implication that non-biological NLC materials might be exploitable as artificial muscles and actuators if these motifs can be incorporated as part of materials design [127, 295–298].

On the atomic scale, there are two remarkably simple chemical systems with helical structures that exhibit NLC under hydrostatic pressure. These are the trigonal polymorphs of elemental selenium and tellurium [299]. Both structures consist of an array of (enantiomorphic) trigonal helices packed on a triangular lattice [Fig. 2.10(a,b)]. Bonding interactions within any given helix are much stronger than those between helices so an interpretation of the bonding as molecular still has relevance despite the semiconducting properties of both systems. The densification required under increasing pressure can then be accommodated in two ways: either through compression of the weaker bonds between helices—which acts to decrease a and leaves c unchanged—or *via* an increase in the 'pitch' of each helix, compressing a at the expense of some expansion along c. That both mechanisms operate for Se and Te is evident from variable-pressure crystallographic measurements [Fig. 2.10] [113, 300]. It is conventional to reparamaterise the three measurable structural parameters—a, c, and u, the single free positional variable for Se/Te—in terms

of the geometric parameters [299]:

$$r = \left[3(ua)^2 + \frac{1}{9}c^2\right]^{1/2}, \tag{2.4}$$

$$R = \left[a^2(1-3u) + r^2\right]^{1/2}, \tag{2.5}$$

$$\theta = \left[2\cos^{-1}(3ua/2r)\right]. \tag{2.6}$$

Here r, R, and θ correspond, respectively, to the strongly-bonded E–E distance, the nearest weakly-bonded E–E distance, and the E–E–E angle within a strongly bonded helix [299]. Experimentally one finds that R decreases most rapidly on increasing pressure: this reflects the rod packing compression mechanism described first above. In contrast, r is essentially constant, meaning that the length of the helical path is essentially incompressible. By themselves, these two observations would not imply NLC. Instead the weak NLC behaviour that does occur [Table 2.3] can only be a consequence of the gentle increase in bond angle θ at higher pressures—*i.e.*, the same pitch-variation mechanism Nature uses in muscle contraction.

Remarkably, this NLC mechanism persists even when Se chains are incorporated within the cavities of zeolite $AlPO_4$-5 single crystals [305]. Interpretation of Raman spectroscopy and optical absorption measurements, together with *ab initio* calculations,

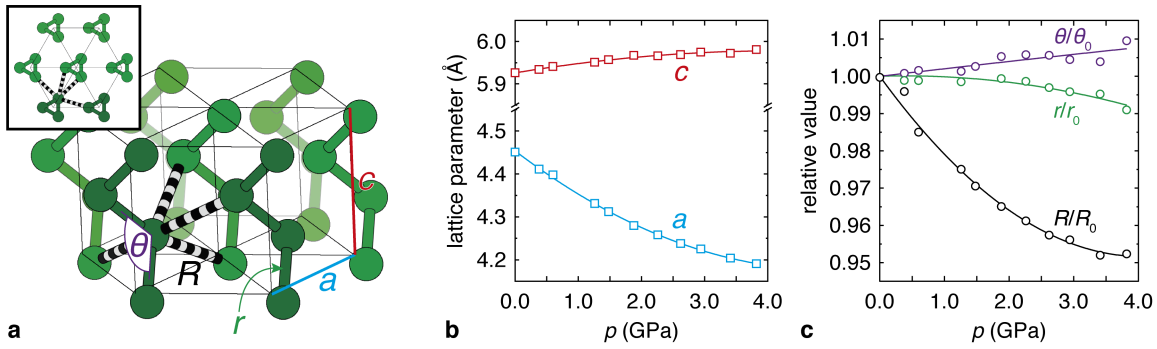

Figure 2.10: The mechanism of NLC in spiral-structured elemental Se and Te. (a) The spiral structure of Te and Se is completely described by the three parameters r, R, θ as described in the text. *(inset)* The crystal structure of selenium and tellurium consists of a triangular array of trigonal helices. (b) Lattice parameter variation under hydrostatic pressure for Te, showing NLC parallel to the helix axis [299] (c) The dominant compression mechanism involves reduction of inter-helix separation R and unwinding of the helices (*i.e.* increasing θ)—it is the latter that gives rise to NLC (Adapted from Ref. 299).

Table 2.3: Compressibilities of spiral-structured elements calculated using PASCAL [101] from reported lattice parameters. Lattice parameters are given in full in Appendix B

	Meth.	K_a (TPa^{-1})	K_c (TPa^{-1})	B_0 (GPa)	Range (GPa)	χ_K (%)	Refs.
Se	[a]	12.0(6)	−2.5(4)	23.0(14)	0–14.0	3.5(6)	113, 300–302
Te	[a]	13.6(9)	−1.8(3)	26.6(13)	0–3.82	0.69(10)	302–304

[a] Calculated from reported lattice parameters and calculated using PASCAL [101]. Lattice parameters are given in full in Appendix B.

converges on the same conclusion that the confined chains of Se do actually elongate under hydrostatic pressure [305]. Indeed, one anticipates that NLC may actually be quite a general phenomenon for ordered structures with helical motifs. It has been suggested elsewhere that the filamentous supramolecular polymer $\{\mathrm{Au}[(\mathrm{C_2H_5})_2\mathrm{NCS_2}]\}_n \cdot x\mathrm{CH_2Cl_2}$ may exhibit negative compressibility *via* such a mechanism [116]; likewise helical metal–organic frameworks such as silver(I) dicyanamide [306, 307] may be interesting candidates for further investigation.

2.2.4 Hinged Frameworks

From an engineering perspective—rather than a biological one—the two geometric motifs most frequently associated with negative compressibility are the wine-rack and honeycomb networks (which are of course related to each other; see Fig. 2.11) [90, 308]. Both are characterised by extreme mechanical anisotropy and both have the property that their volumes are reduced under uniaxial expansion. Molecular framework chemistry offers an attractive means of designing materials that contain these same geometric features on the atomic scale [170, 241]. Not only does the chemist have control over network topology, but the use of molecular linkers in the construction of framework materials leads to systems for which mechanical deformation mechanisms are dominated by framework flexing [180]. It is this feature that enables the mapping between chemical and engineering systems.

Within the field of metal–organic framework chemistry, the family of materials with a crystal structure most obviously resembling the wine-rack topology is probably the so-called MIL-53 system [75]. NLC behaviour was predicted for this family from both first principles [71, 76] and simple empirical [128] considerations; the first experimental verification of this behaviour has only recently appeared in print [249]. The extreme

magnitude of NLC—Ref. 249 reports a compressibility value of $K_{\mathrm{NLC}} = -28\,\mathrm{TPa}^{-1}$ over 0–3 GPa—reflects the shallow energy potential that accompanies framework deformation for these systems and which is implicated in the well-known "breathing" effect upon guest sorption [82]. Within the field there is probably an expectation that such large values are likely a general result for molecular frameworks, arising as a consequence of their low-density structures and the low energies of the supramolecular interactions affected by framework flexing.

In §1.1.3 the remarkable material $Ag_3[Co(CN)_6]$ was discussed in terms of its very unusual properties under changes in temperature and pressure. It is this material that forms the foundation of Chapter 3, and several other studies, where the mechanism of mechanical response identified is related to the 'wine-rack' model. Although an extremely strong NLC effect was identified by neutron diffraction ($K_{\mathrm{NLC}} = -76(9)\,\mathrm{TPa}^{-1}$), in maximising $|K_{\mathrm{NLC}}|$ we find the material becomes sensitive to shear instabilities, going through a shear-driven collapse at $p = 0.19\,\mathrm{GPa}$. There is a clear challenge in balancing large flex-

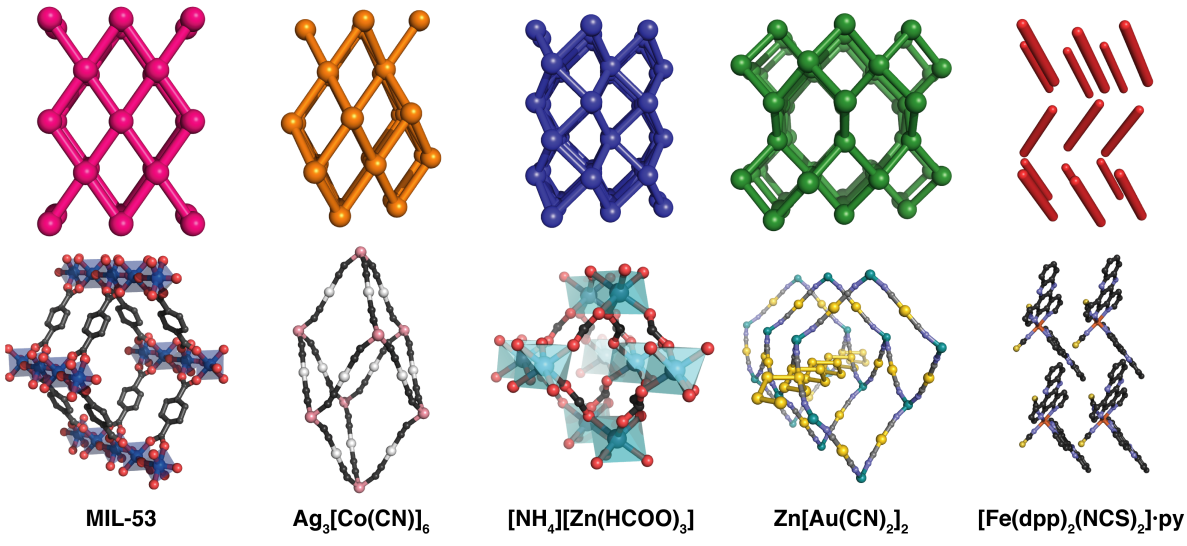

Figure 2.11: Some wine-rack and honeycomb-like topologies known to favour NLC (top) and corresponding chemical systems (bottom). From left–right: the wine-rack (or "Nuremberg scissors") topology of the MIL-53 family [75], trigonally distorted α-Po net of $Ag_3[Co(CN)_6]$ and related ABX_3 dicyanometallates [79], *acs* topology of $[NH_4][Zn(HCOO)_3]$ [248], β-quartz net of $Zn[Au(CN)_2]_2$ [179], and herringbone molecular packing in $[Fe(dpp)_2(NCS)_2]$·py [250]. In all cases the mechanism responsible for NLC is analogous: densification involves extension of the lattice in the vertical direction.

ibility with the propensity for mechanical instability. One strategy employed in my work was to selectively frustrate this collapse by inclusion of counterions in the structure in, for example, $KMn[Ag(CN)_2]_3$. This material remains mechanically stable up to 2.2 GPa, and is (along with structural analogues) the focus of the following chapter.

Already some design rules for maximising NLC begin to emerge. First, mechanical anisotropy is clearly key: NLC requires PLC in an orthogonal direction since volume compressibility must remain positive. Second, maximising this positive compressibility will likely maximise NLC. Third, dynamic instabilities will reduce the pressure range over which NLC can be observed: using rigid molecular linkers and occupying void space with extra-framework cations or sorbate molecules may help extend this stability range. And, fourth, the network topology should likely be related to the wine-rack or honeycomb motifs.

These design principles were the basis of identifying the first so-called "giant" NLC material: namely, zinc dicyanoaurate(I), $Zn[Au(CN)_2]_2$. The study of this material is documented in Chapter 4. The term "giant" demarcates exceptionally strong NLC ($K_{\mathrm{NLC}} < -30\,\mathrm{TPa}^{-1}$) that persists over an industrially relevant pressure range (at least 1 GPa). The quartz-like structure of this particular material is at once both anisotropic and related to the honeycomb net, satisfying respectively the first and fourth principles and so explaining the basic driving force for NLC [219]. The structure also has very little free volume because six of these nets interpenetrate one another [219]; this addresses the third principle and accounts for the extended pressure range over which NLC is observed (0–14.2 GPa). But what sets $Zn[Au(CN)_2]_2$ apart is the strength of NLC is in its ambient phase ($K_{\mathrm{NLC}} = -42(5)\,\mathrm{TPa}^{-1}$ over 0–1.8 GPa), which arises from the extreme compressibility of supramolecular helical "springs" allowing especially strong PLC in a perpendicular direction. It is this feature that addresses the second design principle: just as a spring is more compressible than the steel from which it is made, so too are the linear compressibilities of $Zn[Au(CN)_2]_2$ more extreme than would otherwise be expected.

Table 2.4: Compressibilities of NLC in hinged molecular frameworks and molecular solids.

	Meth.	K_1 (TPa^{-1})	K_2 (TPa^{-1})	K_3 (TPa^{-1})	B_0 (GPa)	Range (GPa)	χ_K (%)	Ref(s).
MIL-53	[b]	−28	23	59		0–3	8.4	249
Ag(mim)	[b]	−4.32(10)	25.8(10)	55(4)	6.0(16)	0–1.0	0.432(10)	128
$KMn[Ag(CN)_2]_3$	[b]	−12.0(8)	33.2(13)	33.2(13)	12.7(11)	0–2.2	2.64(18)	115, 309
$Ag_3[Co(CN)_6]$-I	[b]	−76(9)	115(8)	115(8)	6.5(3)	0–0.19	1.44(17)	78
$Ag_3[Co(CN)_6]$-II	[b]	−5.3(3)	9.6(5)	15.2(9)	11.8(7)	0.19–7.65	4.0(2)	78
$Zn[Au(CN)_2]_2$-I	[b]	−42(5)	52(6)	52(6)	16.7(16)	0–1.8	7.6(9)	130
$Zn[Au(CN)_2]_2$-II	[b]	−6(3)	16(5)	16(5)	27(3)	1.8–14.2	7(4)	130
$[NH_4][Zn(HCOO)_3]$	[b]	−1.8(8)	15.8(9)	15.8(9)	32.8(16)	0–0.93	0.17(7)	248
ZAG-4	[a]	−2.6(15)	7.9(5)	29(3)	13.4(10)	1.65–5.69	1.1(6)	310
$[Fe(dpp)_2(NCS)_2]\cdot py$	[a]	−10(2)	12(3)	53(4)	12.9(6)	0–2.48	2.5(5)	250
$CH_3OH\cdot H_2O$	[a,c]	−2.7(18)	31.9(4)	108.0(9)	3.79(6)	0–0.5	0.16(11)	247
$[(C_6F_5Au)_2(\mu$-1,4-diisocyanobenzene)]	[b]	−13(3)	29(3)	31.3(4)	7.5(7)	0–2.42	3.1(7)	311

[a] Calculated using PASCal [101] from reported lattice parameters. Lattice parameters are given in full in Appendix B. [b] As reported. [c] Birch-Murnaghan coefficients as reported.

NLC is increasingly identified in a wide range of MOFs and molecular crystals beyond the various systems discussed above. Two relevant MOF examples are ammonium zinc(II) formate, $[NH_4][Zn(HCOO)_3]$ [248], and the zinc alkyl gate (ZAG) family [310]. The mechanism responsible for NLC in the former is essentially the same as that discussed for $KMn[Ag(CN)_2]_3$; all that differs between the two is their network topology (*cag vs* α-Po; Fig. 2.11) [248]. In contrast, the 'wine-rack' NLC mechanism originally proposed for ZAGs (Ref. 310) was later shown to be incorrect on the basis of quantum mechanical calculations [312]. Instead it seems that NLC in this system is discontinuous and is instead as a result of pressure-driven proton redistribution—a new mechanism altogether. The NLC behaviour of these MOFs is compared with that of other molecular frameworks in Table 2.4 and Figure 2.11. In terms of molecular crystals, strong NLC effects can occur in situations where packing arrangements mimic the topological motifs known to favour NLC in framework structures [313]. So, for example, the molecular packing arrangements in systems as chemically diverse as methanol monohydrate, $[Fe(dpp)_2(NCS)_2]\cdot py$ (dpp = dipyrido[3,2-*a*:2′3′-*c*]phenazine, py = pyridine) and $[(C_6F_5Au)_2(\mu\text{-}1,4\text{-diisocyanobenzene})]$ are all related to the same wine-rack topology. Moderately strong NLC is observed in each: $K_{NLC} = -2.7(18), -10(2)$, and $-13(3)\,TPa^{-1}$ respectively [247, 250, 311].

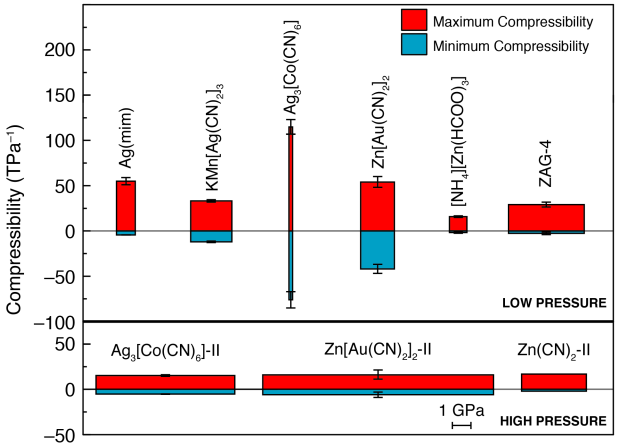

Figure 2.12: Compressibility behaviour of a variety of molecular frameworks. The width of each bar is related to the pressure range over which compressibility is measured, and the height of each bar corresponds to the maximum (red) and minimum (blue) *average* compressibility values over that range. Consequently the area of each bar is a measure of χ_K: those materials with the greatest propensity to expand under pressure are those for which the area of the blue bar is largest.

2.3 Discussion

At the time of Baughman's original review [109], NLC appeared to be a somewhat esoteric phenomenon that occurred in only a handful of peculiar systems. If the enumeration of various NLC materials and mechanisms I have given here leads to any one particular conclusion it is surely that NLC is rather more commonplace than might originally have been expected. From an experimental viewpoint, characterisation of NLC remains somewhat of a niche capability; however, the number of research groups with expertise in high-pressure crystallographic measurements is rapidly growing and one anticipates that NLC will be observed increasingly frequently as the scope of materials studied at high pressures diversifies. This is likely to be particularly true for molecular crystals, where the empirical predisposition towards herringbone-type packing arrangements will intrinsically favour NLC because of its relationship to the wine-rack topology.

But perhaps the most profound recent advance likely to influence our understanding of the true breadth of NLC behaviour is the relative ease and reliability with which first principles calculations can now determine elastic properties [123]. This allows (relatively) rapid screening of entire classes of materials and pre-selection of the most interesting candidates for subsequent experimental investigation. We might expect that the task of calculating elastic tensors for all known MOF structures, for example—once considered an inconceivably difficult process—will not remain computationally intractable for very much longer [312, 314].

If NLC is likely to be discovered in a large number of new systems over the coming years, then what are the criteria for interesting and useful behaviour? Magnitude and range of NLC are two obvious metrics—hence the otherwise-questionable value of labels such as "giant" NLC [130]. But one other aspect of NLC behaviour deserves brief discussion: namely the relationship between NLC and crystal symmetry. Low symmetry intrinsically favours anisotropy—and hence NLC—since there are fewer constraints on the elastic stiffness tensor $\mathbf{C}$. While NLC is likely to be more prevalent in low-symmetry materials, the direction along which NLC occurs is less likely to have a fixed relationship

to the crystal axes (hence bulk sample morphology) and moreover this direction itself will vary with pressure [101]. This matters because practical implementation of NLC requires careful material alignment. So, in general, we anticipate that NLC behaviour in uniaxial or orthorhombic systems will find greatest application because in these cases macroscopic alignment of the NLC axes can be assured.

Having documented NLC in large variety of different chemical families we now explore any universal trends in behaviour that might emerge. The approach used is to compare for these different materials the relationship between magnitude of NLC effect, and pressure range over which the phenomenon is observed. This analysis is summarised in the Ashby-type diagram given in Fig. 2.13. The diagonals in this representation correspond to points of constant χ_K. What becomes obvious is that most NLC materials are distributed around the diagonal corresponding to $\chi_K = 1\%$—this value is probably special only in the sense that it is large enough for NLC to have been noticed experimentally, but is not so large as to be extremely rare. Along this diagonal, those materials for which the mechanically-relevant bonding interactions are strong—the rutiles and framework silicates, for example—are clustered in a region where NLC pressure range is large but K_{NLC} itself is not so very extreme. In contrast, the flexible, open structures of MOFs

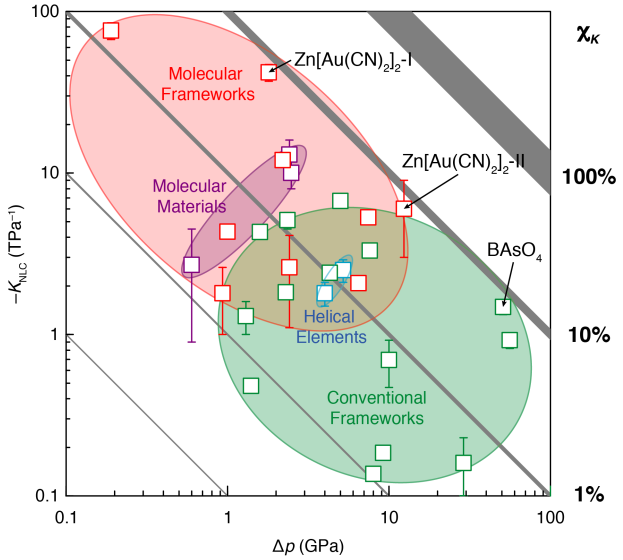

Figure 2.13: Ashby-type diagram relating magnitude of NLC behaviour to pressure range over which it is observed for materials highlighted here. Diagonals correspond to points of constant compressibility capacity.

and molecular frameworks cluster in a region where NLC is very strong but persists only over small pressure ranges. As a result, eventual materials selection will be informed by whether range or magnitude is more critical for a given particular application of NLC. In terms of new materials discovery, the most attractive region of the Ashby plot is of course the (currently empty) top-right corner, where both metrics are maximised. Somehow the materials that exist in this region—if indeed they exist at all—must balance the weak interactions needed to produce strong NLC with the structural integrity required to avoid collapse at high pressures.

Negative Area Compressibility

My focus in this chapter has been almost entirely on materials which exhibit negative compressibility along just one principal axis. Negative area compressibility (NAC) is a natural extension and modest NAC effects have been observed or predicted to occur in a handful of layered materials: silver(I) tricyanomethanide [315], sodium vanadate [316–320], and $TlGaSe_2$ [134] (Table 2.5; we note that reports of NAC in $PbTiO_3$ remain contentious and so are not included [321, 322]). In each of these cases, the mechanism responsible for NAC is related to the so-called Lifshitz mode [Fig. 2.14] [323]. An alternate mechanism—in which specific geometries of the various wine-rack and honeycomb-like topologies identified above couple densification to area expansion—has recently been proposed [132]; the extension to specific helical geometries also follows. Whatever the mechanism, it is reasonable to expect that NAC is unlikely ever to be as strong an effect as NLC. This is because the mechanical stability criterion of positive volume compressibility implies that the PLC effect along the axis perpendicular to the plane of negative compressibility must be at least twice as large as K_{NAC}. In other words, NAC can only ever be half as strong as PLC.

While *continuous* volume compressibility must be positive, there is no formal thermodynamic requirement forbidding volume increase across a pressure-induced phase transition. To the best of our knowledge, the only 'realisation' of this bizarre phenomenon is a theoretical study of a fictitious multicomponent metamaterial assembled from cleverly-

Table 2.5: Compressibilities of NAC materials

	Meth.	K_{NAC} (TPa^{-1})	K_{PLC} (TPa^{-1})	Range (GPa)	Ref(s).
$Ag[C(CN)_3]$	[b]	−7.5(8)	66(20)	0–0.615(6)	315
NaV_2O_5	[a]	−1.7(6)	14.3(12)	2–10.0	316–320
$TlGaSe_2$	[c]	−4.99	33.28	–	134

[a] Calculated from reported lattice parameters and calculated using PASCAL [101]. Lattice parameters are given in full in Appendix B. [b] As reported. [c] Calculated from elastic constants.

chosen pairwise potentials [324]. Translating this study into real materials that exhibit a negative compressibility transition is difficult (perhaps impossible) for three main reasons. First, the expanded phase is only stable at high pressures in the 0 K limit and is metastable at finite temperature. Second, the barrier to relaxation of this metastable state scales inversely with system size. For atomic-scale realisations— *i.e.* materials as discussed here—the barrier is unlikely to be sufficiently high to prevent rapid relaxation to the thermodynamic (compressed) state at high pressures [324]. And, third, the pairwise potentials needed to produce the effect are as unusual as they are specific. Nevertheless, were it possible to realise even a *discontinuous* negative compressibility transition in a chemical system then 'continuous' negative volume compressibility behaviour might be feasible through inhomogeneous chemical doping to 'smear out' the transition pressure—a trick used elsewhere to convert discontinuous thermal volume collapse to "colossal" NTE [325].

Applications and future directions

Whatever the particular manifestation of negative compressibility, what is clear is that its very existence is symptomatic of anomalies in the whole elastic tensor. One area of obvious development in the field is the use of elastic property measurement techniques—

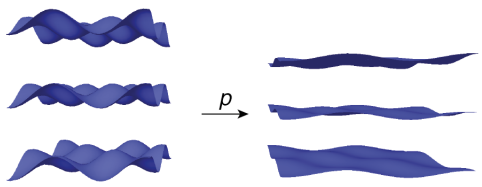

Figure 2.14: Lifshitz mechanism for negative area compressibility. Densification of layered materials usually proceeds *via* collapse in the stacking direction, which in turn results in an expansion in the two perpendicular directions (*i.e.*, within the layer) [323].

historically applied in the fields of materials science, engineering, and metallurgy—in exploring related elastic anomalies in the various chemical systems covered here. One expects that the general trends identified here will resurface irrespective of the particular measurement: strongly-bound materials will be more resistant to applied stress, and open frameworks will give rise to larger magnitude elastic responses. The development of new classes of negative Poisson ratio materials would be one avenue of further research [326].

From a materials chemistry perspective, however, perhaps the most exciting direction to be explored will be the coupling of anomalous elastic behaviour with other materials properties. The potential application of NLC in pressure sensing devices, for example, relies on the effect of simultaneous elongation and densification on optical behaviour [109]. The sensitivity of such devices depends critically on two effects: the rate of variation in refractive index (usually a function of volume compressibility) and also the macroscopic path length (a function of linear compressibility). In 'ordinary' optical materials there is an antagonistic relationship between these two factors such that the optical path length $\phi_{\alpha k}$ changes by a small degree on application of pressure. Using an NLC material, however, one dimension increases in length under increasing pressure, whilst volume still decreases, giving an order-of-magnitude increase in sensitivity [109, 327]. Sensitivity of pressure sensors is critical for the safe management of large civil engineering projects, *e.g.* hydroelectric dams [328].

Beyond this, orbital overlap in superconductors and magnetic materials—itself strongly sensitive to the distances between atoms—may also be tuneable in unexpected ways by exploiting the counterintuitive pressure dependencies attainable of NLC materials [329]. Thinking beyond NLC itself, the coupling of extreme elastic anisotropy (of which NLC is of course a simple consequence) with macroscopic dipole formation may lead to exciting new classes of piezoelectrics, ferroelectrics, and pyroelectrics. Whatever the future holds, the lessons learned from the study of NLC materials—namely the different ways in which chemical, geometric, and topological motifs influence elastic anomalies—are likely to play a crucial role in functional materials design.

Chapter 3

Large NLC in the perovskite-like dicyanometallates $KM[M'(CN)_2]_3$

3.1 Background

Anisotropy is a necessary property of any material that might undergo NLC. We have seen that the existence of linear NTE in particular is a strong predictor of NLC, especially those with cross-linked structures common to many framework materials. The origin of this can be rationalised in two ways: (i) the directional elastic properties of the framework as discussed in §1.2.3 and (ii) pure geometrical arguments [205]. As previously discussed, this relationship led to the discovery of very large NLC in cyanide framework silver hexacyanocobaltate, $Ag_3[Co(CN)_6]$ [78]. The trigonal structure of $Ag_3[Co(CN)_6]$ is made up of three interpenetrating α-Po (cubic) nets [80] which can be considered a three-dimensional wine-rack-analogue. This extremely flexible framework is however especially sensitive to shear instabilities: a shear-driven collapse occurs at $p = 0.19\,\mathrm{GPa}$ resulting in rapid densification and order-of-magnitude reduction in NLC behaviour [78]. Balancing large flexibility with the propensity for mechanical instability in the design of next-generation NLC molecular framework materials is the focus of this chapter. Indeed there is increasing interest in manipulating the flexible properties within the MOF community, for example the recent report of sorption-induced stiffening of metal–organic frameworks [330].

To design a material showing a large and sustained NLC response, focusing on materials that retain the structural features thought to bring about the negative response—but adjusting those that cause structural collapse—is a logical starting point. Fortunately the NLC/NTE mechanism has been the focus of several studies [81, 331–334] highlighting a combination of framework topology and weak 'argentophilic' interactions as critical. The triply-interpenetrated cubic net framework topology acts as a classic 'wine-rack', where

volume reduction is accommodated by compressing the cubes along diagonal directions (collinear with the a lattice parameter), resulting in elongation in the trigonal **c** direction, as shown in Figure 1.16. Very large strains are accommodated in the **a**-**b** plane by very compressible argentophilic interaction cross-linking the nets [Fig. 1.31]. It is the mobility of these cations that permits the displacive phase transition at 0.19 GPa and the consequential collapse of the structure as shown in Figure 3.1 [78, 334].

Our strategy to extend the range over which NLC is observed was to prevent this structural collapse by inclusion of counter-ions within the framework cavities [115]. In the case of $Ag_3[Co(CN)_6]$ this can be achieved by substitution of Mn^{2+} for Co^{3+} while balancing charge with extra-framework K^+ ions [229]. K^+ cations are not covalently bound to the framework; rather they interact electrostatically in channels of the framework surrounded by side-bound cyanides. As the shear instability responsible for volume collapse in $Ag_3[Co(CN)_6]$ is coupled to a translation of two thirds of the Ag^+ ions to a site that in $KMn[Ag(CN)_2]_3$ would result in a very short K^+...Ag^+ contact (*ca* 3.6 Å, *cf.* 4.8 Å in the native compound), the presence of K^+ might be expected to influence strongly the existence of a high-pressure phase transition. Indeed I have previously shown [243] that the resulting compound $KMn[Ag(CN)_2]_3$ remains mechanically stable up to at least 2.2 GPa

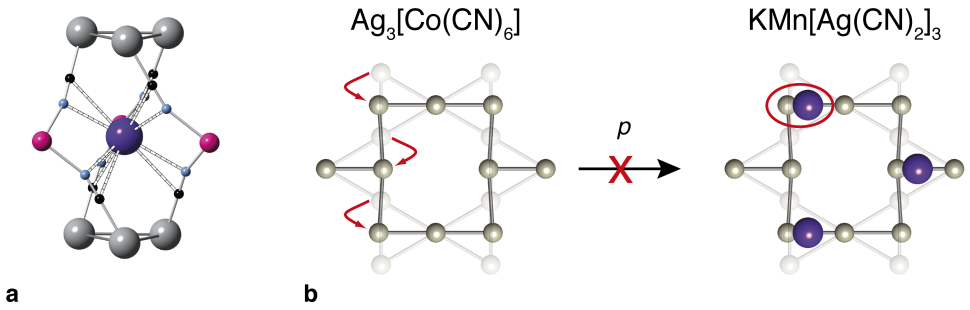

Figure 3.1: Incorporation of K^+ within the wine-rack structure of $KM[M'(CN)_2]_3$ is thought to be critical to prolonging NLC response. (a) The side-bound distorted octahedral coordination of K^+. (b) In $Ag_3[Co(CN)_6]$ NLC is destroyed by shear-induced framework collapse at 0.19 GPa (left); this mechanism is frustrated in $KMn[Ag(CN)_2]_3$ *via* incorporation of extra framework ions (open red circles; right). Rearrangement of the Ag Kagome sublattice, viewed here down the *c*-axis, couples to framework shear in $Ag_3[Co(CN)_6]$. These displacements would give unphysical Ag^+K^+ distances in $KMn[Ag(CN)_2]_3$; the soft mode responsible is stiffened and the phase transition responsible for destroying NLC is avoided.

(the highest pressure for which diffraction patterns have been measured for this system), while retaining respectable NLC properties in the process: $K_{\mathrm{NLC}} = -12.0(8)\,\mathrm{TPa}^{-1}$ over the range 0–2.2 GPa [115]. The mechanism of negative response was shown to be essentially the same as for $Ag_3[Co(CN)_6]$: counter-ions selectively frustrate the soft modes responsible for structure collapse. Since our publication of these results the mechanism of "soft-mode frustration" has been verified using a combination of Raman spectroscopy and first principles calculations [309].

Potassium manganese dicyanoargentate is in fact one of a large family of dicyanometallates based on octahedral metal coordination. These are related to the perovskite family both by formula—replacing oxide with the much longer dicyanometallate—and by underlying framework topology. Many of the structural analogues $AM[M'(CN)_2]_3$ family (A = alkali metal, M = divalent transition-metal cation, and M′ = group 11 mono-cation) were suggested in the early publication of Ref. 227, but not characterised until much later. I have previously investigated the thermomechanical responses of several members of this family [Fig. 3.2].* The responses are found to follow intuitive trends: silver-containing dicyanoargentacte analogues exhibit stronger thermal expansion than gold-containing di-

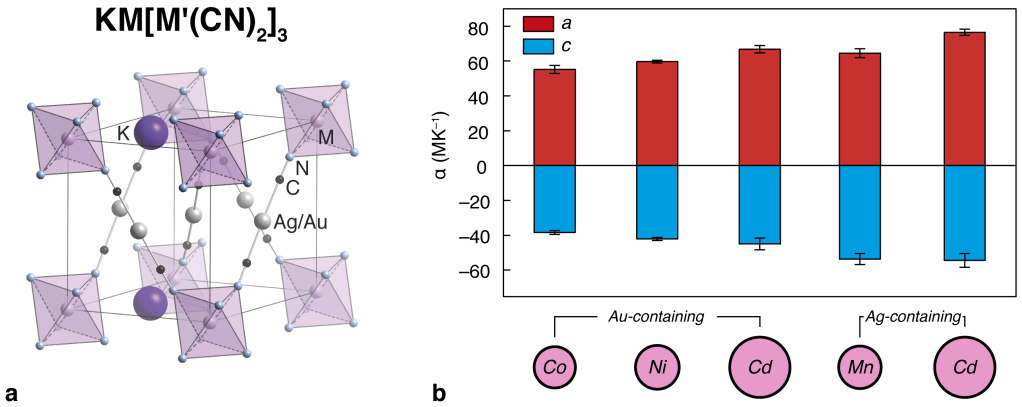

Figure 3.2: Structure and thermomechanical response of the $KM[M'(CN)_2]_3$ family of frameworks (a) *P*312 unit cell for isostructural frameworks of general formula $KM[M'(CN)_2]_3$ (M = 2+ transition metal; M′ = Ag, Au) and (b) the coefficients of thermal expansion calculated with linear fits to VT lattice parameter data.

---

* Honour School of Chemistry, Part II Thesis, Oxford, 2011 [243]. For methods used to calculate the thermal expansion parameters presented see Appendix A and variable-temperature cifs are included on the CD Appendix.

cyanoaurates due to weaker cross-linking, and larger more coordinationally flexible cations result in greater overall framework flexibility.

As the pressure responses are directly linked to the geometric NTE mechanism, NLC is also expected to occur for much of this family and follow similar trends. Confirming this mechanism unambiguously would require observation of the phase transition that does occur to confirm that other soft modes drive such a transition. In this chapter I explore the relationship between NTE, NLC and phase transition behaviour in $KMn[Ag(CN)_2]_3$ and $KCd[Ag(CN)_2]_3$ using a combination of variable-temperature, variable-pressure neutron and X-ray diffraction.

3.2 Experimental

$KMn[Ag(CN)_2]_3$ was synthesised by a similar method to that reported in Ref. 229. 250.6 mg (1.259 mmol) of $KAg(CN)_2$ (Sigma Aldrich, 99%) and 139.9 mg (0.7818 mmol) of $Mn(NO_3)_2{\cdot}xH_2O$ (Sigma Aldrich, 98%) were each dissolved in 3 ml of H_2O and carefully layered with 2 ml of water in a test tube. A polycrystalline sample of $KMn[Ag(CN)_2]_3$ precipitated after 12 h (102.1 mg, 0.1752 mmol, 22.41%). To synthesise large single crystal samples, 551.8 mg (2.773 mmol) of $KAg(CN)_2$ and 269.9 mg (1.929 mmol) of $Mn(NO_3)_2{\cdot}xH_2O$ were dissolved in a small amount of ice-cold water and placed in separate arms of an H-tube. Cold water was carefully layered on top and left for 14 d in dark conditions, after which time large single crystals had formed (57.4 mg, 0.0985 mmol, 5.11%). $KCd[Ag(CN)_2]_3$ was synthesised in a similar manner using $Cd(NO_3)_2$. A faster mixing technique was used instead of an H-tube to make the small single crystals suitable for loading into the diamond anvil pressure cell.

Variable-pressure/variable-temperature neutron diffraction measurements were carried out on $KMn[Ag(CN)_2]_3$ using the High Resolution Powder Diffraction (HRPD) instrument at the ISIS facility, U.K. [335]. Approximately 10 g of sample was prepared, ground to a fine powder, and then loaded into an aluminium gas pressure cell. The cell was pressurised with He (which acts as the pressure transmitting medium) under controlled conditions to its maximum pressure of 0.6 GPa, then placed inside a cryostat in the sample tank

[Fig. A.2.1]. At each pressure point data were collected at 5 temperatures on cooling; the cell was then heated to room temperature and depressurised to the next pressure. This was repeated for 5 pressure intervals with the true T/p logged at each point.

Structural refinement against diffraction data was carried out in three ways, as summarised in Table 3.1 using TOPAS Academic v.4.1 [154]. From Rietveld refinement it was confirmed that $KMn[Ag(CN)_2]_3$ adopts a structure consistent with the $P312$ model proposed at all points of this experiment. For sequential and parametric refinements lattice parameters and peak shape profile variables were refined, while making use of (fixed) atomic coordinates as determined using ambient single-crystal X-ray diffraction measurements. Acceptable fits were obtained at all T/p points and—although not of the same quality as Pawley refinements—are more meaningful in the sense that a structural model is used to determine intensities. Analysis of the lattice parameters confirmed between the different refinement techniques $\Delta\ell/\sigma(\ell) < 1$ in all cases; representative fits are presented in §C.1.1.

For $KCd[Ag(CN)_2]_3$ variable-pressure powder experiments, several $KCd[Ag(CN)_2]_3$ single crystals were ground to a very fine powder and placed in a pre-indented stainless steel gasket within an ETH DAC. A ruby sphere was added for pressure determination

Table 3.1: Refinement strategies for VT/Vp neutron powder diffraction data collected on HRPD.

	Rietveld	**Sequential**	**Parametric**
Background	refined	refined	refined
Lattice parameters a, c	refined	refined	constrained to Eq. 3.1
Instrument peak profile	fixed	fixed	fixed
Sample peak profile	refined	refined against all data*	refined against all data*
Atomic parameters:			
Mn, K	fixed	fixed	fixed
Ag, C, N	distance restraints	fixed	fixed
B_{iso}	refined‡	fixed	fixed
Preferred orientation (spherical harmonic)	refined	refined against all data*	refined against all data*
Scale factor	refined	refined	refined

*Separate parameters refined for 0 GPa and HP data due to different collection strategies and re-packing of sample. ‡ Refined for 0 GPa data and fixed for high pressure collections.

using the standard ruby fluorescence method [336], and Fluorinert FC-77 was used as the pressure transmitting medium.* High pressure X-ray diffraction data were obtained on the beamline BM01A (Swiss-Norwegian beamline) at the ESRF, France [337]. A wavelength of 0.69412 Å was selected using a Si(111) monochromator with a 100 μm focused beam-size. Data were collected using a MAR345 image plate placed at 250.718 mm from the sample position. Calibration and integration of the images was performed using FIT2D [153]. Pawley fits to data were performed at each pressure using space groups as determined from single-crystal experiments using a TCHZ peak shape within TOPAS Academic v4.1 [154]. The data were not of sufficient quality to allow full Rietveld refinement due to preferred orientation and the small amount of sample within the pressure cell; fits are given in §C.2.3.

Single-crystal X-ray diffraction data for $KCd[Ag(CN)_2]_3$ were collected using an Agilent Gemini Diffractometer by J. Haines (Montpellier) at five pressure points at room temperature. A 170 μm × 80 μm × 30 μm single crystal was fixed to one anvil of a Merrill-Bassett DAC (Boehler–Almax diamond anvils) along with a ruby microsphere for pressure calibration. A tungsten gasket was placed on the other anvil and Daphne7474 oil was added as a pressure transmitting medium as the two parts of the cell were assembled. The data collection strategy, indexing and reduction were performed using CrysAlisPro (Agilent); absorption correction was carried out using Absorb7.0 [163] and structure refinements were performed using SHELXL97 [338]. Structures could be solved and refined for all phases; structural models in all cases were based on the group-subgroup relationships from $P312$ by observing the appearance of superlattice reflections as discussed below. The C–N distance was constrained in all refinements, making use of the average value determined in the ambient-pressure phase. Due to the large number of variables for the two high pressure phases, the Ag–C and Cd–N distances were also constrained. C and N atoms were refined with isotropic displacement parameters for the high pressure

* At the time of this study it was thought that the more commonly used 4:1 methanol:ethanol mixture reacted with cyanides under pressure (See Chapter 5), and so the less reactive Fluorinert was used despite the smaller hydrostatic pressure range.

data sets.

3.3 VT/Vp response of KMn[Ag(CN)$_2$]$_3$

Our previous study of KMn[Ag(CN)$_2$]$_3$ confirmed a relatively strong linear-NTE response and revealed a large and prolonged NLC effect [115, 243]. Further development of this system requires a detailed understanding of the origin of this unusual response, in particular the role of extra-framework cations on mechanical response. It is proposed that the electrostatic interaction between the framework and the counter-ion introduces a second energy penalty (the first being argentophilic interactions) to the deformation of the wine-rack like nets, therefore frustrating the soft modes responsible for phase transition. In our original report we were unable to quantify this interaction nor had we been able to resolve the structural changes taking place at high pressure. We therefore carried out a systematic variable-temperature/variable-pressure structural investigation to better understand this mechanism and the relationship between NTE and NLC.

This study focuses on the low-pressure, low-temperature response as it is these conditions that are likely to be encountered in typical applications. Collection of high-resolution neutron diffraction data meant that Rietveld refinement was possible at each T/p point in our investigation. A parametric fitting procedure was also carried out to extract compressibilities and equation of state parameters as a function of temperature, and the thermomechanical response as a function of pressure. This approach was preferred as changes in temperature result in changes in pressure within the gas cell according to the ideal gas law, so extraction of coefficients of thermal expansion at fixed pressure is not possible directly. There is a close correspondence between the two approaches in all cases highlighting the utility of (i) our specific parameterisation in this case and (ii) parametric fitting in general to interpret diffraction data across variations in multiple parameters. We begin by discussing the parametric fitting results—*i.e.* the bulk material response to temperature and pressure—followed by discussion of the structural changes found by Rietveld refinement.

3.3.1 Results

There is no strict thermodynamic requirement for fitting of variable-pressure lattice parameters at fixed temperature [§1.2.2], or fitting lattice parameters under changes in temperature and pressure. Equation of state fitting to VT/Vp data can be carried out by parameterising the temperature dependence of the empirical components of the EoS [86, 339] using: (i) the high-temperature Birch-Murnaghan EoS, (ii) the thermal pressure EoS [340, 341], and (iii) the Mie-Grüneisen-Debye EoS. Here we use a simplified approach by including a linear term in T to the common exponential fitting given by Eq. 1.17 [101], to give

$$\ell = (\ell'_0 + \alpha T) + (\lambda' + \beta T)(p - p_c)^{\nu}. \tag{3.1}$$

The temperature variation of ν was found to be very small so was excluded. Within TOPAS it was possible to fit these data parametrically where empirical parameters are directly refined to fit the entire T/p surface, rather than the structural parameters at each point. This approach increases the number of data points refined per parameter, better constrains the sample-dependent peak shape and gives a physically sensible variation of the lattice parameters in this area of the phase diagram. The refined parameters are given in Table 3.2 and refined lattice parameters and surface fit are shown in 3D in Figure 3.3 (values are given in full in Appendix C, §C.1.3).

From this fit it is possible to calculate the compressibilities (Eq. 1.8) and coefficients of thermal expansion (Eq. 1.4) directly given by:

$$K_\ell(T) = -\frac{1}{(\ell'_0 + \alpha T)} \left[(\lambda' + \beta T)\nu(p - p_c)^{\nu-1}\right], \tag{3.2}$$

and

$$\alpha_\ell(p) = \frac{1}{\ell'_0} \left[\alpha + \beta(p - p_c)^{\nu}\right]. \tag{3.3}$$

It is found that across this area of the phase diagram NLC and NTE are observed along **c** with positive response in perpendicular directions; calculated values are given in Ap-

pendix C. Propagation of errors in these calculations was carried out directly in TOPAS [154]. We compared these values to those obtained from individual refinement of data points and subsequent calculation of α_ℓ and K_ℓ in PASCAL [101]. In the following section we consider the variation in the magnitudes of these responses and what we can conclude about the mechanism of response from these variations.

Full Rietveld refinement was possible at each data point. Lattice parameters refined in this way were very close to those refined as above and we were able to refine atomic positions within the unit cell in each case. Due to the data collection strategy used, the data collections at ambient pressure outside the pressure cell were of much higher quality and therefore allowed more robust refinement of atomic positions and isotropic thermal displacement parameters (B_{iso}) for all atoms. For high-pressure data sets, atomic positions could be refined but thermal parameters could not, as outlined in Table 3.1. Therefore I focus on the temperature variation of atomic parameters at 0 GPa, and the global p dependence of atomic positions, noting at the outset that large errors are found making it definitive conclusions difficult to draw.

3.3.2 Analysis

We first consider the temperature-dependent pressure response of $KMn[Ag(CN)_2]_3$: *i.e.* how the compressibilities and equation of state parameters vary with pressure and what this might tell us about the mechanics of this material. In Figure 3.4 the compressibilities and bulk modulus from a 2nd order B-M fit are plotted as a function of temperature extracted from the parametric fit and calculated from independent refinement of data at

Table 3.2: Empirical parameters of Eq. 3.1 refined against high-resolution powder neutron diffraction data of $KMn[Ag(CN)_2]_3$.

Parameter	a	c
ℓ'_0 (Å)	6.901(16)	8.17(2)
α ($\times 10^{-3}$ Å K^{-1})	0.591(10)	−0.62(2)
λ' (Å GPa^{-1})	−0.317(11)	0.200(19)
β ($\times 10^{-3}$ Å GPa^{-1} K^{-1})	−0.190(8)	0.21(3)
ν	0.604(20)	0.42(5)
p_c (GPa)*	−0.24(2)	−0.24(2)

* Constrained to be equal.

each T/p point. There is close correspondence between the compressibilities calculated in these ways, suggesting the empirical equation proposed captures the response of the material appropriately. It is found on increasing temperature both positive and negative compressibilities are enhanced by $|(\partial K_a/\partial T)| \approx |(\partial K_c/\partial T)| \approx 0.015\,\mathrm{TPa^{-1}\,K^{-1}}$. Variation of K_a and K_c in this way results in an overall decrease in the bulk modulus *i.e.* the material becomes more elastically compliant at higher T. The enhancement of compressibility in this way suggests some sensitivity to thermal population of low-energy phonon modes to the observed response.

In the recent study of $Zn(CN)_2$ the temperature variation of B-M coefficients were analysed to shed light on the anomalous pressure-induced softening (negative value of B') observed [342]. Using a combination of molecular dynamics simulations and neutron diffraction it is found that B' varies non-linearly with pressure. The variation in B'—indeed the pressure-induced softening itself—are both directly related to transverse vibrational mode mechanism of isotropic negative thermal expansion. At a finite temperature the structure is buckled through rotations involving rigid unit modes, which under compression leads to the rapid softening of the structure. At very low temperature, however, these modes are not populated so the only compression mechanism is through direct bond compression. The variation of B' from positive through to a minimum negative

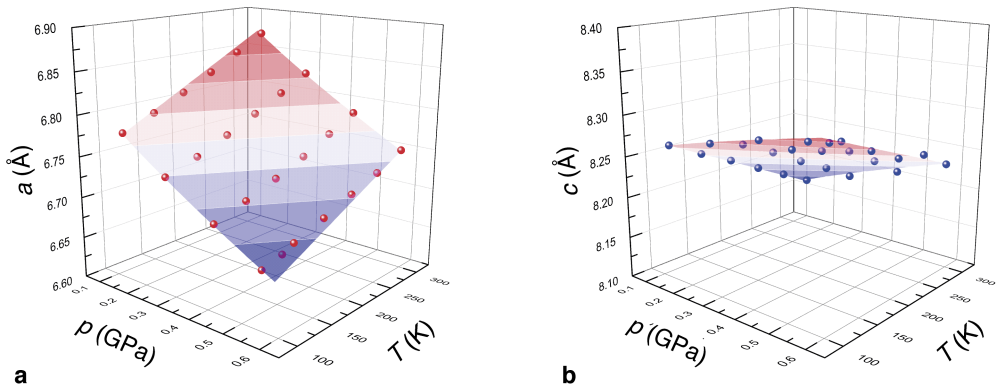

Figure 3.3: Parametric fit of variable-pressure variable-temperature lattice parameters of potassium manganese dicyanoargentate. Variation in (a) lattice parameter *a* and (b) *c* as a function of temperature and pressure. The values given by individual refinement of each data set is given by red or blue spheres in each case and the parametric lattice parameter fit given by the surface shown.

value and finally to around zero is parameterised in Ref. 342.

Here quite different behaviour is observed within the limits of the experimental results. From independent refinements of each data set, B' decreases and becomes increasingly unreliable at low T with a large correlation with B_0. Parametric refinements showB' increases within error at low-T. The small number of pressure points at each temperature means correlation in B_0 and B' is likely in a 3$^{\text{rd}}$-order B-M fit and therefore the 2$^{\text{nd}}$-order fit is preferred. Very little can be concluded from this except that the mechanism of NTE, and therefore of compressibility, are fundamentally distinct between $Zn(CN)_2$ and $KMn[Ag(CN)_2]_3$. The dominant flexibility modes in the former are determined entirely from the low-energy RUM vibrations, whilst the latter's mechanical properties are dominated by wine-rack framework hinging distortions. These flexibility modes are not dependent on thermal excitation in the temperature range studied and therefore there are normal variations in B_0 and B'.

Variation of thermal expansion coefficients with pressure can be extracted directly from the surface fit of lattice parameters and are shown in Figure 3.5. Here coefficients of thermal expansion calculated from individual refinements diverge from the values calculated from parametric fitting due to the change in pressure at each T; these calculations

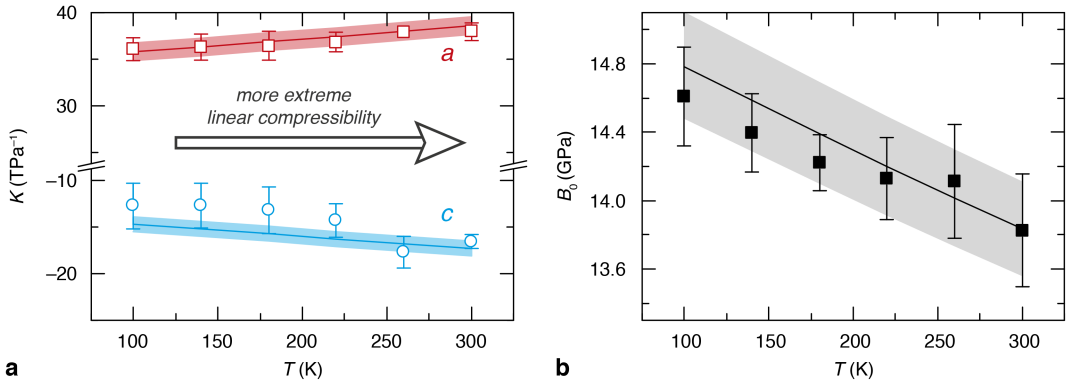

Figure 3.4: Variation in compressibility behaviour of $KMn[Ag(CN)_2]_3$ with temperature. (a) Temperature-dependence of the linear compressibilities in the **a** (red squares) and **c** (blue circles) directions determined using time-of-flight neutron powder diffraction fitted independently (symbols) and parametrically (continuous line). The errors in the case of the latter is given by the shaded error band. (b) Variation of the bulk modulus (B_0) calculated from a 2$^{\text{nd}}$-order B-M fit from independently refined lattice parameters (symbols) and parametrically (continuous line).

are not isothermal and consequently divergence is expected (values given as approximate values). What is shown clearly, however, is that upon pressurisation the magnitudes of the coefficients of thermal expansion decrease. This observation is fully consistent with the mechanism in this case being driven by wine-rack flexibility modes rather than RUM or transverse vibrations. In the case of $Zn(CN)_2$ application of pressure leads to enhancement of the NTE response [343].

Considering the expressions for calculation of α and B_0 together with the Maxwell relation $\partial^2 V/(\partial T \partial p)_{p,T} = \partial^2 V/(\partial p \partial T)_{T,p}$ gives the variation of α_V with pressure as [342]

$$\left(\frac{\partial \alpha_V}{\partial p}\right)_T = \frac{1}{B_0^2}\left(\frac{\partial B_0}{\partial T}\right)_p . \tag{3.4}$$

Using the parametric fit obtained from Eq. 3.1, the values obtained are given in Table 3.3. Whilst in the case of both $Zn(CN)_2$ and $KMn[Ag(CN)_2]_3$ Equation 3.4 holds within experimental error, the responses in these cases are very different. $Zn(CN)_2$ has a well-known negative volumetric thermal expansion that becomes more negative on application of pressure [343]; in comparison $KMn[Ag(CN)_2]_3$ has a *positive* volumetric thermal expansion that becomes less positive on application of pressure. This ensures that for both

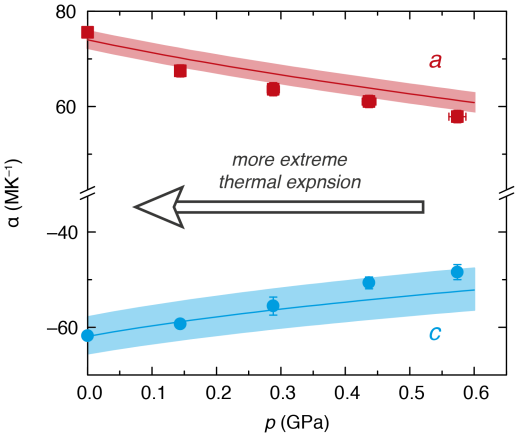

Figure 3.5: Variation in thermal expansion of $KMn[Ag(CN)_2]_3$ with pressure. Pressure-dependence of the linear coefficients of thermal expansion in the **a** (red squares) and **c** (blue circles) directions determined using time-of-flight neutron powder diffraction fitted independently (symbols) and parametrically (continuous line). The errors in the case of the latter is given by the shaded error band. Note the points shown are strictly non-isothermal so divergence from the parametric line is expected.

materials the variation in bulk modulus is as expected; the enhancement of NTE under pressure in the case of $Zn(CN)_2$ is directly linked to the negative value of B' whilst $KMn[Ag(CN)_2]_3$ is well described by a second-order B-M EoS. This analysis suggests, as we determined previously, the mechanical properties are determined by wine-rack flexing rather than transverse vibrational modes, and that this is not strongly temperature dependent.

3.3.3 Mechanism of NTE/NLC

The 'wine-rack' mechanism of response for cross-linked molecular framework materials is distinct to the response of materials such as $Zn(CN)_2$, where unusual properties arise by thermal activation transverse vibrational modes. Here I develop this concept further, showing that the mechanical responses of 'wine-rack' materials are determined primarily by framework geometry by showing that network hinging controls the observed change in material volume as temperature and pressure are changed, that this hinging is not strongly dependent on thermal population of vibrational modes, and this hinging dominates in preference to deformation of framework struts. By defining a framework vector **k**—that corresponds to real framework linkages—we can rationalise bulk response from lattice parameters alone, without the need for full structural refinement. Mechanical responses that are purely geometric will effect only the direction of **k** not its magnitude.

First the microscopic mechanism of response of $KMn[Ag(CN)_2]_3$ was explored further by Rietveld refinement of variable-temperature, variable-pressure neutron diffraction data. The quality of the data resulted in large errors in positions and therefore bond distances

Table 3.3: Comparison of pressure- and temperature-dependent thermal expansion and compressibility parameters for for $Zn(CN)_2$ and $KMn[Ag(CN)_2]_3$. Values for $Zn(CN)_2$ given for molecular dynamics (MD) and experimental (exp) calculations, as given in Ref. 342.

Parameter	$Zn(CN)_2$ *(MD)*	$Zn(CN)_2$ *(exp)*	$KMn[Ag(CN)_2]_3$
α_V (MK^{-1})	−30.1(4)	−47.7(7)	87.63(10)
$(\partial\alpha/\partial p)_T$ (MK^{-1})	−23(2)	−31(21)	−27(2)
$(\partial B_0/\partial T)_p$ ($\times 10^{-3}$ GPa K^{-1})	−27(2)	−35(23)	−4.77(10)
$\bar{B}_0$ (GPa)	39.4(3)	36.9(5)	14.3(3)
$1/(\bar{B}_0^2)$ ($\times 10^{-3}$ GPa^{-2})	0.644(10)	0.73(2)	4.89(10)

making detailed conclusions about the mechanism difficult, especially at elevated pressure. Here we summarise only the variable-temperature behaviour at ambient pressure and the average pressure-dependence of parameters; refined structural parameters and graphs are given in Appendix C, §C.1.5. The structural models confirm that on decreasing temperature and increasing pressure bond lengths on average decrease and bond angle distortion increases. This is seen by the changes in Mn–N and Ag–C bond lengths and the octahedral angles about Mn and the Ag dihedral angle. Changes in the Ag dihedral angle in particular suggests that framework strut buckling does occur, as quantified below.

So we consider the framework as a whole to build a much more intuitive description of this mechanism. For many framework systems the entire set of lattice compressibilities (including the bulk modulus) and thermal expansion coefficients are a function simply of (i) a single linear compressibility or thermal expansion value, and (ii) the aspect ratio of the framework $\rho = c/a$ [132, 308]. In this chapter we make use of this theory to derive expressions for the mechanism of response of the simple 2D 'wine-rack' and the related topology of the $KM[M'(CN)_2]_3$ system; in the next chapter we use similar arguments to show how the response of the honeycomb and β-quartz frameworks are related.

First we consider the 2D 'wine-rack' illustrated in Fig. 3.6(a). The conventional crystallographic structural description is given by the pair of lattice parameters a, c; however it is possible to describe the geometry of this structure with the two alternate parameters k (the strut length) and θ (the folding angle). The two pairs of parameters are related by

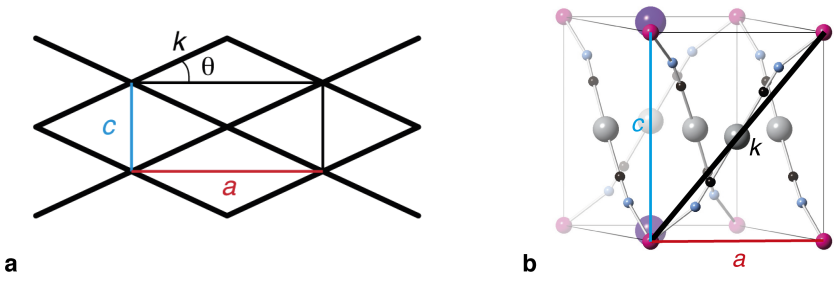

Figure 3.6: Uniaxial network geometries of the 'wine-rack' and extended perovskite-like frameworks

the expressions:

$$a = 2k\cos\theta, \tag{3.5}$$

$$c = 2k\sin\theta. \tag{3.6}$$

In the limit of small distortions to the framework strut lengths, the only parameter that varies under changes in pressure will be θ; *i.e.*, $\mathrm{d}k/\mathrm{d}p = 0$. Hence the derivatives of the lattice parameters a and c with respect to pressure are

$$\frac{\mathrm{d}a}{\mathrm{d}p} = -2k\sin\theta\frac{\mathrm{d}\theta}{\mathrm{d}p}, \tag{3.7}$$

$$\frac{\mathrm{d}c}{\mathrm{d}p} = +2k\cos\theta\frac{\mathrm{d}\theta}{\mathrm{d}p}. \tag{3.8}$$

Substituting $\rho = c/a$ and evaluating for compressibilities, it follows that

$$K_c = -\frac{1}{\rho^2}K_a, \tag{3.9}$$

and hence the value of K_c is determined uniquely by K_a and ρ. The intrinsic NLC effect also follows immediately: a positive value of K_a implies NLC along the c-axis, with the magnitude of NLC proportional to the magnitude of K_a for fixed ρ.

The geometry of the real system of interest shown in Figure 3.6 has a close resemblance to this 2D model. By defining a framework vector $\mathbf{k}$ we can re-cast the measured structural parameters (the lattice parameters a, c) in terms of network geometry. Here we use the Mn...Mn separation as the framework vector. Choosing the vector shown [Mn on special positions (0,0,0) and (1,0,1)], the resulting framework vector is

$$\mathbf{k} = \boldsymbol{a} + \boldsymbol{c}, \tag{3.10}$$

and therefore the relationship between K_a and K_c is identical to Eq. 3.9: K_c is determined uniquely by K_a and ρ. Using the relationship between the bulk modulus B_0 and the linear

compressibilities (Eq. 1.11) in a three-dimensional uniaxial solid:

$$B_0 = \frac{1}{2K_a + K_c}, \tag{3.11}$$

we can furthermore see that, because K_c and K_a are related *via* ρ, the experimental values of B_0 and ρ can be used to predict an expected value for the magnitude of NLC. In the $KMn[Ag(CN)_2]_3$ framework this is given by

$$K_c = \frac{1}{B_0}\left[\frac{1}{1-2\rho^2}\right]. \tag{3.12}$$

Identical consideration of the linear and volume coefficients of thermal expansion gives a similar relationship, as shown in Ref. 132. In both the case of compressibilities and thermal expansion, maximum negative response occurs for lattice parameter ratios approaching the critical geometry, $\rho_{\text{crit}} = \frac{1}{\sqrt{2}} \simeq 0.7071$.

From the refined lattice parameters it is observed that ρ decreases on increasing temperature, and increases on increasing pressure, which is consistent with the temperature-enhancement of compressibilities and pressure-suppression of thermal expansion behaviour [Fig. 3.7]. The magnitudes of these linear responses are related to the bulk modulus, and therefore stiffening of the structure on cooling also results in a decrease in linear com-

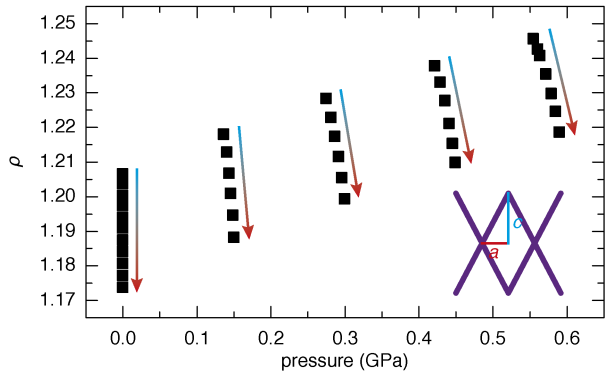

Figure 3.7: Variation in lattice geometry ρ with changing temperature and pressure for $KMn[Ag(CN)_2]_3$. At each pressure values at increasing temperatures are indicated by the colour gradient arrows (blue 100 K to red 300 K). ρ is defined as the c/a ratio as discussed in the text and as illustrated in the inset; propagated standard uncertainties are included within the area of the points.

pressibilities. We do find that analysis of the experimental bulk modulus and value of ρ overestimates the negative compressibility, confirming that linker compressibility (*i.e.* strut buckling) does reduce the magnitude of negative response. However the variation in compressibilities is consistent with a geometry-driven framework flexibility. This 'wine-rack' NTE/NLC mechanism in molecular framework materials is fundamentally different to the response of frameworks such as $Zn(CN)_2$ that show isotropic NTE: the mechanism here is dominated by network hinging rather than thermally-activated transverse vibrational modes.

3.4 V*p* response of $KCd[Ag(CN)_2]_3$

Our study of $KMn[Ag(CN)_2]_3$ provides insight into the relationship between NTE and NLC and the fundamental elastic properties of this system. However we were not able to access the high pressures required to observe phase transition behaviour that would provide direct evidence for the soft mode frustration mechanism proposed. It is only by finding a phase transition (if any) that we would be able to conclusively show that the inclusion of K^+ is responsible for the prolonged pressure range of response in $KMn[Ag(CN)_2]_3$. Therefore we studied the related material $KCd[Ag(CN)_2]_3$ at high pressure using a combination of X-ray single-crystal, X-ray powder diffraction and Raman spectroscopy. From the close correspondence between the themomechanical and piezomechanical properties of these materials, it is predicted that $KCd[Ag(CN)_2]_3$ will have both a desirable enhanced NLC response than $KMn[Ag(CN)_2]_3$, due to the increased flexibility from the effect of the larger Cd^{2+} cation ($r_{Mn^{2+}}$(LS)= 0.67 vs. $r_{Cd^{2+}}$ = 0.95; Ref. 258), as well as lower phase transition pressures.

Our preliminary variable-pressure Raman experiments suggest there are two main pressure-induced phase transitions in this material: one at around 0.5 GPa and the other above 2 GPa [See Appendix C, Fig. C.2.9]. In this chapter we focus on powder and single-crystal diffraction results to characterise the bulk mechanical behaviour of this material and the structures of these new phases. We correlate these structural changes with the major modifications observed in the Raman spectra. The appearance of superlattice

reflections in our scattering experiments confirm the I→II transition occurs at $0.56(10) < p < 0.68(10)$ GPa, and structural refinement shows this is a displacive phase transition resulting in a doubling of the unit cell in **c**. Above 2.25 GPa—in both powder and single-crystal experiments—there is a large change in the diffraction pattern observed due to a reconstructive phase transition to $KCd[Ag(CN)_2]_3$-III with a monoclinic unit cell. In the next section I describe the mechanical responses of phases I and II. and following this the structural characterisation and compressibility of phase III is discussed.

3.4.1 Compressibilities and structural changes of phase I and II

Powder diffraction data were collected at finely-spaced pressure intervals from ambient to 9.7(1) GPa. Over this pressure range the two phase transitions identified from Raman spectroscopy were observed (an additional phase transition, which will be discussed more fully in the next section, was observed at ~ 3.6 GPa). Pawley refinement of lattice parameters of the known $P312$ ambient unit cell against diffraction data reveals strong NLC in the **c** direction, with maximum positive compressibility in perpendicular directions as expected. Refined lattice parameters (and the monoclinic angle β in phase III) across the entire pressure range studied are presented in Figure 3.8.

From our single-crystal diffraction experiments, up to 0.59 GPa the structure could still be refined based on the model of the trigonal ambient pressure phase [Fig. 3.2(a)], and no superlattice reflections were observed. Large negative linear compressibility was also observed in these experiments. From the single-crystal refinements, the $[CdN_6]$ octahedra appear to be relatively rigid and small decreases in the Ag–C and K$\cdots$N distances are observed. There is a significant decrease in the distance between $[CdN_6]$ octahedra which can be linked to a wine rack folding mechanism as discussed for $KMn[Ag(CN)_2]_3$. Atomic positions and lattice parameters refined from single crystal diffraction experiments are given in full in §C.1.5.

Upon further increase in pressure to 1.6 GPa, a large number of superlattice reflections hkl ($l = n/2$) were observed. The vast majority of these reflections could be indexed based on a $P312$ cell, which is doubled along the **c** direction. Less than fifteen very weak

superlattice reflections hkl with a maximum relative intensity of about 0.3% were also observed with $h = n/2$ and/or $k = n/2$ indicating that the unit cell is also doubled along the **a** and **b** directions. Due to the very low intensity of these reflections and the limited high pressure data, the structure was refined using the $P312$ cell doubled along the **c** direction beginning from the undistorted starting model. This new structure corresponds to a distortion of the initial structure with anti-phase tilting of the CdN_6 octahedra about c and thus provides a new compression mechanism for the material [Fig. 3.9]. The cell doubling along **a** and **b** probably is a result of slight tilts about **a** and **b**.

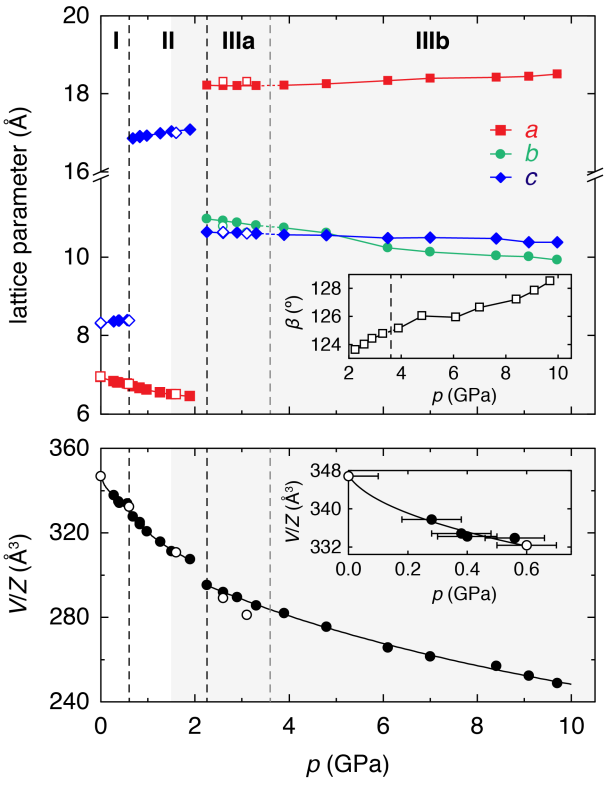

Figure 3.8: Evolution of structural parameters in $KCd[Ag(CN)_2]_3$ on application of hydrostatic pressure. (a) Lattice parameter changes observed during hydrostatic compression: a (red □), b (green ○) and c (blue ◇) for phases I, II, and IIIa/IIIb; closed symbols (powder X-ray diffraction) and open symbols (single-crystal X-ray diffraction). The approximate positions of phase transitions are indicated by dashed vertical lines and the quasi-hydrostatic region for the powder data ($p > 1.5$ GPa) is shaded grey. *(inset)* The variation in the monoclinic cell angle β in phase III. (b) Normalized unit cell volumes (black □) across the full pressure range studied can be fitted to a modified third-order Birch-Murnaghan equation of state as given in Ref. 107. Fits in all cases are to the powder X-ray data only; open/closed symbols and dashed lines are as given above. *(inset)* The B-M fit to the low-pressure data of phase I show rapid structure stiffening approaching the phase I/II transition. Estimated standard uncertainties are included within the area of the symbols.

Turning now to the bulk mechanical response, we can fit our variable-pressure lattice parameters for each phase to extract compressibilities, as given in Table 3.4 and shown in Figure 3.10. It was found that fitting compressibilities for phase I to an empirical equation such as that used in PASCAL was unreliable due to the small number of data points in the very low-p region. We therefore used linear fits to data for phase I. This analysis reveals very large negative compressibility along the c lattice parameter of $K_c = -21(2)\,\mathrm{TPa}^{-1}$, the largest NLC yet found in this family of materials. The compensating PLC is $K_a = +48(8)\,\mathrm{TPa}^{-1}$; fitting the unit cell volumes to the Birch-Murnaghan EoS shows rapid stiffening of the structure and a very small bulk modulus at low pressure.

Across the I/II phase boundary there are no volume nor lattice parameter discontinuities (where $c = c'/2$), probably due to the close relationship between the two phases. Calculating compressibilities across both phases, we confirm that $KCd[Ag(CN)_2]_3$ shows a very large NLC response $K_c = -13.9(11)\,\mathrm{TPa}^{-1}$ up to 2.25 GPa.* B-M fitting for the two phases suggests both phases rapidly stiffen on application of pressure ($B' > 4$), but again robust fits cannot be carried out [Fig. 3.8]. We can however show that the bulk moduli for both phases are lower than $KMn[Ag(CN)_2]_3$, with the second-order B_0 for phase II

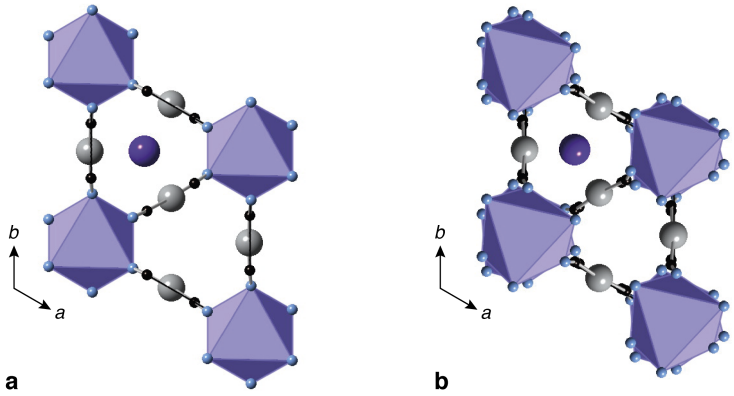

Figure 3.9: A doubling of the unit cell in the c direction allows anti-phase octahedral tilts in the $KCd[Ag(CN)_2]_3$. (a) The ambient-pressure *P*312 and (b) double-*c* phase II structure shown looking directly down **c**. Cd are shown as mauve octahedra, C, N, Ag and K shown as black, blue, silver and purple spheres respectively.

---

* Fitting of our variable-pressure lattice parameters of $KMn[Ag(CN)_2]_3$ previously reported in the same way gives a compressibility of $K_c = -8.5(9)\,\mathrm{TPa}^{-1}$ due to the method of averaging values implemented in PASCAL.

Table 3.4: Linear compressibilities calculated using PASCal [101] from variable-pressure lattice parameters for phase I, II and III of $KCd[Ag(CN)_2]_3$.

Phase	p_c (GPa)	K_a (TPa^{-1})	K_b (TPa^{-1})	K_c (TPa^{-1})	B_0 (GPa)	B'
I	0	+48(8)*		−21(2)*	$< 5^{\dagger}$	$\gg 4^{\dagger}$
II	0.6	+30(2)		−10.0(8)	13.6(10)	$\equiv 4$
I+II	0	+37.6(19)		−13.9(11)	11.9(5)	$\equiv 4$
III	2.25	+12.0(8)	+11.3(13)	−2.7(4)	31(4)	4.0(12)

*Linear fit, †Correlation between B_0 and B' gives large uncertainties on calculated values.

giving an upper bound for this value, and fitting across both phases gives an average bulk modulus of 11.9(5) GPa (*c.f.* 14.5 GPa for $KMn[Ag(CN)_2]_3$). All compressibilities and B-M coefficients calculated using PASCAL [101] are presented in Table 3.4.

3.4.2 High-pressure phase-transition behaviour

At 2.25(10) GPa, a single-crystal diffraction pattern was observed that was very different to the $P312$ cell, which is consistent with the major phase transition observed by our Raman spectroscopic measurements. The unit cell could initially be indexed with a

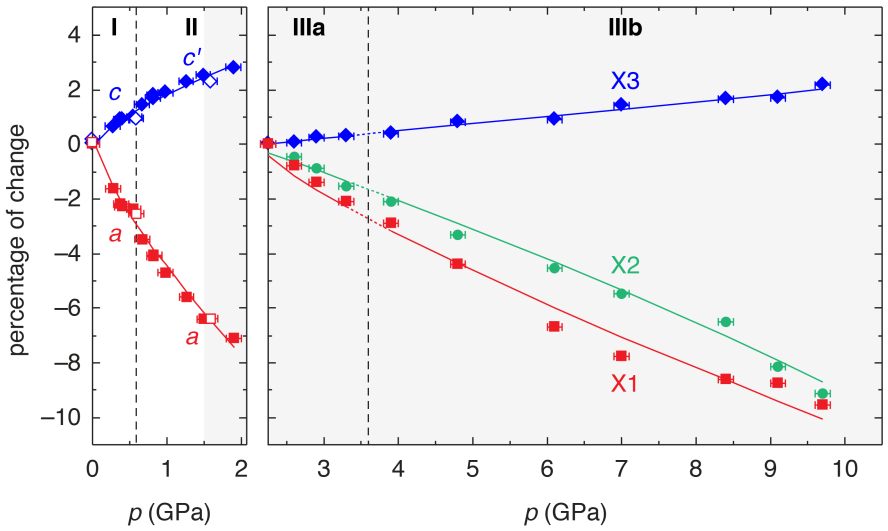

Figure 3.10: Fits to unit cell parameters along principal axes for phase I/II (left panel) and IIIa and IIIb (right panel) using empirical equations. In the trigonal space group of phases I and II, the principal axes are coincident with the a (red □) and c (blue ◇) lattice parameters and one fit is given to both phases using reduced lattice parameters $a' = a$ and $c' = c/2$. Phases I and II are fitted simultaneously as empirical fits to phase I only are not robust, however linear fits to this data give equivalent compressibilities to the fit across both phases as shown. In the high-pressure phase III, the X2 (green ○) principal axis is coincident with *b* whilst X1 and X2 lie approximately along *a* and *c* respectively. Vertical dashed lines indicate phase transition boundaries and the quasi-hydrostatic region for the powder X-ray diffraction data is shaded grey.

rhombohedral symmetry ($R32$) for the two highest pressure points measured based on the observed reflection conditions. Closer inspection of these data indicated that the structure is actually monoclinic and belongs to the $C2$ subgroup of $R32$. This allows for a slight shearing of the structure perpendicular to the c axis. The cell transformation to obtain phase III ($C2$) with respect to the ambient pressure phase $KCd[Ag(CN)_2]_3$-I ($P312$) is

$$\begin{bmatrix} \mathbf{a} \\ \mathbf{b} \\ \mathbf{c} \end{bmatrix}_{C2} = \begin{bmatrix} 1 & 1 & 1 \\ 0 & 2 & 0 \\ -2 & 0 & 1 \end{bmatrix} \begin{bmatrix} \mathbf{a} \\ \mathbf{b} \\ \mathbf{c} \end{bmatrix}_{P312}, \tag{3.13}$$

as verified using ISODISTORT [344]. The transformation for the unit cell dimensions is therefore given as: $\mathbf{a}_{\mathrm{III}} = \mathbf{a}_{\mathrm{I}} - 2\mathbf{c}_{\mathrm{I}}$, $\mathbf{b}_{\mathrm{III}} = \mathbf{a}_{\mathrm{I}} + 2\mathbf{a}_{\mathrm{I}}$, $\mathbf{c}_{\mathrm{III}} = \mathbf{a}_{\mathrm{I}} + \mathbf{c}_{\mathrm{I}}$. As in the case of the intermediate phase, there is also a superstructure in the highest-pressure phase with weak superlattice reflections indicating a further doubling along all three directions giving a very large unit cell that could not be refined.

It was not possible to solve the structure of $KCd[Ag(CN)_2]_3$-III *ab initio* from our high pressure single-crystal data due to twinning during the phase transition. We therefore turned to our powder diffraction data to solve this structure using a model based on the

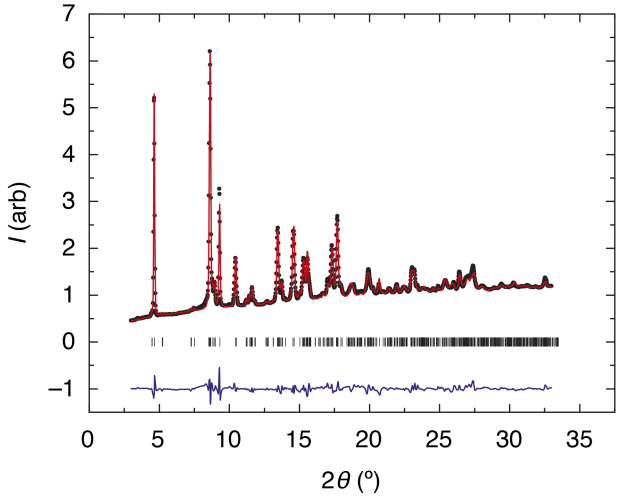

Figure 3.11: Rietveld fit to synchrotron powder diffraction data at 2.25 GPa using a model based on the ambient $P312$ structure transformed using ISODISTORT to the proposed $C2$ high-pressure unit cell. At this pressure $a = 18.1948(18)$ Å, $b = 10.9753(16)$ Å, $c = 10.6216(16)$ Å, $\beta = 123.510(8)°$. Experimental data are given as black points, the fitted profile as a red line and the difference (data−fit) as a blue line, displaced downwards vertically by 1 unit; expected peak positions are shown as black tick marks.

heavy atom positions of the ambient pressure structure. Using the implementation of ISODISTORT [344] within TOPAS [154], the symmetry modes of the distortion could refined against the X-ray powder diffraction data [Fig. 3.11]. These modes describe the allowed atomic shifts based on the symmetry description of the sub-subgroup relationship and therefore has fewer free parameters than a conventional Rietveld refinement. By restricting the modes to those with the highest amplitude in the refinement, a model was proposed and used as the starting point for the single-crystal structure refinement. The C and N atoms were fixed in the powder refinement but were readily located on the difference Fourier maps and refined in the single crystal analysis. Further refinement details, structural parameters and atomic positions are given in full in §C.2.2. The presence of superlattice reflections suggests this solution is in itself still a spatially averaged structure and the true cell is doubled along all three directions, probably due to tilting. The complexity of the true structure prevents its full determination using data obtained at high pressure.

The structure distortions identified from single crystal refinements show that phase III is very similar to the ambient pressure phase, with the major distortions being buckling of the dicyanoargentate linkages and the 'rippling' of layers of argentophilic interactions. The framework and extra-framework cations are shown in Figure 3.12 and this shows

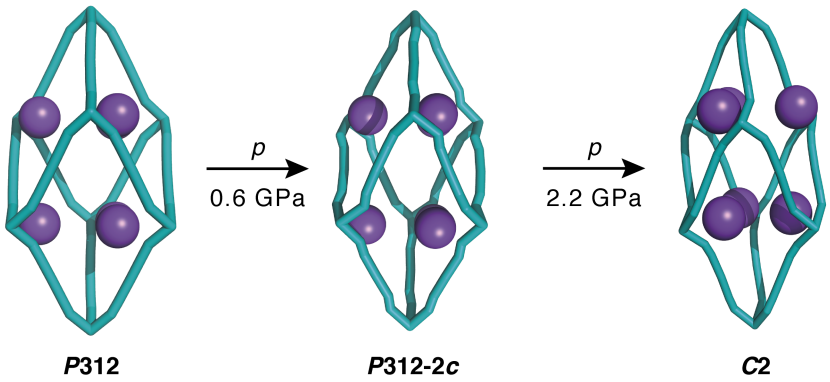

Figure 3.12: Structure buckling upon application of pressure in $KCd[Ag(CN)_2]_3$. Potassium cadmium dicyanoargentate goes through two displacive phase transitions upon application of hydrostatic pressure. The first at $p = 0.6$ GPa is characterised by small polyhedral tilts, whilst the second at $p = 2.2$ GPa involves a shear of the structure and increased framework buckling. NLC is observed in directions parallel to the ambient-pressure unit cell **c** direction at all points. Here Cd, C, N and Ag atoms shown as teal sticks; K shown as purple spheres.

schematically the buckling of the linkages. The major angle change occurs as a result of $[CdN_6]$ rotations with a reduction in the C–$\widehat{N}$–Cd angle from $\sim 158.3°$ in phases I and II to an average value of 150.3° in phase III. The dicyanoargentate linker unit remains remarkably linear with a reduction in C–$\widehat{Ag}$–C of only 2° up to 2.6 GPa; this rigidity is due to the energetically favourable CN back-bonding to Ag which requires good orbital overlap (close to 180°). In the complex high-p structure it is found that all other bond distances decrease and variation in angles suggests a gradual buckling of the structure. Around each K^+ extra-framework cation the side-bound cyanides get progressively closer to create an irregular coordination sphere of cyanide.

Within the argentophilic layers it is found that 1/3 of the Ag^+ remain in the **a**-**b** 'plane' whilst its neighbours displace up and down along **c**, shown schematically in Figure 3.13(a). This rippling distortion maintains favourable argentophilic interactions but allows more extreme buckling of the cubic network as Ag^+ cations are forced into closer contact. In fact these displacements occur for each of the interpenetrated networks in the original **c** direction, and also allow Cd^{2+} to move out of plane to reduce overall crystal volume. Critically this distortion mechanism is distinct from that seen in $Ag_3[Co(CN)_6]$; the soft modes responsible for the transition in the 'unstuffed' version are frustrated and therefore do not cause the phase transition at low pressures.

At ~ 3.6 GPa, an additional set of Bragg reflections appear in our powder diffraction data. Due to the broadening of the Bragg reflections, combined with the fact this scatter-

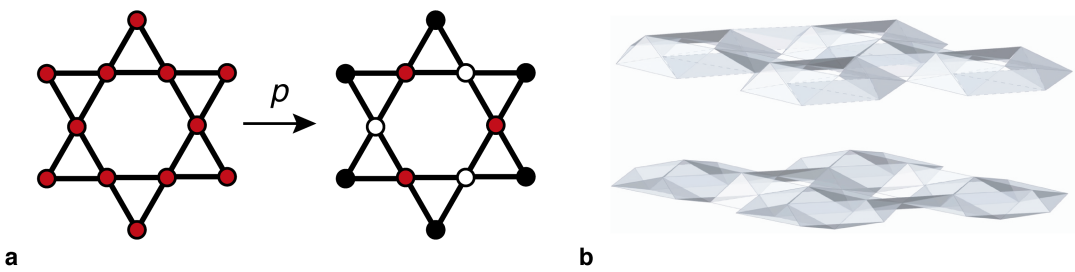

Figure 3.13: Effect of high-pressure phase transition on argentophilic interactions in potassium cadmium dicyanoargentate. (a)The structural transition from phase II to III is characterised by the out-of-plane rippling of the argentophilic kagome lattice such that within each triangle one Ag remains in the plane (red circles), whilst the others move in (white circles) and out of the plane (black circles) by similar displacements in **z**. The resulting 'rippled' layers are shown in (b).

ing was observed well above the hydrostatic limit of our experiment, no further attempt was made to solve this structure. Here we denote this as the transition IIIa→IIIb; there appears to be no hysteresis in either lattice parameter or volume data, so the transition must be continuous. Using the refined lattice parameters for both IIIa/IIIb we can calculate average compressibilities along principal directions [Fig. 3.10] and a bulk modulus for phase III using PASCal [101]. As is expected at high-pressure, the compressibilities decrease and bulk modulus shows significant stiffening of the structure. Reduction in the unit cell volumes of Phase III are well described by $B' \sim 4$, suggesting the structure acts much more like conventional materials than ultra flexible frameworks at these pressures. Remarkably NLC is still observed in along one principal direction that lies approximately along the c axis of the $P312$ cell. This shows that the framework topology is such that, despite significant densification, hinging can still occur.

3.5 Implications

The studies presented here both aim to confirm whether the soft-mode frustration mechanism proposed in our original report of NLC [115] in $KMn[Ag(CN)_2]_3$ is valid. Studying the relationship between NTE and NLC in the low-p and low-T regimes reveals the underlying elastic properties in this family of frameworks. The mechanism of response in these hinged frameworks is shown to be distinct from the transverse vibrational modes responsible for the unusual mechanics of bridged frameworks showing isotropic NTE, such as ZrW_2O_8 and $Zn(CN)_2$. In these frameworks negative response arises from the hinging about metal nodes, whilst the bulk mechanical properties remain dominated by bond compression. This leads to the enhancement of NLC at high-temperature and the suppression of NTE at high pressure.

Parametric fitting of variable-temperature, variable-pressure data has previously been little utilised in the study of flexible framework materials. This approach is however established in other areas, such as studies of geological materials [340, 341]. In general these make use of parameterisation of equation of state parameters (B_0, B') to fit volume data to predict responses at geologically-relevant conditions. Here the pressure and tempera-

ture range studied is much smaller, but the responses are much larger. Furthermore the mechanical responses are anisotropic and so it is required to fit along principal axes to reveal the unusual response of interest. The empirical parameterisation presented here gives coefficients of mechanical responses that are consistent with our other studies, and EoS parameters that are consistent with thermodynamic relationships. The generality of this approach remains to be tested, however similar parametric fitting approaches may find widespread use in other studies.

Convincing evidence that the resistance to pressure collapse in this perovskite-like family of frameworks is due to the included counter-ion is revealed by analysis of the phase transition behaviour of $KCd[Ag(CN)_2]_3$. Upon application of pressure a series of phase transitions occur that relate to the buckling of the framework—*via* octahedral tilting and coordination geometry distortion—and shifting of the three interpenetrated frameworks relative to each other to increase packing density. The phase transition observed in $Ag_3[Co(CN)_6]$ is not observed, demonstrating that the presence of K^+ prevents the displacive shift of Ag^+ within the crystal structure. We observe the transition from the open, responsive framework structure of the ambient-pressure material to a phase that has bulk behaviour much more like conventional materials at high pressure. Significantly, however, NLC is retained across all the phase transitions. $KCd[Ag(CN)_2]_3$ is shown to have the largest NLC response of this family of materials that has been measured, and the correspondence between thermo- and piezomechanical responses has been shown.

Chapter 4

Giant NLC in zinc dicyanoaurate

The unusual behaviour of the perovskite-like dicyanometallate family has been shown to be quite general and so the NLC (and NTE) behaviour can be tuned by varying the chemical building units of the framework, for example changing K^+ for Na^+, Ag^+ for Au^+, Mn^{2+} for Cd^{2+}. This approach of tuning NLC behaviour *via* chemical modification essentially trades *magnitude* for pressure *range* of response. Many applications however require large NLC to persist over many GPa, and so a step-change in approach is needed to identify materials that combined both magnitude and range, therefore maximising the compressibility capacity χ_K. The material on which I focus here is zinc dicyanoaurate, $Zn[Au(CN)_2]_2$, which is shown to be the first material exhibiting 'giant' NLC.

4.1 Background

In this chapter I investigate the mechanical response of molecular framework material zinc(II) dicyanoaurate(I), $Zn[Au(CN)_2]_2$ using a combination of X-ray powder and single-crystal diffraction. It is found that this material exhibits both the most extreme and persistent NLC behaviour yet reported: under increasing hydrostatic pressure its crystal structure expands in the crystallographic c direction at a rate that is an order of magnitude greater than both the typical contraction observed for common engineering materials [83] and also the anomalous expansion in established NLC candidates [109]. This extreme behaviour arises from the honeycomb-like structure of $Zn[Au(CN)_2]_2$ coupling volume reduction to uniaxial expansion [345], and helical Au$\cdots$Au 'aurophilic' interactions [239] accommodating abnormally-large linear strains by functioning as supramolecular springs. Critically it is shown that—within a suitable framework geometry—NLC is limited by the magnitude of PLC, and therefore by maximising positive compressibility by incorporating supramolecular assemblies we can maximise negative response.

$Zn[Au(CN)_2]_2$ has been the focus of several previous structural studies showing NTE

and unusual luminescent properties [219, 221, 231]. Four polymorphs of this material are known [221]; this chapter focuses on the α-polymorph, which is the form most readily synthesised as either a phase-pure powder or as large single-crystals. The topology of this particular $Zn[Au(CN)_2]_2$ framework is identical to that of β-quartz, with the increased Zn...Zn separation given by the extended dicyanoaruate linker allowing for sixfold interpenetration [Fig. 4.1 (a,b)] [219, 221, 231]. Cross-bracing these six interpenetrating honeycomb-like nets are sets of weakly-attractive aurophilic interactions ($30 < \Delta H_{\mathrm{Au...Au}} \sim \Delta H_{\mathrm{Ag...Ag}} < 50\,\mathrm{kJ\,mol^{-1}}$ [225]) that form helical chains oriented perpendicular to the **c** crystal axis and which are responsible for a strong luminescent response [221, 231] [Fig. 4.1(b)].

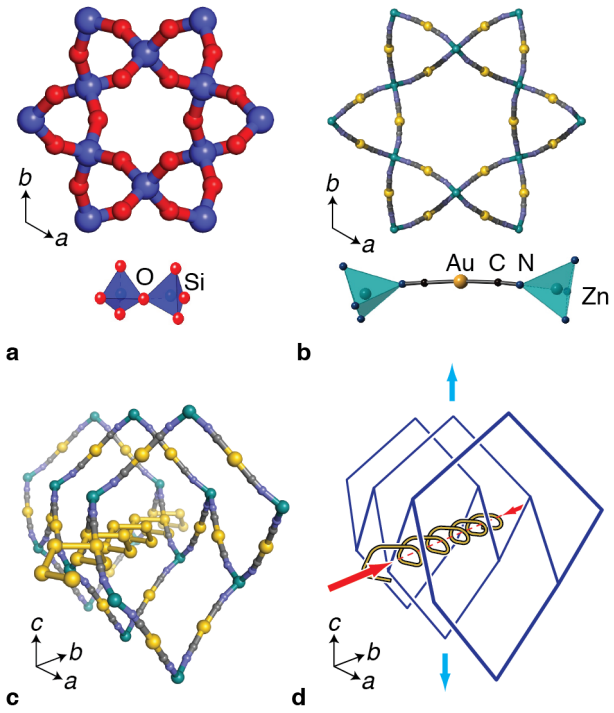

Figure 4.1: The β-quartz-like framework structure of $Zn[Au(CN)_2]_2$ functions as a "molecular honeycomb" to give giant negative linear compressibility. (a) A representation of the crystal structure of β-quartz viewed down its hexagonal axis; the network is assembled from SiO_4 tetrahedra connected at their vertices. (b) One of the six β-quartz-like nets of $Zn[Au(CN)_2]_2$ viewed down its crystallographic *c*-axis; this framework consists of ZnN_4 tetrahedra connected *via* flexible dicyanoaurate (N–C–Au–C–N) molecular linkers. (c) A representation of the net shown in **b** from an alternate view that highlights the honeycomb-like nature of its hexagonal pores and also the cross-bracing effect of helical aurophilic chains running perpendicular to the **c** crystal axis. (d) The mechanism of NLC in $Zn[Au(CN)_2]_2$ involves rapid compression of the aurophilic helices, which is transferred to an expansion of the framework in the **c** direction *via* flexing of the honeycomb-like channels.

4.2 Experimental

Large single crystals of $Zn[Au(CN)_2]_2$ were prepared hydrothermally. Stoichiometric quantities of $Zn(CH_3COO)_2{\cdot}2H_2O$ (Sigma Aldrich, 98%, 14 mg) and $KAu(CN)_2$ (Sigma Aldrich, 98%, 60 mg) were dissolved in H_2O in a teflon-lined reaction vessel (Parr) (23 mL capacity; 10 mL total solution volume). The vessel was sealed and heated to 120 °C for 2 h, and then cooled slowly to room temperature at a rate of 1 °C h^{-1}. The resulting reaction mixture contained large single crystals of $Zn[Au(CN)_2]_2$ (19.9 mg; 54.1%), which formed as colourless bicapped hexagonal prisms as described in Ref. 221. Powder samples were prepared by mechanical grinding of single crystals.

Variable-pressure single-crystal and powder X-ray diffraction measurements were performed in the same way as outlined in Chapter 3. For the powder diffraction studies a wavelength $\lambda = 0.69412$ Å was used and the sample was placed in a stainless steel gasket of an ETH diamond anvil cell together with a single ruby sphere for pressure calibration and a fluorinated oil as pressure transmitting medium. Data were collected at the Swiss-Norwegian beamline at the ESRF as part of experiment HS4434. Diffraction data were collected at six pressure values between 0 and 1.78 GPa for the single-crystal experiments, and at 18 pressure values between 0 and 14.2 GPa for powder measurements.

Refinement of these powder diffraction data was carried out using TOPAS [154]. These data were of sufficient quality only to refine lattice parameters and peak shape profile variables, while making use of (fixed) atomic coordinates as determined using our single-crystal X-ray diffraction measurements. Consequently the fits obtained are not of the same quality as Pawley refinements, but are more meaningful in the sense that a physically-sensible structural model is used to determine intensities. As in previous studies of flexible materials with highly anisotropic mechanical properties, evidence of strong (hkl) dependence in the peak asymmetries was observed [79]. In order to account for this anisotropic strain broadening it was necessary (i) to add to the standard TCHZ peak shape (as defined in Ref. 346) an isotropic broadening term of Lorentzian shape, and (ii) to convolute the resultant peak with an hkl-dependent exponential function in order to

model the observed asymmetry. This asymmetry was evident in some reflections having peak shapes which trailed to high d-spacing and others with peak shapes trailing to low d-spacing.

Variable-temperature single crystal X-ray diffraction measurements were carried out using an Oxford Diffraction (Agilent) SuperNovae diffractometer (MoKα radiation) fitted with a nitrogen cryostream [158]. Data were collected at intervals of 50 K on cooling from 300 to 100 K, at intervals of 20 K on heating from 100 to 400 K, and finally at intervals of 50 K on cooling from 400 to 300 K. Variable-pressure Raman spectroscopy measurements were performed using a membrane diamond anvil cell and a Jobin-Yvon T64000 spectrometer. Variable-pressure Raman spectroscopic measurements were carried out with assistance from D. Maurin and J. Haines (Montpellier). The 676.4 nm line of a Kr^+ laser was used for excitation. The sample was loaded in the cavity of a stainless steel gasket, together with a single ruby chip as pressure calibrant and glycerol as pressure-transmitting medium.

4.3 Results

In the absence of a structural phase transition, it is a thermodynamic requirement that intrinsic volume compressibility be positive [108, 347]. Consequently, the existence of NLC implies stronger positive linear compressibility (PLC) in directions perpendicular to the NLC axis. Indeed it has been shown for simple uniaxial systems that the full mechanical response is determined by (i) framework geometry and (ii) the magnitude of this positive compressibility. So an important consideration for maximising NLC is ensuring that any interactions in these PLC directions are as compressible as possible. In $KMn[Ag(CN)_2]_3$ and the related frameworks of the previous chapter, for example, the relevant motif is a kagome net of Ag...Ag 'argentophilic' interactions. These interactions are already some of the most deformable known, being similar in mechanical strength to the dispersive 'bonds' of solid Xe [348]. So the challenge to the materials chemist becomes how one might engineer a material that is even more compressible than these weakest of interactions, and then translate that large compressibility into extreme NLC behaviour.

The hexagonal crystal symmetry of $Zn[Au(CN)_2]_2$ means that its compressibility is completely described by the pressure-dependence of the a and c lattice parameters. Using a combination of single-crystal and powder X-ray diffraction we observe strong positive compressibility within the (001) crystal plane ($K_a = +52(6)\,\mathrm{TPa}^{-1}$), together with a remarkably strong NLC effect parallel to the **c** crystal axis ($K_c = -42(5)\,\mathrm{TPa}^{-1}$) [Fig. 4.2] [101]. Both effects persist throughout the stability field of the ambient phase ($0 < p < 1.8\,\mathrm{GPa}$). This NLC behaviour is so extreme that the term "giant" is proposed to demarcate NLC behaviour—such as is observed here—that is an order of magnitude

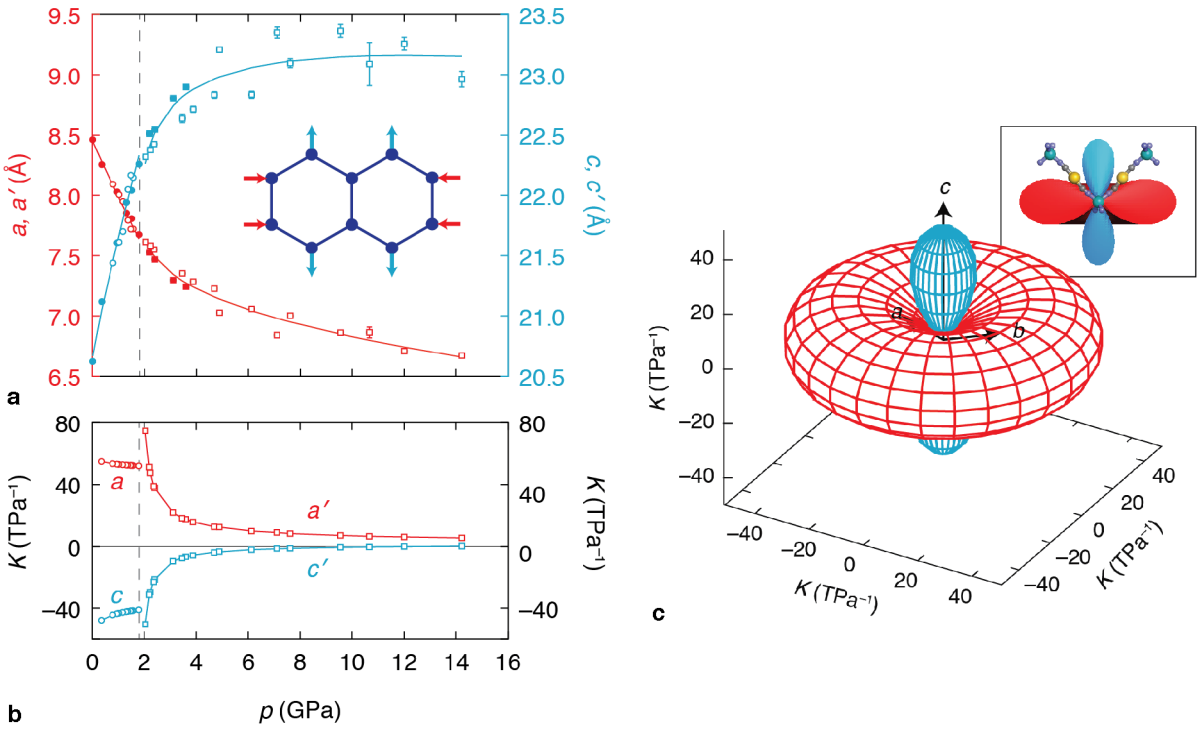

Figure 4.2: The compressibility of $Zn[Au(CN)_2]_2$ is quantified by the variation in crystallographic unit-cell parameters. (a) Lattice parameter changes observed during hydrostatic compression of zinc dicyanoaurate: *a* (red), *c* (blue), single-crystal x-ray diffraction (filled markers), powder x-ray diffraction (open markers), ambient phase (circles) and high-pressure phase (squares). The approximate location of the phase I/II transition is indicated by a dashed vertical line. Reduced lattice parameters $a' = a/2, c' = c/2$ have been used for phase-II data in order to enable direct comparison with phase-I lattice parameters. The inset shows a schematic representation of the compression mechanism for hexagonal honeycomb: compression in one direction (red) is coupled to an expansion in a perpendicular direction (blue). (b) Corresponding lattice compressibilities calculated from the data in (a) for the same pressure range. (c) The compressibility indicatrix of the ambient phase of $Zn[Au(CN)_2]_2$-I, showing the spatial orientation of strong positive and negative linear compressibility axes (colours as above) [101]. The Zn–N–C–Au–C–N–Zn linkages are oriented only along directions for which the uniaxial compressibility vanishes (see inset to (c), which shows a cross-section of the indicatrix on which two representative linkage orientations are superimposed).

stronger than that of the canonical systems described in Chapter 2 (*i.e.*, $K_\ell < -30\,\mathrm{TPa}^{-1}$) [109] and which persists for the *ca* 1 GPa pressure range associated with typical high-pressure applications [343].

4.4 Analysis

As the Zn^{2+} centres occupy special positions within the unit cell [219], and because these positions correspond to the nodes of the quartz-like networks, the geometric response of the framework to increasing pressure is unambiguously determined by the lattice parameter variation. In particular, the volume reduction required thermodynamically is accommodated by narrowing of the honeycomb-like channels parallel to the ⟨100⟩ axes (hence PLC in these directions). This narrowing of channels results in elongation of the crystal along the perpendicular [001] axis by virtue of a well-understood mechanical property of honeycombs (of which the β-quartz net is a three-dimensional analogue)—namely, their large and negative elastic compliance S_{13} that translates horizontal compression into vertical expansion [345]. This effect is conceptually similar to the wine-rack mechanism discussed for $KMn[Ag(CN)_2]_3$; in both cases the assumption is made that compression involves network hinging in preference to deformation of the framework struts.

4.4.1 Geometric origin of NLC

The crystal structure of $Zn[Au(CN)_2]_2$ consists of six interpenetrating β-quartz-like networks. Each net has Zn^{2+} centres as its tetrahedral nodes; these are connected *v*ia almost-linear dicyanoaurate (–N–C–Au–C–N–) linkers, which function geometrically as the framework edges. The similarity to β-quartz as shown in Figure 4.1 is straightforward: Zn^{2+} ions assume the crystallographic sites of Si^{4+} ions, and $[NC–Au–CN]^-$ ions the sites of O^{2-} ions. There is a single Zn atom and one [NC–Au–CN] moiety in the asymmetric unit of the crystallographic unit cell. Like β-quartz itself, $Zn[Au(CN)_2]_2$ crystallises in either one of the two enantiomorphic space groups $P6_222$ or $P6_422$. Each of the six interpenetrating quartz-like nets shares the same handedness, so crystals of $Zn[Au(CN)_2]_2$ are homochiral. This chirality is manifest in the structure in the presence of a number

of helical structural motifs. One such motif concerns the Au$\cdots$Au interactions, whilst a second motif concerns the arrangement of dicyanoaurate linkers surrounding channels *parallel* to the hexagonal axis [Fig. 4.3]. This arrangement is strongly reminiscent of the helical tendon arrays of many limbless tetrapods, squid and octopi [294].

We have seen in the previous chapter that the mechanical response of the $KM[M'(CN)_2]_3$ topology is a direct consequence of geometry. This point can be illustrated with the two simple framework geometries known to give rise to NLC: namely the "wine-rack" (shown previously) and "honeycomb" networks. By extending this analysis a general expression for NLC in the β-quartz topology of $Zn[Au(CN)_2]_2$ can be derived. This approach follows closely the results of Refs. 126 and 345, and was further developed in Ref. 132.

Considering first the two-dimensional honeycomb geometry of Fig. 4.4(a), one finds the following relationship amongst the variables a, c, k, θ:

$$a = 2k\cos\theta, \tag{4.1}$$

$$c = 2k[1+\sin\theta], \tag{4.2}$$

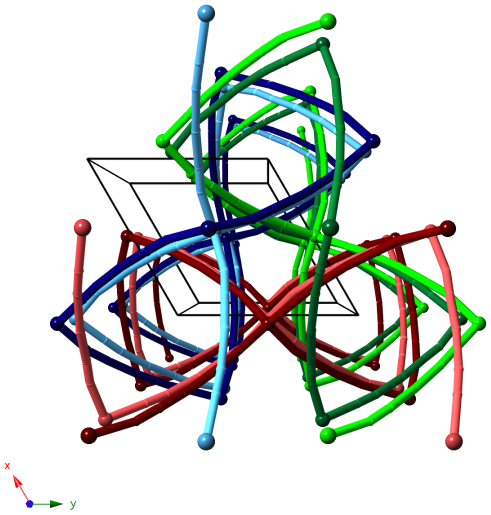

Figure 4.3: The six interpenetrating β-quartz nets of $Zn[Au(CN)_2]_2$ (shown here in various colours) form helical channels parallel to the c crystal axis. The handedness of these helices is determined by the space group chirality.

giving

$$\frac{\mathrm{d}a}{\mathrm{d}p} = -2k\sin\theta\frac{\mathrm{d}\theta}{\mathrm{d}p}, \tag{4.3}$$

$$\frac{\mathrm{d}c}{\mathrm{d}p} = +2k\cos\theta\frac{\mathrm{d}\theta}{\mathrm{d}p}, \tag{4.4}$$

as above. By defining

$$\rho = \frac{c}{a} = \frac{1+\sin\theta}{\cos\theta}, \tag{4.5}$$

one obtains

$$\frac{\mathrm{d}\theta}{\mathrm{d}p} = \frac{2\rho}{\rho^2-1}K_a, \tag{4.6}$$

and hence the result

$$K_c = -\frac{2}{\rho^2-1}K_a. \tag{4.7}$$

So, again, one finds that a positive value of K_a not only implies NLC along the the c-axis but also the magnitudes of the two effects are directly proportional for a given aspect ratio ρ. We note here that the "honeycomb" and "inverse honeycomb" nets are distinguished by positive and negative values of θ, respectively. Within the constraint

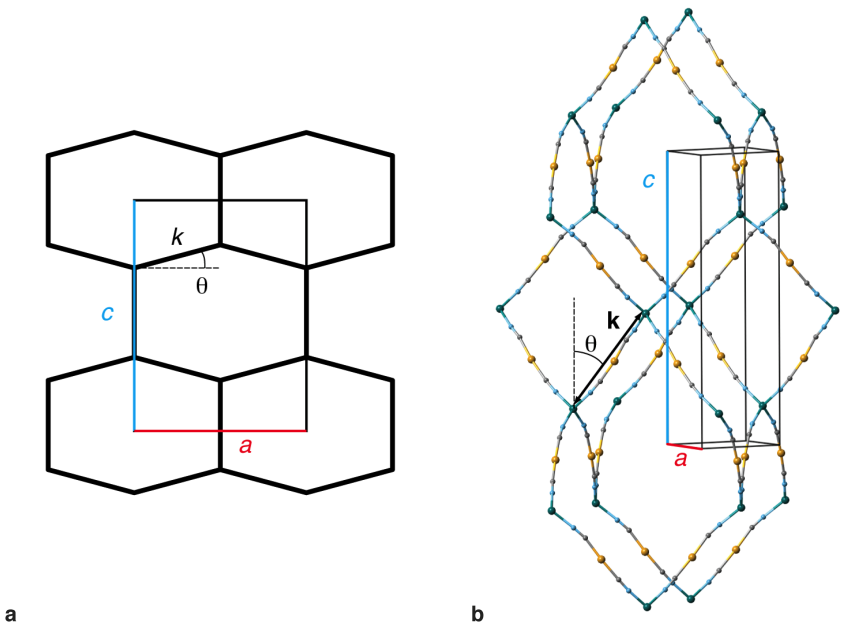

Figure 4.4: Uniaxial network geometries discussed in the text: (a) honeycomb, and (b) β-quartz.

$\theta > 0$ one has $\rho = c/a > 1$ and hence K_c and K_a have opposite signs. By contrast, the inverse honeycomb net gives rise to K_a and K_c values of the same sign (since the prefactor $-2/(\rho^2 - 1)$ is positive in that instance).

Turning to the β-quartz topology of $Zn[Au(CN)_2]_2$, the pair of lattice parameters a, c can be recast in terms of a network vector $\mathbf{k}$ [Fig. 4.4(c)]:*

$$\mathbf{k} = \frac{1}{2}\mathbf{a} + \mathbf{b} + \frac{1}{3}\mathbf{c}. \tag{4.8}$$

The magnitude of this vector

$$k = \sqrt{\frac{3}{4}a^2 + \frac{1}{9}c^2}, \tag{4.9}$$

and the angle θ formed between $\mathbf{k}$ and the unit cell axis $\mathbf{c}$ are sufficient to describe a and c uniquely:

$$c = 3k\cos\theta, \tag{4.10}$$

$$a = \frac{2}{\sqrt{3}}k\sin\theta. \tag{4.11}$$

Following an analysis similar to that above, one obtains the relationship between linear compressibilities

$$K_c = -\frac{27}{4\rho^2}K_a, \tag{4.12}$$

where $\rho = c/a$. Again the magnitude of NLC along $\mathbf{c}$ is directly proportional to the extent of PLC along $\mathbf{a}$.

In order to demonstrate that the above analysis is entirely consistent with our experimental data, we make use of Eq. 1.11 in a three-dimensional uniaxial solid as before:

$$B_0 = \frac{1}{2K_a + K_c}. \tag{4.13}$$

---

* Note the definition used here is equivalent to the (corrected) vector defined in Ref. 231, that is in turn equal to an alternative version used in Ref. 132.

Because K_c and K_a are related via ρ, this means that the experimental values of B_0 ($=$ 16.7 GPa) and ρ ($\simeq 2.8$) can be used to predict an expected value for the magnitude of NLC in $Zn[Au(CN)_2]_2$:

$$K_c = \frac{1}{16.7\,\text{GPa}}\left[1 - \frac{8\rho^2}{27}\right]^{-1} = -45\,\text{TPa}^{-1}. \tag{4.14}$$

The excellent comparison between measured values of K_c and the values anticipated by this expression—as shown in Fig. 4.5—is direct evidence that the compressibility mechanism activated in $Zn[Au(CN)_2]_2$ involves network hinging, but very little network deformation. In other words, the approximation $dk/dp = 0$ holds in this case.

We can be sure that the mechanical behaviour we observe here is indeed a geometric effect and does not involve significant changes to bonding interactions in the solid because the set of directions for which K_ℓ vanishes actually includes the Zn–NC–Au–CN–Zn vectors [Fig. 4.2(c)]. Hence the edge lengths of the covalent network are essentially unaffected by pressure; it is only the network angles that vary. In this sense the geometric response of $Zn[Au(CN)_2]_2$ is similar to that of $KMn[Ag(CN)_2]_3$ and the other "wine-rack" NLC materials, noting that we have found in the case of the latter strut deformation does reduce the predicted magnitude of NLC by $\sim 10\,\text{TPa}^{-1}$.* So the question remains: why

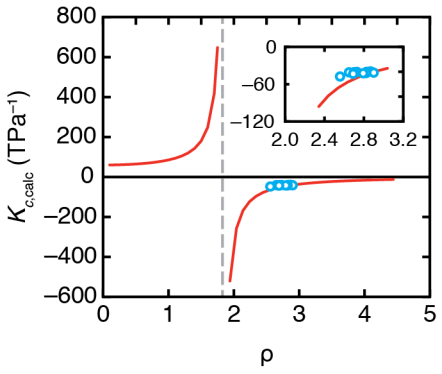

Figure 4.5: Comparison between experimental values of the NLC coefficient K_c and those calculated from Eq. 4.14. (Red line) compressibility in the c direction at arbitrary values of ρ required by the experimental bulk modulus $B_0 = 16.7$ GPa; (blue circles) experimental values.

---

* Here the greater structural integrity of the dicyanoaurate linker is consistent with the known stronger CN–Au bonding due to enhanced back-bonding [177], in contrast to weaker CN–Ag bonding [238].

is NLC so extreme in this particular case?

4.4.2 Supramolecular spring enhancement of NLC

It is proposed that it is the helical nature of the Au···Au interactions that is crucial in driving giant NLC in $Zn[Au(CN)_2]_2$. Just as a steel spring is profoundly more compressible than steel itself, so too might one expect Au···Au helices to be more compressible than the individual interactions. And because it is the repeat length of the helix—rather than the average Au···Au separation—that determines the lattice parameters, the $Zn[Au(CN)_2]_2$ crystal lattice can be more compressible than any of its constituent chemical bonds.

This argument is strongly supported by the results of our variable-pressure crystallographic refinements: (i) the a lattice parameter contracts three times more quickly with increasing pressure than does the average Au···Au distance, and (ii) the helix cross-sectional area (which defines an effective helix radius) increases with increasing pressure as expected for a spring mechanism in compression [Fig. 4.6]. So the extreme PLC effect ob-

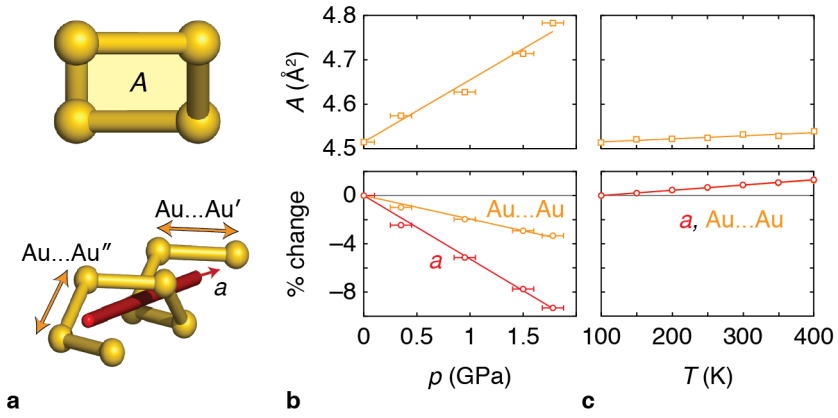

Figure 4.6: Compressibility enhancement in $Zn[Au(CN)_2]_2$ via "spring"-like deformations. (a) By analogy with macroscopic spring mechanics, the crucial structural parameters that describe the mechanical state of the aurophilic helices found in $Zn[Au(CN)_2]_2$ are its pitch (length per turn, given by the lattice parameter a) and its cross-sectional area A. The value of A depends on the magnitude and orientation of the two crystallographically-independent Au...Au vectors, and is independent of the lattice parameters. (b) Under hydrostatic compression, the a lattice parameter decreases approximately three times more rapidly than does the average Au···Au distance; this discrepancy is accommodated by an increase in the cross-sectional area A, allowing a magnitude of compressibility that would not otherwise be attainable. (c) The thermal expansion behaviour of $Zn[Au(CN)_2]_2$ is much more moderate because the entire 'spring' simply expands on heating at the rate expected for aurophilic interactions. The thermal variation in both the lattice parameter a and the average Au···Au separation are shown in the bottom panel but are almost indistinguishable.

served along the ⟨100⟩ directions does not require an equally large change in Au···Au distances because any difference is accommodated by a variation in helix radius [Fig. 4.6(a)]. This situation contrasts that in $KMn[Ag(CN)_2]_3$ where the crystal symmetry demands that the macroscopic PLC behaviour match exactly the average Ag···Ag compressibility [115]. We also find that a spring-like response in $Zn[Au(CN)_2]_2$ is specifically a pressure-induced mechanism, and is not thermally activated: increasing temperature at constant (ambient) pressure simply causes the Au···Au distances, the a lattice parameter, and the cross-sectional area A all to increase at the same relatively modest rate expected for aurophilic interactions [Fig. 4.6(c)] [231, 232].

4.5 Phase transition behaviour

Thermodynamically, the giant NLC observed can not be sustained indefinitely. At a critical pressure $p_c \simeq 1.8\,\text{GPa}$ we observe a displacive transition to a $2 \times 2 \times 2$ supercell of enantiomorphic space group symmetry [Fig. 4.7]. This transition is evident in the emergence of a new set of superlattice Bragg reflections in both single-crystal and powder X-ray diffraction patterns [Fig. 4.8]. The positions of these additional reflections are consistent with phonon-mode softening at the L-point in reciprocal space, corresponding

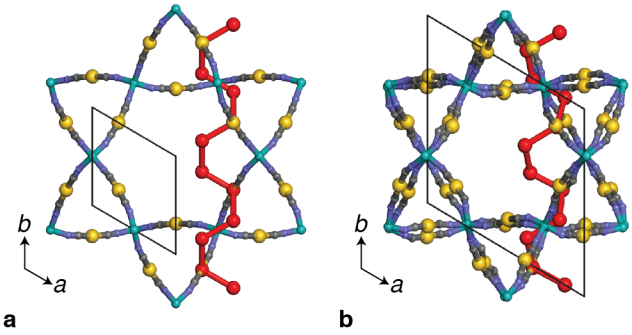

Figure 4.7: Relationship between the ambient (I) and high-pressure (II) phases of $Zn[Au(CN)_2]_2$. (a) The same representation of the *fi*-quartz-like crystal structure of ambient $Zn[Au(CN)_2]_2$ used in Fig. 4.1(b), with the corresponding hexagonal unit cell and one of the aurophilic helices indicated (the latter in red). (b) The high-pressure form $Zn[Au(CN)_2]_2$-II has a unit cell that is doubled along each axis. While the fundamental network connectivity is preserved in the two forms, the high-pressure phase is distinguished by the presence of small concerted tilts of $[ZnN_4]$ tetrahedra that correspond to a soft phonon mode of the parent structure. Aurophilic helices are present in both forms, but are increasingly severely distorted at high pressures.

to a doubling of the hexagonal unit cell along both the **a** and **c** crystal axes. The atomic positions of all atoms in this phase are given in Table C.3.23.

The dominant structural change associated with the transition is a set of small concerted rotations of the Zn-centred coordination tetrahedra associated with mode softening at the Brillouin zone boundary (L-point); in particular there is no change to the network connectivity or crystal symmetry, nor are the lattice strains involved particularly large. The largest difference in relative positions is observed for the Au and C/N atoms, which suggests that vibrational motion within the ambient phase is dominated by transverse displacements of these same atom types. Interestingly, the effect of this transition on the compressibility behaviour of the ambient phase $Zn[Au(CN)_2]_2$-I can be seen in the pressure derivative B' of its bulk modulus: a third-order B-M fit [101] to our $V(p)$ data gives $B' = -1.7(11)$, which indicates that the phase becomes mechanically softer on compression [78, 343]. This softening of vibrational mode frequencies is evident in pressure-dependent spectroscopic measurements, which also reflect the expected symmetry lowering (mode splitting) at the transition pressure (see Appendix C). The pressure dependencies of the phonon frequencies revert to positive values in the high-pressure phase, and a second-order B-M fit ($B' \equiv 4$) describes well the phase-II $V(p)$ data.

The close structural relationship between ambient and high-pressure forms means

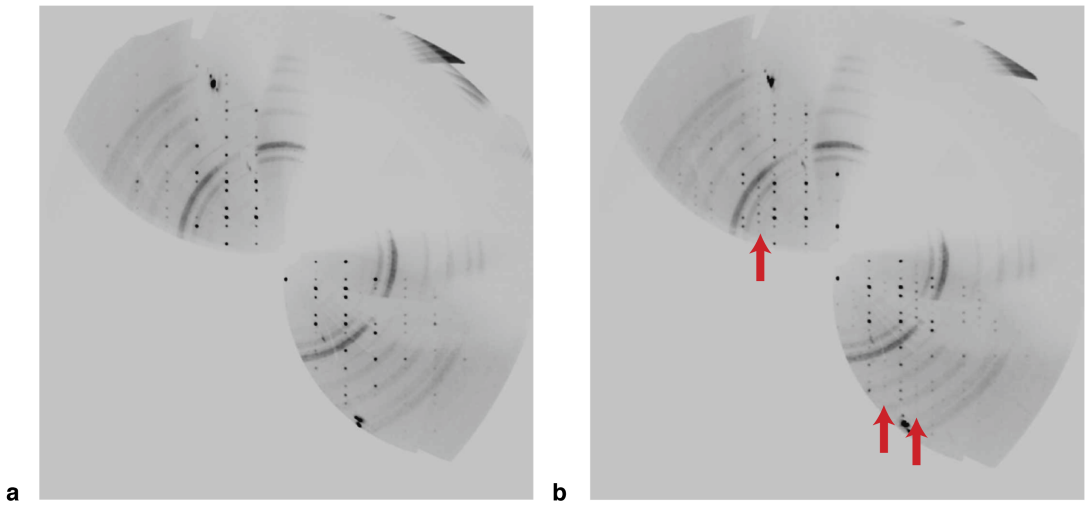

Figure 4.8: Reciprocal space reconstructions for the $(h0l)^*$ scattering plane in $Zn[Au(CN)_2]_2$. (a) Phase I (1.8 GPa, $P6_222$) and (b) Phase II (3.6 GPa, $P6_422$). Positions of new reflections in **b** are highlighted by red arrows.

that the NLC effect we observe at low pressures persists in $Zn[Au(CN)_2]$-II despite the structural transition—albeit at a significantly reduced level ($K_c = -6(3)\,\mathrm{TPa}^{-1}$ for the pressure range $1.8 < p < 14.2\,\mathrm{GPa}$). One generally anticipates a reduction in magnitude of compressibilities at increased pressure, but an additional contributing factor here is the sideways buckling of Au$\cdots$Au helices that likely reduces their effectiveness in accommodating large compressibilities.

4.6 Implications

What has been shown here is that by considering three key structural features negative compressibility has been maximised. First, a suitable geometry of framework ensures that negative response is an intrinsic property as positive response is inextricably linked to a negative response in the perpendicular direction. Whether volume reduction, as is required under increasing hydrostatic pressure, results in negative linear or negative area compressibility is simply a function of geometry [132]. Second, a mechanically rigid linker is used to ensure positive compressibility results in the desired negative response by hinging, and not framework buckling. Here dicyanoaurate appears to be preferable to the dicyanoargentate linker used in our previous studies. Third, positive compressibility must be maximised to increase negative response. Ordinarily dicyanoaurate systems have a less extreme mechanical response due to stronger interactions between Au^+ centres than Ag^+. By using a collective spring-like motif, however, we have engineered a compressibility in the PLC directions that is actually weaker than either of these very weak interactions.

Perhaps the most immediate application of NLC in $Zn[Au(CN)_2]_2$ is as the optical component in interferometric pressure sensors. The combination of large volume compressibility with a *negative* linear compressibility means that giant NLC materials become more dense at the same time as *increasing* their length in one direction. These two responses now interplay synergically to give order-of-magnitude increases in pressure sensitivity [109]. Crucially, $Zn[Au(CN)_2]_2$ is also optically transparent over large spectral regions, including at visible wavelengths [232]. For this specific material, one might also anticipate a strong pressure dependence of its luminescent behaviour, suggesting an

alternate mechanism for optical pressure sensing.

On a fundamental level, there are strong implications associated with understanding the mechanisms of negative compressibility found here. Spiral structures play a crucial role in many biological systems: crossed helical arrays of tendons or muscle respond to increasing internal pressure (negative external pressure) by contracting along the winding axis. Further mechanical amplification gained from linking small changes in cross-sectional diameter to large variations in length means that these are widely-considered to be very efficient biological structures. By analogy, microporous analogues of $Zn[Au(CN)_2]_2$—making use of *e.g.* MOF chemistry [349]—may offer one approach to translating the anomalous mechanical properties of these biological systems into intrinsic material properties: frameworks that contract linearly on guest sorption (*i.e.* 'negative sponges') could find use as nanofluidic actuators or as compensators for undesirable moisture-induced swelling of concrete- and clay-based engineering materials.

Chapter 5

High-pressure phase transition and NLC in $Zn(CN)_2$

5.1 Background

NLC arising as a result of a ferroelastic phase transition is conventionally one of the most widely investigated mechanisms of NLC, however the magnitude of responses are in general very small. Anisotropy arises as a consequence of the phase transition from a high-symmetry (*e.g.* tetragonal) to lower-symmetry (*e.g.* orthorhombic) structure, rather than a framework geometry. If this phase transition is second order (*i.e.* no volume discontinuity), one of the orthorhombic axes must expand as the other contracts [69, 70]. Structurally these phase transitions result in a more close-packed high-pressure structure [65]. In the case of rutile materials, such a high pressure phase is likely related to the $CaCl_2$ structure or defect NiAs-type structure of marcasite (FeS_2).

Consequently there are strong reasons to investigate a high-symmetry molecular framework that has been shown to exhibit large and unusual mechanical responses, arising as a result of low-energy dynamics in the system. As with the proper and improper ferroelastic responses described in §2.2.1, it is expected—but not guaranteed—that any high-pressure transition might be ferroelastic (strain driven) in nature and result in NLC above the transition. Here we explore the piezo-mechanical response of the molecular framework material zinc (II) cyanide, $Zn(CN)_2$.

$Zn(CN)_2$ is the parent compound of the family of most extreme negative thermal expansion (NTE) materials yet discovered [37, 220]. Isotropic NTE (volume reduction on heating), such as that exhibited by $Zn(CN)_2$, remains incredibly rare. Therefore, as a canonical NTE framework material, it has been the focus of many experimental and theoretical studies to determine the structural origins of this unusual response [36, 37, 350].

Despite previous pressure studies on this material, neither the high-pressure phase nor the behaviour above any transition had never before been identified.*

There are two additional reasons for studying $Zn(CN)_2$ under pressure. First, $Zn(CN)_2$ does not undergo any thermally-driven phase transitions across its whole stability range, on cooling to 25 K or on heating to decomposition, *ca* 775 K [37]. In contrast it had been known that the ambient structure is only stable to moderate pressures (up to 0.6–1 GPa; Refs. 343, 351). By identifying structural distortions associated with a phase transitions (the critical response) we can identify the lowest-energy phonon modes in the ambient pressure structure, therefore revealing directly the microscopic origin of NTE response. Secondly the anticuprite aristotype of the $Zn(CN)_2$ structure encompasses materials of incredibly different chemistries—from Cu_2O itself, to $Zn(CN)_2$ and $Cd(CN)_2$, and $Cd(im)_2$ (im = imidazolate). All these materials have particular currency in the field of NTE materials and therefore we address the distinct problem of studying critical behaviour in isostructural frameworks of very different chemistries.

In this chapter I will begin by describing the structure and known mechanical properties of $Zn(CN)_2$ and its relationship to both traditional oxide and metal–organic frameworks. I will then discuss the experimental details and results of our variable-pressure study that reveal, for the first time, the intrinsic phase transition behaviour and NLC behaviour in the high-pressure phase. In the analysis and conclusion, I draw parallels and contrasts to structural analogues of $Zn(CN)_2$, including traditional oxide materials, isostructural $Cd(CN)_2$ and $Cd(im)_2$. These results suggest that the mechanical responses of molecular frameworks are governed heavily by dynamic instabilities of the underlying framework topology.

---

* The study by Chapman *et al.* (Ref. 167) was published back-to-back with our report in *J. Am. Chem. Soc.*, both reporting the structure of $Zn(CN)_2$-II, as detailed here. These studies were carried out completely independently.

5.1.1 Structure and properties of $Zn(CN)_2$

Under ambient conditions $Zn(CN)_2$ adopts the anticuprite structure (space group $Pn\bar{3}m$), in which tetrahedral Zn^{2+} cations are connected *via* linear Zn–C–N–Zn linkages to form a pair of interpenetrating diamondoid networks [176, 352, 353].* The cubic symmetry of this system means that its thermal expansion behaviour is inherently isotropic. On heating, its cubic lattice parameter a (and hence volume V) decreases monotonically [37, 353]. The magnitude of this NTE response can be quantified by the volume coefficient of thermal expansion, $\alpha_V = \frac{1}{V}\frac{dV}{dT}$, taking the value $\alpha_V = -50.7(6)\,MK^{-1}$ over the temperature range 25–375 K [37]. By way of comparison, most materials expand on heating with coefficients of thermal expansion of around $\alpha_V = +30\,MK^{-1}$ [355], so this NTE effect is really very extreme, and is much stronger than that observed for other well-known NTE materials such as ZrW_2O_8 ($\alpha_V = -27.3\,MK^{-1}$; Ref. 356).

The thermodynamic anomaly responsible for driving NTE in systems such as $Zn(CN)_2$ is the existence of a large number of low-energy phonon modes with negative Grüneisen parameters $\gamma = -d\ln\omega/d\ln V$ (*i.e.* modes whose energies decrease with decreasing volume)

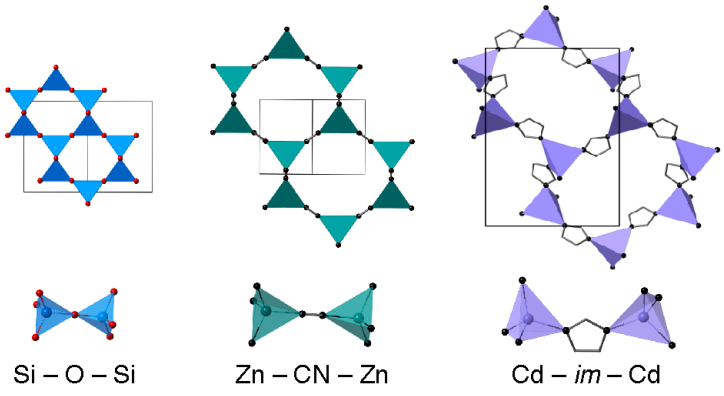

Figure 5.1: Crystal structures and coordination environments of frameworks with anticuprite-like topologies. (left–right) β-cristobalite, $Zn(CN)_2$ and $Cd(im)_2$. A constant scale is used for all diagrams. Both molecular frameworks are in fact doubly-interpenetrated; one of the two networks has been omitted in this representation in order to accentuate the topological similarity amongst the three materials. Formally, the $Zn(CN)_2$ and $Cd(im)_2$ frameworks are topological equivalents of anticuprite (Cu_2O)—itself consisting of two interpenetrating cristobalite nets.

---

* In this space group, the cyanide orientations are disordered throughout the structure such that the C and N atoms cannot be distinguished. The space group assignment has been verified independently by neutron scattering (Ref. 353) and spectroscopic measurements (Refs. 351, 354).

[99]. In the case of $Zn(CN)_2$, previous studies have often focussed on correlated rotations of rigid $Zn(C/N)_4$ tetrahedra as the most likely NTE modes [37, 180, 350, 351, 357]. However, analysis of polarisation vectors obtained in DFT phonon calculations indicate that some poorly-understood translational component is also crucial [358]. In general, the expectation is that the NTE modes involve transverse displacements of the cyanide linkages away from the Zn...Zn axes, resulting in a reduction of the Zn...Zn separation and hence NTE. Because NTE modes decrease in energy with increasing pressure, it is very often the case that pressure-induced mode softening leads to structural phase transitions in NTE materials [94, 359–361]. Identification of the new modulations associated with such a transition then provides insight into the atomic displacements responsible for NTE in the parent phase.

The compression behaviour of ambient-phase $Zn(CN)_2$ is just as anomalous as is its thermal expansivity: in particular, its bulk modulus B_0 decreases with increasing pressure (*i.e.*, the material becomes mechanically softer on compression) and moreover its coefficient of thermal expansion becomes increasingly negative at higher pressures [343]. This pair of observations is fully consistent with a picture in which the phonon modes responsible for NTE in the material are also those that soften most quickly on compression.

There has been remarkably little consensus amongst previous studies concerning the nature of the high-pressure phases of $Zn(CN)_2$. The use of a hydrostatic pressure-transmitting medium (methanol/ethanol/water) produced a completely different series of phase transitions than was observed under non-hydrostatic conditions [351]. By virtue of the complex diffraction behaviour observed, relatively little has been determined other than that the observed transitions involve symmetry lowering (seen also in spectroscopic studies [354]). In preparation for this study, preliminary experiments found strong evidence for reaction of $Zn(CN)_2$ with the methanol/ethanol/water medium, a finding that is consistent with a detailed study of the role of pressure-transmitting media on $Zn(CN)_2$ polymorphism [167] and which almost certainly explains the discrepancies reported elsewhere [351]. Consequently in this work an H_2O-free methanol/ethanol mixture was used

as the pressure-transmitting medium, which did not react with $Zn(CN)_2$.

5.2 Experimental

A sample of finely ground powder of $Zn(CN)_2$ was used as supplied (Sigma Aldrich). Synchrotron X-ray powder diffraction data were collected using the beamline BM01A of the Swiss-Norwegian Beamline, ESRF and all measurements were carried out at room temperature. The data presented here were collected by P. Pattison and V. Dmitriev (ESRF); identical data were also collected in Nov 2012 by A. B. Cairns, A. L. Goodwin, J. Haines, C. Levelut and J. Catafesta as part of experiment HS4434 but these will not be discussed further. An incident wavelength of 0.7092 Å was selected using a Si(111) monochromator, with focussing monochromator and mirror optics providing a focal spot of about 0.5 mm × 0.5 mm which was further reduced with slits to *ca* 0.10 mm × 0.10 mm. The sample was loaded into a ETHZ standard Diamond Anvil Cell (DAC), with a mixture of methanol/ethanol (4:1) as pressure-transmitting fluid and a ruby chip for pressure calibration. All data were collected with the mar345 image plate at a sample-to-detector distance of 250 mm. Initial frame exposure was for 60 s per frame (0–0.83 GPa), and the sample was stationary during the data collection. For data collected at pressures above 1 GPa the exposure time was increased to 180 s per frame. The distance and the detector parameters were calibrated using a LaB_6 reference powder sample; calibration and subsequent integration were performed using FIT2D [153, 362].

Variable-pressure neutron powder diffraction data were collected as a function of neutron time-of-flight using the PEARL diffractometer (ISIS Pulsed Neutron Source, U.K) by M. G. Tucker and A. L. Goodwin in March 2008. Data fitting was carried out for this thesis using the structural model solved from synchrotron diffraction data. A sample of $Zn(CN)_2$ was ground to a fine powder and loaded into and encapsulated TiZr gasket [161]. Deuterated methanol/ethanol (MeOD/EtOD), in the ratio 4 to 1, was added as a pressure transmitting medium and a small lead sphere in the centre of the sample as a pressure marker. The gasket was placed into tungsten carbide (WC) anvils within a Paris-Edinburgh press by applying an initial small loading [363]. Data were collected

at pressures up to 9.3 GPa with clear changes from the cubic ($Zn(CN)_2$-I) to a lower symmetry phase(s) observed between 1 and 2 GPa. Sample pressures were obtained by fitting the measured Pb lattice parameter to the known equation of state for Pb ($\sigma(p) \simeq$ 0.15–0.2 GPa) [364].

Full-structure Rietveld analysis was carried out in each case using GSAS [155] using the EXPGui user interface [365]. At each pressure the background, scale factors, lattice parameters and atomic positions were refined, with a C–N and Zn–(C/N) bond distance restraint used for the high-pressure *Pbca* structure to ensure sensible bond distances in the final solution. Large background subtraction and significant peak broadening terms were required at the highest pressure points. For fitting neutron diffraction, data were modelled with tungsten carbide, nickel and lead as secondary phases to account for background Bragg scattering; the TiZr gasket was alloyed in the correct proportions so as to have an average coherent neutron scattering length of zero, and so did not produce any background Bragg reflections in these data. Representative fits for both x-ray and neutron refinements are shown in Figure 5.3.

5.3 Variable pressure response of $Zn(CN)_2$

The pressure dependence measured for the unit cell parameters of $Zn(CN)_2$ is shown in Fig. 5.2. Considering first the ambient phase, a third-order Birch Murnaghan (B-M) equation-of-state fit to our data gives values for the zero-pressure bulk modulus B_0 and its pressure derivative B' of 36.9(22) GPa and −8.6(13), respectively, that are in good agreement with those reported in Ref. 343 (namely $B_0 = 34.19(21)$ GPa and $B' = -6.0(7)$). This ambient phase is found to persist up to 1.52 GPa, well beyond the phase-transition pressures reported in previous studies using H_2O-containing mixtures as pressure-transmitting media. The value for B' is particularly extreme in comparison other systems that are known to exhibit pressure-induced softening, including $Zn[Au(CN)_2]_2$ (See Chapter 4) and the mineral malayaite, for which $B' = -1.7(11)$ and $-3(5)$, respectively [101, 179, 366].

At a pressure of 1.52 GPa the coexistence of the ambient $Pn\bar{3}m$ phase of $Zn(CN)_2$

with a new phase, termed $Zn(CN)_2$-II, was observed. The diffraction profile of this high-pressure phase is shown in Figure 5.3; the pattern is quite distinct from those reported previously for supposed high-pressure phases of $Zn(CN)_2$ [351], but is fully consistent with the orthorhombic polymorph reported in the independent study of Ref. 167. We were able to index the diffraction pattern using an orthorhombic cell related to the cubic phase by the transformation

$$\begin{bmatrix} \mathbf{a} \\ \mathbf{b} \\ \mathbf{c} \end{bmatrix}_{\text{ortho}} = \begin{bmatrix} 0 & 0 & 2 \\ 1 & 1 & 0 \\ 1 & -1 & 0 \end{bmatrix} \begin{bmatrix} \mathbf{a} \\ \mathbf{b} \\ \mathbf{c} \end{bmatrix}_{\text{cubic}} . \tag{5.1}$$

The observed reflection conditions were consistent with assignment of the orthorhombic space group $Pbca$. Making use of the symmetry relationships between our $Pn\bar{3}m$ and

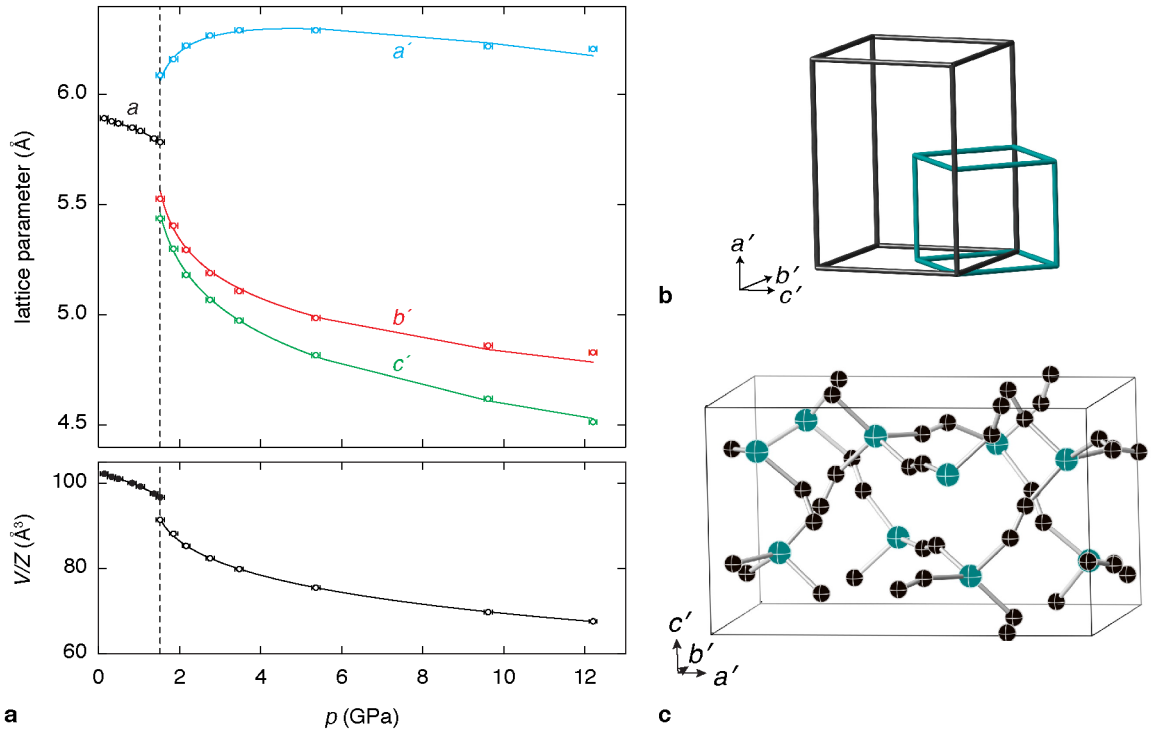

Figure 5.2: Intrinsic high-pressure response and phase transition in $Zn(CN)_2$. (a) Evolution of the cubic (low pressure) and pseudocubic (high-pressure) lattice parameters in $Zn(CN)_2$. The lines show fits to data using a third-order Birch-Murnaghan equation of state in the case of $Zn(CN)_2$-I and empirical Eqs. 5.2 and 5.3 as described in the text in the case of $Zn(CN)_2$-II. The pseudocubic lattice parameters of the high-pressure phase are related to the $Pbca$ lattice parameters by $a' = a/2$, $b' = b/\sqrt{2}$ and $c' = c/\sqrt{2}$. (b) The relationship between the ambient-pressure unit cell (turquoise cell) to the high-pressure, $Pbca$ cell (black cell). The refined structure of $Zn(CN)_2$-II is shown in (c).

Pbca cells a starting model for the structure of $Zn(CN)_2$-II was proposed (Figure 5.2 b,c), from which Rietveld refinement was possible for all synchrotron X-ray data collected at pressures $1.52 < p < 12.2\,\mathrm{GPa}$. Representative fits are shown in Figure 5.3; fits to data for all pressures are given in §C.4. The lattice parameters obtained for this phase at 1.85 GPa (the first pressure point for which no scattering contribution from the ambient $Pn\bar{3}m$ phase was evident in our data) are $a = 12.3212(18)$ Å, $b = 7.6438(9)$ Å, $c = 7.4947(10)$ Å; corresponding atomic coordinates are listed in Table 5.1. For the data collected at the critical transition pressure $p_c = 1.52\,\mathrm{GPa}$ itself, we were able to refine unit cell parameters for both phases (central panels of Fig. 5.3): $V(Pn\bar{3}m)/Z = 193.515(22)$ Å^3

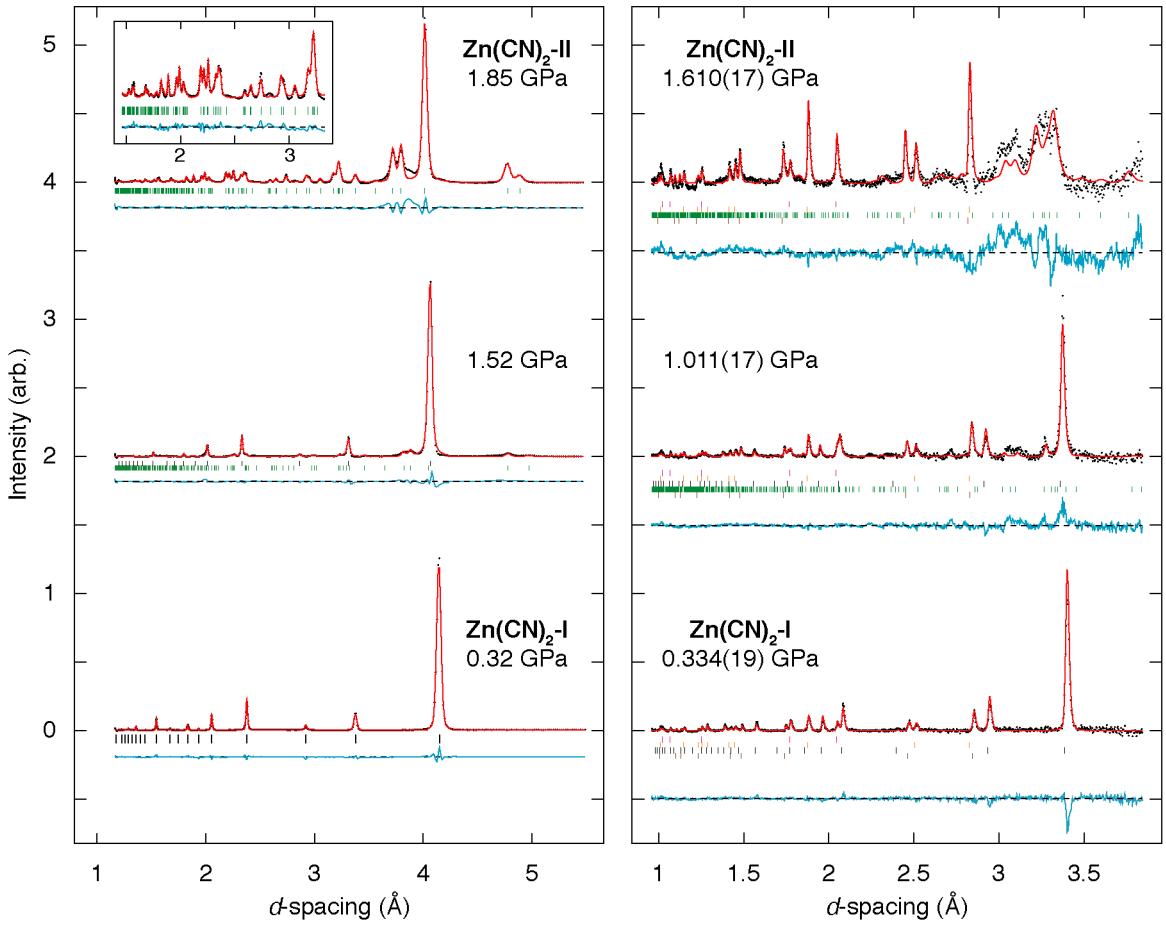

Figure 5.3: Rietveld refinements of powder X-ray and neutron diffraction data for $Zn(CN)_2$ under hydrostatic pressure. *left* Synchrotron X-ray powder diffraction data ($\lambda = 0.7092$ Å) and *right* powder neutron diffraction data collected on PEARL at selected pressure points corresponding to the ambient, mixed and high-pressure phases in each case. Rietveld fits to data are shown in each case. Experimental data are given as points, the fitted profile as a solid red line, and the difference (data−fit) as a blue line, displaced downwards in each case.

and $V(Pbca)/Z = 182.98(27)\,\text{Å}^3$, suggesting a volume collapse of *ca* 5% provides the necessary $p\Delta V$ free energy driving force responsible for the transition. The existence of such a volume discontinuity would suggest the transition is first order in nature.

The pressure dependence of the lattice parameters of $Zn(CN)_2$-II is shown in Figure 5.2. Unlike the ambient phase, this high-pressure phase stiffens at higher pressures. Despite this expected curvature of the $p(V)$ function, the data are not well represented by a second-order B-M equation-of-state ($B' \equiv 4$). Fitting to a third-order B-M equation-of-state fit is possible, but a very large correlation between B_0 and B' prevents robust values from being determined. What can be concluded is that $Zn(CN)_2$-II is initially mechanically very soft on formation, but that the framework stiffens rapidly on further compression with $B' \gg 4$.

Considering the linear compressibilities of the unit cell axes (and noting that these are coincident with the principal axes for this system), the anomalous behaviour is observed along **a**: on compression from $p_c = 1.52\,\text{GPa}$, NLC is observed and continues until a pressure of *ca* 5 GPa, above which positive linear compressibility (PLC) behaviour is observed. In the high pressure phase, empirical fits were used of the form:

$$\ell = \ell_0 + \lambda(p - p_c)^\nu \tag{5.2}$$

for b and c, and of the form:

Table 5.1: Atomic coordinates and isotropic atomic displacement parameters in $Zn(CN)_2$-II determined by Rietveld refinement against X-ray powder diffraction data collected at 1.85 GPa. The atom labels "(C/N)" refer to sites with occupancy $C_{0.5}N_{0.5}$ and reflect the cyanide orientational disorder present in the compound.

Atom	x	y	z	U_{iso} (Å^2)
Zn1	0.1255(12)	0.0510(8)	0.7872(10)	0.069(4)
(C/N)1	−0.020(3)	0.118(4)	0.288(7)	0.079(9)
(C/N)2	0.0378(27)	0.236(4)	0.301(7)	0.079(9)
(C/N)3	0.2397(27)	0.018(7)	0.619(4)	0.079(9)
(C/N)4	0.286(4)	0.033(7)	0.487(4)	0.079(9)

U_{iso} values for (C/N) were constrained to be equal.

$$\ell = \ell_0 + \lambda(p - p_c)^{\nu} + \beta p \tag{5.3}$$

for *a*. The incorporation of an additional linear term in p allows fitting of the NLC/PLC transition (fits to data are shown in Figure 5.2). Compressibilities calculated for the *b* and *c* directions are well described across the whole stability range of $Zn(CN)_2$-II, taking median values of $K_b = +11.2\,\mathrm{TPa}^{-1}$ and $K_c = +16.8\,\mathrm{TPa}^{-1}$. Considering the behaviour along *a* up to $\sim 5\,\mathrm{GPa}$, $K_a = -2.08\,\mathrm{TPa}^{-1}$. This extreme negative mechanical response is comparable to materials showing the most extreme NLC known, and is much greater than NLC response found due to strain-driven (ferroelastic) phase transitions in canonical rutile systems (*e.g.* for NiF_2, $K_{\mathrm{NLC}} = -0.48\,\mathrm{TPa}^{-1}$; Table 2.1). However this response is only accessible at elevated pressures (as a consequence of symmetry breaking transition), therefore it is unlikely to be suited to application.

5.4 Mechanism of NLC in $Zn(CN)_2$-II

Proper ferroelastic phase-transitions have been well characterised as giving rise to NLC responses due to the second-order nature of the symmetry breaking transitions (§2.2.1). For $Zn(CN)_2$ there is clearly a volume discontinuity of around 5% in the variable-pressure data that suggests that the response is first-order, as well as symmetry-breaking. This transition is therefore classed as 'improper' ferroelastic, where spontaneous strain is no longer the primary order parameter responsible for driving the phase transition [251]. Instead ferroelastic strain develops *via* coupling to an alternate— dominant—symmetry-breaking mechanism, such as a phonon instability [367]. The theoretical consideration of symmetry lowering in cubic crystals is valid for both first- and second-order phase transitions and under changes in temperature and pressure, it is expected that there will be a divergence of lattice parameters at the critical points [367]. The Landau conditions change in these situations such that volume discontinuities may be observed, and so there is no strict guarantee of NLC. Nevertheless if the volume collapse on symmetry lowering is small with respect to the subsequent evolution of ferroelastic spontaneous strain, then

NLC may indeed arise.

In Figure 5.4(a) the relationship between the ambient cubic structure of $Zn(CN)_2$ and the high-pressure phase, $Zn(CN)_2$-II is shown. The corresponding atomic displacements involve correlated rotations of connected pairs of $Zn(C/N)_4$ tetrahedra, resulting in coupled expansion/contraction of the crystal lattice perpendicular to the rotation axis in much the same way as described for the rutile-structured systems discussed in Chapter 2 [205]. NLC persists in the high-pressure $Zn(CN)_2$-II phase from the I/II transition at 1.52 GPa up to ∼5 GPa and is reasonably strong over this entire pressure range: $K_{\mathrm{NLC}} = -2.08\,\mathrm{TPa}^{-1}$ and $\chi_K = 0.724\%$.

Structurally, the origin of this unusual behaviour arises due to considerations of packing and coordination. The transition results in a higher-density structure (shown by the

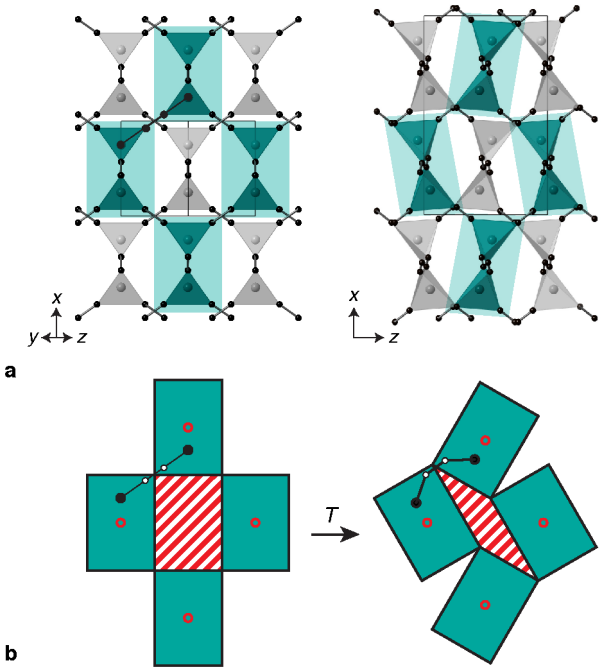

Figure 5.4: The first-order phase transition between $Zn(CN)_2$-I (left) and $Zn(CN)_2$-II (right) involves concerted rotations of columns of [$Zn(C/N)_4$] tetrahedra (a) These rotations occur about an axes that run parallel to ⟨110⟩ directions of the $Pn\bar{3}m$ cell and which pass the midpoints of neighbouring tetrahedra. In this plan view, these displacements take the form of rotations of connected pairs of tetrahedra—as indicated by the shaded regions in the right-hand panel—and as such involve translations of the Zn atoms along the horizontal axis. These concerted rotations give rise to NLC in the ferroelastic phase. (b) The displacement pattern observed on pressure collapse also describes the key NTE modes of the ambient $Zn(CN)_2$-II phase. The rotations shown in (a) give rise to transverse displacements of CN bridges away from the originally-linear Zn–CN–Zn axes, resulting in a contraction of the Zn...Zn separation and a reduction in the extra-framework free volume (shaded region).

reduction in the extra-framework free volume, shaded area) and appears to involve concerted rotations of columns of $[Zn(C/N)_4]$ tetrahedra about axes parallel to the cubic $\langle 110 \rangle$ directions. The axis of rotation does not pass through the centres of individual tetrahedra, but rather through the midpoints of connected pairs of tetrahedra, such that the Zn centres are translated in a direction perpendicular to the rotation axis. These concerted rotations of pairs of tetrahedra cause the "folding-up" of the structure, as shown in the next section, but also the increase in Zn...$\widehat{\text{Zn}}$...Zn angles that contribute to changes along the a' axis in the pressure range $1.52 < p < 5\,\text{GPa}$.

In competition with any ferroelastic NLC mechanism is the tendency for framework buckling, which favours PLC and becomes increasingly important at higher pressures [128]. Switching (NLC/PLC) behaviour is not without precedent in the broader family of molecular frameworks, where the interplay between geometric flexing and bond compression mechanisms is known to allow transitions [128]. It can however be shown that, despite these variations in one lattice parameter, there is a smooth decrease in Zn...(CN) distances such that the high-pressure structure approaches a closer packed structure based on pseudo-octahedral $Zn(CN)_6$ units [Fig. 5.5]. This new structure is directly related to that of the brookite polymorph of TiO_2. As the Zn coordination number progressively increases from four to six, and the resulting volume reduction becomes increasingly significant with respect to the NLC effect of correlated tilts, such that the crystal axis along which NLC is initially observed begins to contract for pressures higher than 5 GPa. Such crossover between NLC and PLC behaviour might be expected to be a reasonably general phenomenon at sufficiently high pressures [128].

5.5 Mechanism of NTE in $Zn(CN)_2$

The phase transition observed for $Zn(CN)_2$ under pressure gives rise to NLC, but has perhaps a much greater significance in shedding light on the mechanism of NTE that has remained unknown. Both computational studies and inelastic neutron spectroscopy measurements point to the existence a large family of soft phonon modes—many of which are implicated in the strong NTE behaviour [36, 37, 342, 358]—but none of these have

been definitively shown as driving the negative thermal expansion response. We have shown that hydrostatic compression to 1.52 GPa results in a first-order displacive phase transition to a denser orthorhombic structure, which is consistent with the condensation of at least one zone-boundary soft mode [167, 205]. Crucially this mode involves Zn translations as well as RUM-like rotations.

Figure 5.4 also illustrates the primary static distortion associated with the I/II phase transition. The implication here is that the key NTE modes of $Zn(CN)_2$-I involve dynamic translations of $Zn(C/N)_4$ tetrahedra in addition to the rotational modes already identified elsewhere [37, 357]—an observation that is fully consistent with the density functional theory (DFT) and neutron spectroscopy results that implicate the transverse acoustic modes in driving NTE [209, 357, 358]. Why this displacement pattern should give rise to NTE is also clear: Zn...Zn separations are reduced as the CN ions translate in a perpendicular direction to the Zn...Zn vectors [Fig. 5.4(b)].

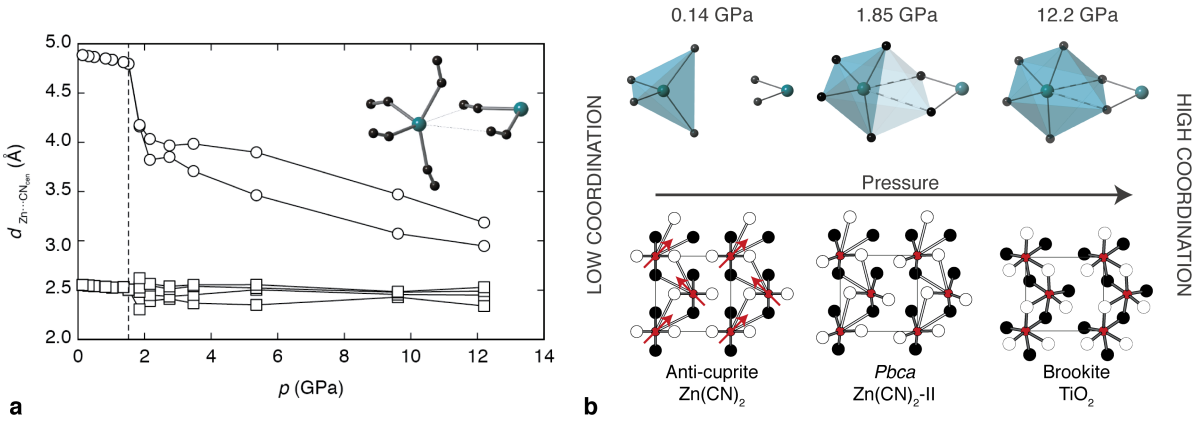

Figure 5.5: Pressure dependence of Zn–CN centroid separations in $Zn(CN)_2$. (a) In the anticuprite $Zn(CN)_2$-I phase there are four well-defined nearest contacts which correspond to the $[Zn(C/N)_4]$ coordination polyhedra. Compression of the $Zn(CN)_2$-II phase does not involve significant changes in these four coordination distances. Rather, two further CN units approach increasingly closely, reflecting a systematic transition toward octahedral coordination, as suggested by the anticuprite–brookite mechanism illustrated. (b) *top* The increase in $Zn(CN)_2$ coordination environment by increasingly close approach of two next-nearest neighbour (CN) molecules (centroids only shown). *bottom* The correspondence between anticuprite and brookite structures involves association of originally tetrahedral cations with two anions from a single neighbouring tetrahedron to form connected chains that run perpendicular to the long a axis of the *Pbca* cell (drawn perpendicular to the *a* axis). Cations are shown as filled red circles and anions as open and filled black circles (positive and negative out-of-plane displacements, respectively, relative to cation positions). The square regions drawn here are guides to the eye but do have the same dimensions as the (100) face of the *Pbca* cell.

The group–subgroup relationship observed for the two phases $Zn(CN)_2$-I and -II is not consistent with the softening of a single mode of the parent structure [368]. Consequently there is a possibility that the transformation occurs *via* an intermediate phase, although there is no experimental evidence for such a phase in our diffraction measurements. Indeed, even in the single data set (collected at a pressure of 1.52 GPa, Fig. 5.3) where both phases I and II coexist there is no unaccounted-for diffraction intensity. In light of the fact that the methanol/ethanol pressure-transmitting medium is still well within its hydrostatic regime at this pressure, this phase coexistence (which itself is likely a feature of relatively slow transformation kinetics) rules out the existence of a third, intermediate, phase.

That such a dynamic distortion might be responsible for the negative thermal expansion of zinc cyanide would not be immediately obvious without identifying its intrinsic critical behaviour. This mode is one of many possible rigid-unit modes (RUMs), but is not one of the simpler distortions considered previously [36, 180], whilst also being fully consistent with the transverse vibrational modes (TVMs) that have been previously observed directly from single-crystal [37] and total-scattering data [350]. Hence it was imperative to identify the intrinsic high-pressure response to untangle previous reports; our findings have subsequently been confirmed by the independent DFT studies or Ref. 342.

5.6 Homologous critical behaviour in $Zn(CN)_2$ and $Cd(im)_2$

The displacive phase transition and dynamical response of $Zn(CN)_2$ led us to consider further these mechanical responses in more complex metal–organic (MOF-like) materials. In the introduction the great importance in understanding displacive phase-transition behaviour of oxide-based materials was highlighted, but there is an emerging realisation that molecular frameworks might display an equally rich set of behaviours. Developing rules—similar to the rules developed to understand, for example, the properties of perovskites—is critical to the future intelligent design of frameworks that might show

multiferroicity, order–disorder transitions and glassy behaviour [193, 194, 369]. Chemical versatility adds significant complexity here, however, and so 'rules' may quickly become intractable. Here we can draw parallels to the dense metal–organic framework cadmium (II) imidazolate Cd(im)$_2$, which is isostructural to Zn(CN)$_2$-II.

The compression mechanism of Zn(CN)$_2$-II on increasing pressure and the collective reorganisations within Cd(im)$_2$ that occur on cooling* both reflect a systematic transition away from the anticuprite geometry toward a brookite-like arrangement. That the anticuprite and brookite structures should be related by a relatively small and accessible set of atomic displacements is perhaps not immediately obvious. The general form of these displacements is illustrated in Figure 5.5. Starting from the anticuprite structure, the cations move in a concerted manner toward a single edge of their tetrahedral coordination environment—the resulting position corresponds to the octahedral sites of the brookite structure. As an aside, we note that a similar mechanism (operating in reverse) has been observed for framework expansion in rutile–TiO$_2$ under negative pressure to give a tetrahedral TiO$_2$ net with the anticuprite topology [370].

By forming the vector dot product of the cation/anion displacements away from

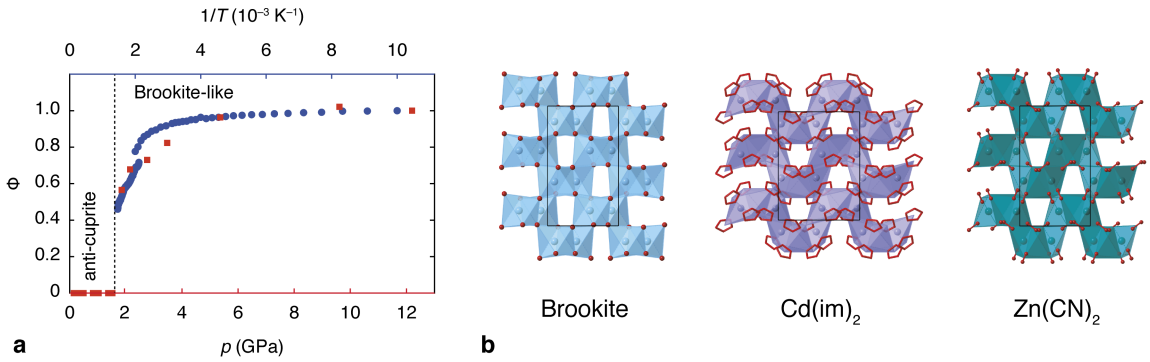

Figure 5.6: Pressure and temperature-evolution of the anticuprite/brookite order parameter for Zn(CN)$_2$ and Cd(im)$_2$. (a) Variation of the anticuprite/brookite order parameter ϕ with increasing pressure (Zn(CN)$_2$; red squares) and decreasing temperature (Cd(im)$_2$; blue circles). (b) The unit cell symmetry and positional coordinates of both Zn(CN)$_2$-II and Cd(im)$_2$ are related to those found in the brookite polymorph of TiO$_2$. The Zn/Cd coordination environments in the former compounds are extended to include two additional nearby ligands parallels the octahedral Ti^{4+} coordination in brookite.

---

* Variable-temperature study on Cd(im)$_2$ carried out by Ines Collings with the homologous critical response analysis developed collaboratively. For more details on these experiments see Ref. 205.

the ideal $Pn\bar{3}m$ sites with those observed in brookite itself, we can calculate an anticuprite/brookite order parameter ϕ for $Zn(CN)_2$ and $Cd(im)_2$. The value of ϕ is equal to zero for the ideal anticuprite geometry (i.e., no brookite-like displacements) and assumes increasingly large and positive values as the structures become more brookite-like. The evolution of ϕ with increasing pressure ($Zn(CN)_2$-II) and decreasing temperature ($Cd(im)_2$) is illustrated in Figure 5.6, where we have normalised the values such that $\max(\phi) = 1$ for each data set. The similarity in critical behaviour between the two systems is clear.

The drive toward brookite-like packing at high pressures and low temperatures can be viewed in two lights. On the one hand, there is the potential to increase the coordination number of the central cation as a means of improving packing efficiency (noted above) and maximising lattice enthalpy. An analysis of the pressure dependence of Zn...CN distances in $Zn(CN)_2$-II indicates a clear progression toward 6-fold coordination at high pressures that is associated with cation off-centering within the $[Zn(C/N)_4]$ tetrahedra [Fig. 5.5]. A similar off-centering mechanism was recently identified in $Cd(CN)_2$—discussed further in the following chapter—and we note here that the 'ice rules' that govern Cd^{2+} displacements in that material are also obeyed in the anticuprite/brookite transition observed here for $Zn(CN)_2$, shown in Figure 5.5(b) [29]. On the other hand, there is the simple consideration of packing efficiency of bulky anions. The anion arrangement in the $Pn\bar{3}m$ aristotype consists of square arrays; that in brookite are close packed. Whereas the focus within framework chemistry is often (rightly) on the topological bonding connectivity of particular framework structures, what this observation highlights is that the physical packing arrangements might also play an important role in determining dynamical and mechanical response.

5.7 Implications

Two main conclusions can be drawn from our pressure investigation of zinc (II) cyanide, a remarkable material with unusual and intriguing properties. Of greatest interest to the field as a whole is the insight gained into the mechanism of NTE by identifying the intrinsic

phase transition behaviour. Not helped by a previous contradictory report on the phase transitions under pressure, conflicting results from structural, inelastic spectroscopic and DFT measurements left the mechanism of NTE largely unknown. We have resolved these issues by finding the true intrinsic phase transition and relating this to the RUM-like description used in many previous studies. Critically the distortions identified involve metal centre translations as well as rotations, consistent with INS and DFT studies.

Second, negative linear compressibility has been identified immediately following the phase transition. This response is improper-ferroelastic in nature, where the strain-driven order parameter is coupled to the symmetry-breaking mechanism that results in volume collapse. The mechanism of response is related to the rotations of coupled tetrahedra (as in the NTE response) that is strongly reminiscent of the rutile ferroelastic NLC mechanism. These distortions drive the structure towards a closer-packed structure that is related to the brookite polymorph of TiO_2 at the highest pressures, highlighting the importance of packing even in molecular framework systems. Further work on the pressure response of rutile-structured and rutile-related frameworks is a clear avenue for further investigation.

Finally we have demonstrated—by considering both $Zn(CN)_2$ and isostructural $Cd(im)_2$—that topology plays a vital role in determining dynamic properties as a consequence of similar dynamical instabilities. This is just as in traditional functional ceramic materials such as perovskites where key structural instabilities (such as octahedral tilting) are known to be key in understanding functional properties. This is one example and further work is required to show if framework materials can be considered 'mineralomimetic' (*i.e.* they mimic the response of minerals) and that simple 'rules' of flexibility exist based purely on topology.

Chapter 6

Structural disorder in molecular framework materials

Through the preceding chapters we have explored mechanical and displacive degeneracy in cyanide materials: for our studies investigating large NLC large mechanical flexibility is key, whilst for $Zn(CN)_2$ displacive modes drive the unusual mechanical responses. Here we continue to explore degeneracy but switch focus to configurational degeneracy, a theme that will be continued into the following chapter. In Chapter 1, we saw how both structural over- and under-constraint gives rise to disordered, configurationally degenerate, states of matter.

These disordered states are often complex and difficult to interpret, especially with scattering techniques, and so do not receive much attention in some fields of research. In contrast to areas of active research into disordered states—such as in frustrated magnetism [14]—disorder has been considered something to be avoided in molecular frameworks, despite evidence that it does play an important functional role some materials [202]. This paradigm is rapidly changing with growing interest in disordered states: for example the possibility of multiferroic frameworks [193, 371, 372], the role of asymmetric anions in the photovoltaic lead halide perovskites [169], and topologically disordered MOFs promising to revolutionise glass science [190, 373, 374] are just three examples. This chapter aims to review the few established, well-characterised disordered molecular framework materials to rationalise our understanding of these states.

The term "disorder" can be unhelpful because it is taken to encompass a very large number of different phenomena [242]. Here four specific aspects are highlighted—topological, static, dynamic, and low-dimensional disorder [Fig. 1.32(d)]—so chosen for their relevance to the key studies in the field. We explain what we mean by each of these in turn, with the four topics assuming a thematic role for each the four main sections that follow. Where

appropriate, discussion of relevant additional experimental techniques, computational approaches, and theoretical models used to characterise and interpret these various types of disorder is included. This chapter concludes with a brief discussion of some interesting examples of disorder that do not obviously fit into the four principal categories, and I give a personal perspective on how this field might continue to develop over the coming years.

6.1 Types of disorder

6.1.1 Topological disorder

The existence of framework topologies with well-defined local geometries but with no long-range periodicity has been recognised for many decades. Perhaps the canonical example is that of silica glass (a-SiO_2). The existence of an amorphous state of silica is attributed to the accessibility of a "continuous random network" (CRN) phase [24], in which all of the Si and O atoms adopt nearly-ideal bonding geometries—hence the lattice enthalpy is comparable to that of the crystalline SiO_2 polymorphs—and yet the network itself does not exhibit any long-range structural periodicity [Fig. 6.1(a)] [375]. Indeed the CRN model is the basis of much of our understanding of glassy systems, including the amorphous allotropic forms of group 14 elements such as silicon and germanium as discussed in Chapter 1. Entropy is thought to play a key role in stabilising these networks, for the simple reason that there are many more CRN-type configurations than there are ordered networks of comparable lattice enthalpies. Because there is no pathway for converting a CRN phase such as a-SiO_2 into any crystalline polymorph without making and breaking bonds, and because CRNs are aperiodic (they have no unit cell), such systems can be said to be *topologically* disordered.

From an experimental viewpoint, the absence of long-range structural periodicity in topologically-disordered systems has a number of observable consequences.

(i) Their X-ray, neutron and/or electron diffraction patterns do not contain any Bragg reflections but consist instead of a smoothly-varying diffuse scattering contribution that has no orientational dependence.

(ii) The absence of translational periodicity removes vibrational selection rules; consequently all vibrational modes of a topologically-disordered solid are both Raman and infrared active.

(iii) Such materials are inherently isotropic—*i.e.* their physical properties have no orientational dependence. This includes mechanical properties (bulk and shear moduli, thermal expansivities) and optical properties (absorption, refraction) alike.

It is likely that topologically-disordered molecular frameworks have been synthesised by many groups for many years, but it is only relatively recently that well-characterised examples have appeared in the literature [374]. This disconnect is almost certainly due

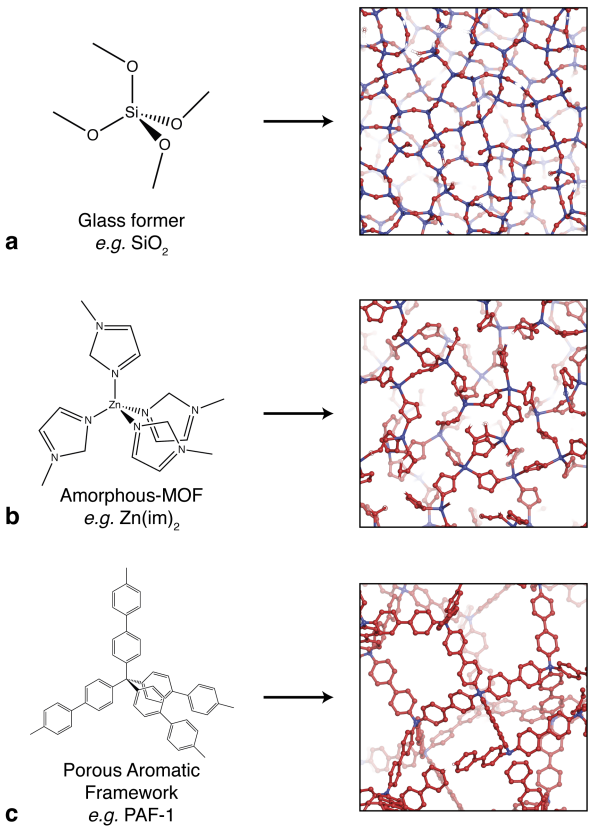

Figure 6.1: Continuous random network structures of amorphous framework materials. (a) The CRN phase of silica consists of tetrahedrally-coordinated Si atoms connected *via* O atoms with approximately-ideal O–Si–O and Si–O–Si angles [375]. (b) Substitution of the Si and O atoms in this CRN by Zn and imidazolate species, followed by suitable expansion of the network to give reasonable bond lengths, yields a CRN of composition Zn(*im*)$_2$ that can be refined successfully against neutron and X-ray PDF data [190]. (c) The same CRN can be used to build a candidate model for the structure of PAF-1. The accessible surface area calculated using this model agrees well with the experimental density and with N_2 sorption measurements [376].

to the experimental difficulty of characterising amorphous frameworks: their chemical composition, phase purity, and density are often difficult to determine; moreover, it is only relatively recently that robust X-ray PDF methods have become accessible to the materials chemist [156]. The particular case of zeolitic imidazolate frameworks (ZIFs) has gained much prominance—a family of molecular frameworks which have been well-studied both for their high thermal and chemical stabilities and for their promising applications as gas-storage candidates [189]. The structural chemistry of ZIFs is straightforward: tetrahedrally-coordinated dications (usually Zn^{2+} or Co^{2+}) are linked *via* imidazolate (im^{-}) or substituted imidazolate linkers. The Zn–*im*–Zn angle is similar to the Si–O–Si angle in silica polymorphs, and so ZIFs can adopt many of the network topologies found in (alumino)silicates—including porous zeolite-like structures.

On heating to temperatures of *ca* 300 °C, a number of porous crystalline ZIF polymorphs undergo a framework collapse that results in the adoption of a common dense topologically-disordered phase with the same $Zn(im)_2$ composition as the crystalline precursors [190, 377]. This temperature-induced amorphisation (TIA) process can be monitored using optical microscopy (the originally anisotropic crystallites become isotropic) and/or using diffraction methods (the Bragg peaks vanish and are replaced by a smoothly-varying diffuse scattering pattern) [Fig. 6.2]. The amorphous "*a*-ZIF" phase so formed is metastable and can be recovered to ambient conditions. Mechanical measurements performed on recovered samples also reflect the loss of mechanical anisotropy expected for a topologically-disordered material. Subsequent heating to *ca* 400 °C gives rise to a second transformation: this time from the amorphous ZIF phase to the densest of the known crystalline ZIF polymorphs, ZIF-zni [190]. The identical composition of initial and final crystalline compounds unambiguously identifies the composition of the disordered intermediate.

There is strong experimental evidence from neutron and X-ray PDF measurements to support an interpretation of the structure of *a*-ZIFs in terms of the same CRN model applied to model systems such as *a*-SiO_2 [Fig. 6.1(b)] [190]. High-resolution neutron PDFs

indicate that the local coordination environment in *a*-ZIFs is essentially identical to that found in the corresponding crystalline ZIF polymorphs [Fig. 6.2]. Moreover, the variation in PDF peak intensity with increasing distance shows remarkable qualitative similarity to that observed in *a*-SiO_2 (taking into account the necessary change in length scale associated with the replacement of Si–O–Si linkers by Zn–*im*–Zn linkers). But perhaps most crucially, a model of the structure of *a*-ZIF derived from the SiO_2 CRN can actually be refined quantitatively against the experimental neutron and X-ray PDF data—such a fit is carried out in a similar fashion to the way in which *e.g.* Rietveld refinement against powder diffraction intensities might be performed. That analogous refinements

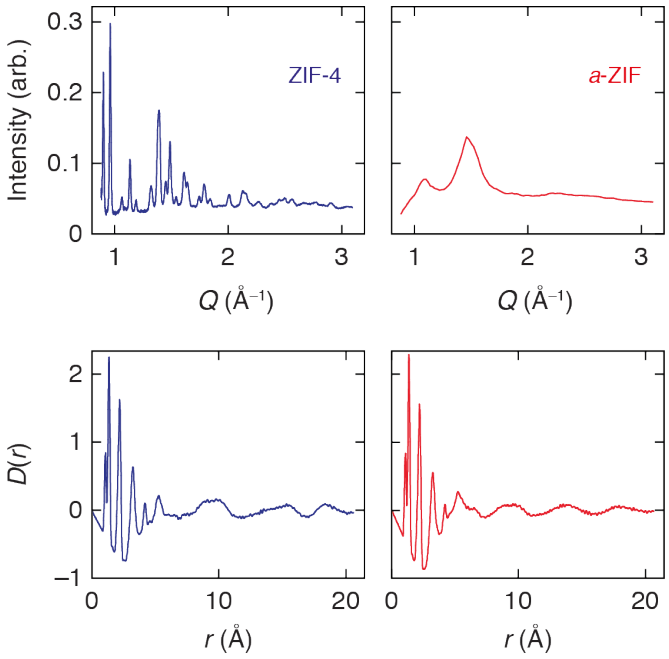

Figure 6.2: The diffraction behaviour of topologically-disordered materials. The top panels show experimental neutron diffraction data collected for (left) the crystalline ZIF-4 polymorph and (right) the amorphous *a*-ZIF phase with identical composition. During TIA all of the sharp Bragg diffraction peaks observed for ZIF-4 (measured here as a function of scattering vector $Q = 4\pi\sin\theta/\lambda$) are successively replaced by broad diffuse scattering features that cannot be analysed using standard crystallographic approaches. The "peaks" in the *a*-ZIF diffraction pattern are not indexable in terms of a unit cell, but instead reflect the regions of maximum scattering intensity in the original ZIF-4 diffraction pattern. Fourier transform of the diffraction patterns gives the PDFs $D(r)$ shown in the lower panels, which represent the weighted probability of finding pairs of atoms separated by a given distance. The PDF is well-defined even in the absence of long-range periodicity. Here the two functions are essentially identical up to $r \simeq 6\,\text{Å}$, indicating that the local ZIF coordination environment is preserved in the TIA phase. The resolution of the PDF depends on the maximum value of Q to which the diffraction pattern is reliably measured; these PDFs are obtained using $Q_{max} = 40\,\text{Å}^{-1}$, which is substantially larger than the value $Q_{max} \simeq 6\,\text{Å}^{-1}$ achievable using standard laboratory X-ray diffractometers.

using starting models based on crystalline ZIF polymorphs do not provide convincing fits to data strongly suggests it is more correct to think of the structure of *a*-ZIF in terms of a CRN than in terms of a periodic network with a large-amplitude distortions of its constituent linkers.

A conceptually-similar model has recently been proposed to describe the structure of "PAF-1" (PAF = porous aromatic framework), a highly-stable organic network polymer which exhibits one of the most extreme accessible surface areas known (BET surface area $5640\,m^2\,g^{-1}$; Langmuir surface area, $7100\,m^2\,g^{-1}$ by N_2 sorption) [376, 378]. As for the *a*-ZIF described above, the X-ray diffraction pattern of PAF-1 exhibits no Bragg component. Yet the broad features in this diffraction pattern, together with ^{1}H MAS NMR measurements and also the N_2 sorption isotherms can all be explained in terms of a structural model derived from the CRN of SiO_2 [Fig. 6.1(c)]. To date, a PDF investigation has not been reported for this system despite many investigations into crystalline versions [379]; however, one might anticipate that such a study would be particularly useful in verifying whether the CRN model proposed in Ref. 376 is indeed valid. Most PAFs are amorphous, and in these systems the absence of long-range periodicity is attributed to the irreversibility of the coupling reaction used during polymerisation [378]. Interestingly, the bridging ligand length used in PAF synthesis appears to play a crucial role in determining microporosity: too small a linker and the network is too densely packed; too large a linker and the network either has sufficient flexibility to interpenetrate itself or the system becomes mesoporous. So it is possible also to establish local-structure/property relationships even in these amorphous systems.

Both the families of *a*-ZIFs and of PAFs show considerable chemical and topological diversity, so there is genuine scope for meaningful materials optimisation in both cases. This allows, in principle at least, the development of new classes of amorphous materials in which in the various attractive mechanical and optical properties of amorphous solids are coupled with desirable chemical and physical functionalities accessible using molecular framework chemistry. So, for instance, the incorporation of chiral ligands, transition

metals, or lanthanides provides strategies for developing, respectively, chiral, magnetic or luminescent glasses. Moreover, because macroscopic flow is observed during TIA of ZIFs [190], there remains the possibility of machining (or casting) homogenous ZIF-based optical lenses [Fig. 6.3]. If one could find a method of retaining some intrinsic microporosity then such lenses could display guest-dependent focal lengths, or act as sensors for the presence of particular sorbates. Finally, the ability to 'switch' molecular frameworks between crystalline and amorphous states is strongly reminiscent of DVD-RAM technology, which is based on similar behaviour in the phase-change chalcogenides. In these systems the extent of crystallinity functions as a means of storing data: the different optical response of the two states allows data reading, and in the case of *a*-ZIFs localised heating might allow a mechanism for switching states (and hence data writing) [Fig. 6.4] [380]. The possibility of irradiation-driven amorphisation/crystallisation in molecular frameworks would appear to be—at least at this stage—a largely unexplored area of research.

6.1.2 Static disorder

Whereas the amorphous molecular frameworks accessed through TIA or precipitation routes have network topologies that are distinct from those of their crystalline analogues, it is possible also to introduce sufficient disorder within crystalline molecular frameworks *without making or breaking bonds* that the systems come to appear just as disordered.

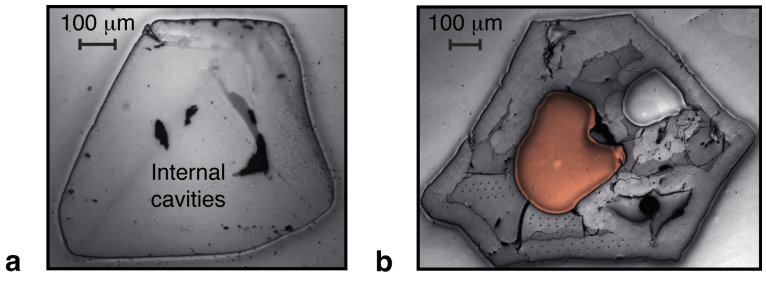

Figure 6.3: Plastic flow during TIA in a-ZIF. Representative micrographs of *a*-ZIF monoliths obtained by heat-treatment of single crystals of ZIF-4: (a) before, and (b) during subsequent transformation to ZIF-zni [190]. A peculiar feature of both is the inclusion of curved cavity regions within the interior of the monoliths (one in (b) is highlighted in red), the presence of which is attributed to density collapse of the ZIF matrix during TIA. The edges of the monoliths—which originate as facets of the ZIF-4 crystals—can also be seen to assume curved morphologies. Both observations indicate macroscopic flow during TIA. Adapted with permission from T. D. Bennett *et al.*, *Phys. Rev. Lett.*, **104**, 115503 (2010). Copyright 2010 by the American Physical Society.

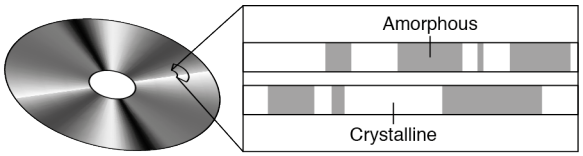

Figure 6.4: DVD-RAM data storage. At its simplest level, data storage in DVD-RAM media exploits both the different optical responses of amorphous and crystalline polymorphs (which enables data reading) and also the ability of materials such as AgInSbTe to switch between amorphous and crystalline states under laser irradiation [380].

Perhaps the most straightforward relevant mechanism is that of applying hydrostatic pressure. It has been known for some time that various oxide-based frameworks will exhibit pressure-induced amorphisation (PIA) at pressures of *ca* 10–100 GPa [381] but the flexible bonding arrangements in molecular frameworks translate to much reduced critical pressures in the case of molecular frameworks. Examples include the canonical metal–organic framework MOF-5 (critical pressure, $p_c = 3.5$ MPa) [196] and also various ZIFs (p_c(ZIF-8) = 0.34 GPa; p_c(ZIF-4) = 6.5 GPa) [131, 382]. In each case there is a sizeable density increase during amorphisation that reflects structural collapse, and again the process is observable experimentally by monitoring the disappearance of Bragg intensities in diffraction patterns. But the fact that the MOF-5 amorphisation process is reversible on pressure release, and also that *a*-ZIF-8 retains some microporosity implies that the amorphous networks produced during this process carry some 'memory' of the original crystalline arrangement. As for the 'topologically-ordered glass' phase of SiO_2 obtained by PIA of a siliceous zeolite [383], the absence of periodicity in pressure-amorphised molecular frameworks reflects not a change in network connectivity but rather the existence of large incoherent static displacements of the molecular linkers [Fig. 6.5].

One important potential application of this PIA behaviour concerns the immobilisation of radioactive byproducts of nuclear energy production. The general strategy is straightforward enough: a crystalline precursor framework is loaded with radioactive guest (*e.g.* I_2) and subsequently exposed to hydrostatic pressures capable of initiating amorphisation [203]. The guest effectively becomes trapped during the framework collapse associated with PIA, with subsequent leaching reduced by at least an order of magnitude in the case of (*a*-)ZIF-8. Structural evidence for the retention of I_2 within the pore network of

a-ZIF-8 was obtained using X-ray PDF measurements, illustrating how—despite the absence of long-range structural periodicity—it remains possible to structurally characterise host-guest interactions within an amorphous system.

The presence of guest molecules within the pore system of a molecular framework effectively places the network itself under negative (*i.e.* internal) hydrostatic pressure. Consequently the removal of guest molecules—for example by straightforward desoprtion—can have a similar effect on the framework as would application of positive (*i.e.* external) hydrostatic pressure. Just as PIA is found to occur in a number of different molecular frameworks, so too is it the case that desorption-induced amorphisation (DIA) is not uncommon. The mechanisms of the two effects also appear to be very similar in that the framework topology is preserved during DIA with crystallinity often recoverable *via* subsequent re-sorption. This point is illustrated with two examples: one recent and one historic.

The metal–organic framework Cu-SIP-3 has been the focus of a number of high-profile

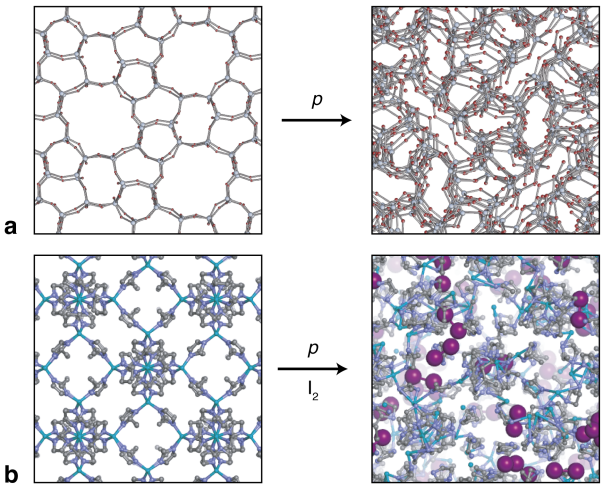

Figure 6.5: Topologically-ordered amorphous phases. (a) The open network structure of a siliceous zeolite silicalite-1-F undergoes a massive volume collapse under application of hydrostatic pressures. The collapsed phase is amorphous in the sense that its diffraction pattern contains no sharp Bragg reflections; however, its PDF can be interpreted in terms of a statically-disordered structure with the same network connectivity as the original crystalline phase but with large-amplitude uncorrelated displacements of large regions of the structure [383]. Adapted with permission from *J. Am. Chem. Soc.*, 2009, **131**, 12333–12338. Copyright 2009 American Chemical Society. (b) A similar mechanism could also describe PIA in the molecular framework ZIF-8. Guest molecules (*e.g.* I_2, shown here as large purple spheres) included within the pore structure of the crystalline phase are effectively trapped within the amorphised host, despite the latter retaining its original network connectivity.

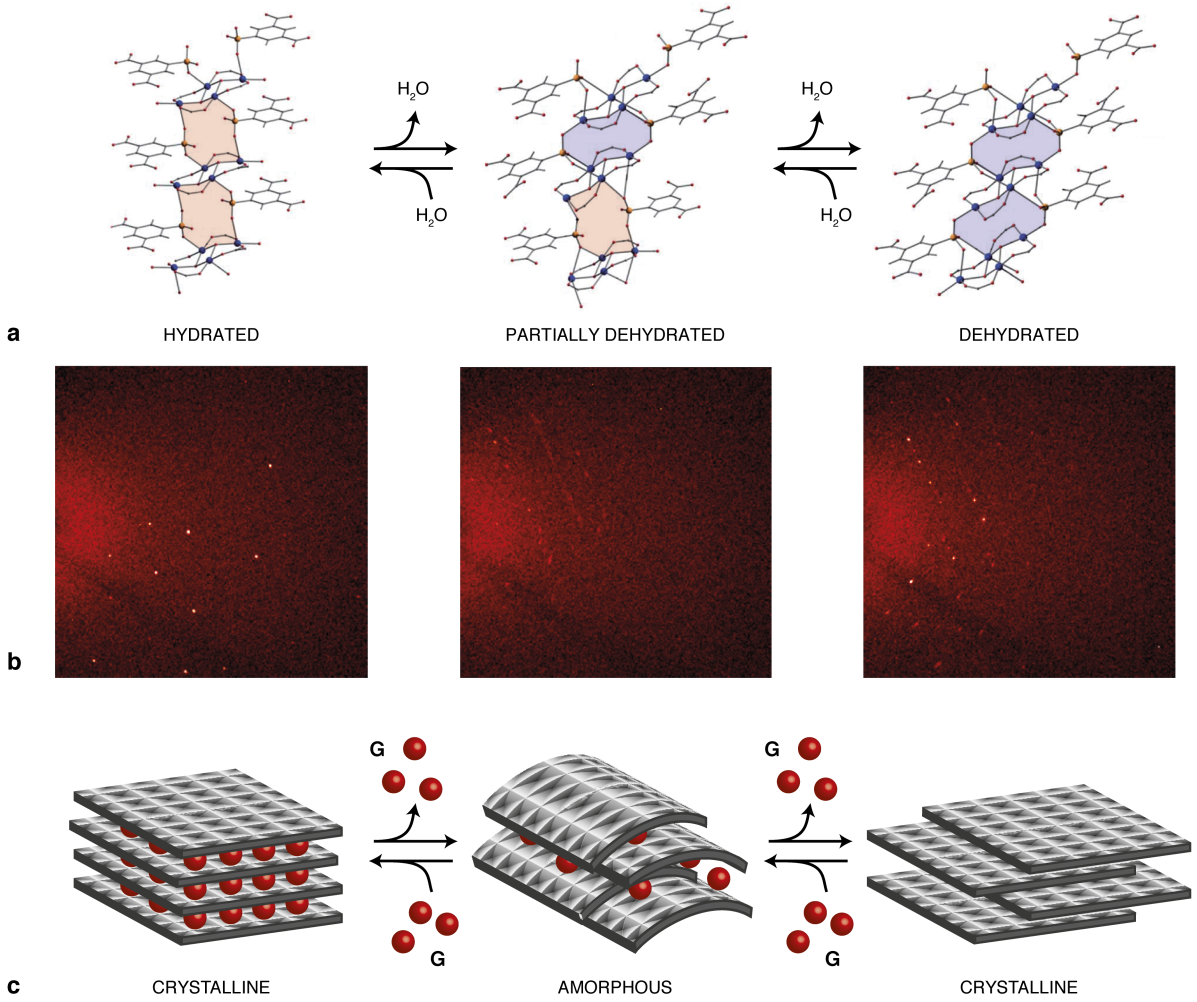

Figure 6.6: Dehydration of crystalline Cu-SIP-3 proceeds via a poorly-ordered partially solvated intermediate, with single crystallinity recovered in the final anhydrous product [384]. (a) Structural models show transition from an inflated, hydrated state (yellow shaded regions) to a collapsed version with the same connectivity (blue regions) *via* a phase with randomly-distributed hydrated regions within each single crystal. Adapted from Ref. 385 with permission of The Royal Society of Chemistry. (b) Single crystal diffraction patterns collected *in situ* during dehydration show the disappearance of strong Bragg reflections during intermediate stages. The mechanism proposed on the basis of X-ray PDF measurements [385] involves uncorrelated large-scale reorganisation of regions of the structure during dehydration as each successively becomes dehydrated. Adapted with permission from *J. Am. Chem. Soc.*, 2010, **132**, 3605–3611. Copyright 2010 American Chemical Society. (c) A schematic representation of the process.

studies, being favoured for its selective uptake and delivery of nitrous oxide for use in biomedical devices [Fig. 6.6(a)] [384–386]. Its framework chemistry is characterised by the presence of some strong and some weak node–linker interactions, the latter having the effect of facilitating large-scale rearrangement of framework components through flexing of weak bonds. The as-prepared (hydrated) form of Cu-SIP-3 is obtainable as high-quality single crystals. Gentle dehydration over the temperature range $370 < T < 405\,\mathrm{K}$ is accompanied by apparent loss of crystallinity, but single-crystallinity is restored by further annealing at temperatures above 405 K [Fig. 6.6(b)] [384]. Not only are the network connectivites of the hydrated and dehydrated forms identical, but the orientation matrices determined during single crystal diffraction measurements indicate that the macroscopic orientation of the pre- and post-transition single crystals are one and the same [Fig. 6.6(c)]. Consequently the amorphous intermediate must retain a 'memory' of the network geometry and orientation; in particular it is certainly anisotropic. This transformation is all the more remarkable for the large structural reorganisations (several Å) and volume collapse ($> 20\%$) involved; moreover the process is entirely reversible on exposure to H_2O.

X-ray PDF measurements have played a crucial role in determining the mechanism for this transformation [385]. They suggest that the amorphous intermediate, which is partially hydrated, is not describable as a simple superposition of two end-member crystalline forms, but instead reflects the same sort of uncorrelated large-scale translations associated with PIA. On exposure to NO gas, the dehydrated phase appears once more to lose its crystallinity as the network re-opens to accommodate the NO guest (effectively the reverse process to that shown in Figure 6.6). The maximum pressures of NO loading investigated (1 atm) were not sufficiently high to observe re-formation of the fully-loaded crystalline phase, but the PDF measurements are consistent with analogous (re/de)-sorption mechanisms for H_2O and NO loading. So, in summary, the very structural flexibility that allows selective guest uptake in Cu-SIP-3 is the same motif responsible for the crystalline–amorphous transitions observed.

An historic example concerns the homochiral 1,3,5-benzenetricarboxylate (*btc*) frameworks of general formula Ni(*btc*)$_{2/3}$(*py*)$_2$Y·{guest} (*py* = pyridine; Y = bis(alcohol) or diol) as described in Ref. 387. Depending on the nature of the alcohol ligand(s), this system crystallises as either a doubly- or a fourfold-interpenetrated (10,3)-a network. The use of 1,2-propanediol templates one of the former systems; ethanol templates one of the latter systems. So, starting with a crystalline sample of the porous, doubly-interpenetrated 1,2-propanediol framework, thermal desolvation then gives an X-ray amorphous solid. Crystallinity returns on re-exposure of this amorphous solid to 1,2-propanediol—an observation which in principle could be accounted for by a mechanism of dissolution and growth. Yet such a mechanism can in fact be discounted because exposure of the same desolvated amorphous phase to ethanol vapour initially yields a crystalline ethanol-containing phase which is doubly- rather than quadruply-interpenetrated. This metastable phase reorganises itself over time into the stable ethanolic configuration in which four (10,3)-a nets interpenetrate. Consequently the disordered desolvated intermediate must retain a memory of the original network topology of the 1,2-propanediol framework—and is consequently a rare (characterised) example of a doubly-interpenetrated amorphous solid.

In these two cases, the extent of static disorder is at its most extreme, in that there is complete loss of structural periodicity. A somewhat less extreme—but no less remarkable—type of static disorder is thought to be responsible for hysteretic sorption of CO_2 in the indium-carboxylate framework NOTT-202 [388]. The material consists of two interpenetrating framework components: one is fully ordered, and the other is ordered over small length-scales but is only partially occupied throughout the entire solid [Fig. 6.7]. Consequently a sizeable portion of the solid is missing, with the defect sites surrounding these vacancies influencing the CO_2 sorption properties of the material. Indeed the unusual multistep adsorption profile observed experimentally can be mapped directly onto the concentrations of defects within this partially-occupied sublattice. It is argued that framework flexibility plays a crucial role in accommodating these defects and also allowing large gas uptake. The general propensity for molecular framework materials of

all types to exhibit large degrees of flexibility suggests that static disorder may in fact be more common in these materials than had previously been recognised [206].

6.1.3 Dynamic disorder

For neutral molecular frameworks there is a direct correspondence between metal:ligand stoichiometries (determined by their respective charges) and the ratio of metal-to-ligand coordination numbers. But it is straightforward to engineer systems where these two factors do not correspond, such that anionic or cationic frameworks are formed instead, with charge balance achieved *via* inclusion of counterions within the framework pore system. A canonical example is given by the divalent transition metal formates: the metal-to-ligand charge ratio of (+)2:(−)1 is incompatible with the metal-to-ligand coordination preference ratio of 6:2. Consequently, transition metal formates favour the general formula $AM(HCOO)_3$ (A^+ = monocation) rather than $M(HCOO)_2$: in general they crystallise with a perovskite-like octahedral (cubic) net in order to satisfy the coordination preferences of each component, but then must include extra-framework cations within the cubic pores of this net in order to obtain charge balance.

The relevance of a discussion concerning counterion inclusion in the broader context of structural disorder comes from the potential for symmetry-mismatch between the

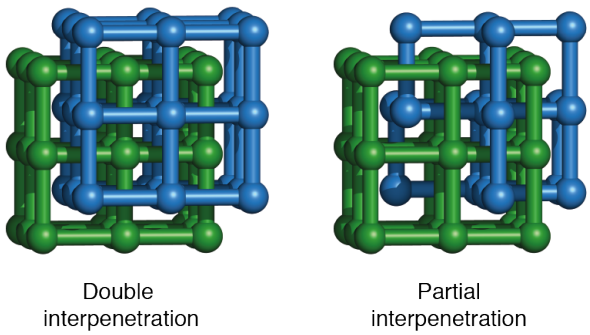

Figure 6.7: Partial interpenetration provides defect sites for gas recognition and storage. The carboxylate-based framework NOTT-202 consists of one fully-occupied and one partially-occupied framework [388]. This is a very unusual form of interpenetration that suggests a new strategy for developing MOF-based catalysts: the fully-occupied framework provides mechanical stability, and the partially-occupied framework provides open binding sites for activation. By controlling vacancy correlations in may even prove possible to develop complex "active sites" within the pore-accessible volume. Adapted by permission from Macmillan Publishers Ltd: *Nature Mater.*, Ref. 388, copyright 2012.

counterion and the shape of the framework cavity it occupies. In the case of many of the $AM(HCOO)_3$ formates, the room-temperature crystal structure has rhombohedral symmetry, with the A^+ ions occupying sites with point symmetry 32 (D_3) [389]. Consequently if the counterion A^+ is chosen such that its molecular symmetry is distinct from D_3 (formally the condition we are considering is where the molecular point group of the counterion is not a supergroup of D_3) then there are only two possibilities: one is that the orientation of the counterion becomes disordered over multiple equivalent sites; the second is that the counterion adopts a single ordered orientation which then results in a symmetry-lowering distortion of the framework. The distinction between these two scenarios relies on the strength of cation–framework interaction energies relative to the available thermal energy $k_\mathrm{B}T$, and consequently there is scope in all such systems for a temperature-driven order/disorder transition when these two energy scales coincide.

A pertinent example is that of the metal–organic framework $[(CH_3)_2NH_2]Mn(HCOO)_3$ [390]. In this case, not only does the dimethylammonium (dma^+) counterion have lower symmetry (C_{2v}) than that of the D_3 crystallographic site it occupies, but it is also polar and so its orientational ordering can affect the macroscopic charge distribution within the the framework itself. Under ambient conditions, the dma^+ ions are *dynamically* disordered over three symmetry-related orientations; the framework exists in the non-polar space group $R\bar{3}m$. But when cooled below 190 K, the counterions no longer have sufficient thermal energy to sample all three orientations and instead settle into a single, ordered state [Fig. 6.8]. This molecular orientational ordering breaks the symmetry of the corresponding crystallographic site, causing a structural transition from $R\bar{3}m$ to the polar space group Cc. The crystallographic details here are important because they illustrate how structural disorder can affect a bulk material property—in this case, polarisation.

This order/disorder transition has a strong signature in the variable-temperature dielectric response of $[(CH_3)_2NH_2]Mn(HCOO)_3$ [390]. Essentially what one is measuring in such an experiment is the extent to which charge can move within the framework in response to an applied electric field. In general, materials containing some dynamically-

disordered dipolar component (*i.e.* a paraelectric material, by analogy with paramagnetism) exhibit a strong dielectric response because the dipoles simply rearrange in order to align with the applied field. Conversely, ordered phases exhibit a much weaker response because the dipoles are 'trapped' in a single orientation. Certainly such a response is observed experimentally for this particular formate [Fig. 6.8], and this measurement provided strong additional support for the description of orientational ordering determined crystallographically.

An order/disorder transition is by no means unique to this particular formate: similar effects are observed when Zn^{2+} or Co^{2+} or Ni^{2+} replace Mn^{2+} [193, 194], or when dma^+ is substituted by *e.g.* NH_4^+ (noting that T_d is not a supergroup of D_3) [369]. Consequently, much of the focus within this very active field lies in understanding the dual roles of transition-metal and counterion substitution in determining (i) the ordering transition temperature, and (ii) the nature of the ordered phase—*i.e.* whether the local dipoles align in the same direction (ferroelectric ordering) or in opposite directions (antiferroelectric ordering) [Fig. 6.9]. Moreover, because magnetic ordering occurs for these same phases (albeit at substantially lower temperatures), there remains the exciting prospect of developing multiferroic frameworks where the order/disorder ferroelectric transition couples with magnetic ordering [193, 371].

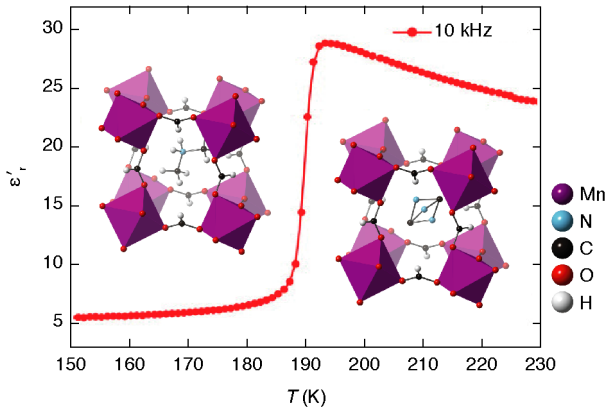

Figure 6.8: A dynamic order/disorder transition in $[(CH_3)_2NH_2]Mn(HCOO)_3$. Dielectric measurements are particularly sensitive to such transitions: cation mobility in the high temperature (disordered) phase is reflected in a large dielectric response that is lost on cooling into the ordered phase. Here the order/disorder process involves reorientations of the dma^+ cation within the perovskite-like cubic pore. Adapted with permission from *Inorg. Chem.* 2010, **49**, 1510–1516. Copyright 2010 American Chemical Society.

The paradigm of symmetry-mismatch-driven dynamic disorder outlined here can also be seen to operate in what is chemically a very different molecular framework material: namely, imidazolium potassium hexacyanoferrate(III), $(H_2im)_2[KFe(CN)_6]$ [391]. As for the formates, the anionic cyanide-bridged host framework of this material adopts a perovskite-like cubic topology, which at temperatures greater than 187 K also crystallises in the $R\bar{3}m$ space group. The approximately-pentagonal imidazolium cations (point group C_{2v}) are situated at the centres of the cubic pores (point symmetry D_3), and consequently are disordered over multiple orientations. In this case—and for reasons that are not well understood—there is actually a pair of dielectric anomalies at two distinct transition temperatures (158 and 187 K), with the lower-temperature phase transition corresponding to orientational ordering of the imidazolium ions and global symmetry lowering to the $C2/c$ space group. That there is such a strong correspondence between this system and the formates despite their different chemistries suggests the likely existence of many families of (anti-)ferroelectric molecular frameworks.

Our final example of a molecular framework that exhibits dynamic disorder concerns

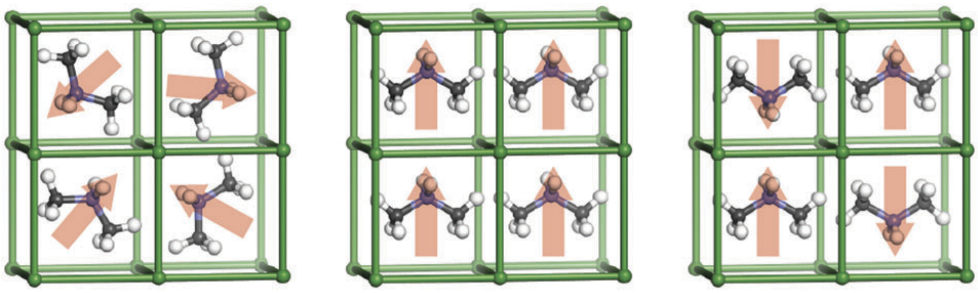

Figure 6.9: Simple order and disorder scenarios in (anti)ferroelectric molecular frameworks. If an extra-framework counterion is polar then its orientation has the potential to influence the polarity of the crystal as a whole. Beyond some critical temperature, the available thermal energy is substantially larger than the counterion–framework interaction and the counterions may be considered to adopt a statistical distribution of possible orientations. In such a state, the molecular dipoles show no long-range order, and the phase is said to be paraelectric (PE). At low temperatures, there will not be sufficient thermal energy to overcome counterion–framework interactions and the system will order so as to optimise these interactions. This generally (but not always!) results in simple ordering of the molecular dipoles: if they are all aligned in the same sense then the phase is said to be ferroelectric (FE); if the alignment is antiparallel at nearest-neighbour distances then the phase is antiferroelectric (AFE). The FE phase is the only one with a net polarisation; this polarisation can be reversed by applying an external field—a process that lies at the heart of the many practical applications of ferroelectric materials.

a system that is arguably of greatest interest for its unusual thermal expansion behaviour. Cadmium cyanide, $Cd(CN)_2$, is isostructural with $Zn(CN)_2$ and also shows large isotropic NTE [37]. On heating this NTE effect is in fact larger than for $Zn(CN)_2$, and is about 2–3 times stronger than the positive thermal expansion of conventional materials. Variable-temperature single crystal measurements of $Cd(CN)_2$ reveal two particularly anomalous effects, both of which indicate that dynamic disorder plays an important role in this system. First, the mean-squared displacement parameter of the Cd centre actually increases on cooling (ordinarily atoms should move less at lower temperatures) [29, 37]; and, second, the diffraction pattern contains an intense, highly-structured and temperature-dependent diffuse scattering component [Fig. 6.10(a)] [29].

The origin of these effects is a tendency at low temperatures for the Cd centres to occupy lower-symmetry sites of higher coordination number that are displaced away from the ideal tetrahedral site by *ca* 1 Å in each of six symmetry-related directions [Fig. 6.10(b)] [29]. At temperatures below 150 K the Cd atoms do not have sufficient thermal energy

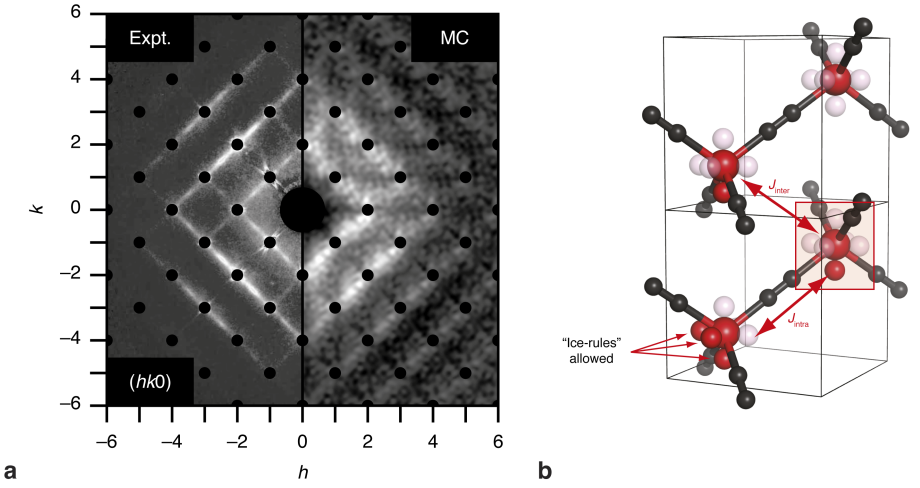

Figure 6.10: Correlated disorder and structured diffuse scattering in $Cd(CN)_2$. (a; left panel) A reconstructed ($hk0$) cut of reciprocal space for $Cd(CN)_2$ obtained using in-house single-crystal X-ray diffraction measurements. Bragg reflections have been obscured by black circles. (b) The disorder mechanism involves the displacement of Cd atoms from their average crystallographic position (large red spheres) by about 1 Å in one of the six symmetry-equivalent ⟨100⟩ directions (small red spheres). By taking into account the likely effect of one type of displacement on that of its neighbours (parameterised here by the coupling constants J_{inter} and J_{intra} for inter- and intra-framework correlations, respectively), it is possible to use Monte Carlo methods to calculate an expected diffuse scattering pattern (a, right). Adapted with permission from V. E. Fairbank, A. L. Thompson, R. I. Cooper, and A. L. Goodwin, *Phys. Rev. B*, **86**, 104113 (2012). Copyright 2012 by the American Physical Society.

to switch between sites and the framework symmetry is lowered accordingly. On heating beyond 150 K each Cd occupies all six sites in turn such that its average position is increasingly well described by the central position—the tetrahedral site. Because displacements away from this site require framework expansion (and hence displacements towards the central site allow compression), the dynamic disorder mechanism is coupled to the NTE effect. This mechanism is directly related to the mechanism of NTE proposed in the previous chapter for $Zn(CN)_2$ by considering these as 'charge-ice'-like displacements as introduced previously.

The existence of structured diffuse scattering indicates that the displacement of one Cd centre is strongly correlated with that of its neighbours [Fig. 6.10] [29]. Ordinarily, diffuse scattering is roughly three orders of magnitude weaker than Bragg scattering, but in this instance the diffuse component is particularly strong by virtue *both* of the large displacements *and* of the large X-ray scattering cross-section of the Cd atoms. In all likelihood, many—if not all—of the dynamically-disordered systems described above would exhibit structured diffuse scattering on some level because the orientation of any one extra-framework counterion is almost certainly not completely decoupled from that of its neighbours. While the interpretation of temperature-dependent diffuse scattering patterns is in general a nontrivial exercise [392], the existence of such scattering is direct experimental evidence not only for dynamic disorder, but also for the importance of correlations in that disorder. Any inference concerning the interactions that control those local correlations can often be tested by using computational tools such as custom-made Monte Carlo simulations or software packages such as DISCUS to calculate the corresponding expected diffuse scattering patterns [27]. A qualitative match between calculated and observed diffuse scattering is usually taken as strong evidence to support the proposed local interaction model. More sophisticated methods are in current development—for example a reverse Monte Carlo method based on the 3D difference PDF [393]—but are not yet in widespread use.

6.1.4 Reduced dimensionality

For the vast majority of the systems described in the various preceding sections, disorder arises by virtue of the low energy scale of key interactions in molecular frameworks—be those within the frameworks themselves or between the framework and some included component. Suitable choice of metal coordination preference and ligand connectivity can in fact yield materials where there are essentially no bonding interactions within certain directions. Columnar and layered systems—in which strong interactions are constrained to either one or two dimensions, respectively—can offer particularly attractive physical properties, including frustrated magnetism, intercalation chemistry, nanofabrication pathways and anomalous mechanical responses [384, 394–397]. For oxide-based frameworks, rational design of low-dimensional systems is often hampered by the propensity for oxide anions to interact either covalently or electrostatically with cations in all possible directions. Conversely, the specific binding preferences of particular molecular linkers can be exploited to impart strong directionality within molecular frameworks and hence enforce low dimensionality.

Here I focus initially on the family of pseudo-binary transition-metal cyanides of specific interest in this thesis [177]. In many cyanide frameworks the metal centres—due to the coordination preference of the particular metal ion in question—dictates framework topology. So for example, the group 11 monocations, which tend to favour linear coordination, form simple chain structures, whereas the group 10 cations, which exhibit the characteristic square-planar d^8 electronic configuration, form layered square grids instead [Fig. 6.11(a)] [396, 398]. In both cases the interchain/interlayer interactions are limited to dispersion forces and weak electrostatic interactions, and in nearly all cases these are not sufficiently strong to drive three-dimensional periodic ordering of the solid as a whole. Rather these materials exhibit strict crystalline periodicity only within the direction(s) which contain the strong metal–cyanide bonds and are disordered to various different extents in the perpendicular direction(s) [399].

Were it possible to perform a ‘single-crystal’ X-ray diffraction measurement for one of

these systems (noting that in most cases structural disorder prohibits growth of sufficiently-large crystals for such a measurement), then the reduced dimensionality of its structure would become apparent in the atypical diffraction pattern observed [Fig. 6.11(b)]. The orientational averaging implicit in a powder diffraction measurement means that these diffuse rods appear similar to Bragg reflections but carry a so-called Warren peak shape, which has a very broad and asymmetric tail [Fig. 6.11(c)] [400]. Columnar systems behave in a conceptually similar manner: their 'single-crystal' diffraction patterns would consist of *planes* of scattering, which also appear as asymmetric and broad Bragg-like features in a powder diffraction pattern. Consequently the observation of Warren peak shapes in powder diffraction patterns for molecular frameworks is a useful means of diagnosing the existence of severe packing disorder—and hence low dimensionality—even if obtaining a complete description of that disorder is not universally feasible.

From a functional materials perspective, what advantageous physical properties might one expect to find in these low-dimensional systems? First, the dynamical properties of low-dimensional materials are dominated by the effects of that reduced dimensionality. Vibrational motion in layered materials consists primarily of 'rippling' of the layers; the analogous modes in columnar structures are skipping-rope-type transverse displacements

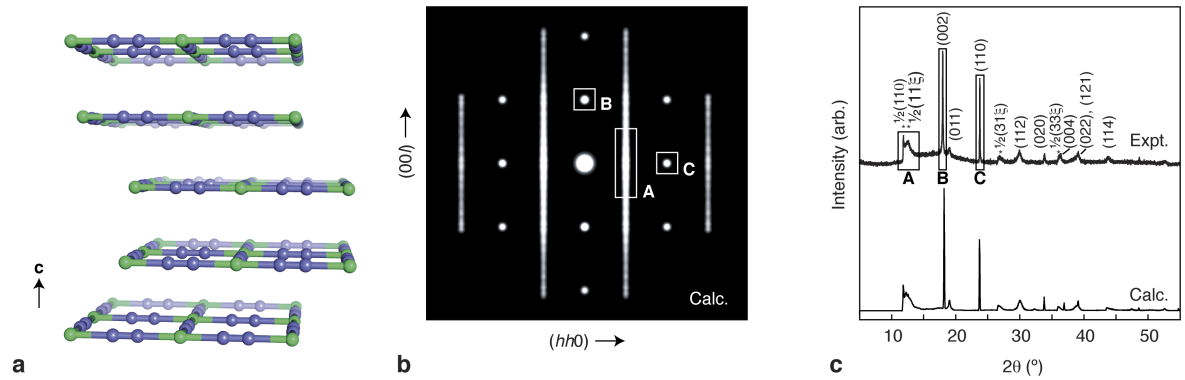

Figure 6.11: Diffraction signatures of layered materials. (a) The structure of $Ni(CN)_2$ consists of square-grid layers that are well ordered in the layer directions, but have no periodic ordering in the perpendicular direction (labelled here as **c**) [399]. (b) The hypothetical single-crystal diffraction pattern of this material contains rods of diffuse scattering parallel to $\mathbf{c}^*$ (which is itself parallel to **c**) and also a set of 'normal' Bragg reflections. (c) Consequently the powder diffraction pattern, which represents an orientational average over the single-crystal pattern shown in (b), contains a set of sharp reflections and also a number of broad features with asymmetric Warren peak shapes [396, 399]. The correspondence between scattering features in (b) and (c) is indicated by by the panels labelled 'A', 'B', and 'C'.

[323]. Both types of distortion are unusual in the sense that their thermal population results in a contraction of the material within the strongly-bonded directions. Accordingly $Ni(CN)_2$ shows area-NTE within the layer directions just as AuCN and AgCN show linear NTE along the chain axis [396, 398]. The same qualitative effects are seen for that simplest of two-dimensional materials—namely, graphite—as indeed they are for more complex layered molecular framework materials such as Cu-SIP-3 [101]. In fact features that resemble diffuse rods are almost discernible in the diffraction pattern the amorphous-like partially-hydrated phase of Cu-SIP-3 [Fig. 6.6(b)] which suggests 2D behaviour during desolvation. Second, the very weak interactions between neighbouring parts of the same material can facilitate the 'top-down' synthesis of nanostructured phases: for example lithium 2,2-dimethylsuccinate is a layered material with weak dispersive interactions between layers and as a consequence its polycrystalline powders are readily converted into exfoliated nanosheets *via* sonication [401]. And, third, there is the propensity for guest intercalation between layers or chains. This type of behaviour has long been known to occur for $Ni(CN)_2$ [395], and can induce visible colour changes during the switching between disordered and fully crystalline states in response to guest binding [396].

6.2 Comments

Perhaps by virtue of the central role played by crystallographic techniques in driving forward the entire field of molecular framework chemistry, for many years the emphasis within the community has (rightly) focussed on understanding well-ordered systems [182, 402]. The increasingly widespread realisation that structural *dis*order can play a crucial role in imparting unusual and useful physical properties of these same materials, coupled with the rapid development of techniques such as PDF that enable structural characterisation of disordered systems, may yet result in some shift in emphasis towards disordered framework materials as potential candidates for the next generation of functional framework materials. In this chapter we have seen but a handful of different types of disorder in molecular frameworks, focusing primarily on families where there exist a number of characterised systems so that comparison is possible. But there are numerous

other types of disorder—many of which are emerging in individual systems for the first time— and rather than devoting entire sections to each case, some of these are noted here and these are used as springboards for discussion of possible future directions of research in the field as a whole.

The first challenge will be to expand the number of framework systems known to exhibit well-characterised structural disorder. To this end, one increasingly popular method for synthesising disordered frameworks is that of mechanical grinding [197, 403]. It has been shown, for example, that amorphous ZIF samples prepared by TIA and by mechanical grinding are essentially indistinguishable except for their particle size (and hence surface area) [197]. The ease with which ball milling preparations can be undertaken suggests a straightforward strategy with which to explore amorphisation processes across a very large number of different systems. This allows one to ask which chemical and which topological features allow or discourage amorphisation—questions which are key to rational design strategies that employ disorder, and also crucial to our understanding of the amorphisation process itself. An important challenge in this emerging field will be to understand in which instances the disordered phases produced by mechanosynthesis are truly amorphous and in which instances any apparent loss of crystallinity reflects nothing more than particle size effects. Indeed the border-line between nanocrystalline and amorphous descriptions of disordered phases remains an area of fertile discussion in the broader field [404].

As we have seen, disorder need not imply a complete absence of crystallinity—in this vein another interesting approach that has emerged very recently is that of designing functionalised disordered MOFs using metal–ligand–fragment coassembly [405]. Here the approach is to use a small fraction of 'defect' non-bridging linker fragments, which are incorporated within the MOF and which can subsequently be functionalised without any reduction in accessible pore volume. Essentially the majority linker holds the framework together, and the minority component acts as the location where catalysis, gas binding and/or chemical modification can take place. Looking further ahead, correlations between

defect locations might then affect co-operativity in binding [185], or in the case of catalysis the formation of complex multi-component 'active sites' within the framework lattice.

It is quite possible that the cooperative phenomena arising from geometric frustration could also be exploited in molecular framework materials. There are hints that 'spin-ice'-like states play a role in driving NTE in the $Cd(CN)_2$ framework discussed above [29], but there is perhaps more general scope for designing frustrated systems by following the strategy outlined in a recent study of liquid-crystal phases [406]. Here the approach is to functionalise linkers with appendages that would protrude into the pore system of the framework and then interact—either favourably or unfavourably—with each other. Depending on the geometry of the lattice, these interactions may then be frustrated, giving rise to complex ordering patterns that affect the dynamics and mesoscale structure of the system as a whole. One could envisage exploiting further the porosity of molecular frameworks to design a system where guest occupancies switch the key interactions from being favourable to unfavourable (or *vice versa*) and hence producing a large series of bulk property changes in response to guest binding.

The potential for molecular frameworks to behave as configurational glasses has not escaped notice: indeed some of the formates described above show relaxation processes that are clearly characteristic of such states [194]. At the very simplest level, these systems may help shed light on the broader phenomenology of the glass transition itself by simply by expanding the range of systems in which glassy behaviour is observed [407]. But there is perhaps an emerging sense in which molecular frameworks might provide a more general playground for the exploration of systems with anomalous configurational entropies, by virtue of the extraordinary control over coordination geometry and network topology that is possible in these systems [408]. Indeed there are hints that MOF glass systems might not just mimic glassy states, but may provide the first experimental evidence for hypothetical glass models.

Finally, and looking to active areas of research in functional oxide frameworks for inspiration, one might expect charge and compositionally-disordered states to play an in-

creasingly high-profile role in molecular framework science. Already there are promising signs that cyanide-based frameworks may find application in ion storage and conduction applications—although it is perhaps not yet clear that they will outperform their oxide cousins [409]. As a final example, relaxor behaviour in perovskites relies on an ability to support concerted displacements of large nanoregions within a framework lattice [13]; surely the intrinsic flexibility of molecular frameworks might facilitate polar nanodomain formation, even if local polarisation densities are intrinsically lower? And, because ferroelectricity and magnetism can readily coexist in molecular frameworks, might not one hope to design magnetic relaxors based on molecular framework chemistry? Perhaps the only certainty amongst these various questions is that our collective understanding and ability to exploit disorder in these systems is certainly at an early stage of its genesis.

Chapter 7

Structural complexity in coinage metal cyanides

7.1 Introduction

Complex collective states have been shown to give rise to interesting and counterintuitive properties throughout this thesis. Whether considering the frameworks of the materials themselves as atomic-scale wine racks, or the intricate spirals of weak interactions that so dramatically enhances the properties of $Zn[Au(CN)_2]_2$, understanding and controlling how atoms are arranged in the crystalline state is a central aim in material design [410]. We now turn out attention to structural complexity arising from geometric frustration [411], and how even very chemically simple systems may give rise to exotic collective states that have implications in many other areas of condensed matter physics.

Structural disorder is not unknown in cyanide and cyanide-containing materials. In the previous chapter we have seen that functional disorder drives the unusual dielectric phase transition in the Prussian blue-like imidazolium potassium hexacyanoferrate(III), $(H_2im)_2[KFe(CN)_6]$ [391], large negative thermal expansion in cadmium (II) cyanide [29], and local structure variation in low-dimensional nickel (II) cyanide [399]. The propensity for low dimensional cyanides to show disorder—and the inherent anisotropy in such systems giving rise to linear and area negative thermal expansion— led us to consider further the structures and properties of one dimensional chain coinage metal cyanides AgCN, AuCN, and the mixed metal chain cyanides, in particular $(Ag_{1/2}Au_{1/2})CN$. These 'simple' 1D cyanides have at once canonical structures, whilst also actually being structurally poorly understood.

In this chapter we explore how complex and unexpected collective states emerge in a frustrated system governed by simple pairwise interactions [412]. These structural

states are explicitly linked to frustrated magnetic systems as supramolecular analogues: the inter-chain potential encodes a supramolecular interactions that can be tuned to mimic interactions between XY spins. Complex magnetic states predicted for triangular XY magnets—including hidden quadrupolar order and emergent spin-vorticies [413]—are confirmed experimentally for the first time.

7.1.1 Structure description

The chemistry of Ag^+ and Au^+ has been discussed previously (§ 1.4.3): both metal d^{10} cations have coordination chemistry largely based on linear geometry (with silver beings more coordinationally flexible than gold), and metallophilic interactions exist between d^{10} metal centres and have structure-directing roles in many complex coordination polymers or molecular materials that include these metals [224, 311]. Silver, gold, and mixed-metal cyanides form one-dimensional structures where each metal is linearly coordinated to two cyanides to form infinite –M–(CN)–M– chains [Fig. 7.1(a)] [398, 414, 415]. These rod-like chains arrange in a close-packed triangular array in the **a**-**b** plane [Fig. 7.1(b)].

Two distinct average structure-types (AgCN and AuCN) are known. These can be characterised by considering the displacement of these chains in relation to each other along the chain direction (the crystallographic c direction, labelled Δz in Fig. 7.1). For AuCN $\Delta z = 0$ and consequently all chains are aligned, the material therefore being in space group $P6/mmm$, $a = 3.396$ and $c = 5.092\,\text{Å}$ [416]. The distance between chains is as is expected for the separation of Au^+ centres involved in aurophilic interactions ($d_{\text{Au}\cdots\text{Au}} \sim 3.4\,\text{Å}$). In contrast for AgCN the average structure is based on chains displaced by $\Delta z = \pm 1/3$, space group $R\bar{3}m$, $a = 5.996$, $c = 5.259\,\text{Å}$.

One source of disorder in these materials is static orientational disorder of the cyanide unit, however there is no consensus of the extent of this disorder. Crystallographic studies suggest that there is no preferential ordering of cyanides along the chain length, with the M–N and M–C bond distances appearing identical to 0.005 Å from total scattering studies. Solid-state carbon-13 magic angle spinning NMR confirms linear coordination, however asymmetry in the observed spectrum suggests only partial head/tail disorder. A

model based on 30(10)% disordered (*i.e.* CN–Ag–NC) and 70(10)% ordered (*i.e.* CN–Ag–CN) sites accounts for the asymmetric spectrum satisfactorily, whereas neither fully ordered nor fully disordered models adequately fits the data [417]. There is therefore a statistical preference for ordered sites, as is also found in CuCN. Using 15-N NMR an upper limit for the CN bond distance was also determined $d_{CN} = 1.194$ Å with bending and torsional librations responsible for a libration correction of 2.5(15)% to give good agreement (= 1.16 Å) with diffraction studies. Head/tail disorder is well known in other homometallic cyanides [418], and was also confirmed in this system by neutron total scattering and infrared studies [415]. The previous study of Ref. 414 appears to have misinterpreted IR results and therefore suggested a fully ordered model.

The structure of CuCN is significantly more complex than these two simple cases, with EXAFS, NMR, NQR evidence suggesting linear chains but a highly polymorphic and disordered long-range structure. Two phases observed on changing temperature: the high temperature (HT) structure is identical to AgCN structure type [419], whilst at low temperatures the chains buckle with a chain repeat of 9 units (space group $C222_1$) [420]. It was initially suggested from infrared measurements that CuCN is isostructural with AgCN at room temperature, but this was later confirmed to be the α (LT) polymorph. Interestingly the interconversion of HT-CuCN and LT-CuCN can be induced by chemical means on addition of aqueous solution of KBr followed by washing in H_2O [420], as well as heating. The chemistry of CuCN is much more varied than the other coinage metal

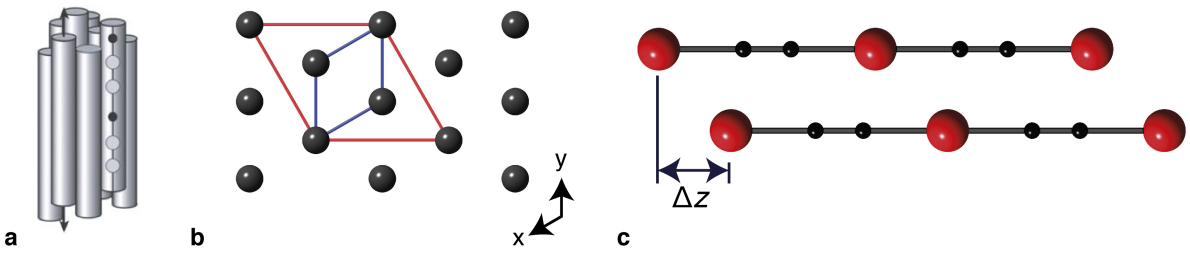

Figure 7.1: The chain structures of the coinage metal cyanides (a) infinite M–CN–M chains pack like rods in a hexagonal array (b) in the crystal structures of AgCN, AuCN, CuCN and mixed-metal variants. The unit cell for AuCN is shown in black and the larger unit cell for AgCN is shown in red. (c) By considering the relative displacement of each chain to its neighbours it is possible to classify the distinct structures of AuCN ($\Delta z = 0$) and AgCN ($\Delta z = \frac{1}{3}$).

cyanides, with formation of several other structural types (1D and 3D) with different counter-ions and under different conditions [419, 421].

Heterometallic mixed-metal coinage metal cyanides $(M_xM'_{1-x})CN$ [M,M′ = Cu, Au, Ag] are known [422]. The mixed-metal Cu/Ag system forms a solid-solution that follow Vegard's law behaviour [168], however in both the Au/Cu and Au/Ag systems line phases are formed that appear isostructural on average with AuCN [Fig. 7.2] [422]. The formation of a 50:50 line phase for the Ag/Au system in particular is curious and is independent of synthesis route. Ref. 422 suggests this arises as a consequence of the formation of strictly alternating Ag and Au in each chain, a conclusion supported by the non coincidence of the (CN) stretching frequencies in both Raman and IR spectroscopic measurements and from total scattering studies [422]. Using the aqueous synthesis route from $Au(CN)_2^-$ and Ag^+, noting that dicyanoaurate does not have significant lability in aqueous solution, gives immediate precipitation of pure 50:50 product.

The diffraction patterns of all these materials are characteristic of low-dimensional disorder. In particular powder diffraction experiments reveal both sharp reflections and a number of broad features, similar to those previously discussed for $Ni(CN)_2$ [400, 423]. Although well described by the average structure models, there is good evidence (and previous local structure studies [415] suggest) that local distortions do exist across different compositions. In previous studies of AgCN and AuCN peak widths were explained using anisotropic particle size effects [398]. The most unusual peak shapes are clearly seen in the $(Ag_{1/2}Au_{1/2})CN$ diffraction pattern. Indexing the pattern gives a unit cell in space group $P6/mmm$ (AuCN-type), with a refined c lattice parameter close to the average of

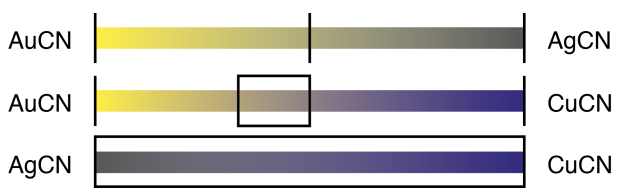

Figure 7.2: Solid-solution and line phases in the mixed-metal Cu/Ag/Au cyanide system For the Ag/Au system, only the 1/2:1/2 line phase is observed, whereas for the Ag/Cu system a full solid-solution range of phases have been characterised. For Au/Cu, line phases at 1/2:1/2 and 2/3:1/3 are known, and intermediate phases have been suggested [422].

AuCN and AgCN $c = 5.158(6)$ Å, whilst the a lattice parameter shows a slight expansion of the AuCN cell compared to the parent ($a = 3.425(5)$ Å) [422]. At first glance, narrower $hk0$ reflections can be rationalised on the basis of static disorder (stacking faults) in the sample in a similar way to the systematic variation in the peak widths of $Ni(CN)_2$. Whilst simply indexing the positions of the Bragg peaks gives a reasonable account of the main structural features, the systematic variation in peak widths and unusual peak shapes is characteristic of correlated disorder and further investigation can give a surprisingly large amount of information on the local structure.

Total scattering data have been collected for this compound but analysis of this data does not provide further insight into the structural details of $(Ag_{1/2}Au_{1/2})CN$ [422]. For example, the M–(C/N) distance could not be resolved satisfactorily so the sense of cyanide bonding could not be found directly; a model based on the ordering (NC–Au–CN–Ag–NC) was preferred based on a previous ^{13}C NMR study on chain fragments encapsulated in tubular cavity of copper (I)-amine host. Broadening of intra- and inter-chain correlations confirms structural features due to the relatively weak bonding between the chains , was noted but not analysed further.

Modelling of these total scattering data was carried out in real space with three superstructures based on the AuCN structure [Fig. 7.3]: (i) $P6/mmm$ ($Z = 1$) with strict alternation of gold and silver planes, (ii) $Immm$ structure where gold and silver form chains of neighbouring aurophilic and argentophilic interactions within each plane, and (iii) $P6/mmm$ ($Z = 3$) where within each plane there are mainly aurophilic or argentophilic interactions with the other metal reducing the number of like-like interactions to three in each layer (alternating predominantly argentophilic and predominately aurophilic planes). The major limitation of these models is that the long-range order introduced in each case results in additional Bragg peaks in reciprocal space that are not observed experimentally. Although each model does fit the real space $T(r)$ data, each of the models (i)-(iii) cannot give insights into the real local structure as it is not consistent with the reciprocal space data [Fig. 7.3]. Only the $P6/mmm$ model with half occupancy of Ag and

Au on the M $(0, 0, 0)$ position fits the average structure, with local order/disorder being encoded within the peak shapes.

Here we note that the strong aurophilic interactions appear to dominate the structure type observed as all gold-containing compounds adopt the AuCN structure type. Although there have been several structural studies on this system there are conflicting opinions on the fundamental question as to why different structure types are observed amongst these materials from both average structure [396, 398, 422] and total scattering experiments [415, 416, 419]. On the one hand it may be straightforward to suggest that the stronger aurophilic interactions are sufficient to overcome the electrostatic repulsion between neighbouring chains and therefore direct the structure of gold-containing compounds [238, 422], but on the other it has been stated that the disordered structure minimising the number of Au$\cdots$Au interactions in $(Ag_{1/2}Au_{1/2})CN$ means these cannot be the driving force to adopt an AuCN-like structure [422].

It was this assertion that drew our attention to the three compounds AgCN, AuCN and $(Ag_{1/2}Au_{1/2})CN$ in particular. Can it be said that aurophilicity plays no role in

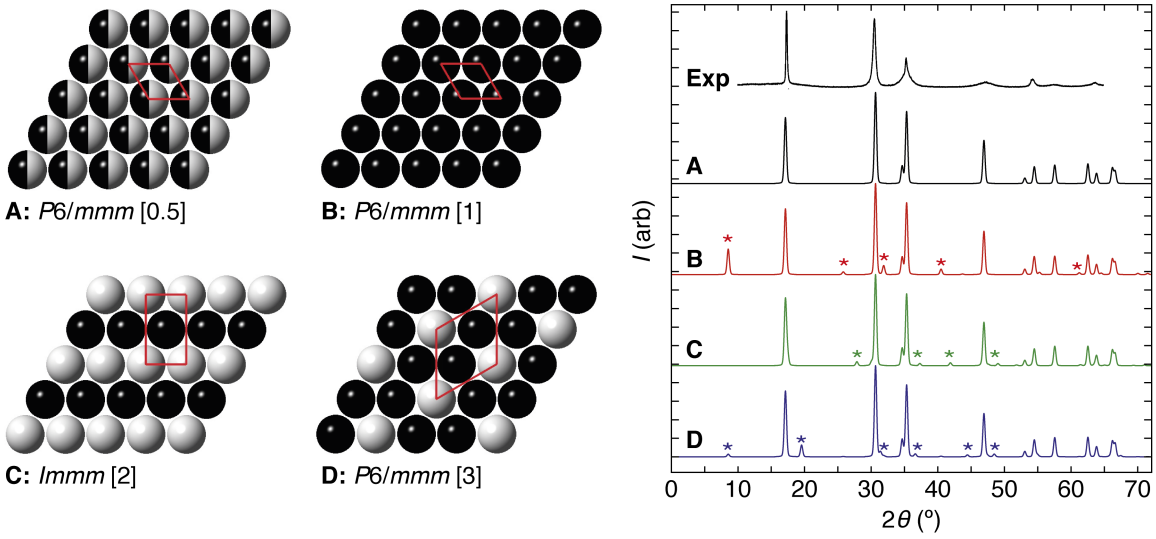

Figure 7.3: Proposed models of $(Ag_{1/2}Au_{1/2})CN$ based on real-space modelling of total-scattering data The four models (A–D) are based on metal positions either at $\Delta z = 0$ (black) or $\Delta z = 0.5$ (white) in the double-c AuCN unit cell and result in the powder diffraction data shown in the right-hand panel. The model based on half-occupancy on each site (A) correctly reproduces the experimental data as presented in Ref. 422, whilst all those introducing additional symmetry in real-space gives rise to additional Bragg peaks in reciprocal space (B–D).

determining the structure and properties of these materials? The balance of interactions between chains—for it can be said for certain that metallophilic interactions exist—must lead to the structure types observed. Disorder must also play some role as even average structure methods show a combination of broad and sharp powder diffraction features, as in $Ni(CN)_2$, but this has not been previously explained. Here we model this order/disorder using Monte Carlo methods to reproduce the previously published experimental diffraction data for AgCN, AuCN and $(Ag_{1/2}Au_{1/2})CN$. Furthermore the elastic properties of these materials are expected to be highly anisotropic, depending in particular on the strength of interactions between chains. Therefore we use hydrostatic pressure to perturb the system (i) to measure the mechanical response of AgCN and (ii) to switch the finely-balanced structure directing interactions. We reveal that this material shows small NLC in the same direction as reported NTE and is extremely incompressible in the chain direction.

7.1.2 Properties of low-dimensional cyanides

The binary coinage metal cyanides are industrially important, being used in electroplating [424], metal extraction [425], and synthesis of ceramic superconductors [2, 177]. All chain-structured cyanides have been shown to exhibit linear NTE in the chain direction [Table 7.1] [422]. The mechanism of NTE proposed involves the increased transverse vi-

Table 7.1: Structure types and coefficients of thermal expansion of chain-structured coinage metal and mixed-metal cyanides. Reproduced from Ref. 422.

Formula	Structure Type†	α_a (MK^{-1})	α_c (MK^{-1})	α_V (MK^{-1})
AuCN	AuCN	61.6	−8.9	115.3
AgCN	AgCN	70.8	−24.8	117.4
HT-CuCN	AgCN	84.1	−30.7	138.2
$(Cu_{0.17}Ag_{0.83})CN$	AgCN	73.9	−26.0	112.5
$(Cu_{0.33}Ag_{0.67})CN$	AgCN	75.5	−29.0	112.5
$(Cu_{0.50}Ag_{0.50})CN$	AgCN	75.8	−34.5	117.2
$(Cu_{0.67}Ag_{0.33})CN$	AgCN	74.5	−37.1	112.5
$(Cu_{0.83}Ag_{0.17})CN$	AgCN	78.3	−40.1	116.5
$(Cu_{2/3}Au_{1/3})CN$	AuCN	86.5	−15.0	160.0
$(Cu_{1/2}Au_{1/2})CN$	AuCN	83.3	−13.8	154.6
$(Ag_{1/2}Au_{1/2})CN$	AuCN	83.9	−9.0	161.0

† AgCN = $R\bar{3}m$, M @ $(0,0,0)$, C/N @ $(0,0,x)$; AuCN = $P6/mmm$, M @ $(0,0,0)$, C/N @ $(0,0,x)$. $x \sim 0.38$.

bration of the cyanide linkers along the chain causing the structure to contract in this direction at high-temperature [398]. In perpendicular directions there are only weak metallophilic interactions leading to large positive thermal expansion in these directions. These dispersive interactions (see §1.4.3) can be structure-directing [224, 426] and critical in the understanding of very unusual physical properties, such as extreme thermal expansion [79], compressibility [130], vapochromic [223] and birefringent [427] behaviour.

Whilst the effect of metallophilicity in determining the structures of AgCN, AuCN, and the mixed-metal cyanides remains unresolved, the variations in mechanical properties are more readily understood. RMC refinements of HT-CuCN, AgCN and AuCN offers dynamical snapshots of the systems and gives information on the vibrations responsible for NTE. Ref. 398 identifies both 'skipping rope' and 'kinky' type motions (transverse vibrations) of cyanide linkers as being responsible for the NTE in the chain direction. The LT-CuCN structure might be thought of as arising from the "locking-in" of dynamic motion into HT-CuCN arising from transverse vibrations of negative thermal expansion along the chain direction. The magnitude of NTE in the chain cyanides is easily controlled by synthesis of the mixed-metal systems, as aurophilic interactions are thought to be stronger than argentophilic interactions [225, 238, 239]. Therefore the responses of gold-containing compounds is found to be less extreme than those based on silver and copper only (by a factor of 3.5 on going from HT-CuCN to AuCN [422]). Including a larger proportion of metals with weaker metallophilic interactions results in a more extreme mechanical response.

Low dimensionality dominates the elastic properties in a range of layered materials, many of which show area negative thermal expansion. In the case of $Ni(CN)_2$, strong area negative thermal expansion is observed ($\alpha_A = \alpha_a + \alpha_b = -11$ to $-16\,MK^{-1}$) arising from the transverse vibration modes within the plane contracting the layers as temperature increases. Essentially the same mechanism is implicated in other area-NTE materials including graphite ($\alpha_A = -2.4\,MK^{-1}$ [428]), low-temperature arsenic ($\alpha_A = -4.0\,MK^{-1}$ [105]) and Cu-SIP-3 ($\alpha_A = -76\,MK^{-1}$ [101, 384]). Disorder within such systems depends

critically on the strength of interactions between planes, with those with the strongest NTE also showing the strongest suggestions of disorder in powder experiments (in the case of $Ni(CN)_2$) and single crystal (in the case of Cu-SIP-3).

7.2 Methods

7.2.1 Synthesis and powder X-ray diffraction

Silver cyanide and gold cyanide were obtained from commercial suppliers and used as received (Sigma Aldrich). Silver cyanide could also be made by addition of stoichiometric (1:1) amount of aqueous solution of $AgNO_3$ to a solution of $KAg(CN)_2$. A fine white precipitate forms immediately. This was filtered, washed with hot water and dried under vacuum at 50°C overnight. $(Ag_{1/2}Au_{1/2})CN$ was prepared by a similar method to that reported in Ref. 422: reaction of $[Au(CN)_2]^-$ and Ag^+ in a 1:1 ratio. $KAu(CN)_2$ was obtained from commercial suppliers and used as received. The two solutions were added whilst stirring resulting in the immediate precipitation of an off-white product. The sample of $(Ag_{1/2}Au_{1/2})CN$ was filtered, washed and dried in the vacuum oven as above. In all experiments it was assumed that AgCN and $(Ag_{1/2}Au_{1/2})CN$ were light sensitive.

High resolution powder diffraction data were collected on a PANalytical Empyrean X-ray diffractometer using Cu Kα_1 radiation. Rietveld refinement against a AuCN-like structural model [Table C.5.37] using a Stephens (hkl)-dependent anisotropic peak shape

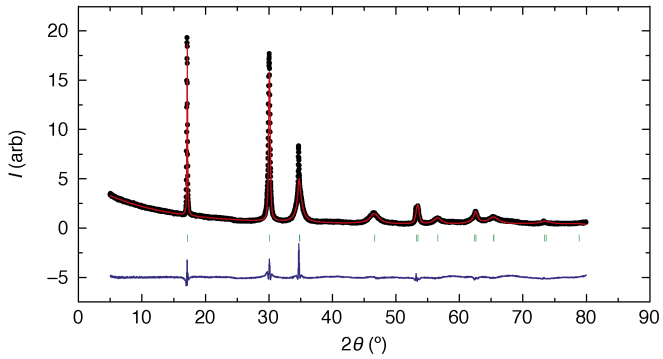

Figure 7.4: Rietveld refinement of X-ray diffraction data for as-synthesised $(Ag_{1/2}Au_{1/2})CN$ using a Stephens anisotropic peak shape. Refined lattice parameters a = 3.4233(6) Å, c = 5.1560(8) Å; data shown as black markers, fit as a red line, difference (data–fit) as blue line displaced downwards by five increments, and green tick marks show expected peak positions.

[429] gave a good fit to data, as shown in Figure 7.4. For all other samples published diffraction data were used to compare Monte Carlo models. Variable temperature total diffraction data for AgCN were collected on the POLARIS diffractometer at the ISIS facility, U.K. POLARIS is a medium-resolution, high flux diffractometer that has high Q range of detectors to give a good resolution of resulting PDF in real space. A sample of AgCN was placed in a thin walled vanadium can and placed in a cryostat within the diffractometer. Data were corrected and processed using MANTID; structural refinement was carried out using TOPAS Academic v.4.1 [154].

Variable pressure powder X-ray diffraction experiments were carried out at beamline I15, Diamond Light Source, U.K. A small amount of AgCN (Sigma Aldrich, 99%) was placed in the pre-indented stainless steel gasket of a gas membrane diamond anvil cell (DAC) together with a single ruby sphere for pressure calibration. A water-free methanol/ethanol mixture (3:1) was used as the pressure transmitting medium. A focused beam of wavelength $\lambda = 0.309960\,\text{Å}$ was selected using a Si(111) monochromator and data were collected using a Mar345 2D detector that was positioned $\sim 350\,\text{mm}$ from the sample position. During data collection the DAC was rocked by 7° to improve powder averaging. Instrument setup was calibrated using a CeO_2 standard and data integration was carried out using Fit2D [153]. Pawley and Rietveld refinement was carried out using TOPAS Academic v.4.1 [154] in space group $R\bar{3}m$ [Table C.6.38, Fig. C.6.21].

7.2.2 Quench Monte Carlo simulations

Custom Quench Monte Carlo codes were written to produce structural models of AgCN, AuCN and the mixed-metal cyanide, $(Ag_{1/2}Au_{1/2})CN$, as outlined below. These programmes use large box models of atoms and refine positions based on an energy to be minimised. In each case random atom movements are accepted based on the Metropolis–Hastings criterion [430], where moves that improve the energy or fit are accepted unconditionally, whilst those that degrade the energy or fit are accepted with a certain probability. The latter is critical in such refinements to prevent trapping in local minima. Initial models were produced as outlined below; further modelling was carried out in col-

laboration with Joseph Paddison and Matthew Cliffe (Oxford) to produce larger models and automate the large number of models required in some cases (not presented here).

The configurations consisted of a $30 \times 18 \times 1$ supercell of the orthorhombic setting of the triangular lattice (1,080 structural units in total). The Monte Carlo energy term used to drive the simulation corresponded to the self-interaction potentials as described in the next section. Simulation progressed in two phases: a high-temperature regime ($T \gg J_i$) in order to allow initial randomisation, followed by a quench cool ($T \ll J_i$). Repeated simulations using this protocol reproduced qualitatively similar structures.

7.2.3 X-ray powder diffraction calculations

X-ray powder diffraction calculations. X-ray powder diffraction patterns were calculated using the CrystalDiffract software package, using the unit cell parameters reported in Ref. 422. Peak shapes were modelled using a Gaussian function of empirically determined width 0.4°. Corrections for preferred orientation were implemented, with the relevant parameters determined by inspection of the experimental data in Ref. 422: a plate-like geometry was used for AuCN and $Au_{1/2}Ag_{1/2}(CN)$ patterns (alignment parameter 0.47) and a needle-like geometry was used for AgCN (alignment parameter 0.29).

7.2.4 Quantum mechanical calculations

Quantum chemical calculations were performed by Prof. François-Xavier Coudert (Chemie ParisTech, Paris). These were carried out in order to measure the variations in enthalpy in pairs of metal cyanide chains as a function of Δz, parameterised as phase shift $\Delta\psi$. For each system, two periodic chains were considered, with their equilibrium geometry and a interchain distance fixed to the crystallographic values. The chains were then shifted by increments of 2°, and for each value of the shift a single-point energy calculation was performed, resulting in $\Delta E(\Delta\psi)$ profiles. In the case of the homometallic AgCN and AuCN chains, where there is assumed to be no order in the orientation of the cyanide ions, a repeating unit equal to four times the basic –M–(CN)– motif was used, in order to account for all four possible orientations of the two cyanide anions.

All calculations were performed in the density functional theory approach with localised basis sets, using the CRYSTAL14 software [124]. The all-electron Triple-Zeta Valence with Polarisation basis sets for C and N atoms were used [431], an energy-consistent relativistic 19-valence-electron pseudopotential and corresponding valence basis set for Ag [432], and an effective core potential for Au [433]. The shrinking factor of the reciprocal space net is set to 8, corresponding to 65 reciprocal space points at which the Hamiltonian matrix was diagonalised. The total energy obtained with this mesh is fully converged. The PBEsol0 global hybrid exchangecorrelation functional [434, 435] was used: of the exchange–correlation functionals benchmarked on the bulk structures of AgCN and AuCN, it gave the best agreement with experimental lattice parameters. Similarly, the effect of empirical dispersion corrections were investigated (in the Grimme scheme [436]), and showed that it did not change the conclusions reached (*i.e.* the relative stability of the different structures studied). However, because the Ag–Ag and Au–Au interatomic distances in this study are close to the cutoff of the empirical correction, it could introduce non-physical behaviour in the energy profiles. As a consequence, all results presented here were obtained without any empirical correction for dispersion.

7.3 Structural analysis

Conceptual mappings between complex magnetic and structural states of matter has long been appreciated [437]. In Chapter 1 we explored structural underconstraint in cubic water ice and the direct mapping to magnetic state of so-called 'spin ice' *e.g.* $Ho_2Ti_2O_7$. In both cases the real material has a characteristically-large configurational entropy [25] and similar magnetic and structural excitations [438]. Here we explore the structural consequences of geometric frustration (overconstraint) rather than underconstraint, and the emergence of complex states of matter over length scales beyond the simple unit cell arising due to the incompatibility lattice structure and relatively simple pairwise interactions.

Using published diffraction data [398, 415, 416, 422] the structures of AuCN, AgCN and the line phase $(Ag_{1/2}Au_{1/2})CN$ are modelled using simple quench Monte Carlo codes.

These simple one-dimensional polymers act as single collective objects, with the interactions between them strictly two-dimensional in nature. Here a quantitive mapping between the structural chemistry of gold(I)/silver(I) cyanides and triangular magnets with continuous (XY) degrees of freedom is established, and the structural features are found to emerge directly from the delicate balance between metallophilic and electrostatic interactions in this system.

7.3.1 AuCN and AgCN

It is well established from both crystallographic and spectroscopic measurements that in all the systems investigated consist of essentially the same –M—(CN)–M– chains of atoms (with head-to-tail disorder in the sense of the cyanide orientation), that pack in a triangular lattice. So in all Monte Carlo programmes the periodicity along (*i.e.* the M–CN–M repeat) and between (*i.e.* the trigonal lattice) each chain were maintained. A simple potential was then introduced to describe the interaction between chains as function of relative chain displacements Δz_j

$$E = \rho \sum_{j \in NN} \cos[2\pi(\Delta z_j)], \tag{7.1}$$

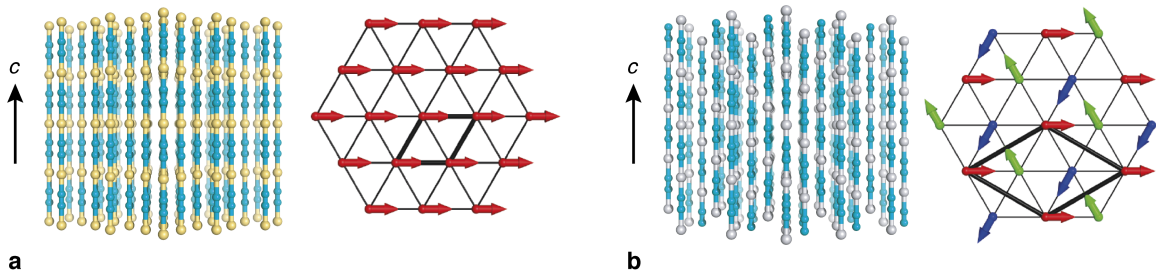

Figure 7.5: Ground state structures of the homometallic chain cyanides AuCN and AgCN and their relationship to the triangular XY ferromagnet and anitferromagnet. (a) The chain structure of AuCN, left, where all metal cations align in layers in the (a,b) plane *i.e.* relative chain displacement $\Delta z_j = 0$, equivalent to a triangular ferromagnet, right. (b) AgCN adopts a structure where relative chain displacements are $\Delta z_j = \pm\frac{1}{3}$, equivalent to the ground state of the triangular XY antiferromagnet. In each case the ground state average structure unit cell is highlighted in bold in the magnetic representations.

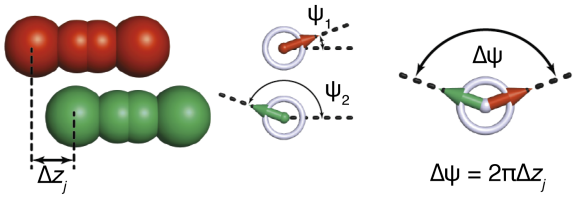

Figure 7.6: Relationship between structural and magnetic degrees of freedom in the trigonal XY system. The relative displacement between neighbouring chains, Δz_j, can be mapped uniquely onto a phase shift $\Delta\psi$ between corresponding XY spins.

where ρ is the relative strength factor determining whether metals align or anti-align, which can be interpreted in terms of the competing inter-chain interactions. Between each chain and its six neighbours two competing interactions are relevant: (i) electrostatic repulsion between oppositely-charged M^+ cations and CN^- anions ($\rho > 0$), and (ii) metallophilic attraction between neighbouring M^+ cations ($\rho < 0$). No assumptions are made as to the strength of these interactions, only their relative strengths. Switching between the dominant interaction (i) or (ii), the AgCN $\Delta z_j = \pm\frac{1}{3}$ and AuCN $\Delta z_j = 0$ structures result respectively from Monte Carlo simulation, in agreement with average structure analysis [Fig. 7.5].

It is possible to re-cast the single structural degree of freedom z_j as a phase angle $\psi_j = 2\pi z_j$ [Fig. 7.6]. The structural configurations consequently map directly onto the triangular arrangements of XY spins $\mathbf{S}_j = S(\cos\psi_j, \sin\psi_j)$ where the chain (for the structural system) or the spin (for the magnetic system) has one degree of freedom.* Spin arrangements corresponding to the AuCN and AgCN structures are shown in Figure 7.5, and are well known as the ground states of the nearest-neighbour XY triangular ferromagnet and antiferromagnet respectively [439].

The mapping between *structural* models considered here and *magnetic* equivalents has significance beyond pure coincidence. Similarities between the lattice geometry and effective degrees of freedom have already been highlighted; the form of the pairwise interactions has however been assumed. To show the form of the pairwise interaction is

---

* We use ψ here to define the phase angle rather than the more conventional θ used for magnetic spins to prevent confusion with scattering angle, θ.

reasonable (and how it is related to the magnetic analogues), quantum mechanical calculations were carried out to determine the form of the supramolecular interaction potential operating on neighbouring MCN chains as a function of phase, $\Delta\psi$ [Fig. 7.6]. We expect two contributions as detailed previously, and indeed our calculations confirm that for AuCN metallophilic interactions dominate (favouring collinear arrangement of chains, $\Delta\psi = 0$) but not in the case of AgCN (energy minimised at $\Delta\psi = \pm\pi$). Crucially, in both cases, the potentials are well approximated by their first-order Fourier component

$$E = J\cos(\Delta\psi), \tag{7.2}$$

with $J = -7.0\,\mathrm{kJ\,mol^{-1}}$ and $+3.7\,\mathrm{kJ\,mol^{-1}}$ for AuCN and AgCN respectively [Figs. 7.7 and 7.8]. Comparing to the spin Hamiltonian for the XY triangular (anti)ferromagent

$$\mathcal{H} = J_{\mathrm{XY}} \sum_{i,j} \mathbf{S}_i \cdot \mathbf{S}_j = J_{\mathrm{XY}} S^2 \sum_{i,j} \cos(\Delta\psi_{ij}), \tag{7.3}$$

where i, j index neighbouring spins, and $\Delta\psi_{i,j}$ describes the angle between spins i and j, the similarity is clear. As Eq. 7.2 approximates well the true interactions as determined by quantum mechanical calculations, there is a single controlling factor *i.e.* J_{XY} in magnetic notation, or the balancing factor ρ defined previously.

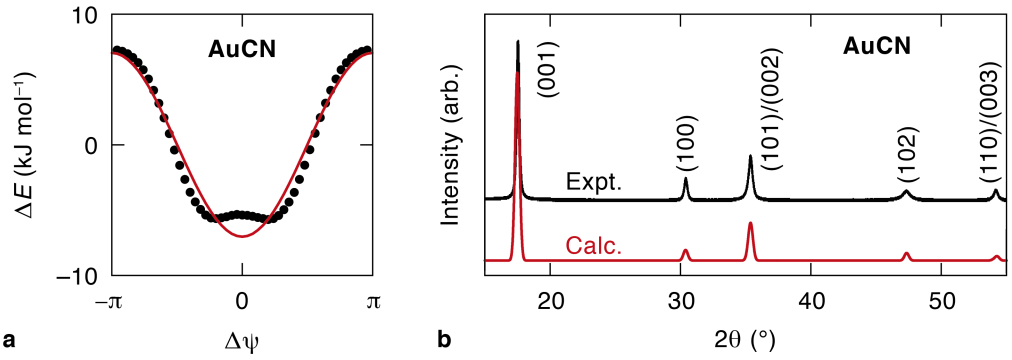

Figure 7.7: Interactions in AuCN. (a) The variation in enthalpy for a pair of AuCN chains from quantum mechanical calculations (black points) and from the first-order Fourier component (Eq. 7.2), separated by their equilibrium distances calculated as a function of phase shift $\Delta\psi$ (shown in Figure 7.6). (b) Comparison of the experimental and calculated X-ray diffraction pattern for AuCN. The structural model used for calculation of the diffraction pattern was derived from the ground state of the triangular XY ferromagnet.

These self-interacting potentials of AgCN and AuCN encodes two very different collective structures, much as the geometries of coordination chemistry building blocks encode differently-shaped polyhedral assemblies. Collective phenomena known to be important in determining the properties of the magnetic analogues may also be seen here, namely excitations and domain effects, particularly for the frustrated antiferromagnetic system equivalent to the solution for AgCN [440]. This system is frustrated as staggering chains by one half of the repeat length cannot be propagated on a triangular lattice, so it therefore adopts the lowest-energy compromise of displacements of $\pm\frac{1}{3}$. Such a system is noted for rich structural variety and how symmetry breaking is critical to the properties of a system based on an extremely simple set of interactions. In Monte Carlo simulations of this spin system it is found that within each triangle the spins arrange 120° to each other; the 'helicity' of each triangle—or 'plaquette'—is defined as $\sum(\Delta\Theta/2\pi)$ where $\Delta\Theta$ is the smallest clockwise change in angle when the triangle is traversed in the clockwise direction [Fig. 7.9] [440]. The inverse of the helicity pattern shown in Fig. 7.9(a) cannot be obtained by rotations alone, and some other symmetry operation like reflection. Domain wall formation is an elementary excitation within the system that separate regions of opposite helicity, where the wall is defined as plaquettes with zero helicity [Fig. 7.9(b)].

Some evidence is found from (quenched) Monte Carlo simulation that nanodomains may exist in the true structure of AgCN and there are symmetry-breaking boundary

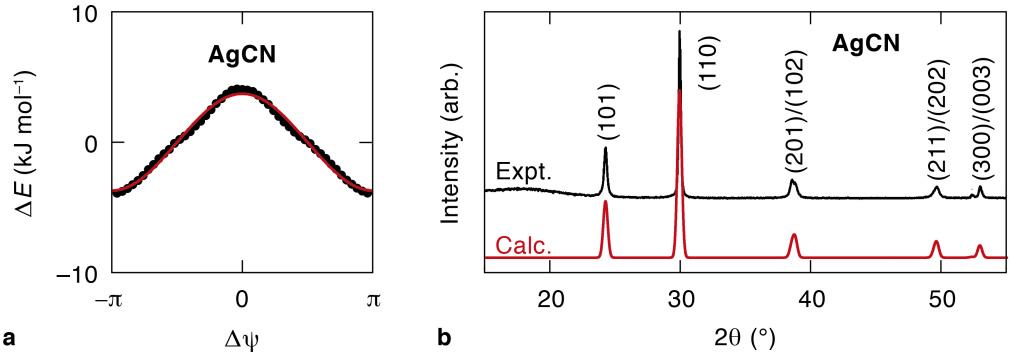

Figure 7.8: Interactions in AgCN. (a) The variation in enthalpy for a pair of AgCN chains and (b) comparison of the experimental and calculated X-ray diffraction pattern for AgCN. Here the structural model used for calculation of the diffraction pattern was derived from the ground state of the triangular XY antiferromagnet. Reflections are indexed and relate, for example, the (100) reflection of AuCN and the (110) reflection of AgCN.

regions, as described for the magnetic case, within our configurations [Fig. 7.9(d)]. The existence of these nano domains and grain boundaries would give rise to the selective peak broadening observed in previous diffraction studies [Fig. 7.8b], namely sharp profiles observed for $(hk0)$ reflections and broader reflections for those with any component of l in reciprocal space. These were previously suggested as being due to anisotropic size effects [415]. In conventional powder diffraction refinement techniques a hkl-dependent broadening of the type proposed by Stephens [429] can be used; a simple estimation of the domain size may be made using the Scherrer equation [441, 442]. From the data presented in Ref. 422, estimated size of domains in AgCN are 24.85 nm for the (101) peak, and 37.71 nm for the (110). The extent of broadening is dependent on the density of dislocations, but this broadening could also arise from shear deformations. In both cases higher-order Fourier components to the real interaction potential will influence subtle features, for example there is likeley to be some buckling of the cation layers in AuCN that arise because energy minima occur for small but nonzero values of $\Delta\psi$.

Mapping these structures onto the XY spin systems serves two purposes. Realisations of triangular magnets in real systems generally differ in their behaviour relative to the theoretical two-dimensional case [443]. So on the one hand we establish physical realisations of theoretical spin models which in principle enables aspects of the models to be tested and studied experimentally. On the other hand, our understanding of the theory of these magnets allows us to interpret and predict structural features (such as the ground

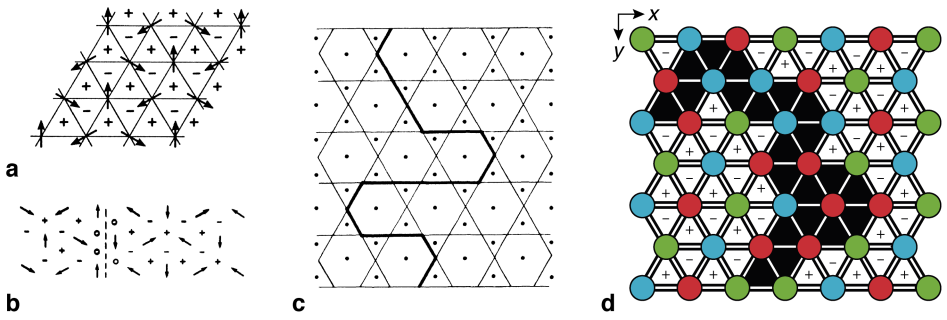

Figure 7.9: Grain boundaries in quenched Monte Carlo AgCN configurations. By colouring chains based on their height in the array of chains used in the simulation, we can see that in general each chain is surrounded by neighbours displaced by $\frac{1}{3}$ above or below (red = chain positioned between $z = 0 - \frac{1}{3}$, blue $z = \frac{1}{3} - \frac{2}{3}$ and green $z = \frac{2}{3} - 1$).

state) of the experimental systems themselves.

7.3.2 $(Ag_{1/2}Au_{1/2})CN$

Whilst the strict alternation of metals along each chain and their triangular packing is well-established in the mixed-metal system $(Ag_{1/2}Au_{1/2})CN$, the arrangement of chains relative to one another remains uncertain [422]. What is clear is that the X-ray diffraction pattern contains regions of structured diffuse scattering that are the signature of the correlated disorder within complex states [28]. There are several goals to exploring this system further: (i) establish the form of the self-interaction potential for Au–CN–Ag–CN–Au chains, (ii) determine a mapping onto a suitable XY triangular magnet, and (iii) interpret the experimental diffraction pattern in terms of a structural model determined by analogy to the corresponding magnetic system.

The energy profile determined by quantum mechanical calculations takes a more complex form than for the homometallic systems, in part due to the Ag/Au alternation and this alternation coupling to CN orientational ordering [417]. Simplifying this interaction we consider now the first two Fourier components that account for both the difference in strength of average metallophilic and electrostatic interactions (as before, now with periodicity $\Delta\psi = \pi$), and the difference in homometallic and hetermetallic interactions (periodicity $\Delta\psi = 2\pi$). It is noted that the phase shift $\Delta\psi$ has a slightly different meaning in this more complex system with both $\psi = 0$ and $\psi = \pi$ corresponding to situations with strong metallophilic interactions (differing if like or unlike atoms are in close contact). The resulting energy term is:

$$E = J_1 \cos(\Delta\psi) + \frac{J_2}{2} \cos(2\Delta\psi), \tag{7.4}$$

$$\equiv J_1 \cos(\Delta\psi) + J_2 \cos^2(\Delta\psi). \tag{7.5}$$

This approximation fits the overall shape near to the energy minimum well with $J_1 = +2.31\,\mathrm{kJ\,mol^{-1}}$ and $J_2 = -1.28\,\mathrm{kJ\,mol^{-1}}$. The small value of J_2 describes the small difference in the strength of average metallophilic and electrostatic interactions while the

strongly positive value of J_1 corresponds to a preference for heterometallic Ag$\cdots$Au rather than homometallic contacts Ag$\cdots$Ag or Au$\cdots$Au.

The relevant magnetic system is now the so-called bilinear biquadratic (BLBQ) XY system [413] characterised by the spin Hamiltonian

$$\mathcal{H} = J_1 \sum_{i,j} \cos(\Delta\psi_{ij}) + J_2 \sum_{i,j} \cos^2(\Delta\psi_{ij}). \tag{7.6}$$

The BLBQ model is most frequently used to describe $S = 1$ systems [444] with J_1 and J_2 terms quantifying the strength of dipolar and quadrupolar interactions, respectively. Considering for a moment the various possible combinations of J_1 and J_2 in the struc-

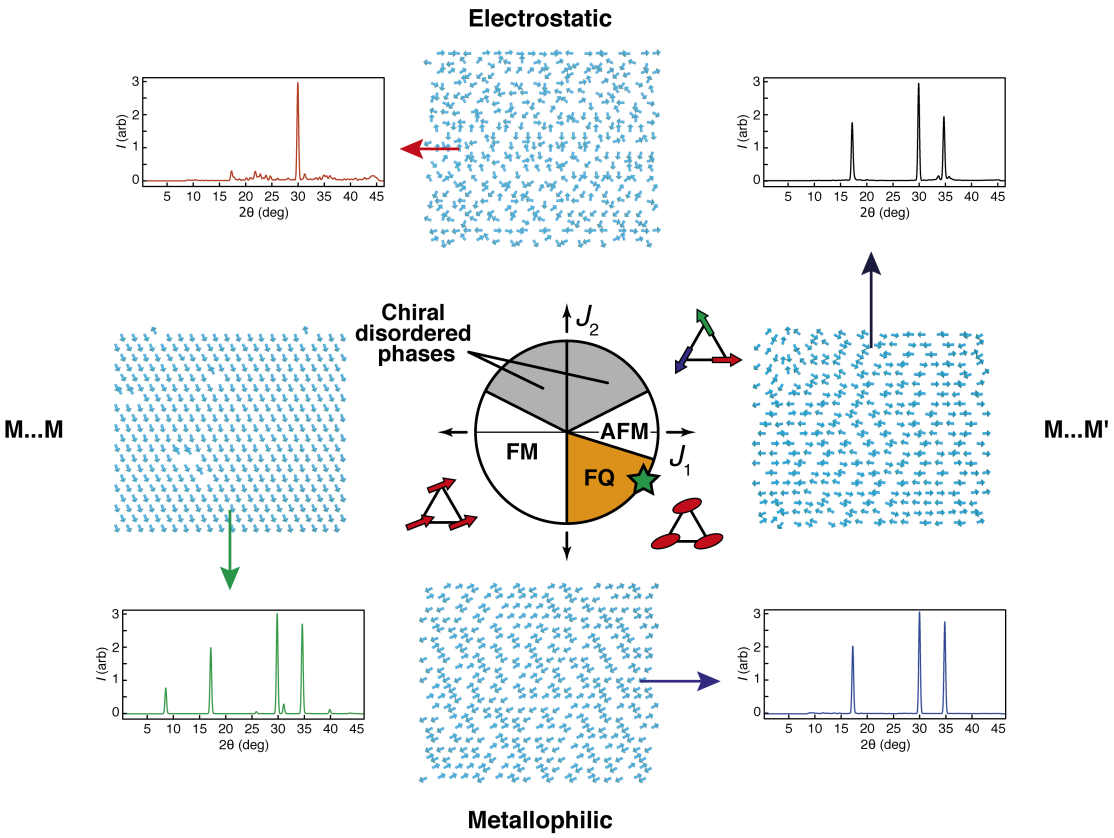

Figure 7.10: Experimental and simulated diffraction patterns for $(Ag_{1/2}Au_{1/2})CN$ using quenched Monte Carlo routines with the bilinear biquadratic Heisenberg potential. The equilibrium phase diagram for the BLBQ triangular XY model is known in theory (adapted from Ref. 413 (centre); quench Monte Carlo routines gives the finite temperature spin configurations shown at each point for various values of J_1,J_2 and result in the diffraction patterns shown for equivalent *structural* models of $(Ag_{1/2}Au_{1/2})CN$. The values of J_1,J_2 determined from quantum mechanical calculations indicate that the correct solution for $(Ag_{1/2}Au_{1/2})CN$ is in the ferroquadrupolar (FQ) region, marked with a green star.

tural system, we can simulate diffraction patterns of diverse possible structural models [Fig. 7.10]. This ranges from the 'double c' model where all Au and Ag are aligned in planes, a random double c AuCN, frustrated AuCN systems, and various complex AgCN-like phases. Our quantum mechanical calculations of J_1 and J_2 suggests the correct structure is in the bottom right quadrant of Figure 7.10, which also gives a quantitive fit to experimental data [Fig. 7.11].

For XY spins the thermodynamic phase diagram is known from theory [413]; the particular combination of J_1, J_2 found here corresponds to a complex "nematic" state in which dipolar disorder is coupled with (hidden) ferroquadrupolar order. This state has not been realised in a physical system [443]; the implication here is that the chains in $(Ag_{1/2}Au_{1/2})CN$ should align to bring metal cations in registry but with a preference for unlike Ag/Au neighbours. This system, like for AgCN, is frustrated as within any triplet of neighbouring M must contain one pair of like atoms. This solution is essentially a superposition of the family of acceptable solutions proposed previously in Ref. 422. Whilst the intensity distribution and reflection conditions are reproduced by a model based on strict quadrupolar order, the peak broadening is significantly underestimated.

This discrepancy in peak widths may be accounted for by considering the finite-temperature effects in the XY model. It has long been known that triangular XY magnets are unstable at finite temperature with respect to the spontaneous formation of spin vortices, which act to broaden Bragg reflections in the magnetic scattering patterns [445]. These structures are topologically-protected emergent quasi-particles with their own peculiar physics—*e.g.* the "K-T" transition that allows vortex unpinning at elevated temperatures [394]—which are themselves related to the magnetic skyrmion states of interest in data storage applications [446]. While it is known that Monte Carlo simulations of XY spin states are known to be extremely sensitive to finite size effects, the simple quench Monte Carlo routine driven by Eq. 7.6 does capture two essential features of interest to our study that also reproduce the experimental data, namely quadrupolar order and spin vortices [Fig. 7.11(b–d)]. The simulated diffraction pattern [Fig. 7.11(a)] has the

correct variation in both intensity and peak widths, showing that our model captures the key structural features of $(Ag_{1/2}Au_{1/2})CN$. Mapping between spin states and chain configurations has translated spin vortices into screw dislocations, which have become topologically-protected emergent objects responsible for the reproducible selective peak broadening observed.

7.4 Variable-pressure behaviour of AgCN

Analysis of the structural consequences of this mapping between supramolecular and magnetic interactions suggests there is scope for drawing similar parallels between excitations in and/or the responses to external stimuli (T, p, H). For example, are the screw dislocations fixed or mobile, and in the homometallic cyanides can the balance between

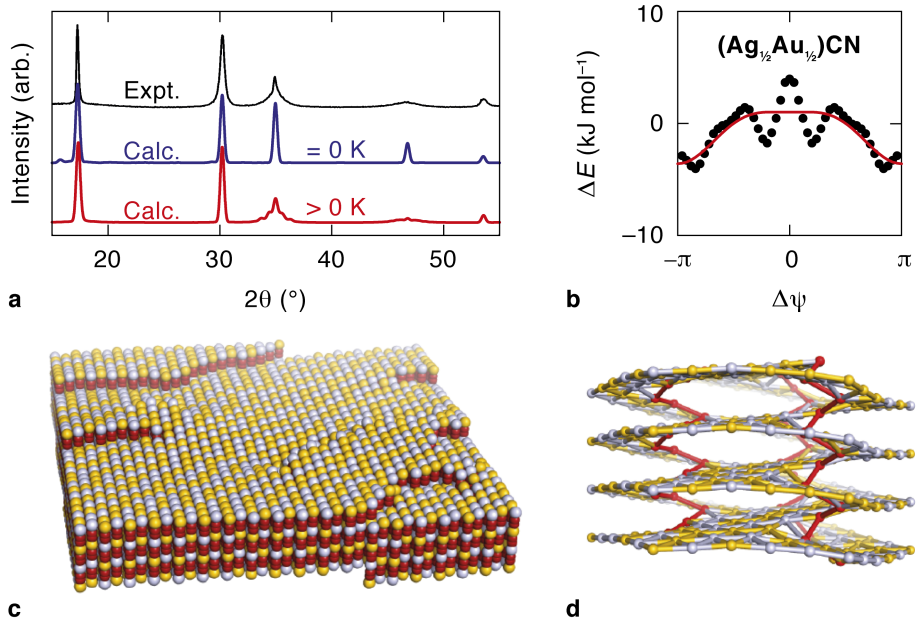

Figure 7.11: Diffraction data and structural models showing order/disorder in Monte Carlo models of $(Ag_{1/2}Au_{1/2})CN$. (a) The experimental (top) and simulated diffraction patterns for ground state (blue) and finite-temperature (red) models from Monte Carlo simulation. (b) The variation in enthalpy for a pair of $(Ag_{1/2}Au_{1/2})CN$ chains, separated by their equilibrium distance calculated as a function of phase shift $\Delta\psi$. Data are shown as filled circles, and the second-order Fourier component is shown as a red line. The parameters J_1, J_2 determined from the fit corresponds to the ferroquadrupolar (FQ) region shown in Fig. 7.10. (c) A representative Monte Carlo structural configuration generated as described in the text in this region show as a side-on representation (note the absence of Ag/Au order within layers) and in an expansed model where C and N atoms have been omitted showing three screw dislocations (vortexes) in red.

dominant metallophilic and electrostatic interactions be switched? Here we explore the variable-pressure response of AgCN for two reasons (i) the potential for unusual elastic properties, in particular NLC, and (ii) structure modification caused by the change in exchange parameters to force the structure into the AuCN-type structure.

Why should hydrostatic pressure cause this change in ground-state structure type? Key factors in the interchain interaction (electrostatic and metallophilic) have contrasting r dependence, where r is the distance between interacting bodies. For two oppositely-charged point charges (q_1, q_2) interacting electrostatically the dependence is given by

$$E_{\text{elec}} \propto \frac{1}{4\pi\varepsilon_0}\frac{q_1 q_2}{r}. \tag{7.7}$$

In contrast metallophilic interactions are dispersive-like and therefore have an interaction strength $E_{\text{metalo}} \propto r^{-6}$ as described in §1.4.3 [239]. On application of pressure the distance between metal chains will decrease (due to the thermodynamic requirement for volume decrease) and therefore the variation of the two structure-directing interactions will be different: the r^{-6}-dependence of metallophilicity means this interaction rapidly increases in strength and may become dominant. So, using pressure as a probe we might be able to cause the transformation of AgCN to a phase isostructural with AuCN.

Pawley refinement of lattice parameters from our variable-pressure X-ray diffraction data was possible at all pressures up to 20 GPa using the ambient pressure space group assignment $R\bar{3}m$ [Fig. 7.12]. The main structural change is clearly large and rapid decrease in the **a**-**b** plane resulting from weak inter-chain interactions. Calculation of compressibilities using empirical equations in these principal directions using PAScal [101] gives the following compressibilities: $K_a = 5.9(3)\,\text{TPa}^{-1}$, $K_c = -0.01(20)\,\text{TPa}^{-1}$ up to 20.5 GPa. The change in lattice parameters up to ~ 2.5 GPa suggests NLC in the c direction based on a linear fit of three data points ($K_c = -3.6(16)\,\text{TPa}^{-1}$). Fitting to the volume data is not robust using B-M EoS; the fit shown in Figure 7.12(b) results from a very small bulk modulus ($B_0 < 5$ GPa) and large positive first derivative ($B' \gg 4$).

This set of observations is consistent with the structural picture we have explored and

the elastic properties expected from a low-dimensional material such as AgCN. The very weak inter-chain interactions results in rapid compression in these directions and therefore volume collapse; the directions of strongest bonding (*i.e.* along the metal cyanide chain) are essentially incompressible as seen in all the wine-rack-like structures in previous chapters. Here small NLC arises from the dampening of the thermally-populated transverse vibrational modes that are responsible for the NTE in this direction. As pressure increases, these modes are suppressed causing expansion in the **c** direction.

As pressure is applied it was observed in our experiment that several sets of new Bragg reflections emerge in addition to those for the ambient-pressure $R\bar{3}m$ structure of AgCN. Here we face several challenges in resolving the origin of these peaks: (i) as pressure is applied all Bragg reflections broaden significantly and (ii) the experiment was carried out over a relatively short time period so kinetics may be hampering any phase transitions occurring. In general kinetics are expected to play a greater role for supramolecular analogues of frustrated magnets than the magnetic systems themselves given that the effective exchange energies involved are larger by one or two orders of magnitude. Furthermore here we might expect additional contributions from steric of packing efficiency at high pressure due to the requirement to reduce volume, potentially favouring the off-set chain model rather than bringing chains into registry.

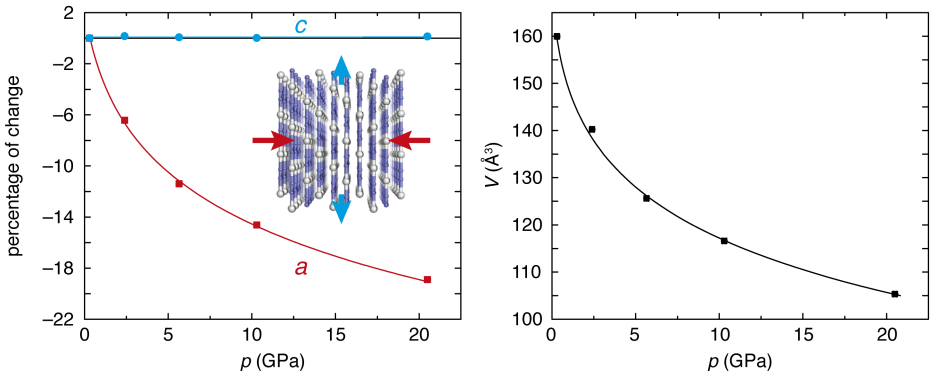

Figure 7.12: Pressure-response of AgCN up to 20 GPa showing rapid decrease in inter-chain separation. (left) Upon application of hydrostatic pressure to over 20 GPa AgCN collapses rapidly in the **a** direction and is essentially incompressible in the **c** direction. This is as a result of weak inter-chain interactions allowing rapid compression in these directions, whilst the direction with strongest bonding is much less compressible. (right) Rapid volume decrease fitted to a third-order B-M EoS gives a very large value of B' and small B_0.

There is scope for optimism though in this preliminary experiment. At the highest pressures investigated a set of Bragg reflections is observed that is consistent with a AuCN-structured AgCN that would come about by inversion of J_{eff} as argentophilic interaction energies increase more rapidly than electrostatic contribution [Fig. 7.13]. At intermediate pressures additional peaks persist that may be related to either phase, and indeed the expected close relationship between the two unit cells ($P6/mmm$ and $R\bar{3}m$) makes differentiating superlattice reflections from new phases very difficult [Appendix C, §C.6]. We can conclude however that the emergence of a Bragg peak at low 2θ ($\sim 3.5°$) shows additional symmetry elements in the unit cell associated by planes of atoms separated by $\frac{1}{2}\mathbf{c}$ (which may by the AuCN-like cell) and that the presence of local minima in the self-interaction potential (as seen for $(Ag_{1/2}Au_{1/2})CN$ in Fig. 7.11(b)) means the high-pressure behaviour of these materials is necessarily complex.

7.5 Implications

The relationship between simple metal cyanides, low-dimensional structure and exotic 2D spin systems might at first seem unlikely. Before further discussion, the other main conclusions of this chapter are summarised. Firstly, we show the surprising direct mapping of frustrated magnetism to the structures of low-dimensional cyanides. The struc-

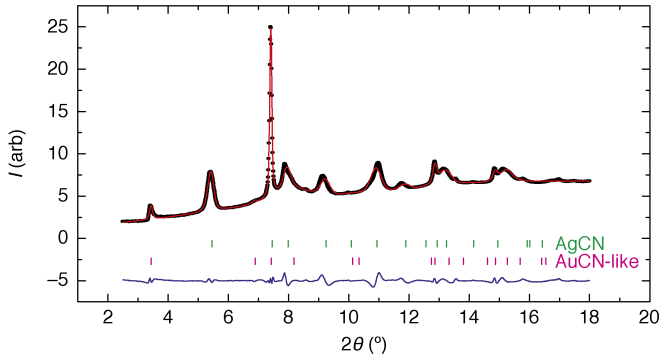

Figure 7.13: Pawley refinement of synchrotron X-ray diffraction data for AgCN at 20.5 GPa showing emergence of an AuCN-like phase. Synchrotron X-ray diffraction data shown as a function of 2θ ($\lambda = 0.309960$ Å) as black markers, fit as a red line, difference (data–fit) as blue line displaced downwards by five increments. Green tick marks show expected peak positions for AgCN ($R\bar{3}m$) with refined lattice parameters $a = 4.766(3)$ Å, $c = 5.287(5)$ Å; pink tick marks for AuCN-like AgCN ($P6/mmm$) with refined lattice parameters $a = 2.7658(11)$ Å, $c = 5.1587(10)$ Å.

tures of AgCN, AuCN and $(Ag_{1/2}Au_{1/2})CN$ are related to the ground state of the XY-antiferromagnetic, ferromagnetic and bilinear biquadratic XY systems by considering displacements in the chain direction as equivalent to spin orientations in a 2D systems.

Our route of investigation in this chapter allows exploration of the underlying relationship between disorder and dynamics, as suggested in Chapter 1 and found elsewhere [185, 202]. The dominance of strong local interactions results in structures that are both mechanically flexible (and show unusual mechanical properties) and show interesting structural disorder. Here, perhaps more than any previous chapter, we see this relationship and the implications for future studies of framework materials. Furthermore we have seen how the interaction potential encoded within a material fragment can be tuned chemically to give rise to a variety of structural phases, the nature of which is remarkably reliably predicted by mapping onto geometrically-related problems.

This rich ordering behaviour is evidenced through the diffraction pattern. So by examining these chemical systems with simple pairwise inter-chain interactions it appears to be possible to study exotic states that have been proposed but not yet realised in real systems. There are few magnetic systems that are strictly two-dimensional in nature, because some degree of interaction in a perpendicular direction always persists [447]. Chemical analogues offer a neat solution to this problem: one-dimensional polymers can behave as single collective objects, with the interactions between them then strictly two-dimensional. In this way, aggregates of polar polymer chains have provided some of the first physical realisations of the canonical triangular and square Ising lattices [397, 448, 449] and have been used to generate complex collective states based on geometric frustration [406].

Interest in exotic collective states is not only fundamental: topologically-protected emergent spin vortices in the skyrmion phases of chiral ferromagnets offer a possible mechanism of ultra-dense data storage [450], and monopole quasiparticles in spin ices may yet be exploited in the emerging field of "magnetronics" [451]. Indeed our study of the variable-pressure response of AgCN has shown that the kinetic effects have the

advantage of stabilising the most interesting phases to ambient conditions—as would be necessary if topological states are actually to be employed in data storage technology—but that interpreting these interesting new statures is difficult when considering only equilibrium models (arguably the mainstay in the field of frustrated magnetism).

Comparing Monte Carlo models to powder diffraction patterns of $(Ag_{1/2}Au_{1/2})CN$ confirms—for the first time—key features of the bilinear biquadratic XY antiferromagnet on a triangular lattice, a system that has been extensively investigated in theory but never found experimentally. Although the system itself is not magnetic this work confirms that in the ferroquadrupolar region we observe the emergence of vortex dislocations in the structure. These vortices account directly for the observed peak broadening of $(Ag_{1/2}Au_{1/2})CN$, with a higher density of vortices giving greater peak broadening. As shown in Figure 7.10, this structure is a direct result of the competition between metallophilicity and dissimilar $M\cdots M'$ neighbours.

The pressure study on AgCN attempted to perturb this system in such a way as to effect the transition between structure types, *i.e.* from antiferro- to ferromagnetically coupled chains. We so see evidence for this (kinetically hindered) transformation between AgCN and AuCN-like structures of AgCN at high pressure (20.5 GPa). Furthermore the elastic behaviour of AgCN is as expected for a low-dimensional material: large positive compressibility is observed in the intra-chain directions and the material is essentially incompressible in the chain direction. In the low-pressure region, NLC is observed in the chain direction due to the suppression of transverse vibrational modes, suggesting a continued correspondence between NTE and NLC. Such a relationship in other low-dimensional materials is a promising avenue for future research.

Chapter 8

Conclusions and future work

I began this thesis by stating that molecular frameworks have given rise to some of the most exciting developments in materials science in the last decade. This is certainly an opinion—so here I reflect on this extraordinary field, what the work presented in this thesis might have added to our understanding, and possible future directions. In this thesis, exploring the structure and responses of a diverse range of cyanide materials has revealed exceptional properties, beautiful structures and unexpected links to other areas of condensed matter physics that helps guide our understanding of each. These properties arise from mechanical, displacive and configurational degeneracy, a consequence of structural underconstraint: molecular frameworks have proved to be a versatile class of materials that can be used in the study of diverse structural phenomena.

Negative linear compressibility was once thought to be an exceptionally rare material property. Furthermore, the responses typically found in traditional NLC materials were very much smaller than the typical positive compressibilities of engineering materials, so making them impractical for application. Despite this, it was known that these materials could make existing pressure sensors ten times more sensitive, be used in smart materials for controlling circuits or directing beams of light, or even to create artificial muscles that respond to pressure, rather than electrical signals. Through this thesis structural motifs responsible for NLC have been examined, including a comprehensive review of NLC materials.

This work lays out a grounding for the rational design of NLC materials. The chemistry of molecular frameworks has opened up the possibility of large, sustained, and functional NLC in a wide variety of materials. By understanding framework materials from a mechanistic point-of-view developed through Chapters 3 and 4, materials are identified that are shown to have record-breaking properties. Such materials may be the basis for the first application of NLC materials. Using measures such as the 'compressibility capacity'

optimisation of materials is possible: in the extended perovskite-like family of materials, for example, we show rules based on cation size, counter ion size and choice of d^{10} metal can predictably adjust the range and magnitude of response use of NLC, *i.e.* moving along lines of constant χ_K on the Ashby-type diagram presented in Chapter 2.

Maximising both magnitude and range of negative response is found to be possible by considering supramolecular motifs in materials design. Collective states—such as the aurophilic 'springs' found in zinc dicyanoaurate—are capable of enhancing responses beyond what individual bonds or interactions might allow. So 'giant' NLC is found for the first time. Developing multi-component assemblies within frameworks (or indeed in molecular materials) is an exciting avenue for future work. Learning from supramolecular chemistry itself, where the chemist has exceptional control over the connectivity of relatively simple building blocks into complex new states, there are many exciting structures that could be incorporated into frameworks. Very recent work has demonstrated some of these and some remain to be investigated: *e.g.* molecular machine shuttles, catalytic active sites, or cross-linking motifs that make materials as compressible as foam. Indeed the coupling of advanced functionalities—electronic, magnetic, piezo and thermo-responsive properties—is a major aim of the field. There have been recent reports of some of these phenomena with the only limitation being our collective imagination to come up with new structural designs.

A property that there is a strong link with NLC is negative thermal expansion (NTE). So for cross-linked 'wine-rack'-type frameworks NTE is a strong predictor for NLC (with a notable exception where close proximity to a critical ratio gives opposite responses, Ref. 129). But there also appears to be a more indirect correspondence between unusual properties in these flexible materials. For example, in the isotropic NTE material zinc(II) cyanide a 'ferroelastic' phase transition from the ambient phase cubic structure to the orthorhombic high-pressure structure gives rise to large NLC above 1.52 GPa. This phase transition behaviour has never before been determined, and it provides important insights into the thermomechanical response of the parent material. For the first time the specific

flexibility modes that give rise to the large NTE response are identified. Here I also describe how the behaviour of a range of molecular frameworks isostructural with $Zn(CN)_2$ are very similar, demonstrating the importance of underlying framework topology on determining dynamical responses.

The spontaneous assembly of simple building blocks into complex *dis*ordered states (by virtue of structural constraints) is most commonly found in the field of magnetism, where the demands of the atomic and magnetic structure can be conflicting. Yet I show how molecular assemblies controlled by simple pairwise interactions might also have a propensity to mimic disordered states most commonly associated with magnetism, *e.g.* ice-like and geometrically frustrated states. The structures and properties of the 'simple' chain cyanides, AgCN, AuCN and $(Ag_{1/2}Au_{1/2})CN$, can be considered in this way, where the relative displacement of chains is governed by pairwise interactions. Mapping this displacement to the rotations of XY spins in the 2D triangular system, the ground state structures of AgCN and AuCN are equivalent to those of the antiferro- and ferromagnetic states. Extending this analysis to the mixed-metal system, addition of extra pairwise interactions maps directly to the bilinear biquadratic XY antiferromagnet. Essential features of this theoretical magnetic system are confirmed in a real (structural) system for the first time, including 'hidden' metal order and vortex excitations. Furthermore we have seen preliminary evidence for the ability to control these structural states with physical stimuli, so forcing AgCN into the alternative AuCN structure-type.

This approach of using simple building blocks—with well-known interactions and geometries—to spontaneously assemble together such that there is a mismatch between local and average symmetry may be very powerful in the study of other disordered systems. Collective states like these may be used to study fundamental interactions and excitations not otherwise accessible. Structural underconstraint may also give rise to unusual functionalities, for example NLC in low-dimensional chain or columnar systems, or NAC in layered systems.

If there is one key result of this thesis, it is that by exploiting degrees of freedom—be

they mechanical or configurational—a variety of interesting, counterintuitive and potentially important properties can be engineered in molecular frameworks. My hope is that the studies presented in this thesis may act as intriguing case studies that illustrate new opportunities and better understanding of cyanides and molecular frameworks more generally, and that this may contribute to the ongoing development of this field.

Bibliography

[1] Cox, P. A. *The Electronic Structure and Chemistry of Solids* (Oxford University Press, Oxford, 1987).

[2] Greenwood, N. N. & Earnshaw, A. *Chemistry of the Elements* (Butterworth-Heinemann, Oxford, 1997), 2nd edn.

[3] Kihara, K. An X-ray study of the temperature dependence of the quartz structure. *Eur. J. Miner.* **2**, 63–78 (1990).

[4] Maes, M., Vermoortele, F., Alaerts, L., Couck, S., Kirschhock, C. E. A., Denayer, J. F. M. & De Vos, D. E. Separation of styrene and ethylbenzene on metal–organic frameworks: Analogous structures with different adsorption mechanisms. *J. Am. Chem. Soc.* **132**, 15277–15285 (2010).

[5] Edelman, G. M. & Gally, J. A. Degeneracy and complexity in biological systems. *Proc. Nat. Acad. Sci. U.S.A.* **98**, 13763–13768 (2001).

[6] Whitacre, J. Degeneracy: a link between evolvability, robustness and complexity in biological systems. *Theor. Bio. Med. Modelling* **7**, 6(17) (2010).

[7] Dove, M. T. *Structure and Dynamics.* Oxford Master Series in Condensed Matter Physics (Oxford University Press, Oxford, 2003).

[8] Dove, M. T. Theory of displacive phase transitions in minerals. *Am. Mineral.* **82**, 213–244 (1997).

[9] Tolédano, J.-C. & Tolédano, P. *The Landau Theory of Phase Transitions: Application to Structural, Incommensurate, Magnetic, and Liquid Crystal Systems.* No. 3 in World Scientific Lecture Notes in Physics (World Scientific, Singapore, 1987).

[10] Guy, A. Reconstructive and displacive phase transformations. *Metall. Trans.* **3**, 2535–2536 (1972).

[11] Fennell, T., Deen, P. P., Wildes, A. R., Schamlzl, K., Prabhakaran, D., Boothroyd, A. T., Aldus, R. J., McMorrow, D. F. & Bramwell, S. T. Magnetic coulomb phase in the spin ice $Ho_2Ti_2O_7$. *Science* **326**, 415–417 (2009).

[12] Božin, E., Malliakas, C. D., Souvatzis, P., Proffen, T., Spaldin, N. A., Kanatzidis, M. G. & Billinge, S. J. L. Entropically stabilized local dipole formation in chalcogenides. *Science* **330**, 1660–663 (2010).

[13] Xu, G., Zhong, Z., Bing, Y., Ye, Z.-G. & Shirane, G. Electric-field-induced redistribution of polar nano-regions in a relaxor ferroelectric. *Nature Mater.* **5**, 134–140 (2006).

[14] Ramirez, A. P. Strongly geometrically frustrated magnets. *Annu. Rev. Mater. Sci.* **24**, 453–480 (1994).

[15] Rosenberg, H. M. *The Solid State* (Oxford University Press, Oxford, 2000), 3rd edn.

[16] Damasceno, P. F., Engel, M. & Glotzer, S. C. Predictive self-assembly of polyhedra into complex structures. *Science* **337**, 453–457 (2012).

[17] Haji-Akbari, A., Engel, M., Keys, A. S., Zheng, X., Petschek, R. G., Palffy-Muhoray, P. & Glotzer, S. C. Disordered, quasicrystalline and crystalline phases of densely packed tetrahedra. *Nature* **462**, 773–777 (2009).

[18] Ramirez, A., Broholm, C., Cava, R. & Kowach, G. Geometrical frustration, spin ice and negative thermal expansion — the physics of underconstraint. *Physica B: Cond. Matter* **280**, 290–295 (2000).

[19] Mosseri, R. Geometrical frustration and defects in condensed matter systems. *C. R. Chimie* **11**, 192–197 (2008).

[20] Klement, W. & Willens, R. H. Non-crystalline structure in solidified gold–silicon alloys. *Nature* **187**, 869–870 (1960).

[21] Zachariasen, W. H. The atomic arrangement in glass. *J. Am. Chem. Soc.* **54**, 3841–3851 (1932).

[22] Cliffe, M. J., Dove, M. T., Drabold, D. A. & Goodwin, A. L. Structure determination of disordered materials from diffraction data. *Phys. Rev. Lett.* **104**, 125501 (2010).

[23] Huang, P. Y., Kurasch, S., Srivastava, A., Skakalova, V., Kotakoski, J., Krasheninnikov, A. V., Hovden, R., Mao, Q., Meyer, J. C., Smet, J., Muller, D. A. & Kaiser, U. Direct imaging of a two-dimensional silica glass on graphene. *Nano Lett.* **12**, 1081–1086 (2012).

[24] Polk, D. E. & Boudreaux, D. S. Tetrahedrally coordinated random-network structure. *Phys. Rev. Lett.* **31**, 92–95 (1973).

[25] Pauling, L. *The Nature of the Chemical Bond* (Cornell University Press, Ithaca, NY, 1966).

[26] Ramirez, A. P., Hayashi, A., Cava, R. J., Siddharthan, R. & Shastry, B. S. Zero-point entropy in 'spin ice'. *Nature* **399**, 333–335 (1999).

[27] Proffen, T. & Neder, R. B. DISCUS, a program for diffuse scattering and defect structure simulations. *J. Appl. Crystallogr.* **30**, 171–175 (1997).

[28] Keen, D. A. & Goodwin, A. L. The crystallography of correlated disorder. *Nature* **521**, 303–309 (2015).

[29] Fairbank, V. E., Thompson, A. L., Cooper, R. I. & Goodwin, A. L. Charge-ice dynamics in the negative thermal expansion material $Cd(CN)_2$. *Phys. Rev. B* **86**, 104113 (2012).

[30] Loidl, A. Orientational glasses. *Annu. Rev. Phys. Chem.* **40**, 29–60 (1989).

[31] Clarke, J. B., Hastie, J. W., Kihlborg, L. H. E., Metselaar, R. & Thackeray, M. M. Definitions of terms relating to phase transitions of the solid state, IUPAC Recommendations. *Pure Appl. Chem.* **66**, 577–594 (1994).

[32] Zhong, W. & Vanderbilt, D. Competing structural instabilities in cubic perovskites. *Phys. Rev. Lett.* **74**, 2587–2590 (1995).

[33] Hammonds, K. D., Dove, M. T., Giddy, A. P., Heine, V. & Winkler, B. Rigid-unit phonon modes and structural phase transitions in framework silicates. *Am. Mineral.* **81**, 1057–1079 (1996).

[34] Landau, L. On the theory of phase transitions. *Ukr. J. Phys.* **53**, 25–35 (2008). Translated and reprinted from Landau L. D. "Collected Papers" (Nauka, Moscow, 1969), Vol. 1, 234–252. Originally published in *Zh. Eksp. Teor. Fiz.* **7**, 19–32 (1937).

[35] Levin, I., Krayzman, V. & Woicik, J. C. Local structure in perovskite $(Ba,Sr)TiO_3$: Reverse Monte Carlo refinements from multiple measurement techniques. *Phys. Rev. B* **89**, 024106 (2014).

[36] Chapman, K. W., Hagen, M., Kepert, C. J. & Manuel, P. Low energy phonons in the NTE compounds $Zn(CN)_2$ and $ZnPt(CN)_6$. *Physica B: Cond. Matter* **385-386**, 60–62 (2006).

[37] Goodwin, A. L. & Kepert, C. J. Negative thermal expansion and low-frequency modes in cyanide-bridged framework materials. *Phys. Rev. B* **71**, 140301(R) (2005).

[38] Umantsev, A. *Field Theoretic Method in Phase Transformations*, vol. 840 of *Lect. Notes Phys.* (Springer, Heidelberg, 2012).

[39] Giddy, A. P., Dove, M. T., Pawley, G. S. & Heine, V. The determination of rigid-unit modes as potential soft modes for displacive phase transitions in framework crystal structures. *Acta Crystallogr.* A**49**, 697–703 (1993).

[40] Cai, Y. & Thorpe, M. F. Floppy modes in network glasses. *Phys. Rev. B* **40**, 10535–10542 (1989).

[41] Hammonds, K. D., Dove, M. T., Giddy, A. P. & Heine, V. CRUSH: A Fortran program for the analysis of the rigid-unit mode spectrum of a framework structure. *Am. Mineral.* **79**, 1207–1209 (1994).

[42] Blundell, S. & Blundell, K. M. *Concepts in Thermal Physics* (Oxford University Press, Oxford, 2010).

[43] Tucker, M. G., Dove, M. T. & Keen, D. A. Simultaneous analysis of changes in long-range and short-range structural order at the displacive phase transition in quartz. *J. Phys.: Condens. Matter* **12**, L723 (2000).

[44] Wells, A. F. *Structural Inorganic Chemistry* (Clarendon Press, Oxford, 1984), 5th edn.

[45] Abraham, T. & McWilliams, A. *BCC Research Report NAN015F*, chap. Advanced Ceramics and Nanoceramic Powders (BCC Research LLC: Wellesley, MA, 2011).

[46] Shirane, G., Hoshino, S. & Suzuki, K. X-ray study of the phase transition in lead titanate. *Phys. Rev.* **80**, 1105–1106 (1950).

[47] Nelmes, R. J. & Kuhs, W. F. The crystal structure of tetragonal $PbTiO_3$ at room temperature and at 700 K. *Solid State Commun.* **54**, 721–723 (1985).

[48] Dove, M. T., Gambhir, M., Hammonds, K. D., Heine, V. & Pryde, A. K. A. Distortions of framework structures. *Phase Transit.* **58**, 121–143 (1996).

[49] Férey, G. & Parmentier, J. The pyrochlore $\rightarrow$ HTP $\rightarrow$ ReO_3 successive phase-transitions of FeF_3. *Eur. J. Solid State Inorg. Chem.* **31**, 697–704 (1994).

[50] Meyer, G. M., Nelmes, R. J. & Hutton, J. High resolution (direct space) studies of anharmonic motion associated with the structural phase transition in $SrTiO_3$. *Ferroelectrics* **21**, 461–462 (1978).

[51] Hui, Q., Tucker, M. G., Dove, M. T., Wells, S. A. & Keen, D. A. Total scattering and reverse Monte Carlo study of the 105 K displacive phase transiton in strontium titanate. *J. Phys.: Condens. Matter* **17**, S111–S124 (2005).

[52] Glazer, A. M. The classification of tilted octahedra in perovskites. *Acta Crystallogr.* B**28**, 3384–3392 (1972).

[53] Angel, R. J., Zhao, J. & Ross, N. L. General rules for predicting phase transitions in perovskites due to octahedral tilting. *Phys. Rev. Lett.* **95**, 025503 (2005).

[54] Hammonds, K. D., Bosenick, A., Dove, M. T. & Heine, V. Rigid unit modes in crystal structures with octahedrally coordinated atoms. *Am. Mineral.* **83**, 476–479 (1998).

[55] Férey, G. & Serre, C. Large breathing effects in three-dimensional porous hybrid matter: facts, analyses, rules and consequences. *Chem. Soc. Rev.* **38**, 1380–1399 (2009).

[56] Ackland, G. J. & Warren, M. C. Soft-mode phase transitions from first principles. *Phase Transit.* **61**, 215–223 (1997).

[57] Stirling, W. G. Neutron inelastic scattering study of the lattice dynamics of strontium titanate. *J. Phys. C: Solid State Phys.* **5**, 2711–2730 (1972).

[58] Goldschmidt, V. M. Die gesetze der krystallochemie. *Naturwissensch.* **14**, 477–485 (1926).

[59] Howard, C. J. & Stokes, H. T. Group-theoretical analysis of octahedral tilting in perovskites. *Acta Crystallogr.* B**54**, 782–789 (1998).

[60] Drake, M. J. & Righter, K. Determining the composition of the earth. *Nature* **416**, 39–44 (2002).

[61] Döhler, G. H., Dandolof, R. & Bilz, H. A topological-dynamical model of amorphicity. *J. Non-Cryst. Solids* **42**, 87–96 (1980).

[62] Tucker, M. G., Squires, M. P., Dove, M. T. & Keen, D. A. Dynamic structural disorder in cristobalite: Neutron total scattering measurement and reverse Monte Carlo modelling. *J. Phys.:Condens. Matter* **13**, 403–423 (2001).

[63] Carpenter, M. A., Salje, E. K., Graeme-Barber, A., Wruck, B., Dove, M. T. & Knight, K. S. Calibration of excess thermodynamic properties and elastic constant variations associated with the $\alpha \rightarrow \beta$ phase transition in quartz. *Am. Mineral.* **83**, 2–22 (1998).

[64] Schmahl, W. W., Swainson, I. P., Dove, M. T. & Graeme-Barber, A. Landau free energy and order parameter behaviour of the $\alpha - \beta$ phase transition of cristobalite. *Z. Kristallogr.* **201**, 125–145 (1992).

[65] Ming, L. C., Manghnani, M. H., Matsui, T. & Jamieson, J. C. Phase transformations and elasticity in rutile-structured difluorides and dioxides. *Phys. Earth Planet. Inter.* **23**, 276–285 (1980).

[66] Cotton, F. A. & Wilkinson, G. *Advanced Inorganic Chemistry* (Wiley, New York, 1988), 5th edn.

[67] Peercy, P. S., Fritz, I. J. & Samara, G. A. Temperature and pressure dependences of the properties and phase transition in paratellurite (TeO_2): ultrasonic, dielectric and Raman and Brillouin scattering results. *J. Phys. Chem. Solids* **36**, 1105–1122 (1975).

[68] Haines, J., Léger, J. M. & Hoyau, S. Second-order rutile-type to $CaCl_2$-type phase transition in β-MnO_2 at high pressure. *J. Phys. Chem. Solids* **56**, 965–973 (1995).

[69] Worlton, T. G. & Beyerlein, R. A. Structure and order parameters in the pressure-induced continuous transition in TeO_2. *Phys. Rev. B* **12**, 1899–1907 (1975).

[70] Anderson, P. W. & Blount, E. I. Symmetry considerations on Martensitic transformations:"ferroelectric" metals? *Phys. Rev. Lett.* **14**, 217–219 (1965).

[71] Ortiz, A. U., Boutin, A., Fuchs, A. H. & Coudert, F.-X. Metal–organic frameworks with wine-rack motif: What determines their flexibility and elastic properties? *J. Chem. Phys.* **138**, 174703 (2013).

[72] Batten, S. R., Champness, N. R., Chen, X.-M., Garcia-Martinez, J., Kitagawa, S., Öhrström, L., O'Keeffe, M., Suh, M. P. & Reedijk, J. Terminology of metal–organic frameworks and coordination polymers (IUPAC Recommendations 2013). *Pure Appl. Chem.* **85**, 1715–1724 (2013).

[73] Ortiz, A. U., Springuel-Huet, M.-A., Coudert, F.-X., Fuchs, A. H. & Boutin, A. Predicting mixture coadsorption in soft porous crystals: Experimental and theoretical study of CO_2/CH_4 in MIL-53(Al). *Langmuir* **28**, 494–498 (2012).

[74] Beurroies, I., Boulhout, M., Llewellyn, P. L., Kuchta, B., Férey, G., Serre, C. & Denoyel, R. Using pessure to provoke the structural transition of metal–organic frameworks. *Angew. Chem. Int. Ed.* **49**, 7526–7529 (2010).

[75] Millange, F., Serre, C. & Férey, G. Synthesis, structure determination and properties of MIL-53*as* and MIL-53*ht*: the first Cr^{III} hybrid inorganic-organic microporous solids: $Cr^{III}(OH)\cdot\{O_2C\text{-}C_6H_4\text{-}CO_2\}\cdot\{HO_2C\text{-}C_6H_4\text{-}CO_2H\}_x$. *Chem. Commun.* 822–823 (2002).

[76] Ortiz, A. U., Boutin, A., Fuchs, A. H. & Coudert, F.-X. Anisotropic elastic properties of flexible metal–organic frameworks: How soft are soft porous crystals? *Phys. Rev. Lett.* **109**, 195502 (2012).

[77] Jasuja, H., Jiao, Y., Burtch, N. C., Huang, Y.-g. & Walton, K. S. Synthesis of cobalt, nickel, copper, and zinc-based, water-stable, pillared metal–organic frameworks. *Langmuir* **30**, 14300–14307 (2014).

[78] Goodwin, A. L., Keen, D. A. & Tucker, M. G. Large negative linear compressibility of $Ag_3[Co(CN)_6]$. *Proc. Nat. Acad. Sci. U.S.A.* **105**, 18708–18713 (2008).

[79] Goodwin, A. L., Calleja, M., Conterio, M. J., Dove, M. T., Evans, J. S. O., Keen, D. A., Peters, L. & Tucker, M. G. Colossal positive and negative thermal expansion in the framework material $Ag_3[Co(CN)_6]$. *Science* **319**, 794–797 (2008).

[80] Pauling, L. & Pauling, P. A trireticulate crystal structure: trihydrogen cobalticyanide and trisilver cobalticyanide. *Proc. Nat. Acad. Sci. U.S.A.* **60**, 362–367 (1968).

[81] Conterio, M. J., Goodwin, A. L., Tucker, M. G., Keen, D. A., Dove, M. T., Peters, L. & Evans, J. S. O. Local structure in $Ag_3[Co(CN)_6]$: Colossal thermal expansion, rigid unit modes and argentophilic interactions. *J. Phys.: Condens. Matter* **20**, 255225 (2008).

[82] Serre, C., Millange, F., Thouvenot, C., Noguès, M., Marsolier, G., Louër, D. & Férey, G. Very large breathing effect in the first nanoporous chromium(III)-based solids: MIL-53 or $Cr^{III}(OH)\cdot\{O_2CC_6H_4CO_2\}\cdot\{HO_2CC_6H_4CO_2H\}_x\cdot H_2O_y$. *J. Am. Chem. Soc.* **124**, 13519–13526 (2002).

[83] Newnham, R. E. *Properties of Materials: Anisotropy, Symmetry, Structure* (Oxford University Press, Oxford, 2005).

[84] Marmier, A., Ntoahae, P. S., Ngoepe, P. E., Pettifor, D. G. & Parker, S. C. Negative compressibility in platinum sulfide using density-functional theory. *Phys. Rev. B* **81**, 172102 (2010).

[85] Nye, J. F. *Physical Properties of Crystals: Their Representation by Tensors and Matrices* (Clarendon Press, Oxford, 1984).

[86] Hazen, R. M. & Downs, R. T. (eds.) *High-Temperature and High-Pressure Crystal Chemistry*, vol. 41 (Mineralogical Society of America Blacksburg, VA, USA, 2000).

[87] Evans, K. E. & Alderson, A. Auxetic materials: Functional materials and structures from lateral thinking! *Adv. Mater.* **12**, 617–628 (2000).

[88] Baughman, R. H. Auxetic materials: Aoiding the shrink. *Nature* **425**, 667–667 (2003).

[89] Evans, K. E. Auxetic polymers: a new range of materials. *Endeavour* **15**, 170–174 (1991).

[90] Grima, J. N., Caruana-Gauci, R., Attard, D. & Gatt, R. Three-dimensional cellular structures with negative Poisson's ratio and negative compressibility properties. *Proc. R. Soc. A* **468**, 3121–3138 (2012).

[91] Liu, Y. & Hu, H. A review on auxetic structures and polymeric materials. *Sci. Res. Essays* **5**, 1052–1063 (2010).

[92] Neumann, F. E. *Vorlesungen Über die Theorie der Elastizität der Festen Körper und des Lichtäthers* (B. G. Teubner-Verlag, Leipzig, 1885).

[93] Authier, A. (ed.) *International Tables for Crystallography*, vol. D, Physical Properties of Crystals (John Wiley & Sons, Chichester, 2013).

[94] Evans, J. S. O., Mary, T. A. & Sleight, A. W. Negative thermal expansion materials. *Physica B* **241**, 311–316 (1997).

[95] Miller, W., Smith, C. W., Mackenzie, D. S. & Evans, K. E. Negative thermal expansion: A review. *J. Mater. Sci.* **44**, 5441–5451 (2009).

[96] Stepanov, I. A. Thermodynamics of substances with negative thermal expansion and negative compressibility. *J. Non-Cryst. Solids* **356**, 1168–1172 (2010).

[97] Takenaka, K. Negative thermal expansion materials: Technological key for control of thermal expansion. *Sci. Technol. Adv. Mater.* **13**, 013001 (2012).

[98] Evans, J. S. O. Negative thermal expansion materials. *J. Chem. Soc., Dalton Trans.* 3317–3326 (1999).

[99] Barrera, G. D., Bruno, J. A. O., Barron, T. H. K. & Allan, N. L. Negative thermal expansion. *J. Phys.: Condens. Matter* **17**, R217–R252 (2005).

[100] Lind, C. Two decades of negative thermal expansion research: Where do we stand? *Materials* **5**, 1125–1154 (2012).

[101] Cliffe, M. J. & Goodwin, A. L. PASCal: a principal axis strain calculator for thermal expansion and compressibility determination. *J. Appl. Crystallogr.* **45**, 1321–1329 (2012).

[102] Blanco, M. A., Francisco, E. & Luaña, V. GIBBS: Isothermal-isobaric thermodynamics of solids from energy curves using a quasi-harmonic debye model. *Comp. Phys. Commun.* **158**, 57–72 (2004).

[103] Ledbetter, H. M. & Reed, R. P. Elastic properties of metals and alloys, I. iron, nickel, and iron–nickel alloys. *J. Phys. Chem. Ref. Data* **2**, 531–617 (1973).

[104] Hellwege, K.-H., Knappe, W. & Lehmann, P. Die isotherme kompressibilität einiger amorpher und teilkristalliner hochpolymerer im temperaturbereich von 20–250°C und bei drucken bis zu 2000 kp/cm^2. *Kolloid. Z. Z. Polym.* **183**, 110–120 (1962).

[105] Munn, R. W. Role of the elastic constants in negative thermal expansion of axial solids. *J. Phys. C: Solid State Phys.* **5**, 535 (1972).

[106] Birch, F. Finite elastic strain of cubic crystals. *Phys. Rev.* **71**, 809 (1947).

[107] Sata, N., Shen, G., Rivers, M. L. & Sutton, S. R. Pressure-volume equation of state of the high-pressure B2 phase of NaCl. *Phys. Rev. B* **65**, 104114 (2002).

[108] Gatt, R. & Grima, J. N. Negative compressibility. *Phys. Status Solidi (RRL)* **2**, 236–238 (2008).

[109] Baughman, R. H., Stafstrom, S., Cui, C. X. & Dantas, S. O. Materials with negative compressibilities in one or more dimensions. *Science* **279**, 1522–1524 (1998).

[110] Hook, J. R. & Hall, H. E. *Solid State Physics* (John Wiley & Sons, Chichester, 1991), 2nd edn.

[111] Ashcroft, N. & Mermin, N. D. *Solid State Physics* (Holt-Saunders Japan, Ltd., Tokyo, 1976).

[112] Angel, R. J., Alvaro, M. & Gonzalez-Platas, J. EosFit7c and a Fortran module (library) for equation of state calculations. *Z. Kristallogr.* **229**, 405–419 (2014).

[113] McCann, D. R., Cartz, L., Schmunk, R. E. & Harker, Y. D. Compressibility of hexagonal selenium by X-ray and neutron diffraction. *J. Appl. Phys.* **43**, 1432–1436 (1972).

[114] Mariathasan, J. W. E., Finger, L. W. & Hazen, R. M. High-pressure behaviour of $LaNbO_4$. *Acta Crystallogr.* B**41**, 179–184 (1985).

[115] Cairns, A. B., Thompson, A. L., Tucker, M. G., Haines, J. & Goodwin, A. L. Rational design of materials with extreme negative compressibility: Selective soft-mode frustration in $KMn[Ag(CN)_2]_3$. *J. Am. Chem. Soc.* **134**, 4454–4456 (2012).

[116] Paliwoda, D., Wawrzyniak, P. & Katrusiak, A. Unwinding $Au^+ \cdots Au^+$ bonded filaments in ligand-supported gold(I) polymer under pressure. *J. Phys. Chem. Lett.* **5**, 2182–2188 (2014).

[117] Migliori, A. & Sarrao, J. *Resonant Ultrasound Spectroscopy* (Wiley, New York, 1997).

[118] Sanchez-Valle, C., Sinogeikin, S. V., Lethbridge, Z. A. D., Walton, R. I., Smith, C. W., Evans, K. E. & Bass., J. D. Brillouin scattering study on the single-crystal elastic properties of natrolite and analcime zeolites. *J. Appl. Phys.* **98**, 053508 (2005).

[119] Tan, J.-C., Civalleri, B., Lin, C.-C., Valenzano, L., Galvelis, R., Chen, P.-F., Bennett, T. D., Mellot-Draznieks, C., Zicovich-Wilson, C. M. & Cheetham, A. K. Exceptionally low shear modulus in a prototypical imidazole-based metal–organic framework. *Phys. Rev. Lett.* **108**, 095502 (2012).

[120] Shirane, G., Shapiro, S. M. & Tranquada, J. M. *Neutron Scattering with a Triple-Axis Spectrometer* (Cambridge University Press, Cambridge, 2002).

[121] Tan, J. C., Bennett, T. D. & Cheetham, A. K. Chemical structure, network topology, and porosity effects on the mechanical properties of zeolitic imidazolate frameworks. *Proc. Nat. Acad. Sci. U.S.A.* **107**, 9938–9943 (2010).

[122] Gale, J. D. GULP: A computer program for the symmetry-adapted simulation of solids. *J. Chem. Soc., Faraday Trans.* **93**, 629–637 (1997).

[123] Coudert, F.-X. Systematic investigation of the mechanical properties of pure silica zeolites: Stiffness, anisotropy, and negative linear compressibility. *Phys. Chem. Chem. Phys.* **15**, 16012–16018 (2013).

[124] Dovesi, R., Orlando, R., Civalleri, B., Roetti, C., Saunders, V. R. & Zicovich-Wilson, C. M. CRYSTAL: A computational tool for the *ab initio* study of the electronic properties of crystals. *Z. Kristallogr.* **220**, 571–573 (2005).

[125] Perger, W. F., Criswell, J., Civalleri, B. & Dovesi, R. *Ab-initio* calculation of elastic constants of crystalline systems with the CRYSTAL code. *Comput. Phys. Commun.* **180**, 1753–1759 (2009).

[126] Barnes, D. L., Miller, W., Evans, K. E. & Marmier, A. Modelling negative linear compressibility in tetragonal beam structures. *Mech. Mater.* **46**, 123–128 (2011).

[127] Baughman, R. H. Muscles made from metal. *Science* **300**, 268–269 (2003).

[128] Ogborn, J. M., Collings, I. E., Moggach, S., Thompson, A. L. & Goodwin, A. L. Supramolecular mechanics in a metal–organic framework. *Chem. Sci.* **3**, 3011–3017 (2012).

[129] Cai, W. & Katrusiak, A. Giant negative linear compression positively coupled to massive thermal expansion in a metal–organic framework. *Nature Commun.* **5**, 4337 (2014).

[130] Cairns, A. B., Catafesta, J., Levelut, C., Rouquette, J., van der Lee, A., Peters, L., Thompson, A. L., Dmitriev, V., Haines, J. & Goodwin, A. L. Giant negative linear compressibility in zinc dicyanoaurate. *Nature Mater.* **12**, 212–216 (2013).

[131] Chapman, K. W., Halder, G. J. & Chupas, P. J. Pressure-induced amorphization and porosity modification in a metal–organic framework. *J. Am. Chem. Soc.* **131**, 17546–17547 (2009).

[132] Collings, I. E., Tucker, M. G., Keen, D. A. & Goodwin, A. L. Geometric switching of linear to area negative thermal expansion in uniaxial metal–organic frameworks. *CrystEngComm* **16**, 3498–3506 (2014).

[133] Grüneisen, E. Zustand des fester köpers. *Handbuch der Physik* **10**, 1–59 (1926). In translation: The State of a Solid Body (Natl. Aeronautics Space Admin., Washington, DC), NASA Publ. No. RE2-18-59W, pp. 1–76.

[134] Seyidov, M. Y. & Suleymanov, R. A. Negative thermal expansion due to negative area compressibility in $TlGaSe_2$ semiconductor with layered crystalline structure. *J. Appl. Phys.* **108**, 063540 (2010).

[135] Coudert, F.-X. Link between NLC and auxeticity (2015). *(Personal Communication).*

[136] Ewald, P. P. (ed.). *Fifty Years of X-ray Diffraction*, chap. 4, 37–42 (N. V. A. Oosthoek's Uitgeversmaatschappij, Utrecht, The Netherlands, 1962).

[137] Bragg, W. L. The diffraction of short electromagnetic waves by a crystal. *Proc. Camb. Phil. Soc.* **17**, 43–57 (1912).

[138] IUCr. Nobel prize winners associated with crystallography. at `http://www.iucr.org/people/nobel-prize` (Last checked Oct 2014).

[139] Sivia, D. S. *Elementary Scattering Theory (for X-ray and Neutron Users)* (Oxford University Press, Oxford, 2010).

[140] Clegg, W. *Crystal Structure Determination.* Oxford Chemistry Primers (Oxford University Press, Oxford, 1998).

[141] Ezquerra, T. A., García-Gutiérrez, M., Nogales, A. & Gómez, M. (eds.) *Applications of Synchrotron Light to Scattering and Diffraction in Materials and Life Sciences*, vol. 776 of *Lect. Notes Phys.* (Springer-Verlag, Berlin Heidelberg, 2009).

[142] Coppens, P. *International Tables for Crystallography*, vol. B: Reciprocal Space, chap. 1, 10–24 (John Wiley & Sons, Chichester, 2013).

[143] Moseley, H. G. The high frequency spectra of the elements. *Phil. Mag.* **26**, 1024 (1913).

[144] Fultz, B. & Howe, J. M. *Transmission Electron Microscopy and Diffractometry of Materials.* Graduate Texts in Physics (Springer-Verlag, Berlin Heidelberg, 2013), 4th edn.

[145] Lang, A. R. Diffracted-beam monochromatization techniques in X-ray diffractometry. *Rev. Sci. Instrum.* **27**, 17–25 (1956).

[146] Wiedemann, H. *Synchrotron Radiation* (Springer-Verlag, Berlin Heidelberg, 2003).

[147] NC State University. Neutron Powder Diffraction Facility at NC State University. at `http://www.ne.ncsu.edu/nrp/npdf.html` (Last checked May 2015).

[148] Hazes, B. The Ewald sphere construction. at `http://hazeslab.med.ualberta.ca/tutorials/data_collection/ewald/ewald-sphere.html` (Last checked May 2015).

[149] HydrateWeb. Single crystal diffraction. at `http://www.hydrateweb.org/single-crystal-diffraction` (Last checked May 2015).

[150] Prince, E. (ed.) *International Tables for Crystallography*, vol. C: Mathematical, Physical and Chemical Tables (John Wiley & Sons, Chichester, 2006).

[151] Betteridge, P. W., Carruthers, J. R., Cooper, R. I., Prout, K. & Watkin, D. J. *CRYSTALS* version 12: software for guided crystal structure analysis. *J. Appl. Crystallogr.* **36**, 1487 (2003).

[152] Sheldrick, G. M. SHELXD - a program for crystal structure solution. Tech. Rep., University of Göttingen, Germany (2002).

[153] Hammersley, A. P. FIT2D: An introduction and overview. Tech. Rep., ESRF Internal Report (1997).

[154] Coelho, A. A. TOPAS-Academic, version 4.1 (Computer Software). Coelho Software, Brisbane.

[155] Larson, A. C. & Von Dreele, R. B. General structure analysis system (GSAS). *Los Alamos National Laboratory Report LAUR* **86-748** (2000).

[156] Young, C. A. & Goodwin, A. L. Applications of pair distribution function methods to contemporary problems in materials chemistry. *J. Mater. Chem.* **21**, 6464–6476 (2011).

[157] Klotz, S., Chervin, J.-C., Munsch, P. & Marchand, G. L. Hydrostatic limits of 11 pressure transmitting media. *J. Phys. D: Appl. Phys.* **42**, 075413 (2009).

[158] Cosier, J. & Glazer, A. M. A nitrogen-gas-stream cryostat for general X-ray diffraction studies. *J. Appl. Crystallogr.* **19**, 105–107 (1986).

[159] Allan, D. R., Miletich, R. & Angel, R. J. A diamond-anvil cell for single-crystal X-ray diffraction studies to pressures in excess of 10 GPa. *Rev. Sci. Instrum.* **67**, 840–842 (1996).

[160] Moggach, S. A., Allan, D. R., Parsons, S. & Warren, J. E. Incorporation of a new design of backing seat and anvil in a Merrill–Bassett diamond anvil cell. *J. Appl. Crystallogr.* **41**, 249–251 (2008).

[161] Klotz, S., Hamel, G. & Frelat, J. A new type of compact large-capacity press for neutron and X-ray scattering. *High Press. Res.* **24**, 219–223 (2004).

[162] Angel, R. J. AVERAGE v. 2.22. at `http://www.rossangel.com/` (Last checked Oct 2012).

[163] Angel, R. J. Absorption corrections for diamond-anvil pressure cells implemented in the software package ABSORB 6.0. *J. Appl. Crystallogr.* **37**, 486–492 (2004).

[164] Takemura, K. & Dewaele, A. Isothermal equation of state for gold with a He-pressure medium. *Phys. Rev. B* **78**, 104119 (2008).

[165] Sidorov, V. A. & Sadykov, R. A. Hydrostatic limits of Fluorinert liquids used for neutron and transport studies at high pressure. *J. Phys.: Condens. Matter* **17**, S3005 (2005).

[166] Moggach, S. A., Bennett, T. D. & Cheetham, A. K. The effect of pressure on ZIF-8: Increasing pore size with pressure and the formation of a high-pressure phase at 1.47 GPa. *Angew. Chem. Int. Ed.* **48**, 7087–7089 (2009).

[167] Lapidus, S. H., Halder, G. J., Chupas, P. J. & Chapman, K. W. Exploiting high pressures to generate porosity, polymorphism, and lattice expansion in the nonporous molecular framework $Zn(CN)_2$. *J. Am. Chem. Soc.* **135**, 7621–7628 (2013).

[168] West, A. R. *Basic Solid State Chemistry* (Wiley-Blackwell, Oxford, 1999), 2nd edn.

[169] Lee, M. M., Teuscher, J., Miyasaka, T., Murakami, T. N. & Snaith, H. J. Efficient hybrid solar cells based on meso-superstructured organometal halide perovskites. *Science* **338**, 643–647 (2012).

[170] Delgado-Friedrichs, O., O'Keeffe, M. & Yaghi, O. M. Taxonomy of periodic nets and the design of materials. *Phys. Chem. Chem. Phys.* **9**, 1035–1043 (2007).

[171] Blatov, V. A., Shevchenko, A. P. & Proserpio, D. M. Applied topological analysis of crystal structures with the program package TOPOSPRO. *Cryst. Growth Des.* **14**, 3576–3586 (2014).

[172] Kitagawa, S., Kitaura, R. & Noro, S. Functional porous coordination polymers. *Angew. Chem. Int. Ed.* **43**, 2334–2375 (2004).

[173] Alexandrov, E. V., Blatov, V. A., Kochetkov, A. V. & Proserpio, D. M. Underlying nets in three-periodic coordination polymers: topology, taxonomy and prediction from a computer-aided analysis of the Cambridge Structural Database. *CrystEngComm* **13**, 3947–3958 (2011).

[174] Furukawa, H., Cordova, K. E., O'Keeffe, M. & Yaghi, O. M. The chemistry and applications of metal–organic frameworks. *Science* **341**, 1230444 (2013).

[175] Griffith, W. P. Cyanide complexes of the transition metals. *Quart. Rev. Chem. Soc.* **16**, 188–207 (1962).

[176] Hoskins, B. F. & Robson, R. Design and construction of a new class of scaffolding-like materials comprising infinite polymeric frameworks of 3D-linked molecular rods. A reappraisal of the zinc cyanide and cadmium cyanide structures and the synthesis and structure of the diamond-related frameworks $[N(CH_3)_4][Cu^{I}Zn^{II}(CN)_4]$ and Cu^{I}[4,4′,4″,4‴-tetracyanotetraphenylmethane]$BF_4 \cdot x C_6H_5NO_2$. *J. Am. Chem. Soc.* **112**, 1546–1554 (1990).

[177] Sharpe, A. G. *The Chemistry of Cyano Complexes of the Transition Metals* (Academic Press, London, 1976).

[178] Cheetham, A. K. & Rao, C. N. R. Materials science: There's room in the middle. *Science* **318**, 58–59 (2007).

[179] Cairns, A. B. & Goodwin, A. L. Structural disorder in molecular framework materials. *Chem. Soc. Rev.* **42**, 4881–4893 (2013).

[180] Goodwin, A. L. Rigid unit modes and intrinsic flexibility in linearly bridged framework structures. *Phys. Rev. B* **74**, 134302 (2006).

[181] Hollingsworth, M. D. Crystal engineering: From structure to function. *Science* **295**, 2410–2413 (2002).

[182] Yaghi, O. M. Reticular synthesis and the design of new materials. *Nature* **423**, 705–714 (2003).

[183] Eddaoudi, M., Kim, J., Rosi, N., Vodak, D., Wachter, J., O'Keeffe, M. & Yaghi, O. M. Systematic design of pore size and functionality in isoreticular MOFs and their application in methane storage. *Science* **295**, 469–472 (2002).

[184] Rowsell, J. L., Spencer, E. C., Eckert, J., Howard, J. A. & Yaghi, O. M. Gas adsorption sites in a large-pore metal–organic framework. *Science* **309**, 1350–1354 (2005).

[185] Cliffe, M. J., Wan, W., Zou, X., Chater, P. A., Kleppe, A. K., Tucker, M. G., Wilhelm, H., Funnell, N. P., Coudert, F.-X. & Goodwin, A. L. Correlated defect nanoregions in a metal–organic framework. *Nature Commun.* **5** (2014).

[186] Wu, H., Yildirim, T. & Zhou, W. Exceptional mechanical stability of highly porous zirconium metal–organic framework UiO-66 and its important implications. *J. Phys. Chem. Lett.* **4**, 925–930 (2013).

[187] Salles, F., Maurin, G., Serre, C., Llewellyn, P. L., Knöfel, C., Choi, H. J., Filinchuk, Y., Oliviero, L., Vimont, A., Long, J. R. & Férey, G. Multistep N_2 breathing in the metal–organic framework Co(1,4-benzenedipyrazolate). *J. Am. Chem. Soc.* **132**, 13782–13788 (2010).

[188] Serre, C., Mellot-Draznieks, C., Surblé, S., Audebrand, N., Filinchuk, Y. & Férey, G. Role of solvent–host interactions that lead to very large swelling of hybrid frameworks. *Science* **315**, 1828–1831 (2007).

[189] Park, K. S., Ni, Z., Cote, A. P., Choi, J. Y., Huang, R., Uribe-Romo, F. J., Chae, H. K., O'Keeffe, M. & Yaghi, O. M. Exceptional chemical and thermal stability of zeolitic imidazolate frameworks. *Proc. Nat. Acad. Sci. U.S.A.* **103**, 10186–10191 (2006).

[190] Bennett, T. D., Goodwin, A. L., Dove, M. T., Keen, D. A., Tucker, M. G., Barney, E. R., Soper, A. K., Bithell, E. G., Tan, J.-C. & Cheetham, A. K. Structure and properties of an amorphous metal–organic framework. *Phys. Rev. Lett.* **104**, 115503 (2010).

[191] Yang, P., He, X., Li, M.-X., Ye, Q., Ge, J.-Z., Wang, Z.-X., Zhu, S.-R., Shao, M. & Cai, H.-L. The first homochiral coordination polymer with temperature-independent piezoelectric and dielectric properties. *J. Mater. Chem.* **22**, 2398–2400 (2012).

[192] Halder, G. J., Kepert, C. J., Moubaraki, B., Murray, K. S. & Cashion, J. D. Guest-dependent spin crossover in a nanoporous molecular framework material. *Science* **298**, 1762–1765 (2002).

[193] Jain, P., Ramachandran, V., Clark, R. J., Zhou, H. D., Toby, B. H., Dalal, N. S., Kroto, H. W. & Cheetham, A. K. Multiferroic behavior associated with an order–disorder hydrogen bonding transition in metal–organic frameworks (MOFs) with the perovskite ABX_3 architecture. *J. Am. Chem. Soc.* **131**, 13625–13627 (2009).

[194] Besara, T., Jain, P., Dalal, N. S., Kuhns, P. L., Reyes, A. P., Kroto, H. W. & Cheetham, A. K. Mechanism of the order–disorder phase transition, and glassy behavior in the metal-organic framework $[(CH_3)_2NH_2]Zn(HCOO)_3$. *Proc. Nat. Acad. Sci. U.S.A.* **108**, 6828–6832 (2011).

[195] Mowat, J. P. S., Miller, S. R., Griffin, J. M., Seymour, V. R., Ashbrook, S. E., Thompson, S. P., Fairen-Jimenez, D., Banu, A.-M., Düren, T. & Wright, P. A. Structural chemistry, monoclinic-to-orthorhombic phase transition, and CO_2 adsorption behavior of the small pore scandium terephthalate, $Sc_2(O_2CC_6H_4CO_2)_3$, and its nitro- and amino-functionalized derivatives. *Inorg. Chem.* **50**, 10844–10858 (2011).

[196] Hu, Y. H. & Zhang, L. Amorphization of metal–organic framework MOF-5 at unusually low applied pressure. *Phys. Rev. B* **81**, 174103 (2010).

[197] Bennett, T. D., Cao, S., Tan, J.-C., Keen, D. A., Bithell, E. G., Beldon, P. J., Friscic, T. & Cheetham, A. K. Facile mechanosynthesis of amorphous zeolitic imidazolate frameworks. *J. Am. Chem. Soc.* **133**, 14546–14549 (2011).

[198] Schneemann, A., Bon, V., Schwedler, I., Senkovska, I., Kaskel, S. & Fischer, R. A. Flexible metal–organic frameworks. *Chem. Soc. Rev.* **43**, 6062–6096 (2014).

[199] Mellot-Draznieks, C., Serre, C., Surblé, S., Audebrand, N. & Férey, G. Very large swelling in hybrid frameworks:a combined computational and powder diffraction study. *J. Am. Chem. Soc.* **127**, 16273–16278 (2005).

[200] Zhou, W., Wu, H., Yildirim, T., Simpson, J. R. & Walker, A. R. H. Origin of the exceptional negative thermal expansion in metal-organic framework-5 Zn_4O(1,4-benzenedicarboxylate)$_3$. *Phys. Rev. B* **78**, 054114 (2008).

[201] Rimmer, L. H. N., Dove, M. T., Goodwin, A. L. & Palmer, D. C. Acoustic phonons and negative thermal expansion in MOF-5. *Phys. Chem. Chem. Phys.* **16**, 21144–21152 (2014).

[202] Cliffe, M. J., Hill, J. A., Murray, C. A., Coudert, F.-X. & Goodwin, A. L. Defect-dependent colossal negative thermal expansion in UiO-66(Hf) metal–organic framework. *Phys. Chem. Chem. Phys.* **17**, 11586–11592 (2015).

[203] Chapman, K. W., Sava, D. F., Halder, G. J., Chupas, P. J. & Nenoff, T. M. Trapping guests within a nanoporous metal–organic framework through pressure-induced amorphization. *J. Am. Chem. Soc.* **133**, 18583–18585 (2011).

[204] Sava, D. F., Rodriguez, M. A., Chapman, K. W., Chupas, P. J., Greathouse, J. A., Crozier, P. S. & Nenoff, T. M. Capture of volatile iodine, a gaseous fission product, by zeolitic imidazolate framework-8. *J. Am. Chem. Soc.* **133**, 12398–12401 (2011).

[205] Collings, I. E., Cairns, A. B., Thompson, A. L., Parker, J. E., Tang, C. C., Tucker, M. G., Catafesta, J., Levelut, C., Haines, J., Dmitriev, V., Pattison, P. & Goodwin, A. L. Homologous critical behavior in the molecular frameworks $Zn(CN)_2$ and Cd(imidazolate)$_2$. *J. Am. Chem. Soc.* **135**, 7610–7620 (2013).

[206] Collings, I. E., Tucker, M. G., Keen, D. A. & Goodwin, A. L. Static disorder and local structure in zinc(II) isonicotinate, a quartzlike metal–organic framework. *Z. Kristallogr.-Cryst. Mater.* **227**, 313–320 (2012).

[207] Keggin, J. F. & Miles, F. D. Structures and formulæ of the Prussian blues and related compounds. *Nature* **137**, 577–578 (1936).

[208] Vaciago, A. & Mugnoli, A. Crystal structure and isomorphism of some hexacyanocobaltates of bivaltent cations. *Atti. Acad. Nazl. Lincei Rend., Classe Sci. Fis. Mat. Nat.* **25**, 531 (1958).

[209] Chapman, K. W., Chupas, P. J. & Kepert, C. J. Compositional dependence of negative thermal expansion in the Prussian Blue analogues $MPt^{IV}Pt^{II}(CN)_6$ (M = Mn, Fe, Co, Ni, Cu, Zn, Cd). *J. Am. Chem. Soc.* **128**, 7009–7014 (2006).

[210] Goodwin, A. L., Chapman, K. W. & Kepert, C. J. Guest-dependent negative thermal expansion in nanoporous Prussian blue analogues $M^{II}Pt^{IV}(CN)_6{\cdot}x\{H_2O\}$ ($0 \leq x \leq 2$; M = Zn, Cd). *J. Am. Chem. Soc.* **127**, 17980–17981 (2005).

[211] Catafesta, J., Haines, J., Zorzi, J. E., Pereira, A. S. & Perottoni, C. A. Pressure-induced amorphization and decomposition of $Fe[Co(CN)_6]$. *Phys. Rev. B* **77**, 064104 (2008).

[212] Kaye, S. S. & Jeffrey, R. Hydrogen storage in the dehydrated Prussian blue analogues $M_3[Co(CN)_6]_2$ (M = Mn, Fe, Co, Ni, Cu, Zn). *J. Am. Chem. Soc.* **127**, 6506–6507 (2005).

[213] Lee, H.-W., Wang, R. Y., Pasta, M., Woo Lee, S., Liu, N. & Cui, Y. Manganese hexacyanomanganate open framework as a high-capacity positive electrode material for sodium-ion batteries. *Nature Commun.* **5**, 5280 (2014).

[214] Asakura, D., Okubo, M., Mizuno, Y., Kudo, T., Zhou, H., Ikedo, K., Mizokawa, T., Okazawa, A. & Kojima, N. Fabrication of a cyanide-bridged coordination polymer electrode for enhanced electrochemical ion storage ability. *J. Phys. Chem. C* **116**, 8364–8369 (2012).

[215] Batten, S. R., Hoskins, B. F. & Robson, R. Structures of [Ag(tcm)], $[Ag(tcm)(phz)_{1/2}]$ and [Ag(tcm)(pyz)] (tcm = tricyanomethanide, $C(CN)_3{}^-$, phz = phenazine, pyz=pyrazine). *New J. Chem.* **22**, 173–175 (1998).

[216] Batten, S. R., Hoskins, B. F., Moubaraki, B., Murray, K. S. & Robson, R. Crystal structures and magnetic properties of the interpenetrating rutile-related compounds $M(tcm)_2$ [M = octahedral, divalent metal; tcm^- = tricyanomethanide, $C(CN)_3{}^-$] and the sheet structures of $[M(tcm)_2(EtOH)_2]$ (M = Co or Ni). *J. Chem. Soc., Dalton Trans.* 2977–2986 (1999).

[217] Batten, S. R., Hoskins, B. F. & Robson, R. Interdigitation, interpenetration and intercalation in layered cuprous tricyanomethanide derivatives. *Chem. Eur. J.* **6**, 156–161 (2000).

[218] Hoskins, B. F., Robson, R. & Scarlett, N. V. Y. Synthesis and structure of $Rb[Cd(Ag(CN)_2)_3]$ containing 3 independent, interpenetrating alpha-polonium-related nets. *Chem. Commun.* **18**, 2025–2026 (1994).

[219] Hoskins, B. F., Robson, R. & Scarlett, N. V. Y. Six interpenetrating quartz-like nets in the structure of $ZnAu_2(CN)_4$. *Angew. Chem. Int. Ed.* **34**, 1203–1204 (1995).

[220] Phillips, A. E., Goodwin, A. L., Halder, G. J., Southon, P. D. & Kepert, C. J. Nanoporosity and exceptional negative thermal expansion in single-network cadmium cyanide. *Angew. Chem. Int. Ed.* **47**, 1396–1399 (2008).

[221] Katz, M. J., Ramnial, T., Yu, H.-Z. & Leznoff, D. B. Polymorphism of $Zn[Au(CN)_2]_2$ and its luminescent sensory response to NH_3 vapor. *J. Am. Chem. Soc.* **130**, 10662–10673 (2008).

[222] Katz, M. J., Kaluarachchi, H., Batchelor, R. J., Bokov, A. A., Ye, Z. G. & Leznoff, D. B. Highly birefringent materials designed using coordination polymer synthetic methodology. *Angew. Chem. Int. Ed.* **46**, 8804–8807 (2007).

[223] Lefebvre, J., Korčok, J. L., Katz, M. J. & Leznoff, D. B. Vapochromic behaviour of $M[Au(CN)_2]_2$-based coordination polymers (M = Co, Ni). *Sensors* **12**, 3669–3692 (2012).

[224] Katz, M. J., Sakai, K. & Leznoff, D. B. The use of aurophilic and other metal–metal interactions as crystal engineering design elements to increase structural dimensionality. *Chem. Soc. Rev.* **37**, 1884–1895 (2008).

[225] O'Grady, E. & Kaltsoyannis, N. Does metallophilicity increase or decrease down group 11? Computational investigations of $[Cl–M–PH_3]_2$ (M = Cu, Ag, Au, [111]). *Phys. Chem. Chem. Phys.* **6**, 680–687 (2004).

[226] Eisenmann, E. T. The precipitation of $KCo[Au(CN)_2]_3$ and similar cyanoaurate complexes. *J. Electrochem. Soc.* **124**, 1957–1958 (1977).

[227] Abrahams, S. C., Bernstein, J. L., Liminga, R. & Eisenmann, E. T. Piezoelectric $KCo[Au(CN)_2]_3$: Room-temperature crystal structure of a cobalt-hardened gold electrodeposition process component. *J. Chem. Phys.* **73**, 4585–4590 (1980).

[228] Abrahams, S. C., Zyontz, L. E. & Bernstein, J. L. Cobalt cyanoaurate: crystal-structure of a component from cobalt-hardened gold electroplating baths. *J. Chem. Phys.* **76**, 5458–5462 (1982).

[229] Geiser, U. & Schlueter, J. A. $KMnAg_3(CN)_6$, a new triply interpenetrating network solid. *Acta Crystallogr.* C**59**, I21–I23 (2003).

[230] Goodwin, A. L., Keen, D. A., Tucker, M. G., Dove, M. T., Peters, L. & Evans, J. S. O. Argentophilicity-dependent colossal thermal expansion in extended Prussian blue analogues. *J. Am. Chem. Soc.* **130**, 9660–9661 (2008).

[231] Goodwin, A. L., Kennedy, B. J. & Kepert, C. J. Thermal expansion matching via framework flexibility in zinc dicyanometallates. *J. Am. Chem. Soc.* **131**, 6334–6335 (2009).

[232] Korčok, J. L., Katz, M. J. & Leznoff, D. B. Impact of metallophilicity on "colossal" positive and negative thermal expansion in a series of isostructural dicyanometallate coordination polymers. *J. Am. Chem. Soc.* **131**, 4866–4871 (2009).

[233] Kondratuk, D. V., Sprafke, J. K., O'Sullivan, M. C., Perdigã, L. M. A., Saywell, A., Malfois, M., O'Shea, J. N., Beton, P. H., Thompson, A. L. & Anderson, H. L. Vernier-templated synthesis, crystal structure, and supramolecular chemistry of a 12-porphyrin nanoring. *Chem. Eur. J.* **20**, 12826–12834 (2014).

[234] Lehn, J.-M. Supramolecular chemistry—scope and perspectives molecules, supermolecules, and molecular devices (Nobel lecture). *Angew. Chem. Int. Ed.* **27**, 89–112 (1988).

[235] Cook, T. R., Zheng, Y.-R. & Stang, P. J. Metal–organic frameworks and self-assembled supramolecular coordination complexes: Comparing and contrasting the design, synthesis, and functionality of metal–organic materials. *Chem. Rev.* **113**, 734–777 (2013).

[236] Zhang, L., Kuang, X., Wu, X., Yang, W. & Lu, C. Supramolecular interactions induced hinge-like motion of a metal–organic framework accompanied by anisotropic thermal expansion. *Dalton Trans.* **43**, 7146–7152 (2014).

[237] Desclaux, J. P. & Pyykkö, P. Dirac-Fock one-center calculations—molecules CuH, AgH and AuH including p-type symmetry functions. *Chem. Phys. Lett.* **39**, 300–303 (1976).

[238] Pyykkö, P. Theoretical chemistry of gold. *Angew. Chem. Int. Ed.* **43**, 4412–4456 (2004).

[239] Schmidbauer, H. The aurophilicity phenomenon: A decade of experimental findings, theoretical concepts and emerging applications. *Gold Bull.* **33**, 3–10 (2000).

[240] Keen, D. A., Dove, M. T., Evans, J. S. O., Goodwin, A. L., Peters, L. & Tucker, M. G. The hydrogen-bonding transition and isotope-dependent negative thermal expansion in $H_3Co(CN)_6$. *J. Phys.: Condens. Matter* **22**, 404202 (2010).

[241] O'Keeffe, M. Design of MOFs and intellectual content in reticular chemistry: A personal view. *Chem. Soc. Rev.* **38**, 1215–1217 (2009).

[242] Ziman, J. M. *Models of Disorder. The Theoretical Physics of Homogeneously Disordered Systems* (Cambridge University Press, Cambridge, 1979).

[243] Cairns, A. B. *Piezoelectricity and Colossal Thermal Expansion in Anomalous Cyanide-Containing Frameworks*. Master's thesis, Inorganic Chemistry Laboratory, Department of Chemistry, University of Oxford (2011).

[244] Salje, E. K. H. *Phase Transitions in Ferroelastic and Co-elastic Crystals* (Cambridge University Press, Cambridge, 1993).

[245] Cairns, A. B. & Goodwin, A. L. Negative linear compressibility. *Phys. Chem. Chem. Phys.* **17**, 20449–20465 (2015).

[246] Miller, W., Evans, K. E. & Marmier, A. Negative linear compressibility in common materials. *Appl. Phys. Lett.* **106**, 231903 (2015).

[247] Fortes, A. D., Suard, E. & Knight, K. S. Negative linear compressibility and massive anisotropic thermal expansion in methanol monohydrate. *Science* **331**, 742–746 (2011).

[248] Li, W., Probert, M. R., Kosa, M., Bennett, T. D., Alagarsamy, T., Burwood, R. P., Parinello, M., Howard, J. A. K. & Cheetham, A. K. Negative linear compressibility of a metal–organic framework. *J. Am. Chem. Soc.* **134**, 11940–11943 (2012).

[249] Serra-Crespo, P., Dikhtiarenko, A., Stavitski, E., Juan-Alcaniz, J., Kapteijn, F., Coudert, F.-X. & Gascon, J. Experimental evidence of negative linear compressibility in the MIL-53 metal–organic framework family. *CrystEngComm* **17**, 276–280 (2015).

[250] Shepherd, H. J., Palamarciuc, T., Rosa, P., Guionneau, P., Molnár, G., Létard, J.-F. & Bousseksou, A. Antagonism between extreme negative linear compression and spin crossover in $[Fe(dpp)_2(NCS)_2]$·py. *Angew. Chem. Int. Ed.* **51**, 3910–3914 (2012).

[251] Salje, E. K. H., Graeme-Barber, A., Carpenter, M. A. & Bismayer, U. Lattice parameters, spontaneous strain and phase transitions in $Pb_3(PO_4)_2$. *Acta Crystallogr.* B**49**, 387–392 (1993).

[252] Redfern, S. A. T., Salje, E., Begemann, B. & Jansen, M. Spontaneous strain and the ferroelastic phase transition in As_2O_5. *J. Phys. C: Solid State Phys.* **21**, 277–285 (1988).

[253] Haines, J. & Léger, J. M. X-ray diffraction study of the phase transitions and structural evolution of tin dioxide at high pressure: relationships between structure types and implications for other rutile-type dioxides. *Phys. Rev. B* **55**, 11144–11154 (1997).

[254] Skelton, E. F., Feldman, J. L., Liu, C. Y. & Spain, I. L. Study of the pressure-induced phase transition in paratellurite (TeO_2). *Phys. Rev. B* **13**, 2605–2613 (1976).

[255] McWhan, D. B., Birgeneau, R. J., Bonner, W. A., Taub, H. & Axe, J. D. Neutron scattering study at high pressure of the structural phase transition in paratellurite. *J. Phys. C: Solid State Phys.* **8**, L81–L85 (1975).

[256] Uwe, H. & Tokumoto, H. Pressure-induced ferroelastic transition and internal displacement in TeO_2. *Phys. Rev. B* **19**, 3700–3707 (1979).

[257] Toledano, P., Fejer, M. M. & Auld, B. A. Nonlinear elasticity in proper ferroelastics. *Phys. Rev. B* **27**, 5717–5746 (1983).

[258] Shannon, R. D. Revised effective ionic radii and systematic studies of interatomic distances in halides and chalcogenides. *Acta Crystallogr.* A**32**, 751–767 (1976).

[259] Jorgensen, J. D., Worlton, T. G. & Jamieson, J. C. Pressure-induced strain transition in NiF_2. *Phys. Rev. B* **17**, 2212–2214 (1978).

[260] Mirgorodsky, A. & Smirnov, M. Soft modes and proper ferroelasticity-3: Rutile-NiF_2. *Ferroelectrics* **159**, 151–153 (1994).

[261] Haines, J., Léger, J. M., Gorelli, F., Klug, D. D., Tse, J. S. & Li, Z. Q. X-ray diffraction and theoretical studies of the high-pressure structures and phase transitions in magnesium fluoride. *Phys. Rev. B* **64**, 134110 (2001).

[262] Zhang, L., Wang, Y., Cui, T., Ma, Y. & Zou, G. First principles study of the pressure-induced rutile-$CaCl_2$ phase transition in MgF_2. *Solid State Commun.* **145**, 283–287 (2008).

[263] Haines, J., Léger, J. M. & Schulte, O. The high-pressure phase transition sequence from the rutile-type through to the cotunnite-type structure in PbO_2. *J. Phys.: Condens. Matter* **8**, 1631–1646 (1996).

[264] Haines, J., Léger, J. M., Chateau, C. & Pereira, A. S. Structural evolution of rutile-type and $CaCl_2$-type germanium dioxide at high pressure. *Phys. Chem. Min.* **27**, 575–582 (2000).

[265] Endo, S., Nitawaki, S., Shige, T., Akahama, Y., Kikegawa, T. & Shimomura, O. X-ray study of SnO_2 under high pressure and temperature generated with sintered diamond anvils. *High Press. Res.* **4**, 408–410 (1990).

[266] Angel, R. J. & Bismayer, U. Renormalization of the phase transition in lead phosphate, $Pb_3(PO_4)_2$, by high pressure: Lattice parameters and spontaneous strain. *Acta Crystallogr.* B**55**, 896–901 (1999).

[267] Angel, R. J., Bismayer, U. & Marshall, W. G. Local and long-range order in ferroelastic lead phosphate at high pressure. *Acta Crystallogr.* B**60**, 1–9 (2004).

[268] Salje, E. K. H. & Devarajan, V. Potts model and phase transition in lead phosphate $Pb_3(PO_4)_2$. *J. Phys. C: Solid State Phys.* **14**, L1029–L1035 (1981).

[269] Kabalkina, S. S., Losev, V. G. & Gasanly, N. M. Polymorphism of InS at high pressures. *Solid State Commun.* **44**, 1383–1385 (1982).

[270] Schwarz, U., Hillebrecht, H. & Syassen, K. Effect of hydrostatic pressures on the crystal structure of InS. *Z. Kristallogr.* **210**, 494–497 (1995).

[271] Takarabe, K. Optical Properties of InS under High Pressure. *Phys. Status Solidi B* **145**, 219–225 (1988).

[272] Oganov, A. R., Price, G. D. & Brodholt, J. P. Theoretical investigation of metastable Al_2SiO_5 polymorphs. *Acta Crystallogr.* A**57**, 548–557 (2001).

[273] Collins, R., Kaner, R., Russo, P., Wold, A. & Avignant, D. High-pressure phase transformation of platinum sulfide. *Inorg. Chem.* **18**, 727–729 (1979).

[274] Wood, I. G., Wadhawan, V. K. & Glazer, A. M. Temperature dependence of spontaneous birefringence in ferroelastic lead orthophosphate. *J. Phys. C: Solid State Phys.* **13**, 5155–5164 (1980).

[275] Decker, D. L., Petersen, S., Debray, D. & Lambert, M. Pressure-induced ferroelastic phase transition in $Pb_3(PO_4)_2$: A neutron-diffraction study. *Phys. Rev. B* **19**, 3552–3555 (1979).

[276] Winter, J. K. & Ghose, S. Thermal expansion and high-temperature crystal chemistry of the Al_2SiO_5 polymorphs . *Am. Mineral.* **64**, 573–586 (1979).

[277] Winkler, B. & Buehrer, W. Lattice dynamics of andalusite: prediction and experiment. *Phys. Chem. Min.* **17**, 453–461 (1990).

[278] Christy, A. G. Isosymmetric structural phase transitions: Phenomenology and examples. *Acta Crystallogr.* B**51**, 753–757 (1995).

[279] Ruce, A. D. & Cowley, R. A. *Structural Phase Transitions* (Francis and Taylor, London, 1981).

[280] Hunt, S. J., Cliffe, M. J., Hill, J. A., Cairns, A. B., Funnell, N. P. & Goodwin, A. L. Flexibility transition and guest-driven reconstruction in a ferroelastic metal–organic framework. *CrystEngComm* **17**, 361–369 (2015).

[281] Dinnebier, R. E., Hinrichsen, B., Lennie, A. & Jansen, M. High-pressure crystal structure of the non-linear optical compound BiB_3O_6 from two-dimensional powder diffraction data. *Acta Crystallogr.* B**65**, 1–10 (2009).

[282] Haussühl, S., Bohatý, L. & Becker, P. Piezoelectric and elastic properties of the nonlinear optical material bismuth triborate, BiB_3O_6. *Appl. Phys. A* **82**, 495–502 (2006).

[283] Stein, W.-D., Cousson, A., Becker, P., Bohatý, L. & Braden, M. Temperature-dependent X-ray and neutron diffraction study of BiB_3O_6. *Z. Kristallogr.* **222**, 680–689 (2007).

[284] de Boer, K., Jansen, A. P. J. & van Santen, R. A. Structure-stability relationships for all-silica structures. *Phys. Rev. B* **52**, 12579–12590 (1995).

[285] Prawer, S., Smith, T. F. & Finlayson, T. R. The room temperature elastic behaviour of CsH_2PO_4. *Aus. J. Phys.* **38**, 63–83 (1985).

[286] Uesu, Y. & Kobayashi, J. Crystal structure and ferroelectricity of cesium dihydrogen phosphate CsH_2PO_4. *Phys. Status Solidi A* **34**, 475–481 (1976).

[287] Kobayashi, Y., Deguchi, K., Azuma, S., Suzuki, E., Ming, L. C., Endo, S. & Kikegawa, T. Phase transitions in CsH_2PO_4 under high pressure. *Ferroelectrics* **285**, 83–89 (2003).

[288] Youngblood, R., Frazer, B. C., Eckert, J. & Shirane, G. Neutron scattering study of the pressure dependence of short-range order in CsD_2PO_4. *Phys. Rev. B* **22**, 228–235 (1980).

[289] Nelmes, R. J. & Choudhary, R. N. P. Structural studies of the monoclinic dihydrogen phosphates: A neutron-diffraction study of paraelectric CsH_2PO_4. *Solid State Commun.* **26**, 823–826 (1978).

[290] Haines, J., Chateau, C., Leger, J. M., Bogicevic, C., Hull, S., Klug, D. D. & Tse, J. S. Collapsing cristobalitelike structures in silica analogues at high pressure. *Phys. Rev. Lett.* **91**, 015503 (2003).

[291] Marmier, A., Lethbridge, Z. A. D., Walton, R. I., Smith, C. W., Parker, S. C. & Evans, K. E. ElAM: A computer program for the analysis and representation of anisotropic elastic properties. *Comput. Phys. Commun.* **181**, 2102–2115 (2010).

[292] O'Keeffe, M. & Hyde, B. G. Cristobalites and topologically-related structures . *Acta Crystallogr.* B**32**, 2923–2936 (1976).

[293] Léger, J. M., Haines, J., Chateau, C., Bocquillon, G., Schmidt, M. W., Hull, S., Gorelli, F., Lesauze, A. & Marchand, R. Phosphorus oxynitride PON, a silica analogue: structure and compression of the cristobalite-like phase; P–T phase diagram. *Phys. Chem. Min.* **28**, 388–398 (2001).

[294] Kier, W. M. & Smith, K. K. Tongues, tentacles and trunks: the biomechanics of movement in muscular-hydrostats. *Zool. J. Linn. Soc.-Lond.* **83**, 307–324 (1985).

[295] Aliev, A. E., Oh, J., Kozlov, M. E., Kuznetsov, A. A., Fang, S., Fonseca, A. F., Ovalle, R., Lima, M. D., Haque, M. H., Gartstein, Y. N., Zhang, M., Zakhidov, A. A. & Baughman, R. H. Giant-stroke, superelastic carbon nanotube aerogel muscles. *Science* **323**, 1575–1578 (2009).

[296] Baughman, R. H. & Cui, C. Materials with negative compressibilities. *Science* **281**, 143a (1998).

[297] Foroughi, J., Spinks, G. M., Wallace, G. G., Oh, J., Kozlov, M. E., Fang, S., Mirfakhrai, T., Madden, J. D. W., Shin, M. K., Kim, S. J. & Baughman, R. H. Torsional carbon nanotube artificial muscles. *Science* **334**, 494–497 (2011).

[298] Spinks, G. M., Wallace, G. G., Fifield, L. S., Dalton, L. R., Mazzoldi, A., De Rossi, D., Khayrullin, I. I. & Baughman, R. H. Pneumatic carbon nanotube actuators. *Adv. Mater.* **14**, 1728–1732 (2002).

[299] Keller, R., Holzapfel, W. B. & Schulz, H. Effect of pressure on the atom positions in Se and Te. *Phys. Rev. B* **16**, 4404–4412 (1977).

[300] McCann, D. R. & Cartz, L. Bond distances and chain angle of hexagonal selenium at high pressure. *J. Appl. Phys.* **43**, 4473–4477 (1972).

[301] McCann, D. R. & Cartz, L. Anisotropy of Compressibility and Thermal Expansion of Hexagonal Selenium. In Graham, M. G. & Hagy, H. E. (eds.) *Thermal Expansion—1971*, vol. 3 of *AIP Conference Proceedings*, 131 (American Institute of Physics, New York, 1972).

[302] Hsueh, H. C., Lee, C. C. & Wang, C. W. Compression mechanisms in the anisotropically bonded elements Se and Te. *Phys. Rev. B* **61**, 3851–3856 (2000).

[303] Jamieson, J. C. & McWhan, D. B. Crystal structure of tellurium at high pressures. *J. Chem. Phys.* **43**, 1149–1152 (1965).

[304] Bridgeman, P. W. The compression of sixty-one solid substances to 25,000 kg/cm^2, determined by a new rapid method. *Proc. Am. Acad. Arts Sci.* **76**, 9–24 (1945).

[305] Ren, W., Ye, J.-T., Shi, W., Tang, Z.-K., Chan, C. T. & Sheng, P. Negative compressibility of selenium chains confined in the channels of $AlPO_4$-5 single crystals. *New J. Phys.* **11**, 103014 (2009).

[306] Britton, D. Silver dicyanamide, $AgN(CN)_2$ — orthorhombic modification. *Acta Crystallogr.* C**46**, 2297–2299 (1990).

[307] Britton, D. & Chow, Y. M. The crystal structure of silver dicyanamide, $AgN(CN)_2$. *Acta Crystallogr.* B**33**, 697–699 (1977).

[308] Grima, J. N., Caruana-Gauci, R., Wojciechowski, K. W. & Evans, K. E. Smart hexagonal truss systems exhibiting negative compressibility through constrained angle stretching. *Smart Mater. Struct.* **22**, 084015 (2013).

[309] Kamali, K., Ravi, C., Ravindran, T. R., Sarguna, R. M., Sairam, T. N. & Kaur, G. Linear compressibility and thermal expansion of $KMn[Ag(CN)_2]_3$ studied by Raman spectroscopy and first-principles calculations. *J. Phys. Chem. C* **117**, 25704–25713 (2013).

[310] Gagnon, K. J., Beavers, C. M. & Clearfield, A. MOFs under pressure: The reversible compression of a single crystal. *J. Am. Chem. Soc.* **135**, 1252–1255 (2013).

[311] Woodall, C. H., Beavers, C. M., Christensen, J., Hatcher, L. E., Intissar, M., Parlett, A., Teat, S. J., Reber, C. & Raithby, P. R. Hingeless negative linear compression in the mechanochromic gold complex [$(C_6F_5Au)_2$(μ-1,4-diisocyanobenzene)]. *Angew. Chem. Int. Ed.* **52**, 9691–9694 (2013).

[312] Coudert, F.-X. Assessing and predicting flexibility in MOFs with molecular simulation. *Acta Crystallogr.* A**70**, C1125 (2014).

[313] Goodwin, A. L. Organic crystals: Packing down. *Nature Mater.* **9**, 7–8 (2010).

[314] de Jong, M., Chen, W., Angsten, T., Jain, A., Notestine, R., Gamst, A., Sluiter, M., Ande, C. K., van der Zwaag, S., Plata, J. J., Toher, C., Curtarolo, S., Ceder, G., Persson, K. A. & Asta, M. Charting the complete elastic properties of inorganic crystalline compounds. *Sci. Data* **2**, 150009 (2015).

[315] Hodgson, S. A., Adamson, J., Hunt, S. J., Cliffe, M. J., Cairns, A. B., Thompson, A. L., Tucker, M. G., Funnell, N. P. & Goodwin, A. L. Negative area compressibility in silver(I) tricyanomethanide. *Chem. Commun.* **50**, 5264–5266 (2014).

[316] Loa, I., Syassen, K. & Kremer, R. K. Structural properties of NaV_2O_5 under high pressure. *Phys. Rev. B* **60**, R6945–R6948 (1999).

[317] Loa, I., Syassen, K. & Kremer, R. K. Vibrational properties of NaV_2O_5 under high pressure studied by Raman spectroscopy. *Solid State Commun.* **112**, 681–685 (1999).

[318] Nakao, H., Ohwada, K., Takesue, N., Fujii, Y., Isobe, M., Ueda, Y., Sawa, H., Kawada, H., Murakami, Y., David, W. I. F. & Ibberson, R. M. Lattice dimerization and strain in inorganic spin-Peierls compound NaV_2O_5. *Physica B* **241–243**, 534–536 (1998).

[319] Bernert, A., Chatterji, T., Thalmeier, P. & Fulde, P. Structure determination, valence, and superexchange in the dimerized low temperature phase of α'-NaV_2O_5. *Eur. Phys. J. B* **21**, 535–546 (2001).

[320] Ohwada, K., Nakao, H., Fujii, Y., Isobe, M. & Ueda, Y. Structural aspects of NaV_2O_5 under high pressure. *J. Phys. Soc. Jpn.* **68**, 3286–3291 (1999).

[321] Nelmes, R. J. & Katrusiak, A. Evidence for anomalous pressure dependence of the spontaneous strain in $PbTiO_3$. *J. Phys. C: Solid State Phys.* **19**, L725–L730 (1986).

[322] Huang, C. W., Ren, W., Nguyen, V. C., Chen, Z., Wang, J., Sritharan, T. & Chen, L. Abnormal Poisson's ratio and linear compressibility in perovskite materials. *Adv. Mater.* **24**, 4170–4174 (2012).

[323] Lifshitz, I. M. On the thermal properties of chain and layered structures at low temperatures. *Zh. Eks. Teor. Fiz.* **22**, 475–486 (1952). *in Russian.*

[324] Nicolaou, Z. G. & Motter, A. E. Mechanical metamaterials with negative compressibility transitions. *Nature Mater.* **11**, 608–613 (2012).

[325] Azuma, M., Chen, W.-t., Seki, H., Czapski, M., Olga, S., Oka, K., Mizumaki, M., Watanuki, T., Ishimatsu, N., Kawamura, N., Ishiwata, S., Tucker, M. G., Shimakawa, Y. & Attfield, J. P. Colossal negative thermal expansion in $BiNiO_3$ induced by intermetallic charge transfer. *Nature Commun.* **2**, 347 (2011).

[326] Greaves, G. N., Greer, A. L., Lakes, R. S. & Rouxel, T. Poisson's ratio and modern materials. *Nature Mater.* **10**, 823–837 (2011).

[327] Sapriel, J., Hierle, R., Zyss, J. & Boissier, M. Acoustic and acoustooptic properties of 3-methyl 4-nitropyridine 1-oxide—a Brillouin scattering study. *Appl. Phys. Lett.* **55**, 2594–2596 (1989).

[328] Fuhr, P. L. & Huston, D. R. Multiplexed fiber optic pressure and vibration sensors for hydroelectric dam monitoring. *Smart Mater. Struct.* **2**, 260–263 (1993).

[329] Goh, S. K., Nakai, Y., Ishida, K., Klintberg, L. E., Ihara, Y., Kasahara, S., Shibauchi, T., Matsuda, Y. & Terashima, T. Anisotropic superconducting properties of optimally doped $BaFe_2(As_{0.65}P_{0.35})_2$ under pressure. *Phys. Rev. B* **82**, 094502 (2010).

[330] Zhao, P., Bennett, T. D., Casati, N. P. M., Lampronti, G. I., Moggach, S. A. & Redfern, S. A. T. Pressure-induced oversaturation and phase transition in zeolitic imidazolate frameworks with remarkable mechanical stability. *Dalton Trans.* **44**, 4498–4503 (2015).

[331] Calleja, M., Goodwin, A. L. & Dove, M. T. Origin of the colossal positive and negative thermal expansion in $Ag_3[Co(CN)_6]$: an ab initio density functional theory study. *J. Phys.: Condens. Matter* **20**, 255226 (2008).

[332] Ghalsasi, P., Poswal, H. K., Tripathi, R., Garg, N., Deo, M. N. & Sharma, S. M. Behaviour of NTE material $Ag_3[Co(CN)_6]$ under pressure. *J. Phys.: Conference Series* **377**, 012009 (2012).

[333] Rao, R., Achary, S. N., Tyagi, A. K. & Sakuntala, T. Raman spectroscopic study of high-pressure behavior of $Ag_3[Co(CN)_6]$. *Phys. Rev. B* **84**, 054107 (2011).

[334] Hermet, P., Catafesta, J., Bantignies, J.-L., Levelut, C., Maurin, D., Cairns, A. B., Goodwin, A. L. & Haines, J. Vibrational and thermal properties of $Ag_3[Co(CN)_6]$ from first principles calculations and infrared spectroscopy. *J. Phys. Chem. C* **117**, 12848–12857 (2013).

[335] Ibberson, R. M., David, W. I. F. & Knight, K. S. The high resolution powder diffractometer (HRPD) at ISIS—a user guide. Tech. Rep., Rutherford Appleton Laboratory, Didcot, U.K. (1992).

[336] Mao, H. K., Xu, J. & Bell, P. M. Calibration of the ruby pressure gauge to 800 kbar under quasi-hydrostatic conditions. *J. Geophys. Res* **91**, 4673–4676 (1986).

[337] European Synchrotron Radiation Facility (ESRF). The Swiss-Norwegian Beamlines: BM01A. at `http://www.esrf.eu/UsersAndScience/Experiments/CRG/BM01/bm01-a` (Last checked May 2015).

[338] Sheldrick, G. M. & Schneider, T. R. SHELXL: High-resolution refinement. *Meth. Enzymol.* **277**, 319–343 (1997).

[339] Uchida, T., Wang, Y., Rivers, M. L. & Sutton, S. R. Stability field and thermal equation of state of ε-iron determined by synchrotron X-ray diffraction in a multianvil apparatus. *J. Geophys. Res.* **106**, 21799–21810 (2001).

[340] Anderson, O. L. An experimental high-temperature thermal equation of state bypassing the Grüneisen parameter. *Phys. Earth Planet. Inter.* **22**, 165–172 (1980).

[341] Anderson, O. L. A universal thermal equation-of-state. *J. Geodyn.* **1**, 185–214 (1984).

[342] Fang, H., Phillips, A. E., Dove, M. T., Tucker, M. G. & Goodwin, A. L. Temperature-dependent pressure-induced softening in $Zn(CN)_2$. *Phys. Rev. B* **88**, 144103 (2013).

[343] Chapman, K. W. & Chupas, P. J. Pressure enhancement of negative thermal expansion behavior and induced framework softening in zinc cyanide. *J. Am. Chem. Soc.* **129**, 10090–10091 (2007).

[344] Campbell, B. J., Stokes, H. T., Tanner, D. E. & Hatch, D. M. ISODISPLACE: a web-based tool for exploring structural distortions. *J. Appl. Crystallogr.* **39**, 607–614 (2006).

[345] Grima, J., Attard, D., Caruana-Gauci, R. & Gatt, R. Negative linear compressibility of hexagonal honeycombs and related systems. *Scripta Mater.* **65**, 565–568 (2011).

[346] Young, R. A. (ed.) *The Rietveld Method*. IUCr Book Series (Oxford University Press, Oxford, 1993).

[347] Lakes, R. & Wojciechowski, K. Negative compressibility, negative Poisson's ratio, and stability. *Phys. Status Solidi B* **245**, 545–551 (2008).

[348] Sears, D. R. & Klug, H. P. Density and expansivity of solid xenon. *J. Chem. Phys.* **37**, 3002–3006 (1962).

[349] Sun, J., Weng, L., Zhou, Y., Chen, J., Chen, Z., Liu, Z. & Zhao, D. QMOF-1 and QMOF-2: Three-dimensional metal–organic open frameworks with a quartzlike topology. *Angew. Chem.* **114**, 4651–4653 (2002).

[350] Chapman, K. W., Chupas, P. J. & Kepert, C. J. Direct observation of a transverse vibrational mechanism for negative thermal expansion in $Zn(CN)_2$: An atomic pair distribution function analysis. *J. Am. Chem. Soc.* **127**, 15630–15636 (2005).

[351] Poswal, H. K., Tyagi, A. K., Lausi, A., Deb, S. K. & Sharma, S. M. Structural phase transitions in $Zn(CN)_2$ under high pressures. *J. Solid State Chem.* **182**, 136–140 (2009).

[352] Shugam, E. & Zhdanov, H. The crystal structure of cadmium cyanide. *Acta Physiochim. U.R.S.S.* **20**, 247–252 (1945).

[353] Williams, D. J., Partin, D. E., Lincoln, F. J., Kouvetakis, J. & O'Keeffe, M. The disordered crystal structures of $Zn(CN)_2$ and $Ga(CN)_3$. *J. Solid State Chem.* **134**, 164–169 (1997).

[354] Ravindran, T. R., Arora, A. K. & Sairam, T. N. A spectroscopic resolution of the structure of $Zn(CN)_2$. *J. Raman Spectrosc.* **38**, 283–287 (2007).

[355] Okaji, M., Yamada, N. & Moriyama, H. Ultra-precise thermal expansion measurements of ceramic and steel gauge blocks with an interferometric dilatometer. *Metrologia* **37**, 165–171 (2000).

[356] Mary, T. A., Evans, J. S. O., Vogt, T. & Sleight, A. W. Negative thermal expansion from 0.3 to 1050 Kelvin in ZrW_2O_8. *Science* **272**, 90–92 (1996).

[357] Zwanziger, J. W. Phonon dispersion and Grüneisen parameters of zinc dicyanide and cadmium dicyanide from first principles: Origin of negative thermal expansion. *Phys. Rev. B* **76**, 052102 (2007).

[358] Mittal, R., Zbiri, M., Schober, H., Marelli, E., Hibble, S. J., Chippindale, A. M. & Chaplot, S. Relationship between phonons and thermal expansion in $Zn(CN)_2$ and $Ni(CN)_2$ from inelastic neutron scattering and *ab initio* calculations. *Phys. Rev. B* **83**, 024301 (2011).

[359] Jorgensen, J. D., Hu, Z., Teslic, S., Argyriou, D. N., Short, S., Evans, J. S. O. & Sleight, A. W. Pressure-induced cubic-to-orthorhombic phase transition in ZrW_2O_8. *Phys. Rev. B* **59**, 215–225 (1999).

[360] Jorgensen, J. D., Hu, Z., Short, S., Sleight, A. W. & Evans, J. S. O. Pressure-induced cubic-to-orthorhombic phase transformation in the negative thermal expansion material HfW_2O_8. *J. Appl. Phys.* **89**, 3184–3188 (2001).

[361] Lind, C., VanDerveer, D. G., Wilkinson, A. P., Chen, J., Vaughan, M. T. & Weidner, D. J. New high-pressure form of the negative thermal expansion materials zirconium molybdate and hafnium molybdate. *Chem. Mater.* **13**, 487–490 (2001).

[362] Hammersley, A. P., Svensson, S. O., Hanfland, M., Fitch, A. N. & Hausermann, D. Two-dimensional detector software: From real detector to idealised image or two-theta scan. *High Press. Res.* **14**, 235–248 (1996).

[363] Marshall, W. G. & Francis, D. J. Attainment of near-hydrostatic compression conditions using the Paris-Edinburgh cell. *J. Appl. Crystallogr.* **35**, 122–125 (2002).

[364] Fortes, A. D., Wood, I. G., Alfredsson, M., Vočadlo, L., Knight, K. S., Marshall, W. G., Tucker, M. G. & Fernandez-Alonso, F. The high-pressure phase diagram of ammonia dihydrate. *High Press. Res.* **27**, 201–212 (2007).

[365] Toby, B. H. EXPGUI, a graphical user interface for GSAS. *J. Appl. Crystallogr.* **34**, 210–213 (2001).

[366] Rath, S., Kunz, M. & Miletich, R. Pressure-induced phase transition in malayaite, $CaSnOSiO_4$. *Am. Mineral.* **88**, 293–300 (2003).

[367] Fradkin, M. A. The effect of strain on the thermodynamics of the weakly first-order phase transition. *J. Phys.: Condens. Matter* **9**, 7925–7932 (1997).

[368] Hatch, D. M. & Stokes, H. T. Isotropy Subgroups for Reducible Representations of Space Groups. In Gilmore, R. (ed.) *XV International Colloquium on Group Theoretical Methods in Physics*, 710–715 (World Scientific, Singapore, 1987).

[369] Xu, G.-C., Ma, X.-M., Zhang, L., Wang, Z.-M. & Gao, S. Disorder-order ferroelectric transition in the metal formate framework of $[NH_4][Zn(HCOO)_3]$. *J. Am. Chem. Soc.* **132**, 9588–9590 (2010).

[370] Liu, Y., Ni, L., Ren, Z., Xu, G., Song, C. & Han, G. Negative pressure induced ferroelectric phase transition in rutile TiO_2. *J. Phys.: Condens. Matter* **21**, 275901 (2009).

[371] Cañadillas-Delgado, L., Fabelo, O., Rodríguez-Velamazán, J. A., Lemée-Cailleau, M.-H., Mason, S. A., Pardo, E., Lloret, F., Zhao, J.-P., Bu, X.-H., Simonet, V., Colin, C. V. & Rodríguez-Carvajal, J. The role of order-disorder transitions in the quest for molecular multiferroics: Structural and magnetic neutron studies of a mixed valence iron(II)–iron(III) formate framework. *J. Am. Chem. Soc.* **134**, 19772–19781 (2012).

[372] Cheong, S. & Mostovoy, M. Multiferroics: a magnetic twist for ferroelectricity. *Nature Mater.* **6**, 13–20 (2007).

[373] Bennett, T. D., Saines, P. J., Keen, D. A., Tan, J.-C. & Cheetham, A. K. Ball-milling-induced amorphization of zeolitic imidazolate frameworks (ZIFs) for the irreversible trapping of iodine. *Chem. Eur. J.* **19**, 7049–7055 (2013).

[374] Bennett, T. D. & Cheetham, A. K. Amorphous metal–organic frameworks. *Acc. Chem. Res.* **47**, 1555–1562 (2014).

[375] Tucker, M. G., Keen, D. A., Dove, M. T. & Trachenko, K. Refinement of the Si–O–Si bond angle distribution in vitreous silica. *J. Phys.: Condens. Matter* **17**, S67–S75 (2005).

[376] Trewin, A. & Cooper, A. I. Porous organic polymers: Distinction from disorder? *Angew. Chem. Int. Ed.* **49**, 1533–1535 (2010).

[377] Bennett, T. D., Keen, D. A., Tan, J.-C., Barney, E. R., Goodwin, A. L. & Cheetham, A. K. Thermal amorphization of zeolitic imidazolate frameworks. *Angew. Chem. Int. Ed.* **50**, 3067–3071 (2011).

[378] Ben, T., Ren, H., Ma, S., Cao, D., Lan, J., Jing, X., Wang, W., Xu, J., Deng, F., Simmons, J. M., Qiu, S. & Zhu, G. Targeted synthesis of a porous aromatic framework with high stability and exceptionally high surface area. *Angew. Chem. Int. Ed.* **48**, 9457–9460 (2009).

[379] Ben, T. & Qiu, S. Porous aromatic frameworks: Synthesis, structure and functions. *CrystEngComm* **15**, 17–26 (2013).

[380] Matsunaga, T., Akola, J., Kohara, S., Honma, T., Kobayashi, K., Ikenaga, E., Jones, R. O., Yamada, N., Takata, M. & Kojima, R. From local structure to nanosecond recrystallization dynamics in AgInSbTe phase-change materials. *Nature Mater.* **10**, 129–134 (2011).

[381] Richet, P. & Gillet, P. Pressure-induced amorphization of minerals: a review. *Eur. J. Miner.* **9**, 907–933 (1997).

[382] Bennett, T. D., Simoncic, P., Moggach, S. A., Gozzo, F., Macchi, P., Keen, D. A., Tan, J. C. & Cheetham, A. K. Reversible pressure-induced amorphization of a zeolitic imidazolate framework (ZIF-4). *Chem. Commun.* **47**, 7983–7985 (2011).

[383] Haines, J., Levelut, C., Isambert, A., Hebert, P., Kohara, S., Keen, D. A., Hammouda, T. & Andrault, D. Topologically ordered amorphous silica obtained from the collapsed siliceous zeolite, Silicalite-1-F: A step toward "perfect" glasses. *J. Am. Chem. Soc.* **131**, 12333–12338 (2009).

[384] Allan, P. K., Xiao, B., Teat, S. J., Knight, J. W. & Morris, R. E. In-situ single-crystal diffraction studies of the structural transition of metal–organic framework copper 5-sulfoisophthalate, Cu-SIP-3. *J. Am. Chem. Soc.* **132**, 3605–3611 (2010).

[385] Allan, P. K., Chapman, K. W., Chupas, P. J., Hriljac, J. A., Renouf, C. L., Lucas, T. C. A. & Morris, R. E. Pair distribution function-derived mechanism of a single-crystal to disordered to single-crystal transformation in a hemilabile metal–organic framework. *Chem. Sci.* **3**, 2559–2564 (2012).

[386] Xiao, B., Byrne, P. J., Wheatley, P. S., Wragg, D. S., Zhao, X., Fletcher, A. J., Thomas, K. M., Peters, L., Evans, J. S. O., Warren, J. E., Zhou, W. & Morris, R. E. Chemically blockable transformation and ultraselective low-pressure gas adsorption in a non-porous metal organic framework. *Nature Chem.* **1**, 289–294 (2009).

[387] Kepert, C. J., Prior, T. J. & Rosseinsky, M. J. A versatile family of interconvertible microporous chiral molecular frameworks: the first example of ligand control of network chirality. *J. Am. Chem. Soc.* **122**, 5158–5168 (2000).

[388] Yang, S., Lin, X., Lewis, W., Suyetin, M., Bichoutskaia, E., Parker, J. E., Tang, C. C., Allan, D. R., Rizkallah, P. J., Hubberstey, P., Champness, N. R., Thomas, K. M., Blake, A. J. & Schröder, M. A partially interpenetrated metal–organic framework for selective hysteretic sorption of carbon dioxide. *Nature Mater.* **11**, 710–716 (2012).

[389] Jain, P., Dalal, N. S., Toby, B. H., Kroto, H. W. & Cheetham, A. K. Order-disorder antiferroelectric phase transition in a hybrid inorganic–organic framework with the perovskite architecture. *J. Am. Chem. Soc.* **130**, 10450–10451 (2008).

[390] Sánchez-Andújar, M., Presedo, S., Yáñez-Vilar, S., Castro-García, S., Shamir, J. & Señarís-Rodríguez, M. A. Characterization of the orderdisorder dielectric transition in the hybrid organic–inorganic perovskite-like formate $Mn(HCOO)_3[(CH_3)_2NH_2]$. *Inorg. Chem.* **49**, 1510–1516 (2010).

[391] Zhang, W., Cai, Y., Xiong, R.-G., Yoshikawa, H. & Awaga, K. Exceptional dielectric phase transitions in a perovskite-type cage compound. *Angew. Chem. Int. Ed.* **49**, 6608–6610 (2010).

[392] Welberry, T. R. & Butler, B. D. Diffuse X-ray scattering from disordered crystals. *Chem. Rev.* **95**, 2369–2403 (1995).

[393] Simonov, A., Weber, T. & Steurer, W. Yell: a computer program for diffuse scattering analysis via three-dimensional delta pair distribution function refinement. *J. Appl. Crystallogr.* **47**, 1146–1152 (2014).

[394] Kosterlitz, J. M. & Thouless, D. J. Ordering, metastability and phase transitions in two-dimensional systems. *J. Phys. C: Solid State Phys.* **6**, 1181 (1973).

[395] Aragòn de la Cruz, F. & Miguel Alonso, S. Interlamellar complexes between n-alkylenediamines and nickel cyanide. *Naturwissensch.* **62**, 298 (1975).

[396] Hibble, S. J., Chippindale, A. M., Pohl, A. H. & Hannon, A. C. Surprises from a simple material—the structure and properties of nickel cyanide. *Angew. Chem. Int. Ed.* **46**, 7116–7118 (2007).

[397] Adamson, J., Funnell, N. P., Thompson, A. L. & Goodwin, A. L. Structural investigation of a hydrogen bond order-disorder transition in a polar one-dimensional confined ice. *Phys. Chem. Chem. Phys.* **16**, 2654–2659 (2014).

[398] Hibble, S. J., Wood, G. B., Bilbé, E. J., Pohl, A. H., Tucker, M. G., Hannon, A. C. & Chippindale, A. M. Structures and negative thermal expansion properties of the one-dimensional cyanides, CuCN, AgCN and AuCN. *Z. Kristallogr.* **225**, 457–462 (2010).

[399] Goodwin, A. L., Dove, M. T., Chippindale, A. M., Hibble, S. J., Pohl, A. H. & Hannon, A. C. Aperiodicity, structure, and dynamics in $Ni(CN)_2$. *Phys. Rev. B* **80**, 054101 (2009).

[400] Warren, B. E. X-ray diffraction in random layer lattices. *Phys. Rev.* **59**, 693–698 (1941).

[401] Saines, P. J., Tan, J.-C., Yeung, H. H.-M., Barton, P. T. & Cheetham, A. K. Layered inorganic–organic frameworks based on the 2,2-dimethylsuccinate ligand: Structural diversity and its effect on nanosheet exfoliation and magnetic properties. *Dalton Trans.* **41**, 8585–8593 (2012).

[402] Gándara, F. & Bennett, T. D. Crystallography of metal–organic frameworks. *IUCrJ* **1**, 563–570 (2014).

[403] Cao, S., Bennett, T. D., Keen, D. A., Goodwin, A. L. & Cheetham, A. K. Amorphization of the prototypical zeolitic imidazolate framework ZIF-8 by ball-milling. *Chem. Commun.* **48**, 7805–7807 (2012).

[404] Treacy, M. M. J. & Borisenko, K. B. The local structure of amorphous silicon. *Science* **335**, 950–953 (2012).

[405] Park, J., Wang, Z. U., Sun, L.-B., Chen, Y.-P. & Zhou, H.-C. Introduction of functionalized mesopores to metal–organic frameworks via metal–ligand–fragment coassembly. *J. Am. Chem. Soc.* **134**, 20110–20116 (2012).

[406] Zeng, X., Kieffer, R., Glettner, B., Nürnberger, C., Liu, F., Pelz, K., Prehm, M., Baumeister, U., Hahn, H., Lang, H., Gehring, G. A., Weber, C. H. M., Hobbs, J. K., Tschierske, C. & Ungar, G. Complex multicolor tilings and critical phenomena in tetraphilic liquid crystals. *Science* **331**, 1302–1306 (2011).

[407] Bennett, T. D., Tan, J.-C., Yue, Y. Z., Ducati, C., Terril, N., Yeung, H. H. M., Zhou, Z., Chen, W., Henke, S., Cheetham, A. K. & Greaves, G. N. Perfect and stable hybrid glasses from strong and fragile metal–organic framework liquids (2015). arXiv: 1409.3980.

[408] Camp, P. J., Fuertes, A. & Attfield, J. P. Sub-extensive entropies and open order in perovskite oxynitrides. *J. Am. Chem. Soc.* **134**, 6762–6766 (2012).

[409] Wessells, C. D., Huggins, R. A. & Cui, Y. Copper hexacyanoferrate battery electrodes with long cycle life and high power. *Nature Commun.* **2**, 550 (2011).

[410] Balazs, A. C. & Epstein, I. R. Emergent or just complex? *Science* **325**, 1632–1634 (2009).

[411] Moessner, R. & Ramirez, A. P. Geometrical frustration. *Physics Today* **Feb**, 24–29 (2006).

[412] Nitschke, J. R. Systems chemistry: Molecular networks come of age. *Nature* **462**, 736–738 (2009).

[413] Žukovič, M. & Idogaki, T. Low-temperature long-range ordering of a classical XY spin system with bilinear-biquadratic exchange Hamiltonian. *Physica B* **329–333**, 1055–1056 (2003).

[414] Bowmaker, G. A., Kennedy, B. J. & Reid, J. C. Crystal structures of AuCN and AgCN and vibrational spectroscopic studies of AuCN, AgCN, and CuCN. *Inorg. Chem.* **37**, 3968–3974 (1998).

[415] Hibble, S. J., Cheyne, S. M., Hannon, A. C. & Eversfield, S. G. Beyond bragg scattering:the structure of AgCN determined from total neutron diffraction. *Inorg. Chem.* **41**, 1042–1044 (2002).

[416] Hibble, S. J., Hannon, A. C. & Cheyne, S. M. Structure of AuCN determined from total neutron diffraction. *Inorg. Chem.* **42**, 4724–4730 (2003).

[417] Bryce, D. L. & Wasylishen, R. E. Insight into the structure of silver cyanide from 13C and 15N solid-state NMR spectroscopy. *Inorg. Chem.* **41**, 4131–4138 (2002).

[418] Hibble, S. J., Chippindale, A. M., Marelli, E., Kroeker, S., Michaelis, V. K., Greer, B. J., Aguiar, P. M., Bilbe, E. J., Barney, E. R. & Hannon, A. C. Local and average structure in zinc cyanide: Toward an understanding of the atomistic origin of negative thermal expansion. *J. Am. Chem. Soc.* **135**, 16478–16489 (2013).

[419] Hibble, S. J., Cheyne, S. M., Hannon, A. C. & Eversfield, S. G. CuCN: A polymorphic material. Structure of one form determined from total neutron diffraction. *Inorg. Chem.* **41**, 4990–4992 (2002).

[420] Hibble, S. J., Eversfield, S. G., Cowley, A. R. & Chippindale, A. M. Copper(I) cyanide: A simple compound with a complicated structure and surprising room-temperature reactivity. *Angew. Chem. Int. Ed.* **43**, 628–630 (2004).

[421] Chippindale, A. M. & Hibble, S. J. Helices, chirality and interpenetration: The versatility and remarkable interconversion of silver–copper cyanide frameworks. *J. Am. Chem. Soc.* **131**, 12736–12744 (2009).

[422] Chippindale, A. M., Hibble, S. J., Bilbé, E. J., Marelli, E., Hannon, A. C., Allain, C., Pansu, R. & Hartl, F. Mixed copper, silver, and gold cyanides, $(M_xM_{1-x})CN$: Tailoring chain structures to influence physical properties. *J. Am. Chem. Soc.* **134**, 16387–16400 (2012).

[423] Warren, B. E. & Averbach, B. L. The effect of cold-work distortion on X-ray patterns. *J. Appl. Phys.* **21**, 595–599 (1950).

[424] Blair, A. Silver plating. *Met. Finish.* **98**, 298,300–303 (2000).

[425] La Brooy, S. R., Linge, H. G. & Walker, G. S. Review of gold extraction from ores. *Miner. Eng.* **7**, 1213–1241 (1994).

[426] Leznoff, D. B., Xue, B.-Y., Batchelor, R. J., Einstein, F. W. B. & Patrick, B. O. Gold–gold interactions as crystal engineering design elements in heterobimetallic coordination polymers. *Inorg. Chem.* **40**, 6026–6034 (2001).

[427] Katz, M. & Leznoff, D. Highly birefringent cyanoaurate coordination polymers: The effect of polarizable C–X bonds (X = Cl, Br). *J. Am. Chem. Soc.* **131**, 18435–18444 (2009).

[428] Bailey, A. C. & Yates, B. Anisotropic thermal expansion of pyrolytic graphite at low temperatures. *J. Appl. Phys.* **41**, 5088–5091 (1970).

[429] Stephens, P. W. Phenomenological model of anisotropic peak broadening in powder diffraction. *J. Appl. Crystallogr.* **32**, 281–289 (1999).

[430] Metropolis, N., Rosenbluth, A. W., Rosenbluth, M. N., Teller, A. H. & Teller, E. Equation of state calculations by fast computing machines. *J. Chem. Phys.* **21**, 1087–1092 (1953).

[431] Peintinger, M. F., Oliveira, D. V. & Bredow, T. Consistent gaussian basis sets of triple-zeta valence with polarization quality for solid-state calculations. *J. Comput. Chem.* **34**, 451–459 (2013).

[432] Doll, K., Pyykkö, P. & Stoll, H. Closed-shell interaction in silver and gold chlorides. *J. Chem. Phys.* **109**, 2339 (1998).

[433] Hay, P. J. & Wadt, W. R. *Ab initio* effective core potentials for molecular calculations. Potentials for K to Au including the outermost core orbitals. *J. Chem. Phys.* **82**, 299 (1985).

[434] Adamo, C. & Barone, V. Toward reliable density functional methods without adjustable parameters: The PBE0 model. *J. Chem. Phys.* **110**, 6158 (1999).

[435] Perdew, J. P., Ruzsinszky, A., Csonka, G. I., Vydrov, O. A., Scuseria, G. E., Constantin, L. A., Zhou, X. & Burke, K. Restoring the density-gradient expansion for exchange in solids and surfaces. *Phys. Rev. Lett.* **100**, 136406 (2008).

[436] Grimme, S. Semiempirical GGA-type density functional constructed with a long-range dispersion correction. *J. Comput. Chem.* **27**, 1787–1799 (2006).

[437] Anderson, P. W. Ordering and antiferromagnetism in ferrites. *Phys. Rev.* **102**, 1008–1013 (1956).

[438] Castelnovo, C., Moessner, R. & Sondhi, S. L. Magnetic monopoles in spin ice. *Nature* **451**, 42–45 (2008).

[439] Tissier, M., Delamotte, B. & Mouhanna, D. XY frustrated systems: Continuous exponents in discontinuous phase transitions. *Phys. Rev. B* **67**, 134422 (2003).

[440] Lee, D. H., Joannopoulos, J. D., Negele, J. W. & Landau, D. P. Symmetry analysis and Monte Carlo study of a frustrated antiferromagnetic planar (XY) model in two dimensions. *Phys. Rev. B* **33**, 450–475 (1986).

[441] Scherrer, P. Bestimmung der größe und der inneren struktur von kolloidteilchen mittels röntgenstrahlen. *Nachrichten von der Gesellschaft der Wissenschaften zu Göttingen, Mathematisch-Physikalische Klasse* **1918**, 98–100 (1918).

[442] Langford, J. I. & Wilson, A. J. C. Scherrer after sixty years: A survey and some new results in the determination of crystallite size. *J. Appl. Crystallogr.* **11**, 102–113 (1978).

[443] Collins, M. F. & Patrenko, O. A. Triangular antiferromagnets. *Can. J. Phys.* **75**, 605–655 (1997).

[444] Läuchli, A., Mila, F. & Penc, K. Quadrupolar phases of the $S = 1$ bilinear-biquadratic Heisenberg model on the triangular lattice. *Phys. Rev. Lett.* **97**, 087205 (2006).

[445] Mermin, N. D. & Wagner, H. Absence of ferromagnetism or antiferromagnetism in one- or two-dimensional isotropic heisenberg models. *Phys. Rev. Lett.* **17**, 1133–1136 (1966).

[446] Mühlbauer, S., Binz, B., Jonietz, F., Pfleiderer, C., Rosch, A., Neubauer, A., Georgii, R. & Böni, P. Skyrmion lattice in a chiral magnet. *Science* **323**, 915–919 (2009).

[447] Nakatsuji, S., Nambu, Y., Tonomura, H., Sakai, O., Jonas, S., Broholm, C., Tsunetsugu, H., Qiu, Y. & Maeno, Y. Spin disorder on a triangular lattice. *Science* **309**, 1697–1700 (2005).

[448] Blunt, M. O., Russell, J. C., Giménez-López, M. d. C., Garrahan, J. P., Lin, X., Schröder, M., Champness, N. R. & Beton, P. H. Random tiling and topological defects in a two-dimensional molecular network. *Science* **322**, 1077–1081 (2008).

[449] Simonov, A., Weber, T. & Steurer, W. Experimental uncertainties of three-dimensional pair distribution function investigations exemplified on the diffuse scattering from a tris-*tert*-butyl-1,3,5-benzene tricarboxamide single crystal. *J. Appl. Crystallogr.* **47**, 2011–2018 (2014).

[450] Nagaosa, N. & Tokura, Y. Topological properties and dynamics of magnetic skyrmions. *Nature Nano.* **8**, 899–911 (2013).

[451] Giblin, S. R., Bramwell, S. T., Holdsworth, P. C. W., Prabhakaran, D. & Terry, I. Creation and measurement of long-lived magnetic monopole currents in spin ice. *Nat Phys* **7**, 252–258 (2011).

[452] ISIS Facility, Didcot, U.K. *HRPD User Manual*. at `http://www.isis.stfc.ac.uk/instruments/hrpd/documents/hrpd-manual6735.pdf` (Last checked April 2015).

[453] Ikeda, S. & Carpenter, J. M. Wide-energy-range, high-resolution measurements of neutron pulse shapes of polyethylene moderators. *Nucl. Instrum. Meth. A* **239**, 536–544 (1985).

[454] Nelson, J. B. & Riley, D. P. An experimental investigation of extrapolation methods in the derivation of accurate unit-cell dimensions of crystals. *Proc. Phys. Soc.* **57**, 160–177 (1945).

[455] Otwinowski, Z. & Minor, W. Processing of X-ray diffraction data collected in oscillation mode. *Method. Enzymol.* **276**, 307–326 (1997).

[456] Altomare, A., Cascarano, G., Giacovazzo, C., Guagliardi, A., Burla, M. C., Polidori, G. & Camalli, M. SIR92. *J. Appl. Crystallogr.* **27**, 435 (1994).

[457] Rohatgi, A. WebPlotDigitizer v.3.6. at `http://arohatgi.info/WebPlotDigitizer` (Last checked January 2015).

[458] Liu, L.-G. Polymorphism and compression of TeO_2 at high pressure. *J. Phys. Chem. Solids* **48**, 719–722 (1987).

[459] Rietveld, H. Line profiles of neutron powder-diffraction peaks for structure refinement. *Acta Crystallogr.* **22**, 151–152 (1967).

[460] Wills, A. S., Zhitomirsky, M. E., Canals, B., Sanchez, J. P., Bonville, P., de Réotier, P. D. & Yaouanc, A. Magnetic ordering in $Gd_2Sn_2O_7$: The archetypal Heisenberg pyrochlore antiferromagnet. *J. Phys.: Condens. Matter* **18**, L37 (2006).

[461] Movshovich, R., Jaime, M., Mentink, S., Menovsky, A. A. & Mydosh, J. A. Second low-temperature phase transition in frustrated UNi_4B. *Phys. Rev. Lett.* **83**, 2065–2068 (1999).

[462] Greedan, J. E., Wiebe, C. R., Wills, A. S. & Stewart, J. R. Neutron-scattering studies of the geometrically frustrated spinel $LiMn_2O_4$. *Phys. Rev. B* **65**, 184424 (2002).

[463] Zheng, X. G., Kubozono, H., Nishiyama, K., Higemoto, W., Kawae, T., Koda, A. & Xu, C. N. Coexistence of long-range order and spin fluctuation in geometrically frustrated clinoatacamite $Cu_2Cl(OH)_3$. *Phys. Rev. Lett.* **95**, 057201 (2005).

[464] Rule, K. C., Ehlers, G., Stewart, J. R., Cornelius, A. L., Deen, P. P., Qiu, Y., Wiebe, C. R., Janik, J. A., Zhou, H. D., Antonio, D., Woytko, B. W., Ruff, J. P., Dabkowska, H. A., Gaulin, B. D. & Gardner, J. S. Polarized inelastic neutron scattering of the partially ordered $Tb_2Sn_2O_7$. *Phys. Rev. B* **76**, 212405 (2007).

[465] Cao, G., Durairaj, V., Chikara, S., Parkin, S. & Schlottmann, P. Partial antiferromagnetism in spin-chain $Sr_5Rh_4O_{12}$, $Ca_5Ir_3O_{12}$, and Ca_4IrO_6 single crystals. *Phys. Rev. B* **75**, 134402 (2007).

[466] Ehlers, G., Ritter, C., Stewart, J. R., Hillier, A. D. & Maletta, H. Phase transition of geometrically frustrated TbNiAl in a magnetic field. *Phys. Rev. B* **75**, 024420 (2007).

[467] Hayes, T. J., Balakrishnan, G., Deen, P. P., Manuel, P., Chapon, L. C. & Petrenko, O. A. Coexistence of the long-range and short-range magnetic order components in $SrEr_2O_4$. *Phys. Rev. B* **84**, 174435 (2011).

[468] Keen, D. A., Hull, S., Hayes, W. & Gardner, N. J. G. Structural evidence for a fast-ion transition in the high-pressure rocksalt phase of silver iodide. *Phys. Rev. Lett.* **77**, 4914–4917 (1996).

[469] Gregoryanz, E., Lundegaard, L. F., McMahon, M. I., Guillaume, C., Nelmes, R. J. & Mezouar, M. Structural diversity of sodium. *Science* **320**, 1054–1057 (2008).

[470] Gardner, J. S., Gingras, M. J. P. & Greedan, J. E. Magnetic pyrochlore oxides. *Rev. Mod. Phys.* **82**, 53–107 (2010).

[471] Champion, J. D. M., Wills, A. S., Fennell, T., Bramwell, S. T., Gardner, J. S. & Green, M. A. Order in the heisenberg pyrochlore: The magnetic structure of $Gd_2Ti_2O_7$. *Phys. Rev. B* **64**, 140407 (2001).

[472] Stewart, J. R., Ehlers, G., Wills, A. S., Bramwell, S. T. & Gardner, J. S. Phase transitions, partial disorder and multi-**k** structures in $Gd_2Ti_2O_7$. *J. Phys.: Condens. Matter* **16**, L321 (2004).

[473] Bonville, P., Hodges, J. A., Ocio, M., Sanchez, J. P., Vulliet, P., Sosin, S. & Braithwaite, D. Low temperature magnetic properties of geometrically frustrated $Gd_2Sn_2O_7$ and $Gd_2Ti_2O_7$. *J. Phys.: Condens. Matter* **15**, 7777 (2003).

[474] Sosin, S. S., Prozorova, L. A., Smirnov, A. I., Bonville, P., Jasmin-Le Bras, G. & Petrenko, O. A. Spin dynamics of the pyrochlore magnets $Gd_2Ti_2O_7$ and $Gd_2Sn_2O_7$ in the paramagnetic state. *Phys. Rev. B* **77**, 104424 (2008).

[475] Sosin, S. S., Smirnov, A. I., Prozorova, L. A., Balakrishnan, G. & Zhitomirsky, M. E. Magnetic resonance in the pyrochlore antiferromagnet $Gd_2Ti_2O_7$. *Phys. Rev. B* **73**, 212402 (2006).

[476] Coelho, A. A. TOPAS Academic: General Profile and Structure Analysis Software for Powder Diffraction Data, version 5 (Computer Software) (2014). Coelho Software, Brisbane.

[477] Ridout, J. & Probert, M. R. Low-temperature and high-pressure polymorphs of isopropyl alcohol. *CrystEngComm* **16**, 7397–7400 (2014).

[478] Goodwin, A. L., Tucker, M. G., Dove, M. T. & Keen, D. A. Magnetic structure of MnO at 10 K from total neutron scattering data. *Phys. Rev. Lett.* **96**, 047209 (2006).

[479] Frandsen, B. A. & Billinge, S. J. L. Magnetic structure determination from the magnetic pair distribution function (mPDF): ground state of MnO. *Acta Crystallogr.* A**71**, 325–334 (2015).

Appendix A

Supplementary methods

A.1 Lattice systems in crystalline materials

Table A.1.1: Lattice group symmetry.

Lattice System	Centering	Axial Distances	Axial Angles
Cubic	P, I , F	$a = b = c$	$\alpha = \beta = \gamma = 90°$
Tetragonal	P, I	$a = b \neq c$	$\alpha = \beta = \gamma = 90°$
Orthorhombic	P, C, I, F	$a \neq b \neq c$	$\alpha = \beta = \gamma = 90°$
Hexagonal	P	$a = b \neq c$	$\alpha = \beta = 90°$, $\gamma = 120°$
Rhombohedral	P	$a = b = c$	$\alpha = \beta = \gamma \neq 90°$
Monoclinic	P, C	$a \neq b \neq c$	$\alpha = \gamma = 90°$, $\beta \neq 90°$
Triclinic	P	$a \neq b \neq c$	$\alpha \neq \beta \neq \gamma \neq 90°$

A.2 Spallation neutron sources and time-of-flight

ISIS and other spallation neutron sources make use of the time-of-flight (TOF) method using neutron pulses. This is in part due to the experimental setup of neutron production [Fig. 1.24]. Spallation starts with the injection and acceleration of hydride (H^-) in a linear accelerator (linac). These pass through as stripping foil made of aluminium oxide as they enter a synchrotron. Here the protons are accelerated to 800 MeV and separated into two bunches. At a frequency of 50 Hz, bunches are 'kicked' from the synchrotron and into one of the extracted proton beam paths: at ISIS one in five bunches is extracted to Target Station 2 (TS2) and the others to Target Station 1 (TS1). At the end of the guide the protons hit the tungsten target and give out about 20–30 neutrons per proton collision.

The neutrons produced have very high energies (in the MeV range) and are too energetic for diffraction studies by a factor of 10^8 [144]. Large moderators are therefore placed between the neutron source (the target) and the instruments. Collisions with small molecules dissipate the excess energy by inelastic collisions: ISIS uses water (298 K), liquid (100 K) or solid (25 K) methane, or liquid hydrogen (20 K) for moderation. After many collisions within the moderator the neutrons become thermalised and mostly have the same characteristic temperature as the moderator.

Leaving each moderator is a high flux of neutrons with a distribution of energies. Monochromation of this radiation would lead to unacceptable drop in flux, so time of flight makes use of the pulsed nature of the beam to utilise all neutrons leaving the moderator for diffraction. It is assumed that all neutrons leave the moderator at the same time then, using banks of detectors at fixed angles and distances, the time taken for the neutron to reach that detector is recorded. From equation 1.34

$$\lambda = \frac{h}{p} = \frac{h}{mv} = \frac{h}{m}\frac{t_{\mathrm{tof}}}{L}, \tag{A.2.1}$$

where t_{tof} is the time taken for the neutron to be detected and L is the total path length [144]. Therefore we can rewrite Bragg's law as

$$d_{hkl} = \left(\frac{h}{2m\sin\theta L}\right) t_{\mathrm{tof}}. \tag{A.2.2}$$

The layout of one instrument used in this work (the High Resolution Powder Diffractometer, HRPD) is shown in Figure A.2.1 [452]. It shows the three fixed detector banks (backscattering, 90° and low angle) positioned around the sample, the 100 m guide and the moderator. The resolution of TOF diffraction measurements is dependent on the timing resolution, which is a function of both the angle of detector bank (varying as $\cot\theta$) and the distance between moderator and detector (L). HRPD makes use of a very long guide to improve the accuracy of neutron timing, with choppers used to prevent pulse overlap. Higher flux, lower resolution instruments use more detector banks closer to the moderator *e.g.* GEM at ISIS has seven detector banks.

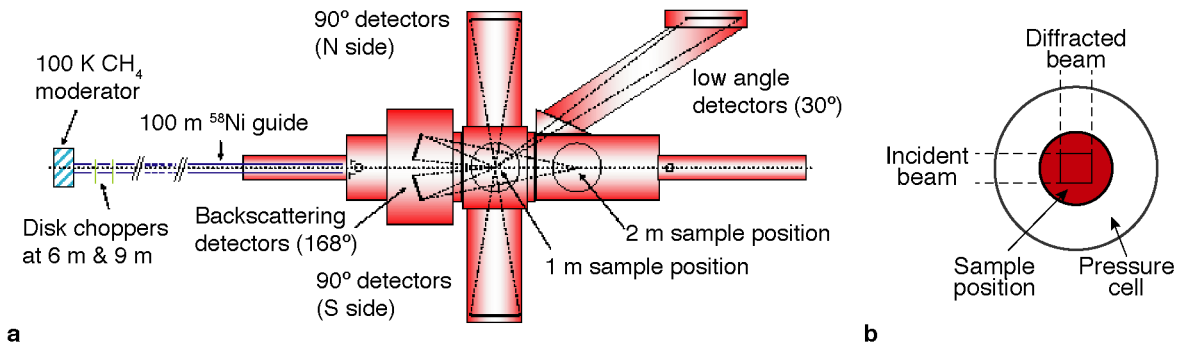

Figure A.2.1: (a) The layout of the HRPD instrument at ISIS spallation neutron source, U.K. [452]. The sample position is to the far right of the diagram, while the very long neutron guide is necessary to give very high resolution. (b) The general setup for high-pressure experiments on HRPD, where colimation is such that the 90° banks are the main diffraction banks (From Ref. 452).

A.3 Powder refinement methods

We have determined that the positions of the Bragg peaks in 2θ arise due to the unit cell of the material, whilst the intensities of peaks arise from the position of atoms within the unit cell. There are two main approaches to analysing data that either just models the former (Pawley or Le Bail refinement) or both contributions (Rietveld refinement). In either case the background of the powder pattern is fitted with a polynomial function; peak shapes (peak profiles) can be modelled by characterising the instrument against a standard, or refinement of a common peak shape. In neutron diffraction peak shapes are in general reproducible and of simple mathematical form, such as a Gaussian function, resulting in the early successes of powder neutron diffraction [144]. A fundamental parameters approach as proposed for use at ISIS based on the Ikeda Carpenter shape [453] is used here. For X-ray diffraction much more complex shapes are used, with the pseudo-Voigt (PV) and modified Thompson-Cox-Hastings pseudo-Voigt (TCHZ) common as defined in Ref. 346.

For Pawley or Le Bail refinement, the additional parameters are the unit cell dimensions and the space group. Both Pawley and Le Bail refinements consider the whole profile to refine the best values for the unit cell dimensions, but they differ slightly in how overlapping peaks are treated within the refinement. This is important in higher symmetry crystals where overlap is significant. In Pawley refinement the intensities of peaks (I_{hkl}) are refined against data, meaning that if two peaks are overlapping then correlation in this refinement becomes very large and unstable. To correct for this a restraint is applied that ensures that $I_1(hkl) = I_2(hkl)$ as the difference between two peaks in 2θ approaches zero. In Le Bail fitting intensities are assigned and iterated in a similar way to the Rietveld method which avoids the instability in the Pawley technique and is faster. For extraction of peak intensities the Pawley method is the preferred route.

Rietveld refinement differs in that intensities of peaks are directly calculated from a structural model. In such a refinement the user inputs the unit cell (from indexing a pattern, for example), the expected atomic positions, space group and starting values for any other parameters such as crystallite size or strain. From this a diffraction pattern is calculated (y_{calc}) and compared to the experimental data (y_{obs}). A weighted residual

chi-squared function is calculated for the whole pattern,

$$\chi_0^2 = \sum_{i=1}^{n} w_i [y_{\text{calc}} - y_{\text{obs}}]^2 \tag{A.3.3}$$

which is minimised though a least-squares routine. Usually this minimisation takes into account the weighted R-factor,

$$R_{\text{wp}} = \left[\frac{\chi_0^2}{\sum w_i y_i^2(\text{obs})} \right]. \tag{A.3.4}$$

As the refinement proceeds, the user determines which parameters may be refined at each stage. The minimisation routine then iteratively changes this variable until the R_{wp} converges, with all changes that improves the fit accepted. Great care must be taken in this procedure to ensure appropriate variables are refined, and that the data are of sufficient quality to extract the parameters refined. If very large numbers of variables are refined against poor quality data the final structural model may be essentially meaningless. Goodness of fit should be assessed visually and by inspection of statistical measures, values and errors on refined parameters, and the correlation matrix.

Three further parameters are generally refined: the zero error accounts for a height offset in the instrumental setup, and strain and crystallite size parameters account for the nature of the sample. An instrumental height off-set—due to inaccurate sample positioning, irregularities of the sample surface, and the X-ray penetration depth [144]—leads to a constant shift in all diffraction peaks in 2θ. This can be calculated within the refinement using various descriptions of the shift in θ, such as the apparent error in ℓ proportional to $\cos 2\theta / \sin\theta + \cos 2\theta/\theta$ proposed by Ref. 454. Strain and crystallite size lead to a θ-dependent broadening of diffraction peaks. In simple terms the peak broadening is proportional to $1/L$ where L is the number of coherently diffracting planes and so is proportional to crystallite size as the allowable range that the Bragg condition is satisfied becomes smaller (and is also affected by which reflection is considered). Isotropic strain ($\varepsilon = \Delta d/d$) has the effect of changing lattice parameter and so we observe a shift in peak position which is strongly θ-dependent. In a real sample a distribution of strains is usually found. In a powder-averaged diffraction pattern therefore a range of strain-dependent lattice parameters are found which has the effect of broadening peaks, often with (hkl) dependent shapes.

A.4 Variable-temperature single-crystal diffraction on $KM[M'(CN)_2]_3$ samples

Variable temperature single crystal X-Ray diffraction measurements were carried out using a Nonius KappaCCD diffractometer (graphite-monochromated Mo Kα radiation, λ = 0.71073 Å) fitted with an Oxford Cryosystems cryostream 600 [158] using a suitable single-crystal prepared by the H-tube method.* Selected single crystals were mounted on a glass fibre using nail varnish. Unit cells were determined for each sample as a function of temperature with short scans; longer scans for structure determination were carried out at 50 K intervals. No evidence for any hysteresis in lattice parameter variation was observed, with essentially linear variation across the whole temperature range. Cell parameters were determined and data reduction carried out using DENZO/SCALEPACK [455]. Structure solution was carried out using SIR92 [456] within CRYSTALS [151]. Selected crystallographic data are presented in Appendix C. Coefficients of thermal expansion calculated using PASCAL [101] are shown in Figure 3.2.

* As previously presented Ref. 243, Honour School of Chemistry, Part II Thesis, Oxford, 2011.

Appendix B

Data for compressibility calculations in Chapter 2

B.1 Lattice parameter data

Lattice parameter data are reported here as previously published in tabular form or as extracted from published figures. Data extraction was carried out using WebPlotDigitizer [457] and standard errors were estimated in pressure measurements. In all cases lattice parameters are presented in a standard form which is suitable for direct input into PASCal for calculation of compressibilities along principal directions [101]. No standard errors in lattice parameters are used in the calculation using PASCal as the inherent experimental scatter is assumed to be the main source of error in the final compressibility calculation; it is also the case that errors on values are not available for published work where data were not reported in raw form.

B.1.1 Ferroelastic systems

Table B.1.1: Variable pressure lattice parameters of TeO_2 as reported in Ref. 69 (Worlton *et al.*, Cs_2 medium and D-methanol medium) and Ref. 458 (Liu *et al.*).

p (GPa)	σ_p (GPa)	a (Å)	b (Å)	c (Å)	α (°)	β (°)	γ (°)
Ref. 69, Cs_2 medium							
1.01	0.02	4.7283	4.8234	7.5808	90	90	90
1.13	0.02	4.6978	4.8355	7.5704	90	90	90
1.39	0.02	4.6616	4.8492	7.5483	90	90	90
1.93	0.03	4.6024	4.8669	7.5418	90	90	90
2.42	0.03	4.568	4.874	7.5435	90	90	90
3.03	0.03	4.5321	4.8822	7.5366	90	90	90
3.25	0.04	4.5247	4.8832	7.5374	90	90	90
Ref. 69, D-methanol medium							
0.98	0.02	4.7418	4.8051	7.5632	90	90	90
1.14	0.02	4.7085	4.8234	7.5525	90	90	90
1.36	0.02	4.6753	4.8366	7.5468	90	90	90
1.66	0.02	4.641	4.8504	7.5364	90	90	90
1.98	0.02	4.6053	4.8557	7.53	90	90	90
Ref. 458							
2.1	0.1	4.603	4.875	7.558	90	90	90
7.6	0.1	4.333	4.89	7.434	90	90	90
8.5	0.1	4.281	4.884	7.414	90	90	90
11	0.1	4.225	4.85	7.333	90	90	90
13.2	0.1	4.161	4.856	7.292	90	90	90
17	0.1	4.084	4.831	7.214	90	90	90
21.5	0.1	3.986	4.833	7.132	90	90	90
24.9	0.1	3.958	4.821	7.104	90	90	90

Compressibilities:

K_1	$-5.1(6)\,\mathrm{TPa}^{-1}$
K_2	$2.1(7)\,\mathrm{TPa}^{-1}$
K_3	$18.4(6)\,\mathrm{TPa}^{-1}$
K_V	$16.7(15)\,\mathrm{TPa}^{-1}$

Birch-Murnaghan Coefficients:

B_0	$52(4)\,\mathrm{GPa}$
B'	$\equiv 4$
V_0	$175.3(5)\,\mathrm{Å}^3$
p_c	$0.9\,\mathrm{GPa}$

Table B.1.2: Variable pressure lattice parameters of NiF_2 extracted from Ref. 259.

p (GPa)	σ_p (GPa)	a (Å)	b (Å)	c (Å)	α (°)	β (°)	γ (°)
2.145	0.2	4.605	4.633	3.072	90	90	90
2.50	0.2	4.596	4.635	3.072	90	90	90
2.89	0.2	4.588	4.637	3.071	90	90	90
3.24	0.2	4.580	4.638	3.070	90	90	90

Compressibilities:

K_1	$-0.48(\text{-})\,\text{TPa}^{-1}$
K_2	$0.61(\text{-})\,\text{TPa}^{-1}$
K_3	$4.42(\text{-})\,\text{TPa}^{-1}$
K_V	$4.57(3)\,\text{TPa}^{-1}$

Birch-Murnaghan Coefficients:

B_0	$226(\text{-})\,\text{GPa}$
B'	$-8(\text{-})$
V_0	$66(\text{-})\,\text{Å}^3$
p_c	$1.8\,\text{GPa}$

Table B.1.3: Variable pressure lattice parameters of β-MnO_2 extracted from Ref. 68

p (GPa)	σ_p (GPa)	a (Å)	b (Å)	c (Å)	α (°)	β (°)	γ (°)
2.036	0.2	4.43	4.366	2.821	90	90	90
2.032	0.2	4.43	4.357	2.821	90	90	90
3.119	0.2	4.432	4.352	2.821	90	90	90
4.202	0.2	4.441	4.34	2.822	90	90	90
5.749	0.2	4.436	4.321	2.821	90	90	90
7.456	0.2	4.44	4.313	2.82	90	90	90
9.546	0.2	4.439	4.291	2.816	90	90	90
12.409	0.2	4.447	4.259	2.814	90	90	90
14.112	0.2	4.442	4.241	2.814	90	90	90
15.424	0.2	4.446	4.218	2.811	90	90	90
19.305	0.2	4.444	4.206	2.811	90	90	90
20.078	0.2	4.454	4.186	2.808	90	90	90
25.35	0.2	4.454	4.161	2.805	90	90	90
29.309	0.2	4.451	4.148	2.802	90	90	90

Compressibilities:

K_1	$-0.16(7)\,\mathrm{TPa}^{-1}$
K_2	$0.269(17)\,\mathrm{TPa}^{-1}$
K_3	$1.82(10)\,\mathrm{TPa}^{-1}$
K_V	$2.06(9)\,\mathrm{TPa}^{-1}$

Birch-Murnaghan Coefficients:

B_0	$280(80)\,\mathrm{GPa}$
B'	$19(11)$
V_0	$54.97(17)\,\mathrm{Å}^3$
p_c	$0.3\,\mathrm{GPa}$

Table B.1.4: Variable pressure lattice parameters of MgF_2 as reported in Ref. 261

p (GPa)	σ_p (GPa)	a (Å)	b (Å)	c (Å)	α (°)	β (°)	γ (°)
9.4	0.1	4.5164	4.4768	2.9845	90	90	90
9.8	0.1	4.5223	4.4634	2.9815	90	90	90
10.4	0.1	4.5227	4.4409	2.977	90	90	90

Compressibilities (linear):

K_1	$-1.3(3)\,\mathrm{TPa}^{-1}$
K_2	$2.51(2)\,\mathrm{TPa}^{-1}$
K_3	$8.05(10)\,\mathrm{TPa}^{-1}$
K_V	$9.4(5)\,\mathrm{TPa}^{-1}$

Birch-Murnaghan Coefficients:

B_0	$68(13)\,\mathrm{GPa}$
B'	$\equiv 4$
V_0	$67.4(12)\,\mathrm{Å}^3$
p_c	$9.1\,\mathrm{GPa}$

Table B.1.5: Variable pressure lattice parameters of PbO_2-I′ extracted from Ref. 263. NLC found up to 6.1 GPa.

p (GPa)	σ_p (GPa)	a (Å)	b (Å)	c (Å)	α (°)	β (°)	γ (°)
4.297	0.2	4.920	4.877	3.398	90	90	90
5.415	0.2	4.932	4.855	3.391	90	90	90
6.095	0.2	4.936	4.842	3.387	90	90	90
7.311	0.2	4.928	4.814	3.381	90	90	90
8.818	0.2	4.923	4.796	3.377	90	90	90
11.443	0.2	4.927	4.740	3.368	90	90	90
12.367	0.2	4.908	4.745	3.364	90	90	90

Compressibilities (linear):

K_1	$-1.83(15))\,\mathrm{TPa}^{-1}$
K_2	$1.76(7)\,\mathrm{TPa}^{-1}$
K_3	$4.00(3)\,\mathrm{TPa}^{-1}$
K_V	$3.94(5)\,\mathrm{TPa}^{-1}$

Table B.1.6: Variable pressure lattice parameters of GeO_2 as reported in Ref. 264. NLC found up to 32 GPa.

p (GPa)	σ_p (GPa)	a (Å)	b (Å)	c (Å)	α (°)	β (°)	γ (°)
28	1	4.2841	4.2098	2.8089	90	90	90
29	1	4.2852	4.1959	2.8062	90	90	90
32	1	4.2866	4.1742	2.7995	90	90	90
35	1	4.2834	4.1508	2.7941	90	90	90
36	1	4.2814	4.1424	2.7919	90	90	90

Compressibilities (linear):

K_1	$-0.137(12)\,\mathrm{TPa}^{-1}$
K_2	$0.827(14)\,\mathrm{TPa}^{-1}$
K_3	$2.02(13)\,\mathrm{TPa}^{-1}$
K_V	$2.74(13)\,\mathrm{TPa}^{-1}$

Table B.1.7: Variable pressure lattice parameters of SnO_2-II as reported in Refs. 253, 265. NLC calculated from lattice parameters reported in Haines *et al.* (only two reported, but strain calculated over many more points in publication but not reported).

p (GPa)	σ_p (GPa)	a (Å)	b (Å)	c (Å)	α (°)	β (°)	γ (°)
Ref. 253							
12.6	0.4	4.6533	4.6313	3.155	90	90	90
15.5	0.5	4.6558	4.5998	3.1514	90	90	90
Ref. 265							
17.2	0.2	4.609	5.528	5.079	90	90	90
18.4	0.2	4.607	5.523	5.07	90	90	90
19.5	0.2	4.599	5.504	5.067	90	90	90
20.8	0.2	4.592	5.507	5.077	90	90	90
21.8	0.2	4.598	5.505	5.065	90	90	90
22.8	0.2	4.591	5.504	5.041	90	90	90
23.6	0.2	4.596	5.498	5.06	90	90	90

Compressibilities (linear):

K_1	$-0.185(\text{-})\,\text{TPa}^{-1}$
K_2	$0.394(\text{-})\,\text{TPa}^{-1}$
K_3	$2.345(\text{-})\,\text{TPa}^{-1}$
K_V	$2.552(\text{-})\,\text{TPa}^{-1}$

Table B.1.8: Variable pressure lattice parameters of $Zn(CN)_2$ as reported in Ref. 205

p (GPa)	σ_p (GPa)	a (Å)	b (Å)	c (Å)	α (°)	β (°)	γ (°)
1.95	0.1	12.504	7.4438	7.2983	90	90	90
2.77	0.1	12.627	7.2315	7.0525	90	90	90
3.57	0.1	12.624	7.137	6.9219	90	90	90
4.44	0.1	12.625	7.0572	6.8064	90	90	90
5.47	0.1	12.589	7.0085	6.7299	90	90	90
7.5	0.1	12.492	6.9195	6.5848	90	90	90
12.2	0.1	12.413	6.83	6.3832	90	90	90
9.61	0.1	12.437	6.8743	6.5322	90	90	90

Table B.1.9: Variable pressure lattice parameters of $Pb_3(PO_4)_2$ as reported in Ref. 266.

p (GPa)	σ_p (GPa)	a (Å)	b (Å)	c (Å)	α (°)	β (°)	γ (°)
0.000	0.1	13.809	5.695	9.431	90	102.367	90
0.158	0.1	13.804	5.673	9.432	90	102.467	90
0.387	0.1	13.798	5.642	9.436	90	102.603	90
0.581	0.1	13.790	5.618	9.438	90	102.688	90
0.799	0.1	13.785	5.590	9.444	90	102.819	90
1.217	0.1	13.773	5.540	9.451	90	102.994	90
1.434	0.1	13.766	5.515	9.458	90	103.082	90
1.594	0.1	13.767	5.495	9.467	90	103.17	90

Compressibilities:

K_1	$-4.3(4)\,\mathrm{TPa}^{-1}$
K_2	$5.0(2)\,\mathrm{TPa}^{-1}$
K_3	$20.98(18)\,\mathrm{TPa}^{-1}$
K_V	$23.5(5)\,\mathrm{TPa}^{-1}$

Birch-Murnaghan Coefficients:

B_0	$38.7(5)\,\mathrm{GPa}$
B'	$\equiv 4$
V_0	$724.1(2)\,\mathrm{Å}^3$

Table B.1.10: Variable pressure lattice parameters of InS as reported in Refs. 269, 270. NLC calculated from more recent study of Schwartz *et al.*

p (GPa)	σ_p (GPa)	a (Å)	b (Å)	c (Å)	α (°)	β (°)	γ (°)
Ref. 270							
0.1	0.1	3.9457	4.453	10.65	90	90	90
0.2	0.1	3.943	4.401	10.654	90	90	90
2.1	0.1	3.924	4.188	10.706	90	90	90
3.6	0.1	3.906	4.059	10.743	90	90	90
4.3	0.1	3.899	4.016	10.763	90	90	90
Ref. 269							
0	0.1	3.944	4.447	10.648	90	90	90
1	0.1	3.94	4.32	10.78	90	90	90
2.7	0.1	3.92	4.12	10.8	90	90	90
3.7	0.1	3.88	4.06	10.8	90	90	90

Compressibilities:

K_1	$-2.41(13)\,\mathrm{TPa}^{-1}$
K_2	$2.9(4)\,\mathrm{TPa}^{-1}$
K_3	$15(2)\,\mathrm{TPa}^{-1}$
K_V	$23.6(13)\,\mathrm{TPa}^{-1}$

Birch-Murnaghan Coefficients:

B_0	$33.2(18)\,\mathrm{GPa}$
B'	$\equiv 4$
V_0	$186.7(7)\,\mathrm{Å}^3$

Table B.1.11: Variable pressure lattice parameters of silimanite calculated by DFT as reported in Ref. 272.

p (GPa)	σ_p (GPa)	a (Å)	b (Å)	c (Å)	α (°)	β (°)	γ (°)
29.922	0.2	7.062	7.253	5.669	90	90	90
32.603	0.2	6.973	7.231	5.673	90	90	90
34.97	0.2	6.878	7.202	5.692	90	90	90
37.503	0.2	6.671	7.18	5.728	90	90	90

Compressibilities:

K_1	$-3.30(\text{-})\,\mathrm{TPa}^{-1}$
K_2	$1.45(\text{-})\,\mathrm{TPa}^{-1}$
K_3	$10.81(\text{-})\,\mathrm{TPa}^{-1}$
K_V	$7.3(5)\,\mathrm{TPa}^{-1}$

B.1.2 Tilting polyhedra

Table B.1.12: Variable pressure lattice parameters of BPO_4 extracted from Ref. 290.

p (GPa)	σ_p (GPa)	a (Å)	b (Å)	c (Å)	α (°)	β (°)	γ (°)
0.000	0.2	4.339	4.339	6.647	90	90	90
3.687	0.2	4.224	4.224	6.632	90	90	90
6.089	0.2	4.159	4.159	6.632	90	90	90
9.162	0.2	4.081	4.081	6.641	90	90	90
11.676	0.2	4.042	4.042	6.648	90	90	90
15.251	0.2	3.985	3.985	6.652	90	90	90
18.827	0.2	3.915	3.915	6.711	90	90	90
24.302	0.2	3.834	3.834	6.744	90	90	90
24.469	0.2	3.807	3.807	6.782	90	90	90
29.274	0.2	3.733	3.733	6.781	90	90	90
31.061	0.2	3.716	3.716	6.794	90	90	90
33.352	0.2	3.660	3.660	6.901	90	90	90
36.034	0.2	3.649	3.649	6.881	90	90	90
41.061	0.2	3.597	3.597	6.907	90	90	90
43.799	0.2	3.597	3.597	6.896	90	90	90
48.939	0.2	3.551	3.551	6.916	90	90	90
49.721	0.2	3.535	3.535	6.901	90	90	90
53.464	0.2	3.527	3.527	6.912	90	90	90
55.810	0.2	3.500	3.500	6.906	90	90	90

Compressibilities:

K_a	$2.83(12)\,\mathrm{TPa}^{-1}$
K_c	$-0.92(10)\,\mathrm{TPa}^{-1}$
K_V	$5.6(5)\,\mathrm{TPa}^{-1}$

Birch-Murnaghan Coefficients:

B_0	$52(9)\,\mathrm{GPa}$	(reported $56(3)\,\mathrm{GPa}$)
B'	$4.9(6)$	(reported $4.7(3)$)
V_0	$135.7(10)\,\mathrm{Å}^3$	

Table B.1.13: Variable pressure lattice parameters of $BAsO_4$ extracted from Ref. 290.

p (GPa)	σ_p (GPa)	a (Å)	b (Å)	c (Å)	α (°)	β (°)	γ (°)
0.000	0.2	4.465	4.465	6.815	90	90	90
2.775	0.2	4.354	4.354	6.797	90	90	90
3.676	0.2	4.331	4.331	6.798	90	90	90
5.768	0.2	4.258	4.258	6.788	90	90	90
6.597	0.2	4.235	4.235	6.794	90	90	90
7.498	0.2	4.212	4.212	6.798	90	90	90
9.588	0.2	4.150	4.150	6.854	90	90	90
11.788	0.2	4.123	4.123	6.866	90	90	90
14.094	0.2	4.073	4.073	6.892	90	90	90
16.005	0.2	4.023	4.023	6.867	90	90	90
20.006	0.2	3.935	3.935	7.030	90	90	90
27.504	0.2	3.788	3.788	7.154	90	90	90
32.010	0.2	3.727	3.727	7.202	90	90	90
37.020	0.2	3.673	3.673	7.247	90	90	90
40.013	0.2	3.658	3.658	7.227	90	90	90
44.013	0.2	3.619	3.619	7.237	90	90	90
49.024	0.2	3.596	3.596	7.217	90	90	90
51.007	0.2	3.585	3.585	7.181	90	90	90

Compressibilities:

K_a	$3.64(11)\,\mathrm{TPa}^{-1}$
K_c	$-1.48(15)\,\mathrm{TPa}^{-1}$
K_V	$6.0(5)\,\mathrm{TPa}^{-1}$

Birch-Murnaghan Coefficients:

B_0	$49(5)\,\mathrm{GPa}$	(reported $49(2)\,\mathrm{GPa}$)
B'	5.1(4)	(reported 5.0(5))
V_0	$126.2(19)\,\mathrm{Å}^3$	

B.1.3 Helical elements

Table B.1.14: Variable pressure lattice parameters of trigonal selenium as reported in Refs. 113, 300.

p (GPa)	σ_p (GPa)	a (Å)	b (Å)	c (Å)	α (°)	β (°)	γ (°)
Ref. 113, *Neutron data*							
0.58	0.1	4.281	4.281	4.993	90	90	120
0.58	0.1	4.286	4.286	4.976	90	90	120
2.4	0.1	4.058	4.058	5.061	90	90	120
2.5	0.1	4.069	4.069	5.031	90	90	120
4.3	0.1	3.937	3.937	5.064	90	90	120
4.3	0.1	3.912	3.912	5.096	90	90	120
6.2	0.1	3.869	3.869	5.085	90	90	120
7.3	0.1	3.767	3.767	5.112	90	90	120
Ref. 113, *X-ray data*							
1.4	0.1	4.169	4.169	5.056	90	90	120
1.8	0.1	4.162	4.162	5.055	90	90	120
1.8	0.1	4.154	4.154	5.072	90	90	120
2.6	0.1	4.027	4.027	5.108	90	90	120
2.9	0.1	4.046	4.046	5.091	90	90	120
3.1	0.1	4.027	4.027	5.122	90	90	120
3.9	0.1	3.937	3.937	5.136	90	90	120
4.4	0.1	3.944	3.944	5.122	90	90	120
4.4	0.1	3.931	3.931	5.139	90	90	120
5.2	0.1	3.878	3.878	5.139	90	90	120
3.3	0.1	4.035	4.035	5.094	90	90	120
6	0.1	3.894	3.894	5.128	90	90	120
10.3	0.1	3.731	3.731	5.178	90	90	120
14	0.1	3.642	3.642	5.147	90	90	120
Ref. 300							
0	0.1	4.368	4.368	4.958	90	90	120
0.12	0.1	4.343	4.343	4.964	90	90	120
2.58	0.1	4.052	4.052	5.038	90	90	120
4.15	0.1	3.956	3.956	5.069	90	90	120
4.99	0.1	3.91	3.91	5.08	90	90	120
6.57	0.1	3.846	3.846	5.095	90	90	120
7.7	0.1	3.81	3.81	5.11	90	90	120
8.64	0.1	3.779	3.779	5.109	90	90	120
9.98	0.1	3.745	3.745	5.119	90	90	120

Compressibilities:

K_a	$12.0(4)\,\mathrm{TPa}^{-1}$
K_c	$-2.5(4)\,\mathrm{TPa}^{-1}$
K_V	$23(2)\,\mathrm{TPa}^{-1}$

Birch-Murnaghan Coefficients:

B_0	$23.0(14)\,\mathrm{GPa}$
B'	$\equiv 4$
V_0	$79.7(7)\,\mathrm{Å}^3$

Table B.1.15: Variable pressure lattice parameters of trigonal tellurium as reported in Ref. 303.

p (GPa)	σ_p (GPa)	a (Å)	b (Å)	c (Å)	α (°)	β (°)	γ (°)
0	0.1	4.451	4.451	5.926	90	90	120
0.38	0.1	4.411	4.411	5.934	90	90	120
0.6	0.1	4.398	4.398	5.941	90	90	120
1.26	0.1	4.331	4.331	5.951	90	90	120
1.48	0.1	4.312	4.312	5.957	90	90	120
1.88	0.1	4.28	4.28	5.967	90	90	120
2.26	0.1	4.258	4.258	5.966	90	90	120
2.62	0.1	4.238	4.238	5.969	90	90	120
2.94	0.1	4.225	4.225	5.975	90	90	120
3.41	0.1	4.204	4.204	5.972	90	90	120
3.82	0.1	4.191	4.191	5.981	90	90	120

Compressibilities:

K_a	$13.6(9)\,\mathrm{TPa}^{-1}$
K_c	$-1.8(3)\,\mathrm{TPa}^{-1}$
K_V	$29.0(17)\,\mathrm{TPa}^{-1}$

Birch-Murnaghan Coefficients:

B_0	$26.6(13)\,\mathrm{GPa}$
B'	$\equiv 4$
V_0	$101.2(3)\,\mathrm{Å}^3$

B.1.4 Hinged systems

Table B.1.16: Variable pressure lattice parameters of Ag(mim) as reported in Ref. 128.

p (GPa)	σ_p (GPa)	a (Å)	b (Å)	c (Å)	α (°)	β (°)	γ (°)
0	0.01	7.8926	5.9767	10.8739	90	92.47	90
0.305	0.005	7.726	5.9233	10.888	90	92.73	90
1.08	0.08	7.433	5.8092	10.9101	90	93.736	90
2.17	0.14	7.2027	5.6926	10.9057	90	94.504	90
3.27	0.08	7.0544	5.6024	10.8873	90	95.062	90
3.8	0.16	6.992	5.559	10.875	90	95.344	90
4.85	0.04	6.9259	5.5072	10.8549	90	95.667	90
5.6	0.3	6.871	5.467	10.8393	90	95.878	90
6.4	0.4	6.828	5.4298	10.8209	90	96.076	90

Table B.1.17: Variable pressure lattice parameters of $KMn[Ag(CN)_2]_3$ as reported in Ref. 115.

p (GPa)	σ_p (GPa)	a (Å)	b (Å)	c (Å)	α (°)	β (°)	γ (°)
0.22	0.12	6.82042	6.82042	8.1961	90	90	120
0.5	0.15	6.73777	6.73777	8.2387	90	90	120
0.86	0.12	6.64413	6.64413	8.2842	90	90	120
1.2	0.17	6.56392	6.56392	8.3215	90	90	120
1.52	0.17	6.4973	6.4973	8.3543	90	90	120
1.78	0.15	6.4543	6.4543	8.3722	90	90	120
1.98	0.15	6.427	6.427	8.377	90	90	120
1.95	0.18	6.4227	6.4227	8.382	90	90	120
2.15	0.15	6.3888	6.3888	8.387	90	90	120

Table B.1.18: Variable pressure lattice parameters of ZAG-4 as reported in Ref. 310.

p (GPa)	σ_p (GPa)	a (Å)	b (Å)	c (Å)	α (°)	β (°)	γ (°)
0	0.1	18.515	8.291	8.265	90	113.837	90
1.65	0.1	17.991	8.000	8.0643	90	117.609	90
2.81	0.09	17.685	8.147	7.7557	90	119.697	90
5.69	0.03	17.1996	8.139	7.4651	90	122.431	90
7.32	0.07	17.023	8.066	7.4078	90	123.227	90

Compressibilities:

K_1	$-2.6(15)\,\mathrm{TPa}^{-1}$
K_2	$7.8(5)\,\mathrm{TPa}^{-1}$
K_3	$29(3)\,\mathrm{TPa}^{-1}$
K_V	$55(3)\,\mathrm{TPa}^{-1}$

Birch-Murnaghan Coefficients:

B_0	$13.4(10)\,\mathrm{GPa}$
B'	$\equiv 4$
V_0	$1163(10)\,\mathrm{Å}^3$

Table B.1.19: Variable pressure lattice parameters of $[Fe(dpp)_2(NCS)_2]\cdot py$ as reported in Ref. 250.

p (GPa)	σ_p (GPa)	a (Å)	b (Å)	c (Å)	α (°)	β (°)	γ (°)
0	0.1	13.379	8.7384	16.3583	90	104.247	90
0.48	0.1	13.585	8.236	16.306	90	103.3	90
1.82	0.1	13.614	7.741	16.059	90	102.55	90
2.48	0.1	13.562	7.541	15.878	90	101.57	90
0	0.1	13.3756	8.6951	16.3247	90	104.261	90
0.2	0.1	13.44	8.548	16.2728	90	103.8	90
0.3	0.1	13.511	8.349	16.23	90	103.663	90
0.85	0.1	13.59	8.07	16.21	90	103.33	90

Compressibilities:

K_1	$-10(2)\,\mathrm{TPa}^{-1}$
K_2	$12(3)\,\mathrm{TPa}^{-1}$
K_3	$53(4)\,\mathrm{TPa}^{-1}$
K_V	$55(3)\,\mathrm{TPa}^{-1}$

Birch-Murnaghan Coefficients:

B_0	$12.9(6)\,\mathrm{GPa}$
B'	$\equiv 4$
V_0	$1842(9)\,\mathrm{Å}^3$

Table B.1.20: Variable pressure lattice parameters of methanol monohydrate as reported in Ref. 247.

p (GPa)	σ_p (GPa)	a (Å)	b (Å)	c (Å)	α (°)	β (°)	γ (°)
0.0106	0.1	4.6422	14.0303	4.6823	90	90	90
0.052	0.1	4.6437	13.9422	4.6739	90	90	90
0.102	0.1	4.6437	13.8503	4.6642	90	90	90
0.1545	0.1	4.6446	13.7542	4.6545	90	90	90
0.202	0.1	4.6457	13.673	4.646	90	90	90
0.255	0.1	4.6476	13.5853	4.6364	90	90	90
0.302	0.1	4.6493	13.5131	4.6293	90	90	90
0.35	0.1	4.6507	13.4347	4.6228	90	90	90
0.4015	0.1	4.6516	13.3658	4.6162	90	90	90
0.453	0.1	4.6545	13.2947	4.609	90	90	90
0.5	0.1	4.6554	13.2392	4.6035	90	90	90

Compressibilities:

K_1	$-2.7(18)\,\mathrm{TPa}^{-1}$
K_2	$31.9(4)\,\mathrm{TPa}^{-1}$
K_3	$108.0(9)\,\mathrm{TPa}^{-1}$
K_V	$143(4)\,\mathrm{TPa}^{-1}$

B.1.5 NAC Systems

Table B.1.21: Variable pressure lattice parameters of $PbTiO_3$ as reported in Ref. 321.

p (GPa)	σ_p (GPa)	a (Å)	b (Å)	c (Å)	α (°)	β (°)	γ (°)
0	0.05	3.8977	3.8977	4.1526	90	90	90
0.32	0.05	3.8977	3.8977	4.132	90	90	90
1.41	0.05	3.9000	3.9000	4.0682	90	90	90
1.7	0.05	3.9006	3.9006	4.0513	90	90	90
2.05	0.05	3.8985	3.8985	4.0409	90	90	90
2.6	0.05	3.8968	3.8968	4.0252	90	90	90
3.0	0.05	3.8956	3.8956	4.0123	90	90	90
3.25	0.05	3.8955	3.8955	4.0056	90	90	90
3.6	0.05	3.8933	3.8933	3.9954	90	90	90
4.05	0.05	3.8896	3.8896	3.9818	90	90	90
4.8	0.05	3.8881	3.8881	3.9656	90	90	90
5.63	0.05	3.8843	3.8843	3.9498	90	90	90
5.94	0.05	3.8829	3.8829	3.9454	90	90	90
6.2	0.05	3.8818	3.8818	3.9399	90	90	90
6.35	0.05	3.8805	3.8805	3.9370	90	90	90

Table B.1.22: Variable pressure lattice parameters of NaV_2O_5 extracted from Ref. 316.

p (GPa)	σ_p (GPa)	a (Å)	b (Å)	c (Å)	α (°)	β (°)	γ (°)
0	0.1	11.32978	3.61335	4.79150	90	90	90
0.57377	0.1	11.29585	3.61749	4.68632	90	90	90
1.88525	0.1	11.27901	3.61766	4.54885	90	90	90
2.78689	0.1	11.27489	3.62183	4.45183	90	90	90
4.01639	0.1	11.27930	3.62605	4.35076	90	90	90
5.32787	0.1	11.28801	3.63432	4.24162	90	90	90
6.88525	0.1	11.30524	3.65073	4.13251	90	90	90
9.42623	0.1	11.31411	3.65107	4.00330	90	90	90
12.86885	0.1	11.28908	3.65558	3.90255	90	90	90
15.40984	0.1	11.25964	3.65593	3.85432	90	90	90
18.77049	0.1	11.22182	3.65233	3.80213	90	90	90
21.47541	0.1	11.18816	3.64460	3.75391	90	90	90
29.26230	0.1	11.04885	3.62136	3.66589	90	90	90

Compressibilities:

K_1	$-1.2(5)\,\mathrm{TPa}^{-1}$
K_2	$-0.48(16)\,\mathrm{TPa}^{-1}$
K_3	$14.3(11)\,\mathrm{TPa}^{-1}$
K_V	$14.5(9)\,\mathrm{TPa}^{-1}$

Birch-Murnaghan Coefficients:

B_0	$23(6)\,\mathrm{GPa}$
B'	$14(3)$
V_0	$196(2)\,\mathrm{Å}^3$

B.2 Elastic data

Table B.2.23: Elastic stiffness data in GPa for CsH_2PO_4 determined from ultrasonic velocity measurements from Ref. 285.

$C_{11} = 28.83$	$C_{12} = 11.4$	$C_{35} = 7.50$
$C_{22} = 26.67$	$C_{13} = 42.87$	$C_{46} = -2.25$
$C_{33} = 65.45$	$C_{15} = 5.13$	
$C_{44} = 8.10$	$C_{23} = 14.5$	
$C_{55} = 5.20$	$C_{25} = 8.4$	
$C_{66} = 9.17$		

Appendix C

Supplementary Data

C.1 $KMn[Ag(CN)_2]_3$

C.1.1 Representative fits to data neutron powder diffraction data

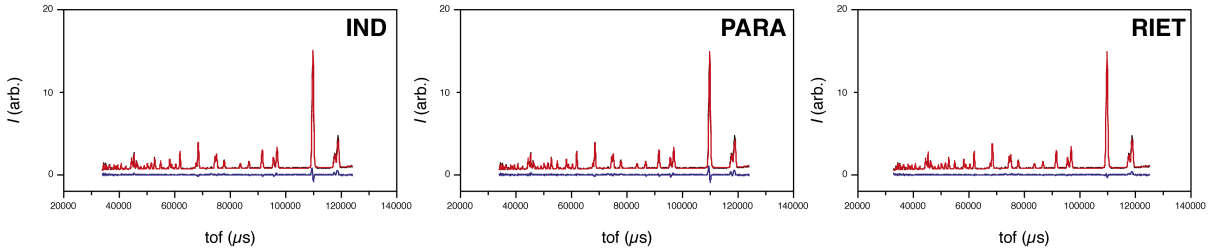

Figure C.1.1: Refined neutron diffraction data for $KMn[Ag(CN)_2]_3$ at $p = 0$ GPa and $T = 100$ K. Fits are given for independent, parametric and Rietveld refinement of data as described in Chapter 3. Data = black line; fit = red line; difference = blue line.

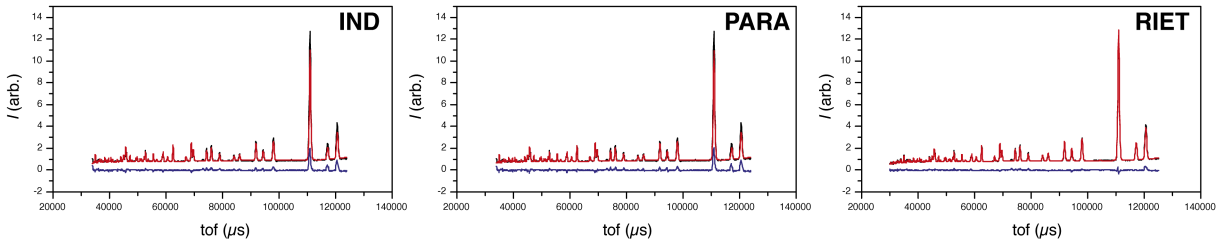

Figure C.1.2: Refined neutron diffraction data for $KMn[Ag(CN)_2]_3$ at $p = 0$ GPa and $T = 300$ K. Fits are given for independent, parametric and Rietveld refinement of data as described in Chapter 3. Data = black line; fit = red line; difference = blue line.

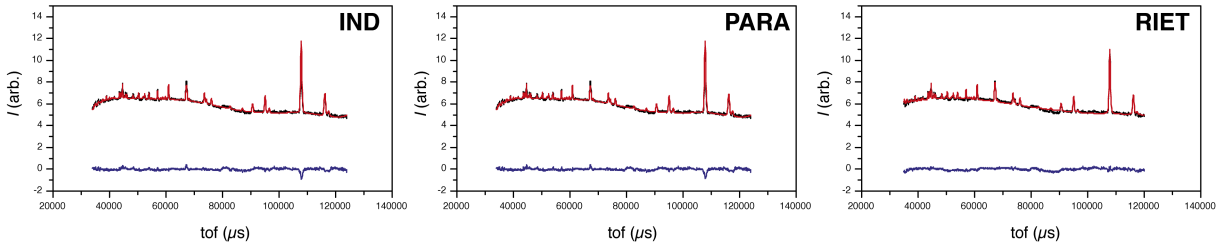

Figure C.1.3: Refined neutron diffraction data for $KMn[Ag(CN)_2]_3$ at $p = 0.5548\,\text{GPa}$ and $T = 100\,\text{K}$. Fits are given for independent, parametric and Rietveld refinement of data as described in Chapter 3. Data = black line; fit = red line; difference = blue line.

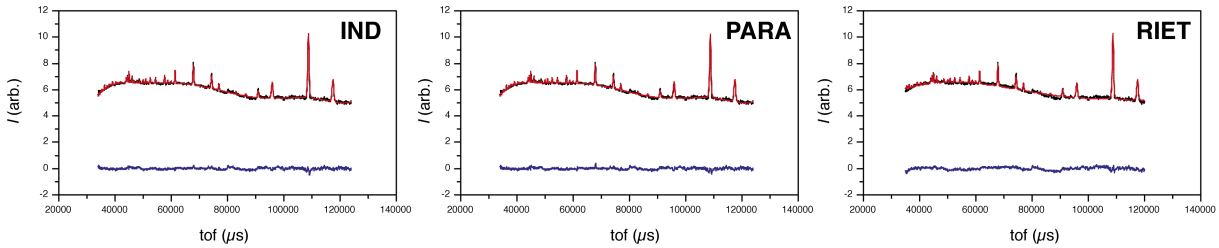

Figure C.1.4: Refined neutron diffraction data for $KMn[Ag(CN)_2]_3$ at $p = 0.5898\,\text{GPa}$ and $T = 300\,\text{K}$. Fits are given for independent, parametric and Rietveld refinement of data as described in Chapter 3. Data = black line; fit = red line; difference = blue line.

C.1.2 Comparison between lattice parameters refined parametrically and independently

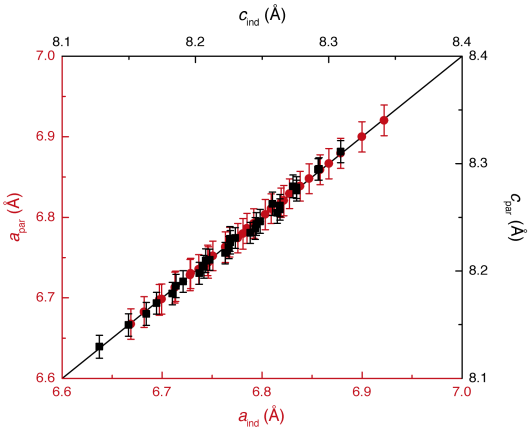

Figure C.1.5: Plot of lattice parameters a (red circles) and c (black squares) for $KMn[Ag(CN)_2]_3$ refined independently and parametrically against VT/Vp powder neutron diffraction data as described in the main text. The line is shown is given by $(x = y)$.

C.1.3 Refined lattice parameters

Table C.1.1: Structural parameters refined by independent fits to VT/Vp neutron diffraction data of $KMn[Ag(CN)_2]_3$.

T (K)	p (GPa)	a (Å)	σ_a (Å)	c (Å)	σ_c (Å)	V (Å^3)	σ_V (Å^3)
300.009	0.5898	6.7461	0.00034	8.22587	0.00163	324.20392	0.0721
300.01	0.4494	6.7808	0.00033	8.20777	0.00158	326.82637	0.0705
300.02	0.29963	6.82182	0.00035	8.18547	0.00153	329.89414	0.07009
300.01	0.15027	6.86676	0.00036	8.16314	0.00154	333.34323	0.07163
300	0	6.92204	0.00012	8.12799	0.00028	337.27299	0.01611
260.031	0.5846	6.72794	0.00041	8.24861	0.00182	323.35207	0.08127
260.03	0.4455	6.76331	0.0003	8.22607	0.00147	325.86852	0.06508
260.031	0.29578	6.80321	0.00033	8.20627	0.00149	328.93051	0.06761
260.03	0.14838	6.84696	0.00033	8.18265	0.00142	332.2152	0.06581
260	0	6.89993	0.00011	8.1498	0.00026	336.02144	0.01492
220.039	0.5787	6.71288	0.0003	8.25774	0.00145	322.26246	0.06329
220.038	0.4409	6.74558	0.00036	8.2456	0.00164	324.93123	0.07337
220.039	0.29143	6.78485	0.00029	8.22517	0.0014	327.9116	0.06255
220.038	0.14607	6.82736	0.00032	8.20287	0.00139	331.13235	0.06397
220	0	6.87851	0.0001	8.17083	0.00024	334.80032	0.01403
180.004	0.5718	6.69729	0.00026	8.27312	0.00135	321.36495	0.05832
180.005	0.43522	6.72849	0.00032	8.26347	0.00147	323.9875	0.06532
180.01	0.28658	6.76759	0.00028	8.24478	0.00137	327.02247	0.06074
180.005	0.14342	6.809	0.0003	8.22229	0.00135	330.13354	0.06136
180	0	6.85801	0.00009	8.19079	0.00023	333.62026	0.01302
139.98	0.56357	6.68195	0.00026	8.2927	0.00125	320.65184	0.05419
139.983	0.42867	6.71347	0.00025	8.27576	0.00129	323.02199	0.0558
139.983	0.28099	6.75079	0.00036	8.26347	0.00159	326.13876	0.07159
139.984	0.14022	6.79158	0.00026	8.24112	0.00126	329.19949	0.05616
140	0	6.83799	0.00009	8.2107	0.00022	332.48185	0.01231
100.043	0.5548	6.66872	0.00026	8.309	0.00114	320.01048	0.0503
100.042	0.42103	6.69956	0.00024	8.29204	0.00122	322.31782	0.0529
100.041	0.27435	6.73669	0.00028	8.27593	0.00131	325.26694	0.05803
100.041	0.13607	6.77562	0.00026	8.26137	0.00126	328.45854	0.05598
100	0	6.81901	0.00008	8.22983	0.00021	331.4091	0.01159

Table C.1.2: Structural parameters refined by parametric fits to VT/Vp neutron diffraction data of $KMn[Ag(CN)_2]_3$.

T (K)	p (GPa)	a (Å)	σ_a (Å)	c (Å)	σ_c (Å)	V (Å^3)	σ_V (Å^3)
300.009	0.5898	6.74386	0.0195	8.22984	0.01147	324.14502	1.89398
300.01	0.4494	6.77949	0.01914	8.20959	0.01115	326.77311	1.85468
300.02	0.29963	6.82075	0.01888	8.18613	0.01087	329.8176	1.81965
300.01	0.15027	6.8666	0.01879	8.16007	0.01068	333.20231	1.79504
300	0	6.92029	0.01901	8.12955	0.01069	337.16709	1.79089
260.031	0.5846	6.72827	0.01937	8.24623	0.01116	323.29065	1.8799
260.03	0.4455	6.76293	0.01902	8.22675	0.01086	325.85848	1.84131
260.031	0.29578	6.80344	0.01876	8.20398	0.0106	328.86072	1.80655
260.03	0.14838	6.84788	0.01865	8.17899	0.01043	332.15632	1.78237
260	0	6.89985	0.01886	8.14978	0.01045	336.01305	1.77788
220.039	0.5787	6.7128	0.01926	8.26257	0.01087	322.44325	1.86704
220.038	0.4409	6.74651	0.01891	8.24384	0.0106	324.952	1.8291
220.039	0.29143	6.78622	0.01864	8.22178	0.01036	327.90865	1.7946
220.038	0.14607	6.82926	0.01853	8.19787	0.01021	331.11497	1.77079
220	0	6.87942	0.01871	8.17001	0.01023	334.85502	1.76593
180.004	0.5718	6.69751	0.01915	8.27883	0.01063	321.60778	1.85532
180.005	0.43522	6.73032	0.0188	8.26083	0.01037	324.06045	1.81795
180.01	0.28658	6.7691	0.01853	8.23955	0.01015	326.96122	1.7838
180.005	0.14342	6.8107	0.01841	8.21673	0.01001	330.07518	1.76032
180	0	6.85899	0.01857	8.19024	0.01004	333.69305	1.75503
139.98	0.56357	6.68246	0.01905	8.29498	0.01042	320.7886	1.84464
139.983	0.42867	6.71429	0.01871	8.27775	0.01018	323.17865	1.80793
139.983	0.28099	6.75213	0.01843	8.25726	0.00996	326.02258	1.77409
139.984	0.14022	6.79227	0.01831	8.23553	0.00984	329.04289	1.75094
140	0	6.83855	0.01844	8.21047	0.00986	332.52718	1.74521
100.043	0.5548	6.66744	0.01896	8.31114	0.01025	319.97062	1.83525
100.042	0.42103	6.69844	0.01862	8.2946	0.01002	322.30925	1.79899
100.041	0.27435	6.73536	0.01834	8.27489	0.00981	325.09764	1.76543
100.041	0.13607	6.77413	0.01821	8.25417	0.00969	328.02844	1.74261
100	0	6.81812	0.01832	8.2307	0.00971	331.35746	1.73648

C.1.4 Parameters calculated from VT/Vp data

Table C.1.3: Compressibilities and Birch-Murnaghan coefficients for $KMn[Ag(CN)_2]_3$ calculated from variable-pressure data at different temperatures using independent refinement of each data set.

T (K)	B_0 (GPa)	V_0 (Å^3)	B'	K_a (TPa^{-1})	K_a (TPa^{-1})	B_0 (GPa)
300	11.94(4)	337.277(10)	11.70(18)	38.0(9)	−16.5(8)	13.8(3)
260	12.21(15)	336.02(3)	11.8(7)	37.9(5)	−17.7(17)	14.1(3)
220	12.8(3)	334.78(6)	9.2(20)	36.8(11)	−14.3(18)	14.1(2)
180	13.31(16)	333.61(3)	7.6(6)	36.4(15)	−13(3)	14.22(16)
140	13.3(6)	332.51(11)	8(2)	36.3(14)	−13(2)	14.4(2)
100	13.4(10)	331.49(17)	9(4)	36.1(12)	−13(2)	14.6(3)

Table C.1.4: Compressibilities and Birch-Murnaghan coefficients for $KMn[Ag(CN)_2]_3$ calculated from variable-pressure data at different temperatures using parametric refinement of each data set.

T (K)	B_0 (GPa)	V_0 (Å^3)	B'	K_a (TPa^{-1})	K_a (TPa^{-1})	B_0 (GPa)
300	12.30(11)	337.15(3)	10.1(5)	38.6(11)	−17.3(8)	13.8(3)
260	12.44(11)	336.00(3)	10.3(5)	38.0(11)	−16.8(8)	14.0(3)
220	12.57(11)	334.84(2)	10.6(5)	37.4(11)	−16.3(8)	14.1(3)
180	12.71(11)	333.68(2)	10.9(5)	36.9(10)	−15.7(7)	14.4(3)
140	12.86(11)	332.51(2)	11.2(5)	36.3(11)	−15.2(7)	14.6(3)
100	13.01(11)	331.35(2)	11.5(5)	35.8(10)	−14.7(7)	14.8(3)

Table C.1.5: Thermal expansion coefficients calculated of $KMn[Ag(CN)_2]_3$ from variable-temperature data at different pressures using independent refinement of each data set.

p (GPa)	α_a (MK^{-1})	α_c (MK^{-1})	α_V (MK^{-1})
0.000(1)	75.6(10)	−61.8(7)	88.7(11)
0.144(5)	67.5(13)	−59.31(17)	75(2)
0.288(9)	63.6(14)	−55.5(19)	71.2(8)
0.437(11)	61.1(13)	−50.7(12)	71.1(15)
0.574(13)	57.9(13)	−48.4(16)	67(2)

Table C.1.6: Thermal expansion coefficients of $KMn[Ag(CN)_2]_3$ calculated from variable-temperature data at different pressures using parametric refinement of each data set.

p (GPa)	α_a (MK^{-1})	α_c (MK^{-1})	α_V (MK^{-1})
0.000(1)	74.916(3)	−61.4696(11)	87.63(10)
0.144(5)	68.28(17)	−56.72(6)	79.21(19)
0.288(9)	63.43(17)	−53.4(5)	72.9(2)
0.437(11)	60.5(2)	−51.21(7)	69.3(3)
0.574(13)	57.4(5)	−49.14(6)	65.1(3)

C.1.5 Rietveld refinements of powder neutron diffraction data

117

Table C.1.7: Lattice parameters, unit cell volumes and ρ values determined from Rietveld refinement of powder neutron diffraction data of $KMn[Ag(CN)_2]_3$.

T (K)	p (kbar)	R_{wp}	a (Å)	c (Å)	V (Å^3)	ρ
300	0	2.926	6.91685(18)	8.1188(4)	336.39(2)	1.17378(8)
280	0	3.250	6.90566(10)	8.1298(2)	335.754(13)	1.17727(5)
240	0	3.100	6.88375(8)	8.1510(2)	334.951(12)	1.18409(4)
200	0	3.031	6.86241(8)	8.1720(2)	333.284(11)	1.19084(4)
160	0	2.987	6.8416(8)	8.1925(2)	332.093(10)	1.19745(4)
120	0	2.940	6.82208(7)	8.2121(2)	330.991(10)	1.2037(3)
300	0	3.177	6.91701(10)	8.1186(2)	336.395(14)	1.17372(5)
260	0	3.177	6.89474(9)	8.1405(2)	335.134(13)	1.18069(5)
220	0	3.057	6.87326(8)	8.1614(2)	333.902(12)	1.18741(4)
180	0	3.066	6.85271(8)	8.1818(2)	332.738(11)	1.19395(4)
140	0	3.089	6.83267(8)	8.2015(2)	331.593(11)	1.20034(4)
100	0	2.821	6.81357(8)	8.2206(2)	330.508(9)	1.20650(4)
300	1.5027	1.272	6.862(4)	8.1539(18)	332.52(8)	1.1882(3)
260	1.4838	1.328	6.8423(3)	8.1736(16)	331.40(7)	1.1946(3)
220	1.4607	1.311	6.8227(3)	8.1933(15)	330.30(7)	1.2009(3)
180	1.4342	1.355	6.8045(3)	8.2107(15)	329.23(7)	1.2067(3)
140	1.4022	1.361	6.7867(3)	8.2308(15)	328.31(7)	1.2128(3)
300	2.9963	1.302	6.8174(3)	8.1763(17)	329.09(7)	1.1993(3)
260	2.9578	1.304	6.7987(4)	8.1958(18)	328.08(8)	1.2055(3)
220	2.9143	1.362	6.7802(3)	8.2152(17)	327.07(7)	1.2116(3)
180	2.8658	1.350	6.7628(3)	8.2328(17)	326.08(7)	1.2174(3)
139	2.8099	1.372	6.7465(4)	8.2497(19)	325.18(8)	1.2228(3)
100	2.7435	1.409	6.7317(3)	8.2685(19)	324.50(8)	1.2283(3)
300	4.494	1.323	6.7763(4)	8.198(2)	326.01(9)	1.2098(4)
260	4.455	1.264	6.7587(3)	8.2138(19)	325.93(8)	1.2153(3)
220	4.409	1.310	6.7411(4)	8.232(2)	323.95(10)	1.2211(4)
180	4.3522	1.298	6.7240(4)	8.255(2)	323.23(9)	1.2277(4)
139	4.2867	1.306	6.7084(3)	8.271(2)	322.36(7)	1.2330(3)
100	4.2103	1.293	6.6945(3)	8.286(2)	321.60(6)	1.2378(3)
300	5.898	1.522	6.7411(5)	8.215(3)	323.30(13)	1.2187(5)
260	5.846	1.530	6.7242(6)	8.234(3)	322.42(14)	1.2245(6)
220	5.787	1.577	6.7087(5)	8.230(3)	321.54(12)	1.2297(5)
180	5.718	1.561	6.6923(4)	8.267(2)	320.66(9)	1.2353(4)
139	5.6357	1.588	6.6769(3)	8.285(2)	319.86(8)	1.2408(4)
125	5.6074	1.855	6.6718(4)	8.291(2)	319.61(9)	1.2427(4)
100	5.548	1.620	6.6637(3)	8.3000(17)	319.18(7)	1.2456(3)

Table C.1.8: Bond angles and lengths determined from Rietveld refinement of powder neutron diffraction data of $KMn[Ag(CN)_2]_3$.

T (K)	p (kbar)	Mn–N (Å)	∠ N–Mn–N 1 (°)	∠ N–Mn–N (2) (°)	∠ N–Mn–N (3) (°)	∠ N–Mn–N (av) (°)	Ag–C (Å)	∠ C–Ag–C (°)
300	0	2.2385(18)	87.42(6)	90.02(7)	95.28(13)	90(3)	2.048(3)	178.2(4)
280	0	2.2380(19)	87.43(6)	90.13(8)	95.14(14)	90(3)	2.049(3)	177.3(4)
240	0	2.235(2)	87.22(7)	90.74(9)	94.90(18)	90(3)	2.049(3)	176.4(5)
200	0	2.233(2)	87.04(6)	91.13(8)	94.86(17)	90(3)	2.047(3)	177.5(3)
160	0	2.2315(19)	86.95(6)	90.92(8)	95.27(15)	90(4)	2.049(3)	178.5(4)
120	0	2.229(2)	86.79(7)	93.20(18)	93.21(9)	90(3)	2.044(3)	176.9(4)
300	0	2.237(2)	87.38(7)	90.36(8)	94.99(16)	90(3)	2.048(4)	176.0(7)
260	0	2.236(2)	87.19(7)	90.81(10)	94.9(2)	90(3)	2.047(4)	176.0(7)
220	0	2.234(2)	87.15(7)	91.50(10)	94.24(19)	90(3)	2.046(3)	176.7(5)
180	0	2.232(2)	87.00(7)	91.57(9)	94.47(18)	90(3)	2.046(3)	177.0(4)
140	0	2.230(2)	86.91(7)	92.19(9)	94.01(19)	90(3)	2.047(3)	176.7(4)
100	0	2.226(3)	86.71(9)	92.2(2)	94.46(12)	90(4)	2.043(5)	177.5(5)
300	1.5027	2.234(12)	89.0(4)	89.6(5)	92.5(9)	90.0(15)	2.071(14)	170.7(18)
260	1.4838	2.2(1)	88.6(3)	89.0(4)	93.9(7)	90(2)	2.060(12)	174.7(19)
220	1.4607	2.237(8)	88.1(3)	89.8(3)	94.1(5)	90(3)	2.060(11)	175.8(15)
180	1.4342	2.237(8)	88.3(3)	90.0(3)	93.5(5)	90(2)	2.049(13)	177.2(13)
140	1.4022	2.227(10)	87.6(3)	91.3(4)	93.5(9)	90(3)	2.042(17)	170(2)
100	1.3607	2.234(11)	87.9(3)	91.9(4)	92.3(8)	90(2)	2.058(11)	163.0(19)
300	2.9963	2.232(12)	88.0(4)	91.5(9)	92.5(5)	90(2)	2.070(12)	158.6(15)
260	2.9578	2.234(10)	87.9(3)	90.2(4)	94.1(8)	90(2)	2.047(11)	177.4(8)
220	2.9143	2.219(12)	86.9(4)	92.8(5)	93.4(10)	90(3)	2.034(18)	167(2)
180	2.8658	2.215(12)	87.0(4)	92.6(5)	93.4(10)	90(3)	2.033(18)	169(2)
140	2.8099	2.215(11)	86.7(4)	93.0(5)	93.7(9)	90(4)	2.029(17)	170(2)
100	2.7435	2.233(9)	86.8(3)	91.2(4)	95.2(7)	90(4)	2.036(10)	177.6(16)
300	4.494	2.216(14)	87.0(4)	92.7(6)	93.2(12)	90(3)	2.04(2)	166(2)
260	4.455	2.229(12)	87.3(4)	92.3(9)	93.1(5)	90(3)	2.058(11)	157.9(15)
220	4.409	2.228(11)	87.2(4)	92.3(9)	93.3(5)	90(3)	2.051(12)	157.9(15)
180	4.3522	2.227(11)	87.0(3)	92.3(8)	93.8(4)	90(3)	2.051(12)	158.5(15)
140	4.2867	2.230(10)	86.9(3)	92.6(8)	93.6(4)	90(3)	2.049(10)	161.6(15)
100	4.2103	2.229(9)	86.5(3)	93.3(4)	93.6(7)	90(4)	2.041(10)	163.0(15)
300	5.898	2.204(12)	85.9(4)	91.9(5)	96.3(9)	90(5)	2.033(17)	166.5(19)
160	5.846	2.202(14)	85.9(5)	94.0(11)	94.1(6)	90(4)	2.03(2)	163(2)
220	5.787	2.202(14)	85.7(5)	94.2(11)	94.4(6)	90(5)	2.03(2)	163(2)
180	5.718	2.203(13)	85.8(4)	94.1(5)	94.3(10)	90(4)	2.03(2)	167(2)
140	5.6357	2.201(12)	85.8(4)	93.9(10)	94.5(5)	90(4)	2.03(2)	169(2)
125	5.6074	2.199(12)	85.7(4)	94.1(5)	94.5(10)	90(5)	2.04(2)	169(2)
100	5.548	2.203(12)	85.6(4)	94.3(5)	94.4(9)	90(5)	2.03(2)	170(2)

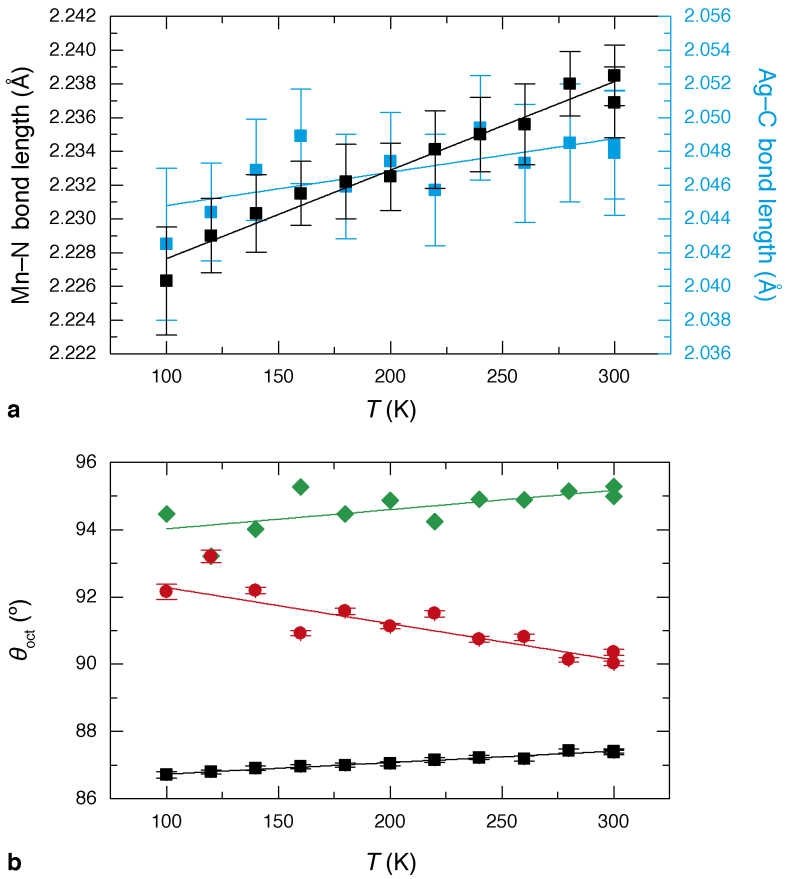

Figure C.1.6: Variation in bond lengths and angles of $KMn[Ag(CN)_2]_3$ upon heating. (a) Bond lengths: Mn–N (black squares) and Ag–C (blue squares) and (b) bond angles around Mn. Linear fits to data are shown.

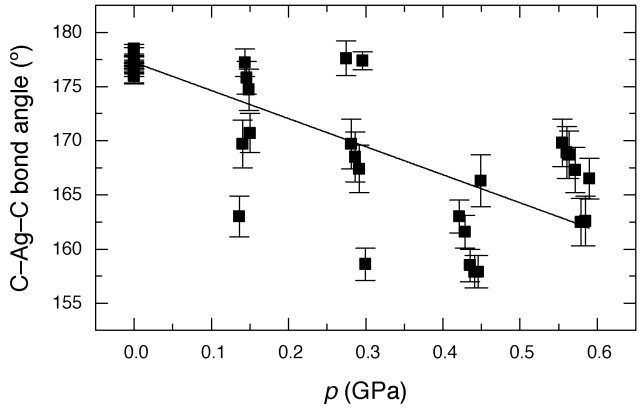

Figure C.1.7: Variation in C–Ag–C bond angles of $KMn[Ag(CN)_2]_3$ at high pressure. Linear fit to data is shown as a guide to the eye.

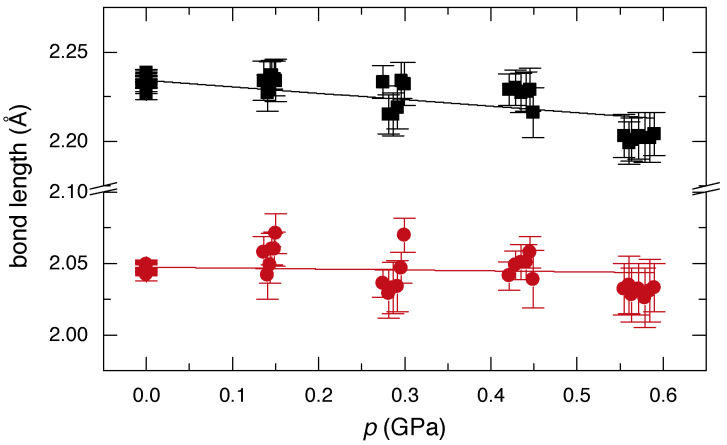

Figure C.1.8: Variation in bond lengths of $KMn[Ag(CN)_2]_3$ at high pressure. Mn–N bond lengths shown as black squares; Ag–C bond lengths as red circles. Linear fits to data are shown as a guide to the eye.

C.2 $KCd[Ag(CN)_2]_3$

C.2.1 Variable-pressure Raman spectroscopy

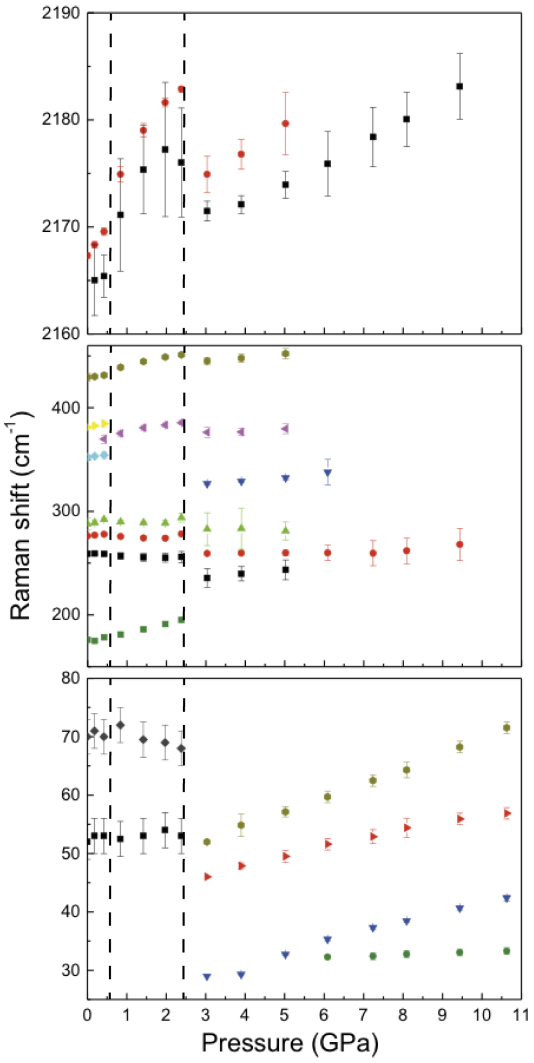

Figure C.2.9: Pressure dependence of the Raman vibrational frequencies over the range $0 < p < 11$ GPa for $KCd[Ag(CN)_2]_3$. The approximate position of phase transitions are indicated by dashed vertical lines.

C.2.2 Variable-pressure single crystal X-ray diffraction

Table C.2.9: Single crystal X-ray diffraction data collection details for $KCd[Ag(CN)_2]_3$ at high pressure.

Diffractometer	Agilent Gemini				
Wavelength (Å)	0.71073				
P (GPa)	Ambient	0.6	1.6	2.6	3.1
Space group	$P312$	$P312$	$P312$	$C2$	$C2$
Z (Z supercell)	1	1	2(8)	6(48)	6(48)
range of h, k, l	$-10 \leq h \leq 10$	$-8 \leq h \leq 8$	$-8 \leq h \leq 8$	$-11 \leq h \leq 11$	$-11 \leq h \leq 11$
	$-10 \leq k \leq 10$	$-8 \leq k \leq 8$	$-8 \leq k \leq 8$	$-14 \leq k \leq 13$	$-13 \leq k \leq 13$
	$-12 \leq l \leq 11$	$-2 \leq l \leq 2$	$-5 \leq l \leq 59$	$-11 \leq l \leq 11$	$-9 \leq l \leq 9$
no. of measured reflns	8886	2013	3453	4896	4716
no. of unique reflns	819	171	320	1192	1174
no. of observed reflns ($I > 2\sigma$)	730	137	153	825	789
R_{equiv}	0.0702	0.2220	0.1487	0.1920	0.2221
R_{sigma}	0.0250	0.0743	0.0840	0.1366	0.1414
Refinement					
R ($F_{\text{obs}} > 4\sigma$)	0.0163	0.0390	0.0743	0.0659	0.0789
χ^2	1.078	1.045	1.176	0.992	1.012
no. of params	29	19	30	130	123

Table C.2.10: Structural parameters from refinement of single crystal diffraction data for $KCd[Ag(CN)_2]_3$.

p (GPa)	a (Å)	b (Å)	c (Å)	β (°)	V (Å^3)
ambient	6.9458(2)	–	8.3224(2)	–	347.72(2)
0.6	6.7651(12)	–	8.386(13)	–	332.4(5)
1.6	6.497(2)	–	17.00(2)	–	621.4(8)
2.6	18.312(6)	10.7833(8)	10.636(3)	124.33(4)	1734.4(8)
3.1	18.311(6)	10.6211(7)	10.604(3)	125.11(4)	1687.1(7)

Table C.2.11: Fractional atomic coordinates and thermal displacement parameters for $KCd[Ag(CN)_2]_3$ ($P312$) at ambient pressure.

Atom	x	y	z	U_{eq} ($\times 10^{-2}$ Å^2)
Cd	0	0	0.5	2.326(8)
K	0.6667	0.3333	0.5	4.00(3)
Ag	0.49535(3)	−0.00931(6)	0	5.17(1)
C	0.6484(4)	−0.0029(5)	0.2132(2)	3.93(4)
N	−0.2635(3)	0.0065(4)	0.32991(17)	3.97(3)

Table C.2.12: Fractional atomic coordinates and thermal displacement parameters for $KCd[Ag(CN)_2]_3$ ($P312$) at 0.6 GPa.

Atom	x	y	z	U_{eq} ($\times 10^{-2}$ Å^2)
Cd	0	0	0.5	3.9(5)
K	−0.3333	−0.6667	0.5	4.7(1.4)
Ag	0.49600(16)	−0.0080(3)	0	5.7(6)
N	−0.272(3)	0.002(3)	0.324(5)	4.7(3)*
C	0.644(3)	−0.002(3)	0.205(5)	3.9(3)*

* Refined isotropically.

Table C.2.13: Fractional atomic coordinates and thermal displacement parameters for $KCd[Ag(CN)_2]_3$-II ($P312-2c$) at 1.6 GPa.

Atom	x	y	z	U_{eq} ($\times 10^{-2}$ Å^2)
Cd	0	0	0.2546(7)	2.7(1)
K	0.6667	0.3333	0.227(2)	6.0(5)
Ag1	0.4984(4)	−0.0032(8)	0	3.8(8)
Ag2	0.4997(4)	−0.0007(8)	0.5	4.2(8)
N1	0.728(6)	1.014(6)	0.167(2)	4.1(7)*
C1	0.669(6)	0.000(7)	0.101(2)	2.6(6)*
N2	0.686(5)	0.965(5)	0.666(2)	4.1(7)*
C2	0.607(6)	0.969(6)	0.606(2)	2.6(6)*

* Refined isotropically.

Table C.2.14: Fractional atomic coordinates and thermal displacement parameters for $KCd[Ag(CN)_2]_3$-III ($C2$) at 2.6 GPa.

Atom	x	y	z	U_{eq} ($\times 10^{-2}$ Å^2)
Cd1	0	0.0429(9)	0	3.8(5)
Cd2	0.3000(2)	0.0432(7)	0.6997(2)	3.6(3)
Ag1	0	0.0388(9)	0.5	3.6(6)
Ag2	0.7477(4)	−0.2043(8)	−0.0038(6)	4.8(4)
Ag3	0.3148(3)	0.0348(8)	0.2145(4)	4.3(5)
Ag4	0.0453(4)	−0.2177(7)	0.6785(5)	4.4(3)
Ag5	0.0550(4)	−0.6881(8)	0.6908(5)	4.4(3)
K1	0	0.6667	0	2.5(10)
K2	0.8126(7)	−0.7692(8)	0.6238(9)	2.5(1.0)
N1	−0.046(2)	0.054(2)	−0.256(3)	2.6(7)*
N2	0.347(2)	0.061(2)	0.956(3)	2.9(6)*
N3	0.271(2)	−0.010(3)	0.450(4)	3.1(7)*
N4	0.186(2)	0.181(2)	0.643(3)	2.6(6)*
N5	0.211(2)	−0.112(2)	0.672(4)	4.2(8)*
N6	0.393(2)	−0.318(2)	−0.054(3)	2.2(6)*
N7	0.431(2)	−0.065(2)	0.785(3)	2.2(6)*
N8	0.373(2)	0.202(2)	0.675(3)	3.0(6)*
N9	0.099(3)	−0.116(2)	0.035(4)	3.7(9)*
C1	0.843(3)	−0.138(3)	−0.026(4)	2.5(10)*
C2	0.847(3)	−0.771(3)	−0.029(4)	2.0(8)*
C3	0.138(2)	−0.762(2)	0.655(3)	1.3(7)*
C4	0.151(3)	−0.155(3)	0.665(4)	2.9(9)*
C5	−0.026(3)	−0.609(3)	0.750(4)	3.7(9)*
C6	0.338(2)	0.057(3)	0.053(4)	3.3(8)*
C7	−0.023(2)	0.049(5)	−0.336(4)	3.8(9)*
C8	−0.068(2)	−0.266(2)	0.674(3)	1.7(6)*
C9	0.294(2)	0.005(2)	0.372(5)	2.3(8)

* Refined isotropically.

Table C.2.15: Fractional atomic coordinates and thermal displacement parameters for $KCd[Ag(CN)_2]_3$-III ($C2$) at 3.1 GPa.

Atom	x	y	z	U_{eq} ($\times 10^{-2}$ Å^2)
Cd1	0	0.0449(11)	0	2.8(6)
Cd2	0.2983(3)	0.0450(10)	0.7009(3)	3.4(4)
Ag1	0	0.0392(11)	0.5	3.8(4)
Ag2	0.7475(5)	−0.2016(10)	−0.0059(7)	4.0(4)
Ag3	0.3158(3)	0.0384(10)	0.2189(4)	4.0(4)
Ag4	0.0449(5)	−0.2197(10)	0.6787(7)	3.8(4)
Ag5	0.0521(5)	−0.6844(10)	0.6892(6)	3.8(4)
K1	0	0.6667	0	6(2)
K2	0.8120(9)	−0.7656(11)	0.6226(11)	3.3(15)
N1	−0.045(2)	0.061(3)	−0.256(4)	2.5(8)*
N2	0.342(2)	0.063(3)	0.956(3)	3.3(9)*
N3	0.267(2)	−0.014(3)	0.458(4)	2.9(8)*
N4	0.185(2)	0.183(3)	0.648(4)	2.6(8)*
N5	0.204(3)	−0.110(3)	0.672(5)	4.9(13)*
N6	0.387(3)	−0.317(3)	−0.053(4)	1.8(7)*
N7	0.437(3)	−0.062(2)	0.787(4)	1.7(6)*
N8	0.377(3)	0.214(3)	0.676(4)	3.4(9)*
N9	0.102(3)	−0.118(3)	0.035(4)	2.9(10)*
C1	0.838(3)	−0.130(4)	−0.030(5)	3.4(15)*
C2	0.845(3)	−0.768(3)	−0.021(4)	1.1(8)*
C3	0.135(3)	−0.761(3)	0.655(4)	1.7(5)*
C4	0.147(3)	−0.154(3)	0.673(4)	1.7(5)*
C5	−0.024(3)	−0.608(4)	0.746(5)	3.4(11)*
C6	0.338(3)	0.060(3)	0.060(3)	2.3(9)*
C7	−0.024(2)	0.044(5)	−0.338(4)	2.4(7)*
C8	−0.065(4)	−0.267(4)	0.667(6)	5.0(15)*
C9	0.290(2)	0.009(3)	0.382(4)	1.7(8)

* Refined isotropically.

C.2.3 Synchrotron powder X-ray diffraction

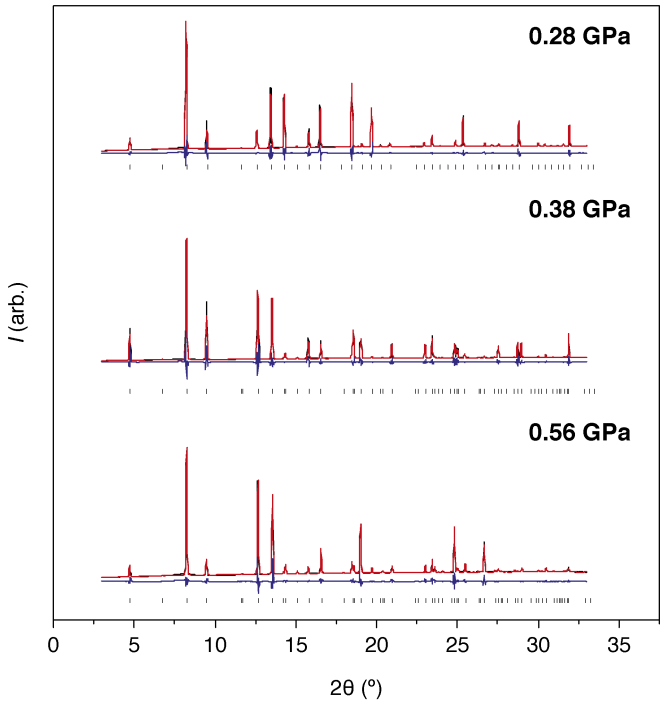

Figure C.2.10: Pawley fits (red lines) to synchrotron powder X-ray diffraction data (black line) collected for $KCd[Ag(CN)_2]_2$-I. The difference (data−fit) is shown in blue under each data set. Successive data sets, fits and difference functions are off-set vertically and the pressures of each collection are indicated.

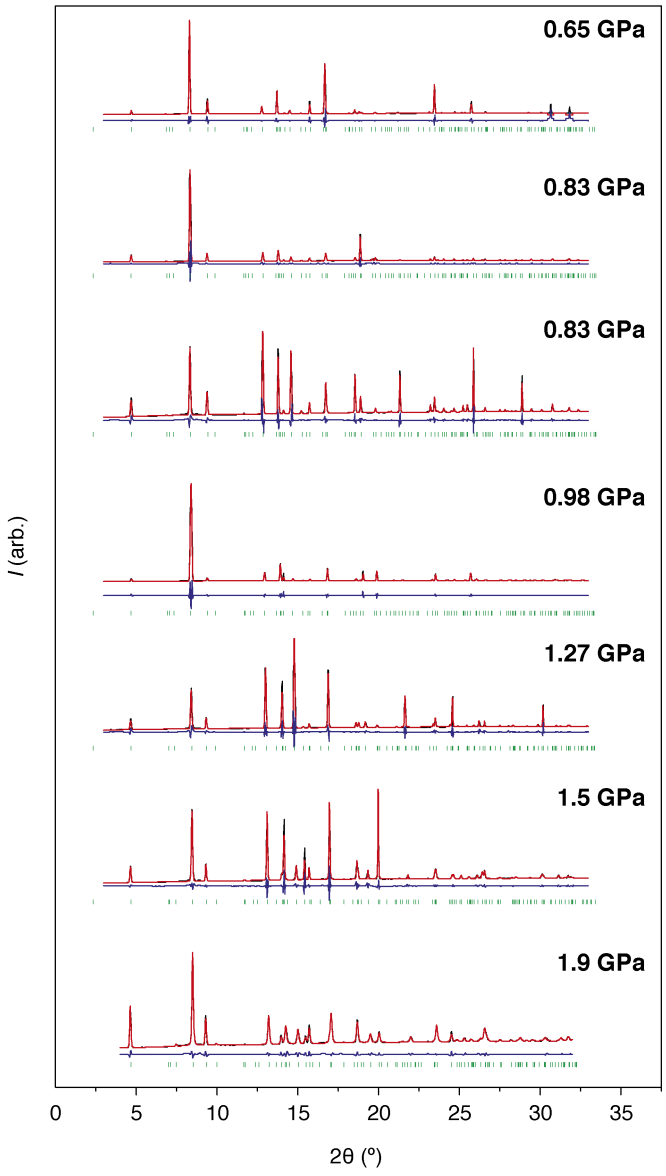

Figure C.2.11: Pawley fits (red lines) to synchrotron powder X-ray diffraction data (black line) collected for $KCd[Ag(CN)_2]_2$-II. The difference (data−fit) is shown in blue under each data set. Successive data sets, fits and difference functions are off-set vertically and the pressures of each collection are indicated.

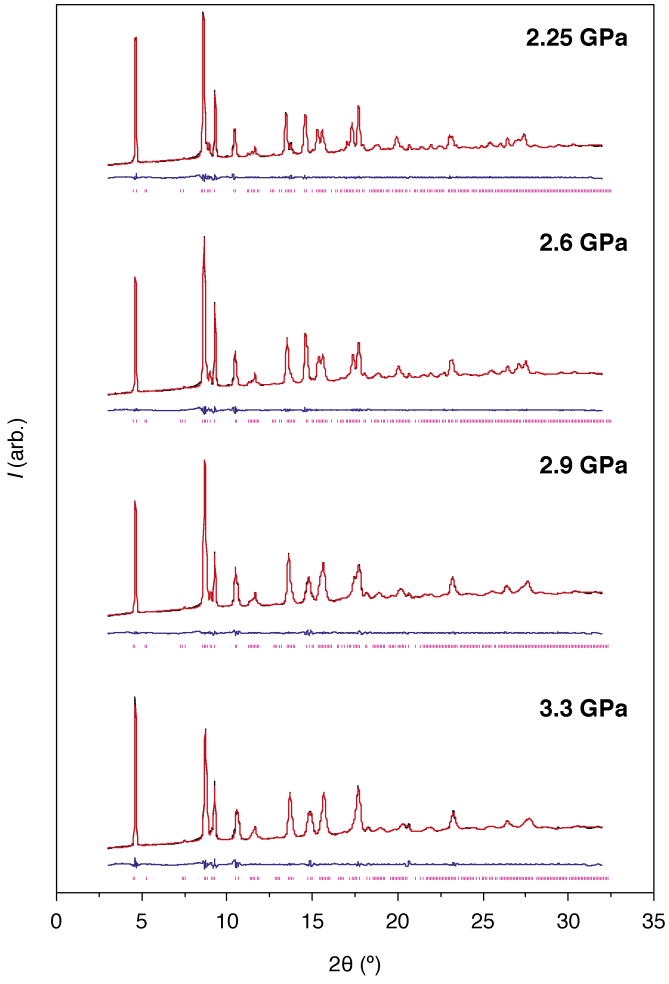

Figure C.2.12: Pawley fits (red lines) to synchrotron powder X-ray diffraction data (black line) collected for $KCd[Ag(CN)_2]_2$-IIIa. The difference (data−fit) is shown in blue under each data set. Successive data sets, fits and difference functions are off-set vertically and the pressures of each collection are indicated.

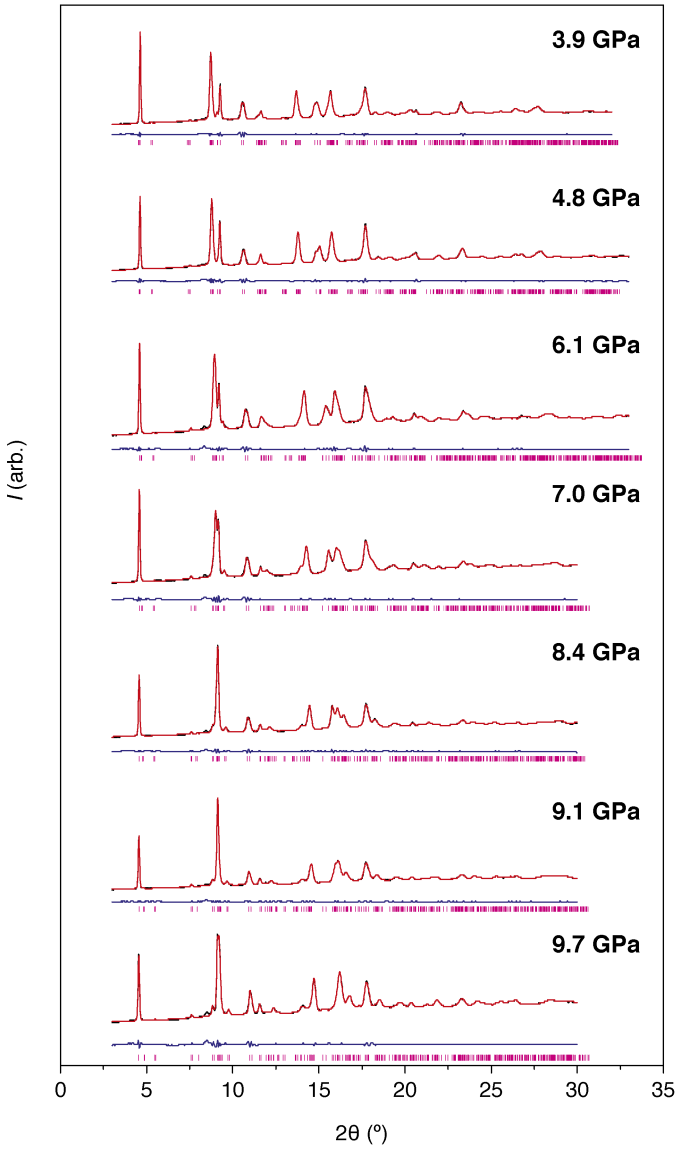

Figure C.2.13: Pawley fits (red lines) to synchrotron powder X-ray diffraction data (black line) collected for $KCd[Ag(CN)_2]_2$-IIIb. The difference (data−fit) is shown in blue under each data set. Successive data sets, fits and difference functions are off-set vertically and the pressures of each collection are indicated.

Table C.2.16: Variable-pressure lattice parameters from synchrotron powder X-ray diffraction for $KCd[Ag(CN)_2]_3$-I. Estimated standard deviation in pressure is 0.1 GPa at each point.

p (GPa)	a (Å)	c (Å)	V (Å^3)
0	6.9422(4)	8.3098(8)	346.83(5)
0.28	6.8295(3)	8.3618(4)	337.76(3)
0.38	6.7899(3)	8.3864(3)	334.83(3)
0.40	6.7844(4)	8.3846(4)	334.22(4)
0.56	6.7771(3)	8.3943(2)	333.89(3)

Table C.2.17: Variable-pressure lattice parameters from synchrotron powder X-ray diffraction for $KCd[Ag(CN)_2]_3$-II. Estimated standard deviation in pressure is 0.1 GPa at each point.

p (GPa)	a (Å)	c (Å)	V (Å^3)
0.68	6.6999(3)	16.8566(6)	655.30(5)
0.83	6.6614(4)	16.9203(11)	650.24(10)
0.83	6.6558(17)	16.8963(10)	648.21(5)
0.98	6.6131(6)	16.932(2)	641.29(14)
1.27	6.5517(4)	16.9929(8)	631.70(8)
1.5	6.4960(4)	17.0376(11)	622.64(8)
1.9	6.4471(4)	17.0841(15)	614.96(9)

Table C.2.18: Variable-pressure lattice parameters from synchrotron powder X-ray diffraction for $KCd[Ag(CN)_2]_3$-III. Estimated standard deviation in pressure is 0.1 GPa at each point.

p (GPa)	a (Å)	b (Å)	c (Å)	β (°)	V (Å^3)
2.25	18.220(2)	10.97606(18)	10.6381(18)	123.606(8)	1771.9(5)
2.6	18.2022(17)	10.92516(8)	10.6211(14)	123.993(7)	1751.2(3)
2.9	18.210(2)	10.882(2)	10.623(2)	124.400(9)	1737.0(6)
3.3	18.204(4)	10.809(5)	10.600(4)	124.749(12)	1713.7(11)
3.9	18.216(18)	10.747(7)	10.565(11)	125.12(4)	1692(3)
4.8	18.25(2)	10.613(13)	10.552(12)	126.04(7)	1653(4)
6.1	18.335(6)	10.240(4)	10.484(5)	125.939(17)	1593.7(12)
7.0	18.393(16)	10.126(7)	10.496(12)	126.63(3)	1569(3)
8.4	18.4232(17)	10.033(6)	10.477(8)	127.22(4)	1542(2)
9.1	18.443(9)	10.014(6)	10.383(8)	127.85(2)	1514.2(18)
9.7	18.5095(19)	9.927(5)	10.384(2)	128.507(10)	1493.0(8)

C.3 $Zn[Au(CN)_2]_2$

C.3.1 V*p* single-crystal X-ray diffraction: Phase I

Table C.3.19: Representative single-crystal X-ray diffraction data collection and refinement details for $Zn[Au(CN)_2]_2$-I at $T = 298\,K$ and $p = 0.35(10)\,GPa$.

Radiation	Mo $K\alpha$, $\lambda = 0.71073$ Å			
Formula	$ZnAu_2C_4N_4$			
M, g mol^{-1}	563.39			
Z	6			
Crystal Size (mm)	0.050 x 0.050 x 0.065			
Crystal System	Hexagonal			
Space Group	$P6_222$			
a (Å)	8.2549(7)			
c (Å)	21.1181(16)			
V (Å^3)	1246.27(17)			
$wR_p(F^2)$	0.053			
Flack parameter	−0.03(6)			
Atom	x	y	z	U_{eq}, Å^2
Zn	−0.5000	−0.5000	0.20664(16)	0.0237(2)
Au	0.00203(18)	0.31458(13)	0.29248(3)	0.0314(2)
C	0.607(2)	0.831(3)	0.3003(10)	0.022(6)
C	−0.184(3)	−0.394(2)	0.1111(8)	0.007(5)
N	−0.449(2)	−0.290(2)	0.2649(7)	0.021(5)
N	−0.296(2)	0.136(2)	0.1840(7)	0.018(5)

Estimated standard errors are given in parentheses.

Table C.3.20: Pressure dependence of key crystallographic parameters and derived quantities from single crystal X-ray diffraction measurements of $Zn[Au(CN)_2]_2$-I. The data collected at a pressure of 1.3 GPa were of sufficient completeness for accurate lattice parameter determination, but not for full structure solution.

p (GPa)	0	0.35	0.95	1.3	1.5	1.78
a (Å)	8.4624(3)	8.2549(7)	8.0278(5)	7.8537(6)	7.8066(5)	7.6743(7)
c (Å)	20.6220(7)	21.1181(16)	21.6073(14)	21.9417(12)	22.0406(9)	22.2592(17)
V (Å^3)	1278.93(14)	1246.3(3)	1205.94(23)	1172.06(24)	1163.26(20)	1135.32(29)
Au...Au′ (Å)	3.1116(6)	3.0781(15)	3.0448(16)	-	3.009(2)	3.002(19)
Au...Au″ (Å)	3.1599(7)	3.132(2)	3.104(2)	-	3.0797(19)	3.061(2)
∠ Au–Au–Au (°)	115.023(11)	114.23(3)	113.29(3)	-	112.43(2)	111.92(3)
Zn–N* (Å)	1.959(5)	1.95(4)	1.943(9)	-	1.979(9)	1.9608(11)
Au–C* (Å)	1.984(6)	1.98(22)	1.986(8)	-	1.949(4)	1.955(10)
C–N* (Å)	1.142(7)	1.1455(17)	1.1385(6)	-	1.139(12)	1.145(5)
∠ Au–C–N* (°)	176.5(13)	171(5)	173.0(14)	-	175.3(18)	169.3(18)
∠ Zn–N–C* (°)	169.5(12)	172(4)	168(7)	-	164(6)	165(9)
∠ N–Zn–N* (°)	109.5(23)	110(6)	110(6)	-	110(6)	110(8)
∠ C–Au–C (°)	175.9(3)	173.9(10)	173.7(9)	-	175.8(9)	173.0(9)

Estimated standard errors are given in parentheses.

*Multiple independent bond lengths or angles of the same type have been averaged and the estimated standard deviation is given in parentheses.

C.3.2 VT single-crystal X-ray diffraction: Phase I

Table C.3.21: Representative single-crystal X-ray diffraction data collection and refinement details for $Zn[Au(CN)_2]_2$-I at $T = 100\,K$ and at ambient pressure.

Radiation	Mo $K\alpha$, $\lambda = 0.71073$ Å			
Formula	$ZnAu_2C_4N_4$			
M, g mol^{-1}	563.39			
Z	6			
Crystal Size (mm)	0.106 x 0.130 x 0.210			
Crystal System	Hexagonal			
Space Group	$P6_222$			
a (Å)	8.3967(2)			
c (Å)	20.9219(7)			
V (Å^3)	1277.47(7)			
$wR_p(F^2)$	0.062			
Flack parameter	−0.02(3)			
Atom	x	y	z	U_{eq}, Å^2
Zn	0.5000	0.0000	0.62602(6)	0.0085
Au	0.31639(4)	0.31687(4)	0.459548(10)	0.0107
C	0.4020(13)	0.2187(13)	0.5289(4)	0.0131
C	0.2149(16)	0.3985(13)	0.3881(4)	0.0175
N	0.4455(11)	0.1532(12)	0.5697(3)	0.0131
N	0.7123(12)	0.1491(11)	0.6820(3)	0.0130

Estimated standard errors are given in parentheses.

Table C.3.22: Temperature dependence of key crystallographic parameters and derived quantities from single crystal X-ray diffraction measurements of $Zn[Au(CN)_2]_2$-I.

T (K)	100	150	200	250	300	350	400
a (Å)	8.3967(2)	8.4132(3)	8.4351(3)	8.4535(3)	8.4106(3)	8.4873(3)	8.5066(4)
c (Å)	20.9219(7)	20.8546(8)	20.7859(9)	20.7138(8)	20.6408(9)	20.5680(9)	20.4954(11)
V (Å^3)	1277.47(7)	1278.36(7)	1280.79(8)	1281.92(8)	1282.58(9)	1283.11(9)	1284.39(11)
Au...Au′ (Å)	3.0794(6)	3.0860(6)	3.0966(7)	3.1065(7)	3.1131(11)	3.1235(11)	3.1318(18)
Au...Au″ (Å)	3.1467(7)	3.1531(8)	3.1568(8)	3.1602(8)	3.1662(14)	3.1671(14)	3.1721(18)
∠ Au–Au–Au (°)	115.034(10)	115.002(12)	115.013(12)	115.008(11)	114.99(2)	115.00(2)	114.99(3)
Zn–N* (Å)	1.968(7)	1.964(19)	1.9693(23)	1.9657(6)	1.968(17)	1.972(5)	1.958(14)
Au–C* (Å)	1.989(22)	1.984(4)	1.9855(7)	1.983(9)	1.983(15)	1.987(12)	1.985(8)
C–N* (Å)	1.15(3)	1.144(25)	1.140(4)	1.146(10)	1.15(3)	1.127(18)	1.15(3)
∠ Zn–N–C* (°)	168.5(6)	168.7(21)	169.35(7)	169.4(11)	166.25(21)	168.7(9)	168.4(4)
∠ Au–C–N* (°)	176.7(4)	177.1(18)	176.3(3)	176.4(10)	177.1(16)	177.4(3)	176(3)
∠ N–Zn–N* (°)	109.5(25)	109.5(25)	109.5(26)	109.5(21)	109.5(10)	109.5(18)	109.5(19)
∠ C–Au–C (°)	176.0(4)	175.5(4)	176.2(4)	175.7(4)	176.1(4)	175.7(4)	176.4(4)

Estimated standard errors are given in parentheses.

*Multiple independent bond lengths or angles of the same type have been averaged and the estimated standard deviation is given in parentheses.

C.3.3 V*p* single-crystal X-ray diffraction: Phase II

Table C.3.23: Representative single-crystal X-ray diffraction data collection and refinement details for $Zn[Au(CN)_2]_2$-II at $T = 298$ K and $p = 3.5(10)$ GPa.

Radiation	Mo $K\alpha$, $\lambda = 0.71073$ Å
Formula	$Zn_8Au_{16}C_{32}N_{32}$
M (g mol^{-1})	4507.06
Z	6
Crystal Size (μm)	50 x 50 x 65
Crystal System	Hexagonal
Space Group	$P6_422$
a, Å	14.485(2)
c, Å	45.796(6)
V, Å^3	8321(2)
$wR_p(F^2)$	0.090
Flack parameter	0.01(7)

Atom	x	y	z	U_{eq}, Å^2
Au1	0.1130(4)	0.1135(4)	0.10339(12)	0.0290(15)
Au2	−0.3275(5)	−0.3165(5)	0.10621(12)	0.0442(14)
Au3	0.6569(5)	0.1684(5)	0.10811(13)	0.057(2)
Au4	0.3815(4)	−0.0057(4)	0.06074(11)	0.0278(15)
Au5	0.8713(5)	0.3732(5)	0.10271(12)	0.0442(14)
Au6	−0.3696(5)	−0.4931(4)	0.06550(10)	0.0325(16)
Au7	0.1789(4)	−0.0108(5)	0.06080(9)	0.0191(12)
Au8	0.8349(4)	0.5128(4)	0.05883(9)	0.0197(13)
Zn1	0.4860(9)	0.2394(10)	0.1455(3)	0.013(4)*
Zn2	0.5071(10)	0.2555(12)	0.0236(3)	0.035(5)*
Zn3	0.0020(12)	0.7544(11)	0.1447(3)	0.015(4)*
Zn4	0.0042(13)	0.7580(11)	0.0193(3)	0.028(4)*
N1	0.611(2)	0.254(4)	0.0508(8)	0.008(3)*
N2	0.411(3)	0.126(4)	0.1161(10)	0.008(3)*
N3	0.4146(17)	0.280(4)	0.1749(9)	0.008(3)*
N4	0.396(2)	0.253(4)	0.0490(7)	0.008(3)*
N5	0.814(2)	0.449(3)	0.1597(8)	0.008(3)*
N6	0.574(4)	0.364(3)	0.1203(9)	0.008(3)*
N7	0.443(4)	0.135(2)	−0.0037(8)	0.008(3)*
N8	−0.0381(5)	0.826(3)	0.1741(9)	0.008(3)*
N9	−0.068(3)	0.791(4)	0.0509(10)	0.008(3)*
N10	−0.075(4)	0.670(3)	0.1103(8)	0.008(3)*
N11	0.113(3)	0.879(3)	−0.0035(7)	0.008(3)*
N12	0.692(2)	0.048(3)	0.1582(10)	0.008(3)*
N13	0.581(3)	0.379(3)	−0.0023(10)	0.008(3)*

Continued on next page

Table S2 continued from previous page

N14	0.929(3)	0.281(4)	0.0508(9)	0.008(3)*
N15	0.097(4)	0.838(3)	0.1131(9)	0.008(3)*
N16	−0.069(4)	0.649(4)	−0.0108(10)	0.008(3)*
C1	0.134(5)	0.928(6)	−0.0246(10)	0.010(4)*
C2	0.613(6)	0.435(5)	−0.0218(10)	0.010(4)*
C3	0.411(6)	0.073(6)	0.0977(10)	0.010(4)*
C4	0.339(7)	−0.075(5)	0.0225(8)	0.010(4)*
C5	0.137(7)	0.909(5)	0.0975(9)	0.010(4)*
C6	−0.070(6)	0.855(6)	0.1926(9)	0.010(4)*
C7	0.601(6)	0.424(5)	0.1017(10)	0.010(4)*
C8	−0.063(5)	−0.147(4)	0.0671(9)	0.010(4)*
C9	0.370(7)	0.274(8)	0.0701(11)	0.010(4)*
C10	−0.327(7)	−0.417(7)	0.0282(10)	0.010(4)*
C11	0.630(7)	0.223(7)	0.0716(11)	0.010(4)*
C12	0.358(4)	0.276(4)	0.1928(10)	0.010(4)*
C13	0.924(6)	0.337(4)	0.0674(10)	0.010(4)*
C14	−0.121(6)	0.602(5)	0.0944(10)	0.010(4)*
C15	0.669(8)	0.094(6)	0.1423(11)	0.010(4)*
C16	0.834(7)	0.416(7)	0.1396(11)	0.010(4)*

Estimated standard deviations are given in parentheses.
* U_{eq} have been constrained to be equal in atoms of the same type.

Table C.3.24: Pressure dependence of key crystallographic parameters and derived quantities from single crystal X-ray diffraction measurements of $Zn[Au(CN)_2]_2$-II. The data collected at pressures of 2.2 and 3.1 GPa were of sufficient completeness for accurate lattice parameter determination, but not for full structure solution.

p (GPa)	2.2	2.4	3.1	3.6
a (Å)	15.054 (3)	14.936 (3)	14.594 (4)	14.485 (2)
c (Å)	45.025 (5)	45.092 (7)	45.609 (7)	45.796 (6)
V (Å^3)	8837 (5)	8712 (5)	8413 (6)	8321 (3)
Au...Au′ * (Å)	-	3.01 (4)	-	2.98 (6)
Au...Au″ * (Å)	-	3.0 5(8)	-	3.05 (5)
Additional Au...Au (Å)	-	-	-	3.32 (5)
∠ Au—Au—Au* (°)	-	111 (8)	-	110 (10)
Zn—N* (Å)	-	1.970 (8)	-	1.965 (9)
Au—C* (Å)	-	1.960 (7)	-	1.966 (9)
C—N* (Å)	-	1.146 (19)	-	1.4 (4)
∠ Au—C—N* (°)	-	163 (8)	-	165 (8)
∠ Zn—N—C* (°)	-	164 (8)	-	160 (8)
∠ N—Zn—N* (°)	-	110 (12)	-	110 (25)
∠ C—Au—C* (°)	-	169 (6)	-	172.5 (18)

Estimated standard errors are given in parentheses.
*Multiple independent bond lengths or angles of the same type have been averaged and the estimated standard deviation is given in parentheses.

C.3.4 Analysis of Powder X-ray Diffraction Data

The powder X-ray diffraction data were of sufficient quality only to refine lattice parameters and peak shape profile variables, while making use of (fixed) atomic coordinates as determined using our single-crystal X-ray diffraction measurements. Consequently the fits obtained are not of the same quality as Pawley refinements, but are more meaningful in the sense that a physically-sensible structural model is used to determine intensities. As in previous studies of flexible materials with highly anisotropic mechanical properties, we found evidence of strong (hkl) dependence in the peak asymmetries.[79] This occurs because individual crystallites expand and contract in different directions as a function of hydrostatic pressure, and this results in an inhomogeneous distribution of inter-particle stresses throughout the polycrystalline sample. The presence of both NLC and PLC axes means that there are some crystal axes along which the compressibility is close to zero; for reflections that correspond to crystal directions parallel to these axes, the stresses are very small (hence the reflections show small peak asymmetries). For reflections corresponding to crystal directions parallel to the strongest NLC and PLC axes, the stresses are very large (hence these reflections show large peak asymmetries). Within the truly-hydrostatic fluorinert regime ($p < 2\,\mathrm{GPa}$) the contrast between sharp and broadened peaks is sufficiently large that completely satisfactory fits to the very sharpest intense peak (the (104) reflection by virtue of the relation $K_a^2/K_c^2 \simeq 4a/c$) are not in fact feasible.

Lattice parameters were derived using the Rietveld method [459] as implemented within the TOPAS suite of programs [154], which is suited for its ability to model unusual peak shape functions. Peak shapes were fitted initially using a normal pseudo-voigt function. In order to account for the anisotropic strain broadening it was necessary (i) to add to this function an isotropic broadening term (of Lorentzian shape), and (ii) to convolute the resultant peak with an hkl-dependent exponential function in order to model the observed asymmetry. This asymmetry was evident in some reflections having peak shapes which trailed to high d-spacing and others with peak shapes trailing to low d-spacing. In our analysis we found that a suitable fourth-order spherical harmonic function reproduced this asymmetry well, with both the isotropic strain term and anisotropic broadening contribution varying smoothly towards zero at room temperature. The corresponding fits to data are shown in Figs. C.3.14 and C.3.15 for the ambient and high-pressure phases, respectively. The lattice parameters derived from these fits are listed in Tables C.3.25 and C.3.26.

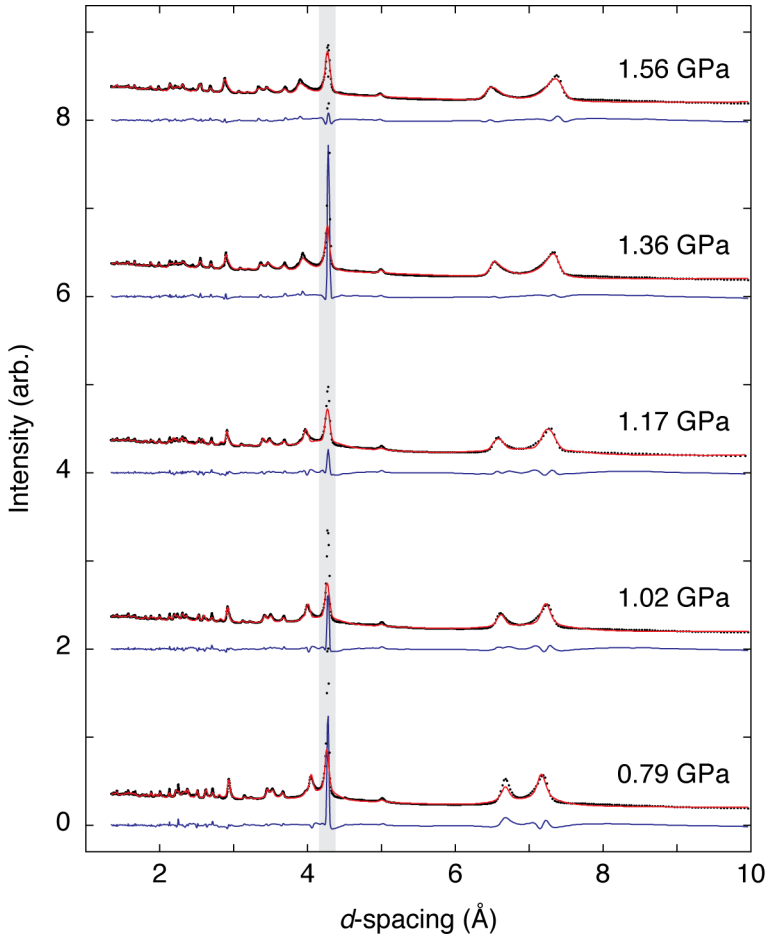

Figure C.3.14: Rietveld fits (red lines) to synchrotron powder X-ray diffraction data (filled black circles) collected for $Zn[Au(CN)_2]_2$-I. The difference (data−fit) is shown in blue under each data set. Successive data sets, fits and difference functions are shifted vertically by two units. The sharpest intense peak (the (104) reflection), for which quantitative fits are not feasible, occurs within the shaded region.

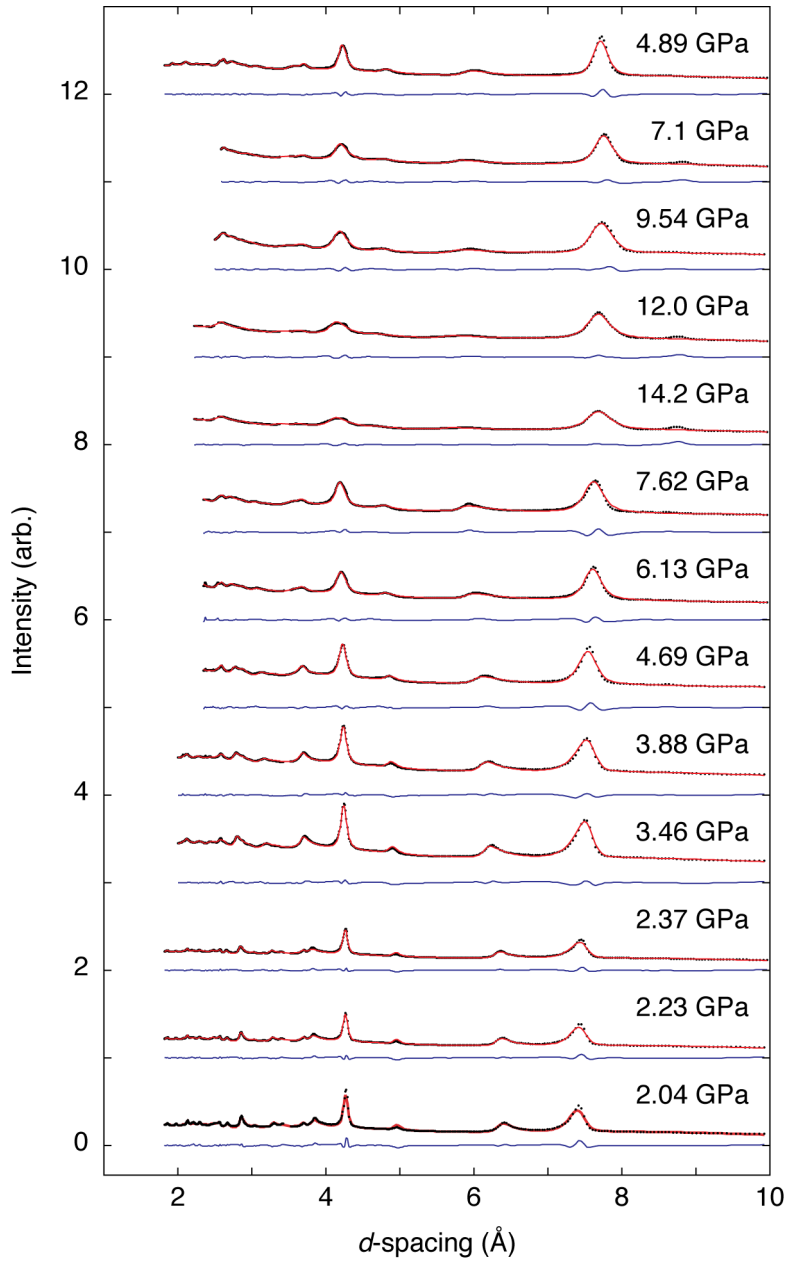

Figure C.3.15: Rietveld fits (red lines) to synchrotron powder X-ray diffraction data (filled black circles) collected for the high pressure phase $Zn[Au(CN)_2]_2$-II. The difference (data−fit) is shown in blue under each data set. Successive data sets, fits and difference functions are shifted vertically by one unit.

Table C.3.25: Variable pressure lattice parameters from synchrotron powder X-ray diffraction for $Zn[Au(CN)_2]_2$-I.

p (GPa)	a (Å)	c (Å)	V (Å^3)
0.79(10)	8.0921(22)	21.438(7)	1215.7(11)
1.02(10)	8.0051(27)	21.612(9)	1199.4(13)
1.17(10)	7.949(5)	21.700(14)	1187.6(22)
1.36(10)	7.793(7)	22.048(17)	1160(3)
1.56(10)	7.7208(28)	22.147(13)	1143.3(15)

Table C.3.26: Variable pressure lattice parameters from synchrotron powder X-ray diffraction for $Zn[Au(CN)_2]_2$-II.

p (GPa)	a (Å)	c (Å)	V (Å^3)
2.04(10)	15.227(8)	44.64(4)	8963(18)
2.23(10)	15.165(8)	44.75(4)	8913(16)
2.37(10)	15.101(7)	44.85(3)	8857(14)
3.46(10)	14.71(3)	45.27(7)	8481(50)
3.88(10)	14.570(10)	45.43(5)	8353(22)
4.69(10)	14.452(11)	45.66(5)	8260(23)
6.13(10)	14.117(19)	45.67(6)	7880(30)
7.62(10)	14.005(18)	46.19(7)	7850(30)
10.66(10)	13.73(9)	46.2(4)	7530(160)
14.22(10)	13.342(23)	45.93(13)	7080(40)

C.3.5 Raman mode frequencies

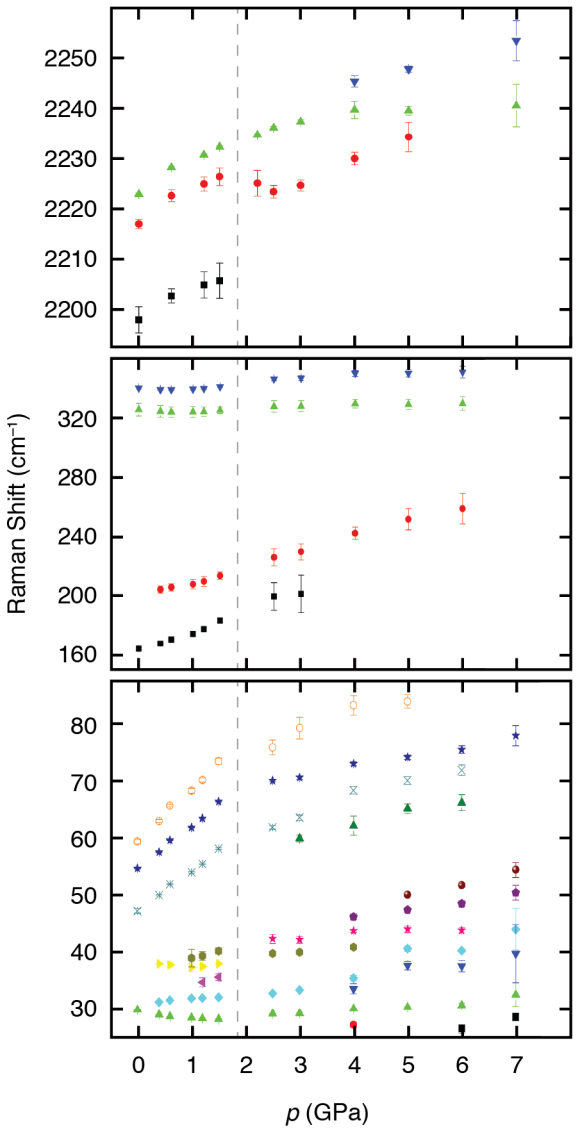

Figure C.3.16: Pressure dependence of the Raman vibrational frequencies for $Zn[Au(CN)_2]_3$ over the range $0 < p < 7$ GPa. The approximate position of the I/II phase transition is indicated by a dashed vertical line.

C.4 $Zn(CN)_2$

Full-structure Rieveld analysis was carried out using GSAS within the EXPGUI user interface. At each pressure background, scale, lattice parameters and atomic positions were refined, with a C–N and Zn–(C/N) bond distance restraint used for the high-pressure *Pbca* structure to ensure sensible bond distances in the final solution. Refinements for each pressure on compression are presented. Figure C.4.17 shows fits up to the transition pressure, Figure C.4.18 shows the co-existence of $Zn(CN)_2$-I and $Zn(CN)_2$-II at 1.53(10) GPa, as referred to in the main text, and Figure C.4.19 shows fits up to 12.2(1) GPa. Large background subtraction and significant peak broadening terms were required at the highest pressure points.

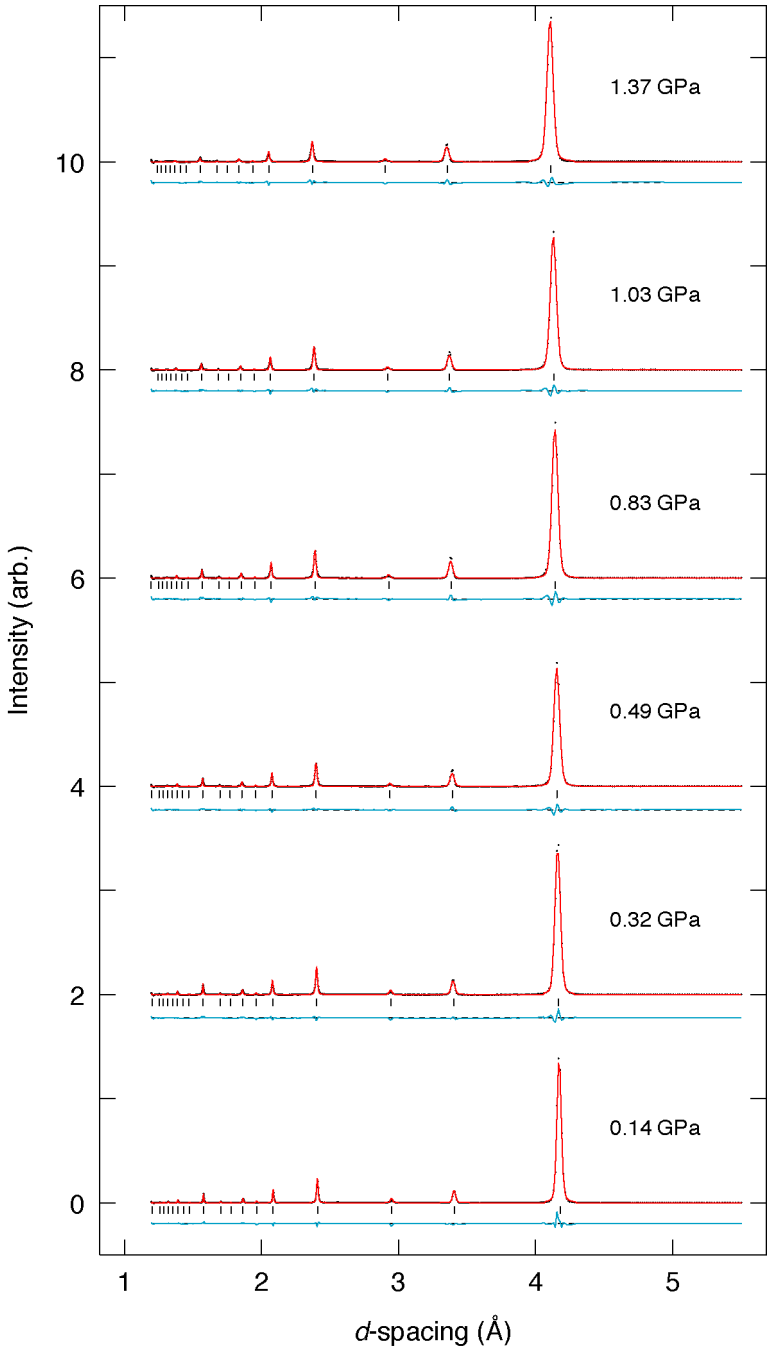

Figure C.4.17: Background-subtracted Rietveld fits (red line) to X-ray powder diffraction data (black points) for compression of $Zn(CN)_2$ up to 1.37 GPa. Estimated uncertainty in p is 0.1 GPa at all pressures and successive data sets are shifted upwards in the vertical axis by units of two. Difference curve (data−fit) shown in blue; black tick marks correspond to $Zn(CN)_2$-I.

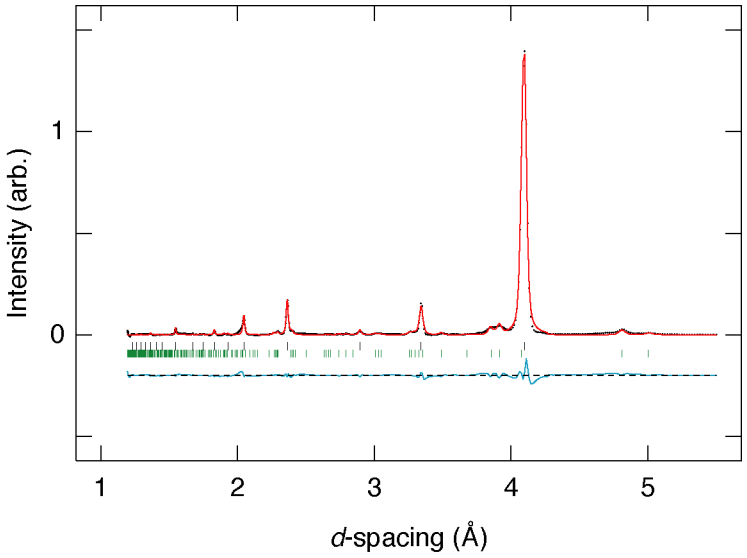

Figure C.4.18: Background-subtracted Rietveld fit (red line) to X-ray powder diffraction data (black points) for $Zn(CN)_2$ at 1.52(10) GPa. Difference curve (data−fit) shown in blue; tick marks correspond to $Zn(CN)_2$-I (black) and $Zn(CN)_2$-II (green).

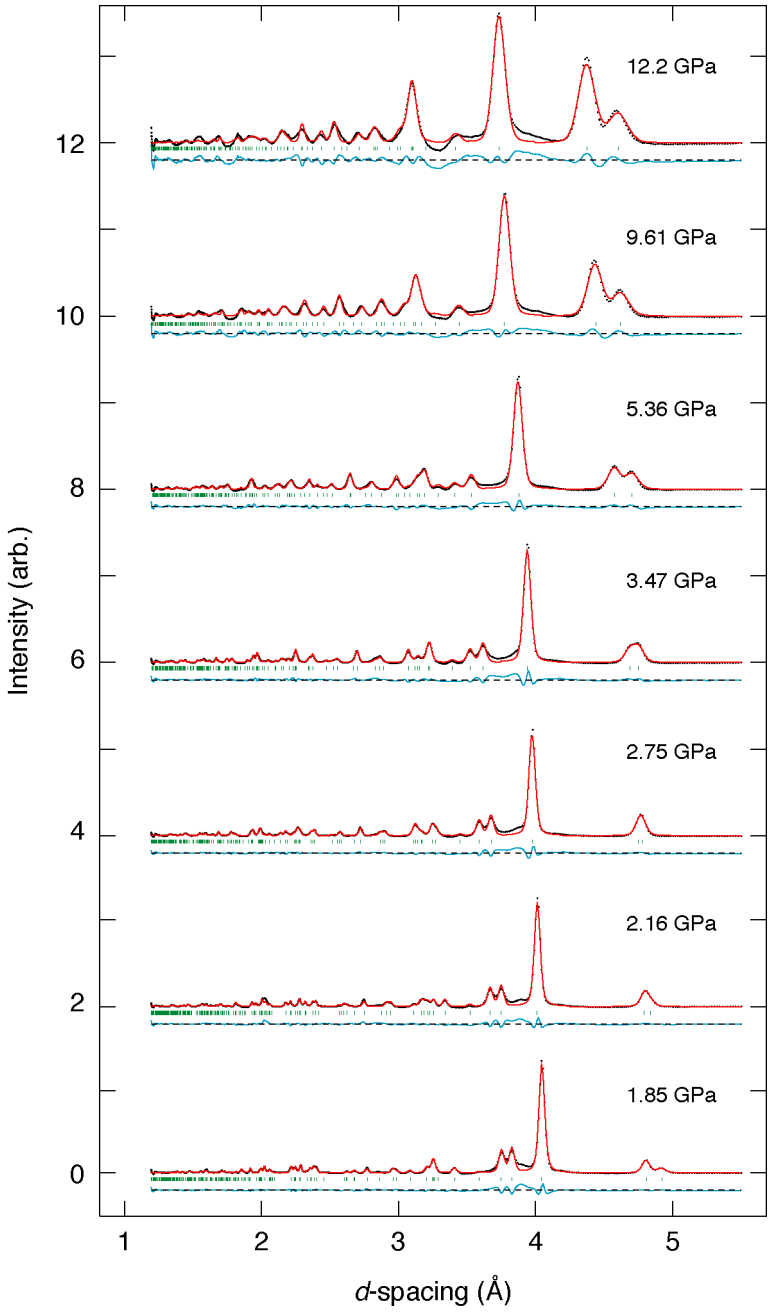

Figure C.4.19: Background-subtracted Rietveld fits (red line) to X-ray powder diffraction data (black points) for compression of $Zn(CN)_2$ from 1.85 GPa to 12.21 GPa. Estimated uncertainty in p is 0.1 GPa at all pressures and successive data sets are shifted upwards in the vertical axis by units of two. Difference curve (data−fit) shown in blue; green tick marks correspond to $Zn(CN)_2$-II.

C.4.1 Lattice parameters

Table C.4.27: Variable pressure lattice parameters from synchrotron powder diffraction for $Zn(CN)_2$-I on compression and decompression. Estimated uncertainty in p is 0.1 GPa at all pressures.

p (GPa)	a (Å)	V (Å^3)
0.14	5.89235(12)	204.582(12)
0.32	5.8790(3)	203.19(3)
0.49	5.86888(16)	202.146(16)
0.83	5.8505(4)	200.25(4)
1.03	5.8348(4)	198.64(4)
1.37	5.8011(4)	195.22(5)
1.52	5.7845(6)	193.55(6)
0.68*	5.8630(4)	201.54(4)

* Decompression

Table C.4.28: Variable pressure lattice parameters from synchrotron powder diffraction for $Zn(CN)_2$-II on compression and decompression. Estimated uncertainty in p is 0.1 GPa at all pressures.

p (GPa)	a (Å)	b (Å)	c (Å)	V (Å^3)
1.52	12.145(8)	7.817(3)	7.691(3)	731.9(11)
1.85	12.3212(18)	7.6438(9)	7.4947(10)	705.85(8)
2.16	12.445(2)	7.4891(11)	7.3283(12)	683.00(10)
2.75	12.536(4)	7.3402(17)	7.1681(19)	659.60(13)
3.47	12.585(3)	7.2242(14)	7.0350(15)	639.58(11)
5.36	12.584(4)	7.052(3)	6.8128(18)	604.57(12)
9.61	12.437(4)	6.874(3)	6.532(2)	558.48(15)
12.2	12.413(6)	6.830(4)	6.383(3)	541.18(19)
7.50*	12.492(4)	6.920(3)	6.585(2)	569.17(14)
5.47*	12.589(4)	7.009(2)	6.730(2)	593.78(14)
4.44*	12.625(5)	7.057(2)	6.806(2)	606.44(14)
3.57*	12.624(4)	7.137(2)	6.922(2)	623.65(13)
2.77*	12.627(4)	7.2315(17)	7.0525(18)	643.95(12)
1.95*	12.504(3)	7.4438(12)	7.2983(14)	679.3(3)

* Decompression.

C.4.2 Crystallographic information

Table C.4.29: Crystallographic details determined by powder X-ray diffraction for $Zn(CN)_2$-I at 0.14(10) GPa.

Space Group	$Pn\bar{3}m$				
a (Å)	5.89235(12)				
V (Å^3)	204.582(12)				
Z	2				
wR_p	0.0445				
Atom	occ	x	y	z	U_{iso} (Å^2)
Zn	1.0	0.25	0.25	0.25	0.0976(19)
C	0.5	0.4294(8)	0.4294(8)	0.4294(8)	0.059(5)
N	0.5	0.4294(8)	0.4294(8)	0.4294(8)	0.059(5)

Table C.4.30: Crystallographic details determined by powder X-ray diffraction for $Zn(CN)_2$-II at 1.85(10) GPa.

Space Group	*Pbca*				
a (Å)	12.3212(18)				
b (Å)	7.6438(9)				
c (Å)	7.4947(10)				
V (Å^3)	705.85(8)				
Z	8				
wR_p	0.0279				
Atom	occ	x	y	z	U_{iso} (Å^2)
Zn	1.0	0.1255(12)	0.0510(8)	0.7872(10)	0.069(4)
C	0.5	−0.020(3)	0.118(4)	0.288(7)	0.079(9)*
C	0.5	0.038(3)	0.236(4)	0.301(7)	0.079(9)*
C	0.5	0.240(3)	0.018(7)	0.619(4)	0.079(9)*
C	0.5	0.286(4)	0.033(7)	0.487(4)	0.079(9)*
N	0.5	−0.020(3)	0.118(4)	0.288(7)	0.079(9)*
N	0.5	0.038(3)	0.236(4)	0.301(7)	0.079(9)*
N	0.5	0.240(3)	0.018(7)	0.619(4)	0.079(9)*
N	0.5	0.286(4)	0.033(7)	0.487(4)	0.079(9)*

* U_{iso} constrained to be equivalent for all cyanides.

Table C.4.31: Crystallographic details determined by powder X-ray diffraction for $Zn(CN)_2$-II at 12.2(1) GPa.

Space Group	*Pbca*				
a (Å)	12.413(6)				
b (Å)	6.830(4)				
c (Å)	6.383(3)				
V (Å^3)	541.18(19)				
Z	8				
wR_p	0.0218				
Atom	occ	x	y	z	U_{iso} (Å^2)
Zn	1.0	0.1283(12)	0.0646(14)	0.8720(18)	0.132(8)
C	0.5	−0.043(6)	0.139(8)	0.244(10)	0.151(17)*
C	0.5	0.031(5)	0.218(6)	0.315(18)	0.151(17)*
C	0.5	0.225(7)	0.125(8)	0.637(12)	0.151(17)*
C	0.5	0.295(5)	0.140(7)	0.520(15)	0.151(17)*
N	0.5	−0.043(6)	0.139(8)	0.244(10)	0.151(17)*
N	0.5	0.031(5)	0.218(6)	0.315(18)	0.151(17)*
N	0.5	0.225(7)	0.125(8)	0.637(12)	0.151(17)*
N	0.5	0.295(5)	0.140(7)	0.520(15)	0.151(17)*

* U_{iso} constrained to be equivalent for all cyanides.

C.4.3 Zn–CN centroid distances

Table C.4.32: Calculated Zn–(CN) centroid distances, *d*. Estimated uncertainty in *p* is 0.1 GPa.

p (GPa)	d_1 (Å)	d_2 (Å)	d_3 (Å)	d_4 (Å)	d_5 (Å)	d_6 (Å)
0.14	2.5515(3)	2.5515(3)	2.5515(3)	2.5515(3)	4.8857(3)	4.8857(3)
0.32	2.5263(3)	2.5263(3)	2.5263(3)	2.5263(3)	4.8780(3)	4.8780(3)
0.49	2.5220(3)	2.5220(3)	2.5220(3)	2.5220(3)	4.8696(3)	4.8696(3)
0.83	2.5141(3)	2.5141(3)	2.5141(3)	2.5141(3)	4.8544(3)	4.8544(3)
1.03	2.5073(3)	2.5073(3)	2.5073(3)	2.5073(3)	4.8413(3)	4.8413(3)
1.37	2.5119(3)	2.5119(3)	2.5119(3)	2.5119(3)	4.8100(3)	4.8100(3)
1.52	2.4857(3)	2.4857(3)	2.4857(3)	2.4857(3)	4.7996(4)	4.7996(4)
1.85	2.446(12)	2.483(11)	2.490(10)	2.526(10)	4.161(9)	4.176(9)
2.16	2.39(3)	2.450(11)	2.547(10)	2.564(10)	3.823(9)	4.034(9)
2.75	2.412(12)	2.436(12)	2.511(11)	2.538(11)	3.852(10)	3.967(9)
3.47	2.368(10)	2.452(9)	2.539(9)	2.554(9)	3.708(8)	3.985(9)
5.36	2.350(9)	2.503(8)	2.522(8)	2.555(9)	3.463(8)	3.898(9)
9.61	2.429(10)	2.455(11)	2.478(10)	2.484(10)	3.073(10)	3.472(10)
12.2	2.339(12)	2.449(12)	2.491(12)	2.529(13)	2.948(12)	3.186(13)

Table C.4.33: Crystallographic details determined by powder X-Ray diffraction for $Zn(CN)_2$-I at 0.14(10) GPa.

Space Group	$P\bar{n}3m$				
a, Å	5.89235(12)				
V, Å^3	204.582(12)				
Z	2				
wR_p	0.0693				
Atom	occ	x	y	z	B_{iso}, Å^3
Zn	1.0	0.25	0.25	0.25	0.0976(19)
C	0.5	0.4294(8)	0.4294(8)	0.4294(8)	0.059(5)
N	0.5	0.4294(8)	0.4294(8)	0.4294(8)	0.059(5)

Estimated standard errors are given in parentheses.

Table C.4.34: Crystallographic details determined by powder x-ray diffraction for $Zn(CN)_2$-II at 1.85(10) GPa.

Space Group	Pbca				
a, Å	12.3212(18)				
b, Å	7.6438(9)				
c, Å	7.4947(10)				
V, Å^3	705.85(8)				
Z	8				
wR_p	0.0512				
Atom	occ	x	y	z	B_{iso}, Å^3
Zn	1.0	0.1255(12)	0.0510(8)	0.7872(10)	0.069(4)
C	0.5	-0.0196(31)	0.118(4)	0.288(7)	0.079(9)
C	0.5	0.0378(27)	0.236(4)	0.301(7)	0.079(9)
C	0.5	0.2397(27)	0.018(7)	0.619(4)	0.079(9)
C	0.5	0.286(4)	0.033(7)	0.487(4)	0.079(9)
N	0.5	-0.0196(31)	0.118(4)	0.288(7)	0.079(9)
N	0.5	0.0378(27)	0.236(4)	0.301(7)	0.079(9)
N	0.5	0.2397(27)	0.018(7)	0.619(4)	0.079(9)
N	0.5	0.286(4)	0.033(7)	0.487(4)	0.079(9)

Estimated standard errors are given in parentheses.

C.4.4 Lattice Parameters

Table C.4.35: Variable pressure lattice parameters from synchrotron powder diffraction for $Zn(CN)_2$-I (low pressure phase).

Run Number	p (GPa)	σ_p (GPa)	a (Å)	σ_a (Å)	V (Å^3)
9	1.52	0.1	5.7845	0.0006	193.5519166
8	1.37	0.1	5.8011	0.0004	195.2230331
7	1.03	0.1	5.83475	0.00035	198.6400236
6	0.83	0.1	5.8505	0.0004	200.2529631
5	0.49	0.1	5.86888	0.00016	202.1462499
3	0.32	0.1	5.87899	0.00032	203.1927296
2	0.14	0.1	5.89235	0.00012	204.5811459

Table C.4.36: Variable pressure lattice parameters from synchrotron powder diffraction for $Zn(CN)_2$-II (high pressure phase).

Run Number	p (GPa)	σ_p (GPa)	a (Å)	σ_a (Å)	b (Å)	σ_b (Å)	c (Å)	σ_c (Å)	V (Å^3)	σ_V (Å^3)
24	1.95	0.1	12.504	0.0026	7.4438	0.0012	7.2983	0.0014	679.3	0.1
23	2.77	0.1	12.627	0.004	7.2315	0.0017	7.0525	0.0018	643.95	0.12
22	3.57	0.1	12.624	0.004	7.137	0.002	6.9219	0.0021	623.65	0.13
21	4.44	0.1	12.625	0.005	7.0572	0.0024	6.8064	0.0022	606.44	0.14
20	5.47	0.1	12.589	0.004	7.0085	0.0024	6.7299	0.0021	593.78	0.14
19	7.5	0.1	12.492	0.004	6.9195	0.0027	6.5848	0.0023	569.17	0.14
18	12.2	0.1	12.413	0.006	6.83	0.004	6.3832	0.0034	541.18	0.19
17	9.61	0.1	12.437	0.004	6.8743	0.0029	6.5322	0.0024	558.48	0.15
15	5.36	0.1	12.584	0.004	7.0516	0.0019	6.8128	0.0018	604.57	0.12
14	3.47	0.1	12.5847	0.0032	7.2242	0.0014	7.035	0.0015	639.58	0.11
13	2.75	0.1	12.536	0.004	7.3402	0.0017	7.1681	0.0019	659.6	0.13
12	2.16	0.1	12.4449	0.0023	7.4891	0.0011	7.3283	0.0012	683	0.1
11	1.85	0.1	12.3212	0.0018	7.6438	0.0009	7.4947	0.001	705.85	0.08

C.4.5 Compressibility of $Zn(CN)_2$

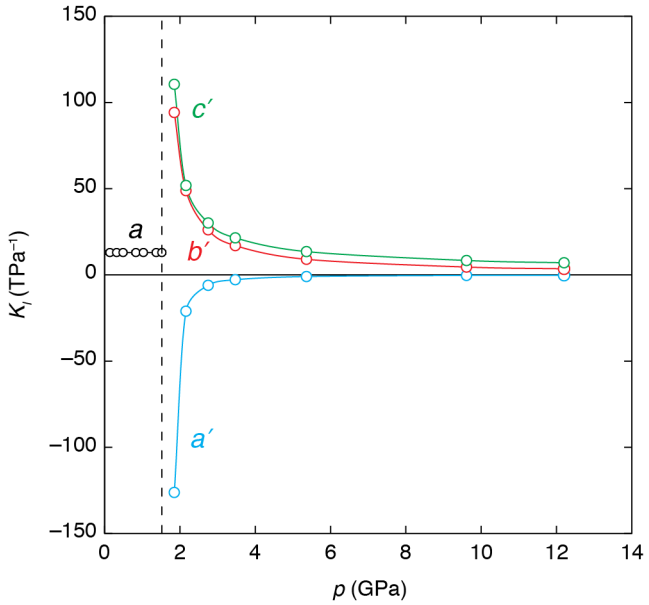

Figure C.4.20: Calculated compressibilities of $Zn(CN)_2$ across the entire pressure range studied.

C.5 $(Ag_{1/2}Au_{1/2})CN$

C.5.1 Crystallographic information

Table C.5.37: Crystallographic details determined by powder X-Ray diffraction for $(Ag_{1/2}Au_{1/2})CN$.

Space Group	$P6/mmm$				
a, Å	3.4233(6)				
c, Å	5.1560(8)				
V, Å^3	52.328(19)				
Z	0.5				
R_{wp}	7.562				
Atom	occ	x	y	z	B_{eq}, Å^3
Ag	0.5	0	0	0	1.65(8)
Au	0.5	0	0	0	1.65(8)
C	0.5	0	0	0.3833(24)	0.5(5)
N	0.5	0	0	0.3833(24)	0.5(5)

Estimated standard errors are given in parentheses.

C.6 Vp study of AgCN

Table C.6.38: Variable pressure lattice parameters from synchrotron powder X-ray diffraction up to 20.5 GPa for AgCN.

p (GPa)	a (Å)	c (Å)	V (Å^3)
0	6.067	5.2318	
0.3	5.9087(14)	5.2904(12)	159.96(8)
2.4	5.5283(5)	5.2985(13)	140.24(5)
5.65	5.2347(17)	5.2933(18)	125.61(4)
10.3	5.0444(3)	5.291(3)	116.59(7)
20.5	4.7915(8)	5.297(3)	105.32(7)

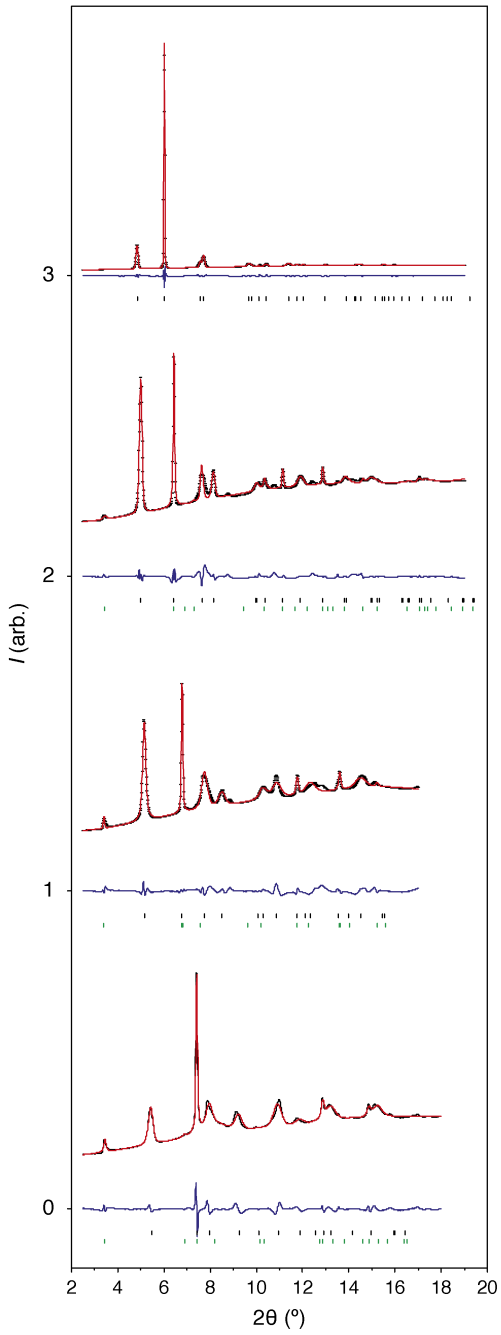

Figure C.6.21: Pawley fits (red line) to synchrotron X-ray powder diffraction data (black points) for compression of AgCN. From top–bottom, data collected at $p = 0.3$ GPa; $p = 2.4$ GPa; $p = 5.65$ GPa; $p = 20.5$ GPa. Estimated uncertainty in p is 0.1 GPa at all pressures and successive data sets are shifted upwards in the vertical axis by one unit. Difference curve (data−fit) shown in blue; green tick marks correspond to AuCN-structured AgCN-II.

Appendix D

Partial magnetic order in the frustrated antiferromagnet $Gd_2Ti_2O_7$

D.1 Background

Exotic magnetic states that arise due to geometrical frustration have been of great interest to the condensed-matter community—both theoreticians and experimentalists—for many years. Such states, where the lattice symmetry is incompatible with the magnetic interactions, give an insight into the interplay between order and disorder [460]. Geometrically frustrated systems can be categorised as either (i) spin liquids, where frustration inhibits long range order completely, and (ii) spin solids where perturbations to the frustrated interactions eventually generate magnetic order [411]. Between these two extremes a surprisingly large number of systems are known to exhibit partial magnetic order, where only some spins order at low temperature [461–467]. These partially ordered states play an important role in determining the properties of materials such as fast-ion conductors and high-pressure elemental phases [468, 469].

The frustrated antiferromagnet $Gd_2Ti_2O_7$ is a canonical partially-ordered magnetic system where the magnetic Gd^{3+} ions ($S = 7/2$) make up a pyrochlore network of corner-sharing tetrahedra [470]. At low temperature, $Gd_2Ti_2O_7$ undergoes two magnetic phase transitions ($T_1 = 1.1\,\mathrm{K}$ and $T_2 = 0.75\,\mathrm{K}$) to different states each with magnetic propagation vector $\mathbf{k} = \left[\frac{1}{2}\frac{1}{2}\frac{1}{2}\right]^*$ [471, 472]. Previous studies have identified two possible magnetic

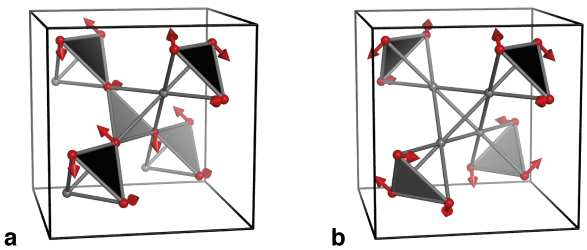

Figure D.1.1: Partially-ordered low temperature magnetic models of $Gd_2Ti_2O_7$. (a) 1-$\mathbf{k}$ and (b) 4-$\mathbf{k}$ magnetic structure candidates. In both cases only the pyrochlore of Gd^{3+} ions are shown and ordered spin sites are shown in red, the disordered site is shown in grey and the average spin orientations are shown as red arrows. A single crystallographic unit cell is shown; spin orientations are reversed in adjacent unit cells in each case.

structures below the second ordering temperature ($T \ll T_2$). These are known as the 1-**k** structure and 4-**k** structures: the former is based on a distortion with a single propagation vector, and the latter involves a superposition of the four symmetry equivalent $\mathbf{k} \in \langle \frac{1}{2}\frac{1}{2}\frac{1}{2} \rangle^*$. In both cases 3/4 of the spins participate in long-range order, as shown in Figure D.1.1 and differ by the distance between the remaining disordered (paramagnetic) spins as well as average symmetry [472]. Both candidate structures are equally constant with most experimental data, including local probes [473–475] and magnetic powder Bragg scattering [471, 472]. Evidence for the 4-**k** solution was argued in Ref. 472 on the basis of diffuse magnetic scattering data.

In contrast, recent reanalysis of magnetic total scattering neutron diffraction data is in fact consistent with the 1-**k** model and results obtained from field-dependent magnetic single crystal scattering are only consistent with 1-**k** model. Here I present results from Rietveld analysis of powder diffraction data collected on HRPD as part of this wider study—not presented here in full—of $Gd_2Ti_2O_7$ that aims to resolve this dispute. Careful analysis of the powder diffraction data does suggest a 1-**k** structure based on the subtle lowering of symmetry from cubic to rhombohedral below T_2.

D.2 Experimental

High-resolution powder diffraction measurements were performed on the HRPD diffractometer at ISIS at $T = 1.1\,\mathrm{K}$ and $T = 0.03\,\mathrm{K}$ [452]. This instrument was used as it has among the highest available reciprocal-space resolution of any neutron instrument ($\Delta Q/Q \approx 5 \times 10^{-5}$) [335, 452]. This experiment was carried out by Joseph Paddison (Oxford), Dmitry D. Khalyavin, Pascal Manuel, Aziz Daoud-Aladine and J. Ross Stewart (ISIS facility) using the same ^{160}Gd-enriched sample used in previous studies [471, 472]. For this experiment the packed into a Cu sample holder with deuterated isopropyl alcohol (d-IPA) to improve thermal contact, and then placed into a cryostat equipped with a dilution-refrigerator insert to reach the sub-Kelvin temperatures required.

D.3 Rietveld refinement results

The emergence of magnetic order in the 1-**k** low-temperature structure of $Gd_2Ti_2O_7$ involves lowering of symmetry from cubic to tetragonal. This symmetry change is not seen in the competing 4-**k** structure. This is because the magnetic domains in the 1-**k** case select different $\mathbf{k} \in \langle \frac{1}{2}\frac{1}{2}\frac{1}{2} \rangle^*$, resulting in a symmetry lowering and a different single crystal

diffraction pattern, while 4-**k** domains are related only by translational and time-reversal symmetries so on average the crystal remains cubic. Simple single crystal diffraction studies cannot distinguish these two cases however as a macroscopic 1-**k** sample is expected to contain equal populations of the four degenerate $\mathbf{k} \in \langle \frac{1}{2}\frac{1}{2}\frac{1}{2} \rangle^*$, therefore appearing identical to neutrons as the 4-**k** model.

Presence of non-cubic domain structure would be detected by powder diffraction measurements as a rhombohedral splitting of the cubic peaks. The size of this distortion depends on the magnitude of mangeto-elastic coupling and may therefore be very small, necessitating the use of a high-resolution diffraction instrument. In principle such a distortion is always present if the correct structure is 1-**k** rather than 4-**k**.

A series of Rietveld refinements to the HRPD data were performed in which the extent of rhombohedral distortion was systematically varied. Inspection of the nuclear and magnetic Bragg peaks at low time of flight showed no obvious signs of splitting at $T = 0.03\,\mathrm{K}$, however careful analysis showed a very small distortion to be present [Fig. D.3.2]. These refinements challenged even the very high-resolution of HRPD and are therefore very much part of a more complex study that aims to unambiguously confirm which model is correct.

Two models were refined against the data above and below the transition temperature using TOPAS Academic v5.0 [476]: the cubic space group that would be obtained

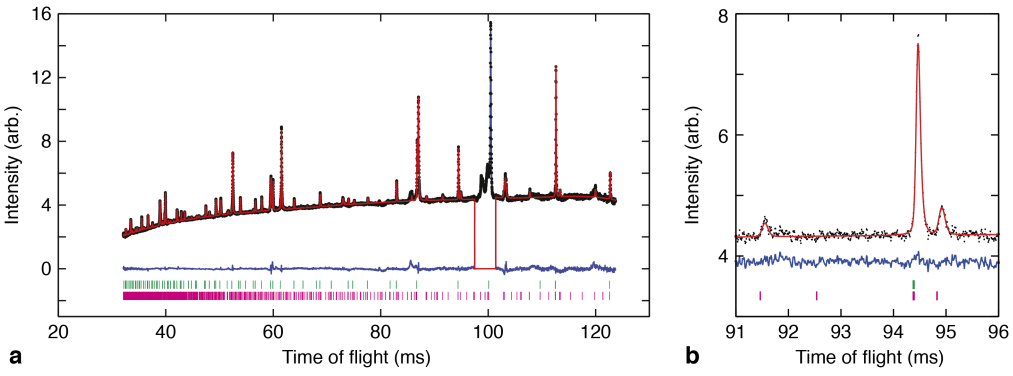

Figure D.3.2: Best fit to high-resolution powder neutron-diffraction patterns of $Gd_2Ti_2O_7$ at 0.03 K. (a) Fit to data for a distortion parameter $D = 0.00022(4)$ (as defined in the text). The region around 100 ms was excluded as it contains a large background contribution from d-IPA that could not be robustly refined. (b) Expanded region of the neutron-diffraction data and fit at high time-of-flight, showing the magnetic and nuclear peak-shapes. The magnetic peak-shape was constrained to be the same as the nuclear peak-shape convoluted with a Gaussian broadening function. In both cases experimental data are shown as black circles, Rietveld fit as a red line, and data−fit as a blue line. The upper green tick marks indicate the positions of nuclear Bragg peaks and the lower pink tick marks indicate the positions of magnetic Bragg peaks.

for a 4-**k** structure (magnetic space group $F_S\bar{4}3m$) and the rhombohedral space group obtained for a 1-**k** distortion (magnetic space group $R_I\bar{3}m$, no. 166.102). ISODISTORT was used to generate structural models in each case [344], and in each refinement the background, sample-dependent peak profile and a Pawley fit to the background Cu and V Bragg peaks were refined. The instrument-dependent peak profile was fixed [453]. The contribution from solid d-IPA could not be robustly refined but was consistent with the recently reported solid structure (space group $P21/c$) [477]; consequently a small region around 100 ms was excluded from the refinement as this contained a strong contribution from d-IPA that overlapped with sample reflections.

The degree of distortion was quantified by defining a distortion parameter

$$D = \frac{c}{\sqrt{6}a} - 1, \tag{D.3.1}$$

where a and c are the lattice parameters of the magnetic unit cell in the hexagonal setting of the rhombohedral space group $R\bar{3}m$. For the undistorted structure $D = 0$ as $c = \sqrt{6}a$ and the rhombohedral model has an identical powder diffraction pattern to the cubic 4-**k** structural model [471]. Because the distortion is expected to be subtle (if present at all) systematic refinements against data were performed where D was fixed and the dependence of the weighted-profile goodness-of-fit (R_{wp}) was recorded (allowing the unit cell volume, V to refine in each case). In the low temperature refinements, the magnetic peak shape was constrained to be equal to the (resolution-limited) nuclear peak shape, convoluted with a Q-dependent Gaussian broadening function. This broadening term corresponds to a finite magnetic domain size ξ_{domain}; the size of the magnetic moment μ_{ord} was also refined in each case.

The dependence of the goodness-of-fit (described by the weighted-profile R-factor R_{wp}) on D is shown in Figure D.3.3. For refinement to the $T = 1.1$ K data, R_{wp} has a symmetric minimum around $D = 0$; hence no lattice distortion exists in the paramagnetic phase within the resolution of our data. For refinement to the $T = 0.03$ K data however there is an asymmetric distribution and the minimum R_{wp} is found where $D > 0$. Free refinement of the a and c lattice parameters gives a rhombohedral distortion $D = 0.00022(4)$ with lattice parameters $a = 7.19352(9)$ Å and $c = 17.6244(6)$ Å. The rhombohedral distortion is statistically-significant: $|c - c_0|/\sigma(c) = 4$, where $c_0 = 17.62177(3)$ Å is obtained for refinement to the $T = 0.03$ K data with the cubic constraint $D = 0$. This behaviour also persists when the peak shape is independently refined, when a different form of

convolution is added including an asymmetric peak shape profile. The magnetic moment $\mu_{\mathrm{ord}} = 6.7(1)\,\mu_{\mathrm{B}}$ for the ordered site, consistent with previous studies [471, 472].

Finally, we investigate whether the sensitivity to this distortion arises primarily from the magnetic or nuclear peaks, by performing a further set of refinements to the $T = 0.03\,\mathrm{K}$ data where the magnetic phase was not included in the model. We find that the sensitivity of the data to a rhombohedral distortion is greatly reduced for these refinements. This result suggests that the rhombohedral distortion does not persist over the length-scale of the powder crystallites but only over the finite magnetic-domain size $\xi_{\mathrm{domain}} = 2.4(2)\times10^{3}\,\text{Å}$—an unusual behaviour that has also been reported for the small monoclinic distortion present in MnO at low temperature [478, 479].

D.4 Implications

From our refinements it can be concluded that there is evidence for a rhombohedral distortion in $Gd_2Ti_2O_7$ in the magnetically-ordered phase, but not in the paramagnetic phase. This result suggests that the low-temperature magnetic structure of $Gd_2Ti_2O_7$ is 1-**k**, in agreement with the single-crystal diffraction results in an applied magnetic field. This distortion is subtle, and the analysis used here operates close to both the resolution limit of HRPD and to the noise level in the data. Notwithstanding this, the result is statistically significant. Moreover, the same result is obtained consistently regardless of the details of the refinement (*e.g.*, choice of magnetic peak shape).

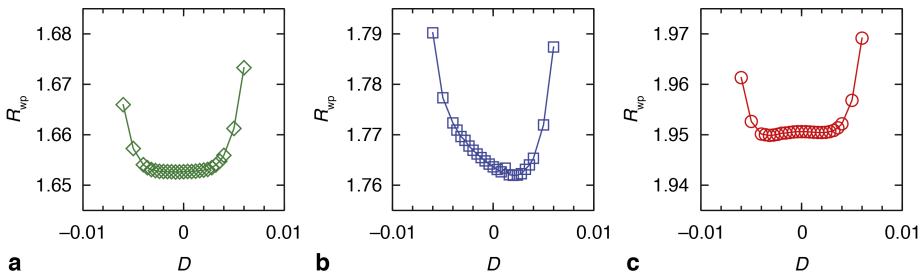

Figure D.3.3: Dependence of goodness-of-fit $R_{\mathbf{wp}}$ on the distortion parameter D (defined in the text) for Rietveld refinement to high-resolution powder neutron-diffraction data. (a) Green diamonds show refinement of the nuclear phase to $T = 1.1\,\mathrm{K}$ ($> T_1$) data, (b) blue squares refinement of the magnetic + nuclear phase to $T = 0.03\,\mathrm{K}$ ($\gg T_2$) data, and (c) red circles refinement of the nuclear phase only to $T = 0.03\,\mathrm{K}$ data.

Appendix E

Contents of CD Appendix

- An electronic copy of this thesis document.
- Variable-temperature crystallographic information files (cifs) for the $KM[M'(CN)_2]_3$ system presented in the introduction to Chapter 3.
- Variable-temperature and -pressure single-crystal cifs for $Zn[Au(CN)_2]_3$ as presented in Chapter 4.
- Variable-pressure powder cifs for $Zn(CN)_2$ as presented in Chapter 5.
- Configuration for $(Ag_{1/2}Au_{1/2})CN$ from Monte Carlo simulation as presented in Chapter 7.
- Fortran Monte Carlo programme for modelling $(Ag_{1/2}Au_{1/2})CN$ for various values of J_1, J_2, as described in the text.